

LASER ABSORPTION SPECTROSCOPY AND TOMOGRAPHY OF GAS FLOWS

A thesis submitted to The University of Manchester for the degree of

Doctor of Philosophy (PhD)

In the Faculty of Science & Engineering

2016

James Foo

SCHOOL OF CHEMICAL ENGINEERING AND ANALYTICAL
SCIENCE

LIST OF CONTENTS

LIST OF CONTENTS	2
LIST OF FIGURES	6
LIST OF TABLES	14
LIST OF ABBREVIATIONS	15
LIST OF NOMENCLATURE	16
ABSTRACT	18
DECLARATION	19
COPYRIGHT STATEMENT	20
ACKNOWLEDGEMENTS	21
1 INTRODUCTION	22
1.1 AIMS AND OBJECTIVES	22
1.1.1 DESIGNING A LINE-OF-SIGHT LASER SYSTEM TO MONITOR RELATIVE HUMIDITY	22
1.1.2 DESIGNING A 3D AND TEMPORAL TOMOGRAPHY SYSTEM	23
1.2 THESIS OUTLINE	24
2 LITERATURE REVIEW	25
2.1 CHAPTER OVERVIEW	25
2.2 OPTICAL IMAGING TECHNIQUES FOR COMBUSTION	25
2.3 CATEGORIES OF OPTICAL IMAGING TECHNIQUES	26
2.3.1 PLANAR IMAGING	26
2.3.2 TOMOGRAPHIC IMAGING	28
2.4 3D TOMOGRAPHY AND MULTIPLEXING	31
2.4.1 3D TOMOGRAPHY	31
2.4.2 MULTIPLEXING	32
2.5 CHAPTER SUMMARY	34
3 THEORY	35
3.1 CHAPTER OVERVIEW	35
3.2 NEAR INFRARED ABSORPTION SPECTROSCOPY	35
3.2.1 LINE BROADENING	37
3.2.2 BEER-LAMBERT LAW AND TWO-LINE THERMOMETRY	40
3.2.3 LINE SELECTION PROCESS	43
3.3 UNIT CONVERSIONS	44
3.4 TOMOGRAPHIC ALGORITHM	46
3.4.1 FILTERED BACK PROJECTION (FBP)	46
3.4.2 FOURIER SLICE THEOREM	48
3.4.3 ALGEBRAIC RECONSTRUCTION TECHNIQUE (ART)	49
3.5 KEY EQUIPMENT THEORY	51
3.5.1 DISTRIBUTED FEEDBACK (DFB) DIODE SEMICONDUCTOR LASER	51
3.5.2 FIBRE OPTICS	52
3.6 CHAPTER SUMMARY	53

4 TUNABLE DIODE LASER (TDLAS) LINE OF SIGHT (LOS) MONITORING IN ICE CLOUD CHAMBER	54
4.1 CHAPTER OVERVIEW	54
4.2 BACKGROUND ON SUPPRESSED SNOMAX IMMERSION FREEZING	54
4.2.1 DETAILS OF THE EXPERIMENTAL SITE	57
4.3 TDL EQUIPMENT AND SETUP DESIGN	58
4.4 RESULTS	64
4.4.1 CALIBRATIONS AND VALIDATIONS	64
4.4.2 COMPARISON OF TDLAS MONITORING WITH SIMULATION	66
4.5 CHAPTER SUMMARY	69
5 OPTICAL TOMOGRAPHY CONCEPT DESIGN AND DEVELOPMENT	70
5.1 CHAPTER OVERVIEW	70
5.2 FAN BEAM OPTICAL TOMOGRAPHY SYSTEM	70
5.2.1 EQUIPMENT ARCHITECTURE OF FAN BEAM TOMOGRAPHY SYSTEM	70
5.2.2 DEVELOPMENTS TO ORIGINAL PUBLICATION	73
5.2.3 WAVEFORM MODULATION, PEAK SELECTION AND ANALYSIS	74
5.2.4 RESULTS OF FAN BEAM TOMOGRAPHY EXPERIMENT	83
5.2.5 CHALLENGES	84
5.3 DESIGN OF TEMPORAL AND 3D TOMOGRAPHY SYSTEM	86
5.3.1 FRAMEWORK AND DIRECTION OF TOMOGRAPHY ALGORITHM	86
5.3.2 DESIGN ITERATION OF 3D TOMOGRAPHY SYSTEMS	88
5.3.3 EQUIPMENT AND SETUP DESIGN OF TEMPORAL AND 3D TOMOGRAPHY SYSTEM	91
5.3.4 BURNER DETAILS	95
5.3.5 SATISFYING THE DESIGN FRAMEWORK	101
5.4 CONTRIBUTIONS, DEVELOPMENTS AND CHAPTER SUMMARY	102
6 IMPLEMENTATION, COMPARISON AND VALIDATION OF TOMOGRAPHY ALGORITHMS	103
6.1 CHAPTER OVERVIEW AND EXPERIMENTAL CONDITIONS	103
6.1.1 EXPERIMENTAL CONDITIONS	103
6.2 DATA PRIMING	103
6.3 FILTERS AND ZERO PADDING	105
6.3.1 VARIATION OF ZERO PADDING	107
6.4 FILTERED BACK PROJECTION (FBP)	109
6.5 FOURIER SLICE RECONSTRUCTION (FSR)	115
6.6 DIRECT FOURIER RECONSTRUCTION (DFR)	119
6.7 VALIDATIONS	123
6.7.1 ANALYSING THE RECONSTRUCTED IMAGE	123
6.7.2 VALIDATION USING RADON SLICES AND THERMOCOUPLE	124
6.7.3 PHANTOM VALIDATIONS	127
6.8 SIMULATIONS OF VARYING DATA SAMPLING CONDITIONS	129
6.9 COMPARISON OF METHODS	133
6.10 CHAPTER SUMMARY	135
7 3D AND TEMPORAL TOMOGRAPHY RESULTS	136
7.1 CHAPTER OVERVIEW	136
7.1.1 EXPERIMENTAL CONDITIONS	136
7.2 3D RECONSTRUCTIONS	136
7.3 TEMPORAL EXPERIMENTS	144
7.4 IMAGE RESOLUTION	146
7.4.1 PIXEL RESOLUTION VARIATION	147

7.4.2	SPATIAL RESOLUTION	149
7.5	REPEATABILITY	154
7.6	CHAPTER SUMMARY	154
8	DISCUSSION, CONCLUSIONS AND FURTHER WORK	156
8.1	ON THE DESIGNING OF LINE-OF-SIGHT (LOS) LASER SYSTEM	156
8.1.1	SHORT NOTE ON DESIGNING THE LOS SYSTEM FOR MICC	156
8.1.2	REVIEW OF AIMS AND OBJECTIVES OF LOS SYSTEM FOR MICC	156
8.1.3	CONCLUSIONS ON THE LOS SYSTEM FOR THE MICC	157
8.2	ON THE DEVELOPMENT OF TOMOGRAPHY SYSTEM	157
8.2.1	SHORT NOTE ON DEVELOPING THE TOMOGRAPHY SYSTEM	157
8.2.2	REVIEW OF AIMS AND OBJECTIVES ON DEVELOPING THE TOMOGRAPHY SYSTEM	158
8.2.3	CONCLUSIONS ON DEVELOPING THE TOMOGRAPHY SYSTEM	159
8.3	FUTURE WORK AND POTENTIAL APPLICATIONS	160
8.3.1	FUTURE WORK	160
8.3.2	POTENTIAL APPLICATIONS	161
9	REFERENCES	162
10	PUBLICATIONS AND ACHIEVEMENTS	175
10.1	UNIVERSITY OF MANCHESTER	175
10.2	OTHERS	175
10.3	PENDING PUBLICATION	175
11	APPENDICES	176
11.1	ORIGINAL HORIZONTAL SLICES FOR 3D TOMOGRAPHY	176
11.2	TOMOGRAPHY MOTOR CONTROL AND DATA ACQUISITION	177
11.2.1	OVERVIEW	177
11.2.2	MOTOR OPERATION LOOP	177
11.2.3	LASER CONTROL	177
11.2.4	PRIMARY DATA ACQUISITION LOOP	178
11.2.5	OUTPUT SAVE LOOP	178
11.3	SPECTRUM FITTING	182
11.3.1	OVERVIEW	182
11.3.2	WHILE-LOOP USED TO OPEN PROJECTION FILES	182
11.3.3	FOR-LOOP TO SEPARATE AND PROCESS RAY DATA	182
11.3.4	FILE SAVING	183
11.4	FILTERED BACK PROJECTION (FBP) USING MATLAB	186
11.4.1	OVERVIEW	186
11.4.2	PREPPING DATA FOR RECONSTRUCTION	186
11.4.3	INTERPOLATION OF DATA IN BETWEEN RAYS	187
11.4.4	DECREASING THE INTERVAL BETWEEN EACH STEP SIZE	188
11.4.5	CREATING THE FILTER	188
11.4.6	RECONSTRUCTION	188
11.4.7	RECOVERY OF SPATIAL TEMPERATURE DISTRIBUTION	190
11.4.8	RECOVERY OF SPATIAL CONCENTRATION DISTRIBUTION	190
11.4.9	MATLAB CODES	190
11.5	FOURIER SLICE RECONSTRUCTION (FSR) USING MATLAB	198
11.5.1	OVERVIEW	198
11.5.2	PREPPING DATA FOR RECONSTRUCTION	198
11.5.3	INTERPOLATION OF DATA IN BETWEEN RAYS	198
11.5.4	DECREASING THE INTERVAL BETWEEN EACH STEP SIZE	198
11.5.5	ZERO PADDING THE DATA	198

11.5.6	FILTERING AND RECONSTRUCTION	199
11.5.7	RECOVERY OF SPATIAL TEMPERATURE DISTRIBUTION	200
11.5.8	RECOVERY OF SPATIAL CONCENTRATION DISTRIBUTION	200
11.5.9	FOURIER SLICE RECONSTRUCTION (FSR) MATLAB CODES	200
11.6	DIRECT FOURIER RECONSTRUCTION (DFR) USING MATLAB	210
11.6.1	OVERVIEW	210
11.6.2	PREPPING DATA FOR RECONSTRUCTION	210
11.6.3	INTERPOLATION OF DATA IN BETWEEN RAYS	210
11.6.4	DECREASING THE INTERVAL BETWEEN EACH STEP SIZE	210
11.6.5	ZERO PADDING THE DATA	210
11.6.6	FILTERING AND RECONSTRUCTION	210
11.6.7	RECOVERY OF SPATIAL TEMPERATURE DISTRIBUTION	212
11.6.8	RECOVERY OF SPATIAL CONCENTRATION DISTRIBUTION	212
11.6.9	FOURIER SLICE RECONSTRUCTION (FSR) MATLAB CODES	212

LIST OF FIGURES

Figure 1 Simplified example of a PLIF experimental setup.[18]	27
Figure 2 NIR line list for H ₂ O and CO ₂ , at room temperature based on HITRAN 2012 and extracted from www.spectralcalc.com .	29
Figure 3 (a) Simplified example schematic of fan beam optical tomography setup. (b) Distribution of laser projections (green) in 5 'fans' of 11 projections over two heaters (purple).	30
Figure 4 (a) Current ramps of Laser 1 and 2. (b) Photodetector signal with both laser's attenuation signals.	33
Figure 5 (a) Current ramp of both Lasers 1 and 2. (b) Photodetector signals, each with individual laser attenuation signal.	33
Figure 6 The change in dipole moment (shown in green) produced by different vibration (a) for ν_1 , (b) for ν_2 , (c) for ν_3) of the water molecule.[161]	36
Figure 7 Vibrational levels and the types of transitions. x	36
Figure 8 NIR line list for H ₂ O at room temperature with the lasers utilised in research shown. Based on HITRAN 2012 line list obtained from www.spectralcalc.com .	37
Figure 9 (a) The characteristics of an absorbent peak (b) The uncertainty principle is depicted in the shaded area of ΔE_1 and ΔE_2 .	38
Figure 10 (a) The damped oscillation profile, where X_0 is the initial amplitude, decreasing as time (t) is increased (b) The normalised frequency distribution profile of the damped oscillation after being Fourier transformed. γ is the damping constant ω_0 while ω is the frequency no damping.	38
Figure 11 The comparison of the Lorentzian line profile with the Gaussian line profile.	39
Figure 12 The depiction of absorption process with a sample cell of length L.	40
Figure 13 Example of object in 2D function (x, y) with individual line integrals forming a Radon Transform.	47
Figure 14 The translation of projection slices from the space domain to the frequency domain Fourier slices via Fourier Transform.	48
Figure 15 Superimposed grid over object, with the ratio of cell exposed to passing projection located within points ABCD.	50
Figure 16 (a) The population distribution for energy levels at thermal equilibrium (b) Population inversion occurs at higher level	51
Figure 17 (a) The bandgap between the semiconductor terminals. The conduction band or the n-type, contributes the free electrons while the valence band, the p-type, contains valence electrons or the holes for recombination. (b) The layout of the semiconductor diode laser (c) Depiction of stimulated emission in the active layer.	51
Figure 18 (a) The layout of a DFB laser (b) The reflected portions of stimulated photons from the grating.	52
Figure 19 The schematic of a fibre optic, with the core is wrapped by the cladding. The light propagating through the core is shown in red.	53
Figure 20 The radiation budget of incoming solar radiation and outgoing longwave radiation.[2]	55

-
- Figure 21 The schematic of the MICC. The locations of the temperature probes (T) are listed in red, pressure probes (P) as grey, chilled mirror as (CM) and the TDLAS system (TDL) as green. 57
- Figure 22 The schematic and relevant photos of the equipment setup. 59
- Figure 23 Schematic of laser path length and location of key equipment. The red arrow depicts laser path, while black arrows depict fibre optic cables. 60
- Figure 24 The simulated H₂O absorption spectra at 296 K accessible by the laser at different laser temperatures. Extracted from HITRAN 2012 from www.spectralcalc.com. 61
- Figure 25 Voltage modulation waveform used for tuning the laser wavenumber is shown in red. The blue signal represents the signal acquired at the end of the photodetector with the laser passing through a Fabry-Perot etalon. 62
- Figure 26 A transmission fitting of a sample experimental spectrum. The experimental spectrum is in dashed green, the fitted spectrum is blue and the residual of the fit is in red (secondary y-axis). 62
- Figure 27 Line strengths above threshold deemed significant enough to contribute to peak fitting process. Extracted from HITRAN 2012 at room temperature from www.spectralcalc.com. 63
- Figure 28 The known parameters are shown in green. The integrated absorbance data from the calibration is shown in red and the number density calibration process shown in blue. 64
- Figure 29 The comparison of the chilled mirror hygrometer sampling against the TDL sampling at constant pressure of 0.99 atm and at similar temperature. 66
- Figure 30 Taken from E. Simpson's first year PhD report, the simulation of the cloud parcel with the relative humidity of 2 separate scenarios at the same expansion speed. The first scenario, marked in green involves only IN particles, where super saturation occurs, of which the relative humidity of water falls as ice crystals are formed. The second scenario, marked as red involves the mixture of CCN and IN particles, and does not form any ice crystals as the relative humidity did not decrease and stayed at saturation throughout. [197] 67
- Figure 31 The monitoring of relative humidity change per time with error bars (blue). The red dots mark the decrease of pressure over time. 68
- Figure 32 Photo of fan beam tomography system setup. 71
- Figure 33 Diagram and description of fan beam system. 71
- Figure 34 Example of laser projection travelling from source and directed by mirrors on the laser platform. 72
- Figure 35 Example of laser projection being directed by mirror into the photodetector on the detector platform. 72
- Figure 36 Voltage modulation waveform used for current ramping of laser. The photodiode output is given in red and the same signal passed through a Fabry-Perot etalon is shown in blue. 74
- Figure 37 Simulated H₂O absorption spectra at four different temperatures (296 K, 696 K, 896 K, 1096 K) using HITRAN 2012 at different laser operating temperatures (15 °C , 23 °C , 30 °C , 35 °C). Obtained from www.spectralcalc.com. 75
- Figure 38 Zoomed in portion of Figure 37 for regions of wavelength accessible by laser at 30°C and 35°C. 77
-

-
- Figure 39 Zoomed in portion of Figure 37 for regions of wavelength accessible by laser at 15°C and 23°C. 78
- Figure 40 Depicts the changes of line strength of peaks 4b (blue) and 4a (red) with temperature (left vertical axis). The ratio of the two line strengths as a function of temperature is shown in green (right vertical axis). 79
- Figure 41 Fitting of a sample spectrum after wavenumber conversion. The experimental spectrum is in blue, with the peak fitting in red dashes (both left vertical axis). The residual is in green (right vertical axis). 80
- Figure 42 Relative wavenumber as a function of data points. 80
- Figure 43 Line strengths above threshold deemed significant enough to contribute to peak fitting process. Extracted from HITRAN 2012 at room temperature from www.spectralcalc.com. 81
- Figure 44 Laser operating at 15°C wavenumber sweep from 7179.2 cm⁻¹ to 7183.4 cm⁻¹ in comparison to HITRAN 2012 data simulated at same experimental conditions. Simulation data obtained from www.spectralcalc.com. 82
- Figure 45 Line-of-sight of H₂O integrated absorbance at 7181.93 cm⁻¹ at ambient temperature of 296 K and relative humidity of 42%. 83
- Figure 46 (a) Experiment results of 3D visualisation of 2D temperature spatial distribution over the two heaters. (b) Thermocouple validations of the experiment at the same heater settings and configuration. 84
- Figure 47 Various views and drawing of the first iteration of 3D tomography system. 88
- Figure 48 (a) Overall view of the full setup from the top. (b) The corresponding photo of the setup, with each primary section boxed out in blue (Exoskeleton), green (Rotator) and red (Carrier). (c) Exploded view of the setup, with each primary section removed for a clearer view of the individual segments. 90
- Figure 49 Alternative views of the final design, with simplified annotations of main components. 91
- Figure 50 All the dimensions of the setup are in (cm). The Exoskeleton is located in the blue section, the Rotator in the green section and the Carrier in the red section. (Green Rotator section) The red object indicates the burner. The detector is the rectangle in blue and the laser source is the rectangle in purple. (Red Carrier section) The pulleys are indicated by the green rectangles. 92
- Figure 51 The schematic layout of the software control loop. The laptop is coloured in grey and signifies the main control interface. It communicates with the motor via LabVIEW through the servo motor controller PCB. The motor is then activated and moves the rotating carriage. The DAQ (teal) controls the rest of the equipment setup. The DAQ handles both output commands as well as input commands. The output actions are listed in pink and the input data receiving is in blue. The DAQ controls both the laser current and temperature controller, which is connected to the butterfly mount. The laser sitting on the mount will lase through a 1 x 4 coupler across the one side of the rotating carriage to the other end. The detectors will receive the signal and send it back to the laptop via the DAQ. 93
- Figure 52 The dimensions of the image are provided in (cm). The Rotator is pictured as the outer black square while the Carrier is pictured as the inner
-

- black square. The layout of laser source emitters (cyan rectangles) and photo detectors (green rectangles) are shown sitting on the Rotator. Four laser beams are shown as red. Two yellow discs located are located in the centre of the Carrier. The current layout of this arrangement is pictured at theta at 0 degrees. The locations of the laser source emitters and Rotator mid point are located in the bottom of the figure in (cm). The mid point of the rotator is 18.5 cm. 94
- Figure 53 The top view of the 9cm in diameter burner plate and the image of the fuel canister used. The perforated edge along the circumference is the holes where the gas exits from the gas canister. 96
- Figure 54 Selected frames from a video recording of the adjustment of a burner, from gas notch 2 to gas notch 3. Video was recorded using GoPro HERO4, 12 MP at 32 fps. 97
- Figure 55 (a) A sample image of collected integrated absorbance through the laser beams along the angle of projection. (b) Compiled integrated absorbance along the angle of projection. (c) A compiled sinogram of each projection slice (Radon slice) at each projection angle of sampling. 104
- Figure 56 A sample Fourier transformed signal from Section 6.5 with different sample filters and their shape and cut off points. 105
- Figure 57 The effects of varying the degree of zero padding. The intensity of 'salt and pepper' noise could be seen diminishing as the degree of zero padding increases. No discernable improvement could be observed above zero padding of 700. However a trade off over computational time occurs with the increment of zero padding. 107
- Figure 58 The sampled and expanded version of zero padded images as shown in the results section. Note that deficient zero padding creates 'salt and pepper' noise in the reconstructed image, more notably present in high temperature zones. 108
- Figure 59 Methodology of programming pathways for applying the FBP technique in MATLAB 109
- Figure 60 Flow chart of how the experimental data were primed for reconstruction and the procedures of the reconstruction procedures of FBP method. 109
- Figure 61 Walkthrough of MATLAB execution of the Filtered Back Projection method. 110
- Figure 62 Sample sinograms of peaks 1 and 2. Peak 1 corresponds to 7181.93 cm⁻¹ and Peak 2 corresponds to 7179.8 cm⁻¹. 111
- Figure 63 The ramp filter is shown in the left with its impulse function depicted on the left. 111
- Figure 64 Example of the back smearing process. On the left (a), the integrated absorbance is not divided equally among the number of cells travelled, resulting in twice the amount of integrated absorbance at the end. On the right (b), the integrated absorbance is divided equally among the total amount of cells travelled, resulting in the correct final value coming out of the grid. 112
- Figure 65 Comparison of two image grids. (a) Grid of arbitrary values (b) Grid of values 3 times larger than grid a. Both grids yields the same image with respect to their number scale even though their values are different within

-
- each cell. This is due to the fact that the image is constructed based on the ratios each cell relative to their neighbours. 112
- Figure 66 Comparison of sample experiment integrated absorbance distribution of two peaks. Even though the images look different at this point, once the correct temperature dependent line strength is applied to each cell with respective to their corresponding absorption peaks, the final concentration distribution will yield the same result. 113
- Figure 67 The reconstructed temperature and water concentration distribution using the FBP method. 114
- Figure 68 Flow chart of the procedures of the reconstruction procedures of FSR method. 115
- Figure 69 Walkthrough of MATLAB execution of the Fourier Slice Reconstruction method. 116
- Figure 70 Fourier transformed sinograms as compared to previous sinograms in Figure 62. 117
- Figure 71 (a) Fourier transform projection slice sample of sinogram 1 at projection angle 0. (b) Fourier transformed projection slice of sinogram 2 at projection angle 0. (c) Filtered projection slice sample of sinogram 1 at projection angle 0. (d) Filtered projection slice sample of sinogram 2 at projection angle 0. 117
- Figure 72 Back smeared reconstructed images of integrated absorbances of peaks 1 and 2. 118
- Figure 73 Cropped reconstructions of integrated absorbance distributions of peaks 1 and 2. 118
- Figure 74 The temperature and concentration distribution sample images reconstructed by the FSR method. 118
- Figure 75 Flow chart of the procedures of the reconstruction procedures of DFR method. 119
- Figure 76 Walkthrough of MATLAB Direct Fourier Reconstruction implementation. 120
- Figure 77 Example of how the spatial domain projection slices are converted to the frequency domain. The Fourier transformed slices are allocated in the polar coordinates in the frequency domain grid, and requires conversion to Cartesian distribution prior to interpolation. 121
- Figure 78 Allocated Fourier slices interpolated into the frequency domain of Peaks 1 and 2. 121
- Figure 79 Conversion from a 1D ramp filter to a 2D ramp filter. 121
- Figure 80 The temperature and concentration distribution sample images reconstructed by the DFR method. 122
- Figure 81 The correlation between the reconstructed temperature image with the schematics and photo of flame exit points of the burner. Burner 1 is the back burner, while Burner 2 is the front burner. 123
- Figure 82 (a) The numerical comparison of experimental (green) integrated absorbance at radon slice of projection angle 0 with Filtered Back Projection method reconstructed (blue) integrated absorbance at radon theta 0. (b) The reconstructed integrated absorbance image of Peak 2 that was used for the validation process. 125
-

-
- Figure 83 Comparison of thermocouple sampling of the optical plane with FBP reconstruction presented in ($^{\circ}\text{C}$). Note the difference in temperature scale of both images. 125
- Figure 84 (a) The numerical comparison of experimental (green) integrated absorbance at radon at theta 0 with Fourier Slice Reconstruction method reconstructed (blue) integrated absorbance at radon theta 0. (b) The reconstructed integrated absorbance image of Peak 2 that was used for the validation process. 126
- Figure 85 Comparison of thermocouple sampling of the optical plane with FSR reconstruction presented in ($^{\circ}\text{C}$). Note the difference in temperature scale of both images. 126
- Figure 86 (a) The numerical comparison of interpolated (green) integrated absorbance at radon slice of projection angle 0 with Direct Fourier Reconstruction method reconstructed (blue) integrated absorbance at radon theta 0. (b) The reconstructed integrated absorbance image of Peak 2 that was used for the validation process. 127
- Figure 87 Comparison of thermocouple sampling of the optical plane with DFR reconstruction presented in ($^{\circ}\text{C}$). Note the difference in temperature scale of both images. 127
- Figure 88 Depiction of flame patterns via photograph and schematic, compared to thermocouple sampling with image reconstructions for a sample scenario. 128
- Figure 89 Three different scenarios with different flame patterns. Scnerio A depicts both burners in operation, B with the back burner in operation and front burner off and C with back burner off and front burner in operation. 128
- Figure 90 The comparison of reconstruction methods with a Phantom image. The reconstruction methods are based on sampling the original Phantom under experimental conditions of 4 known data per projection slice. 130
- Figure 91 The comparison of reconstruction methods with a Phantom image. The reconstruction methods are based on full sampling of the original Phantom, and have a data-sampling ratio of 55 data to 37 cm per radon projection angle. The ratio to colour representation scale is set to be the same for direct value comparison. 131
- Figure 92 Both (a) and (b) depicts the same exact Filtered Back Projection reconstructed image, with a different ratio to colour representation scale. In (a), the ratio value to colour scale is consistent as Figure 91, while in (b) is set with respect to contrast base on its own variation in numbers within the image. 132
- Figure 93 Sample of steaks of artefacts known as beam hardening, circled in green. The last image is left untouched for uninhibited viewing. 133
- Figure 94 Sample of potential helical artefacts are circled in white. Sample of steaks of artefacts known as beam hardening are circled in green. The last image is left untouched for uninhibited viewing. 134
- Figure 95 Visual representation of how the Carrier moves down a stationary optical plane instead of the optical plane moving around the object of study. (a) The Carrier at position 1 (optical plane 1 cm above burners). The red line depicts the position of the stationary optical plane. (b) The Carrier moves down, thus lengthening the distance from the optical plane. (c) The z-
-

-
- axis that is shown here represents the total distance between first and final position of the carrier with respect to optical plane to flames. 137
- Figure 96 The individual reconstructed temperature slices vertically spaced 1 cm apart shown in 2 views. The slice at the bottom is the slice closest to the flames, which registers higher temperatures. View-1 depicts a tighter configuration of 75% transparent slices to simulate a translucent volume. View-2 shows similar 75% transparent slices that are more spaced out, with the maximum temperatures and locations by the two burners marked out. 138
- Figure 97 Visual representatives of the locations of vertical slices (shown in red) moving across the x-axis within the 3D boundary shown via the orange cuboid. 138
- Figure 98 Individual vertical slices of interpolated temperature with respect to the x-axis, from -17 cm to 17 cm. Note that vertical slice of x-axis at -18 cm and 18 cm were omitted from this figure. 139
- Figure 99 Individual vertical slices of interpolated temperature with respect to the y-axis, from -17 cm to 17 cm. Note that vertical slice of y-axis at -18 cm and 18 cm were omitted from this figure. 140
- Figure 100 Sample of vertical temperature slices moving along the x-axis. 141
- Figure 101 The location of the vertical slices is each shown on the top row as a red line superimposed on the bird eye view of the bottom most z-axis plane. The temperature and concentration vertical slices are individually shown below their slice location. 141
- Figure 102 The location of the vertical slices is each shown on the top row as a red line superimposed on the bird eye view of the bottom most z-axis plane. The temperature and concentration vertical slices are individually shown below their slice location. 142
- Figure 103 The combined volume is made of 51 slices from the x-axis (-25 cm to 25 cm) and 51 slices from the y-axis (-25 cm to 25 cm). Each slice is set at a transparency of 95% to create a final “translucent” looking volume. 143
- Figure 104 The location of the back burner (A) and the front burner (B) shown in both schematic and reconstructed image. 144
- Figure 105 Temporal results of temperature distribution with time. The time taken for reconstruction since experimental start time (0 s) is shown in orange while the gas regulator notch settings of each burner is identified under Burner A and Burner B. 145
- Figure 106 Variation of pixel resolution to the same image. 147
- Figure 107 Resulting reconstructions from variation of theta step size with number of projections 149
- Figure 108 Zoomed in view of 2 sets of line-pairs structures to allow clearer view of smaller line-pairs structures, ranging from 0.5 to 5 lp/cm. The original dimension of the phantoms is 36 by 36 cm. 151
- Figure 109 Zoomed in view of reconstruction using 512 equally spaced beams per projection. 152
- Figure 110 Comparison of simulations of different beams per projection simulation scenarios, where 37 beams per projection mimic the experimental scenarios. 153
- Figure 111 Consecutive reconstructions in the span of 1 minute. 154
- Figure 112 Individual 2D measurement slices in the z-axis. 176
-

Figure 113 The front panel of the data acquisition program.	179
Figure 115 Exploded version of the laser current output section from the block diagram.	181
Figure 116 Front panel of the peak-fitting program.	183
Figure 118 The expanded sub-VI block diagram of the curve fitting model.	185

LIST OF TABLES

Table 1 Sample TAS TDL research conducted on H ₂ O and CO ₂	28
Table 2 The coefficients for the partition function of H ₂ O. (Low and medium temperature range). [168]	43
Table 3 Comparison of number density and integrated absorbance values of water during calibration process	65
Table 4 Details of fan beam tomography equipment setup	73
Table 5 Parameters of polynomial relationship between line strength ratios as a function of temperature.	79
Table 6 Parameters of polynomial relationship between relative wavenumber as a function of data points.	81
Table 7 Summary table of reconstruction method comparison	135
Table 8 Relationship of theta step size with number of parallel projections	150
Table 9 Review of MICC experiment objectives.	156
Table 10 Review of tomography experiments objectives	158

LIST OF ABBREVIATIONS

1D – One-dimensional
2D – Two-dimensional
3D – Three-dimensional
ART- Algebraic reconstruction technique
APCIM - Aerosol Cloud Precipitation Interaction Model
APCVD – Atmospheric pressure chemical vapour deposition
CCN – Cloud condensation nuclei
CVD – Chemical vapour deposition
DFB - Distributed feedback diode laser
FBP - Filtered back projection
FWHM - Full width at half maximum
GHG – Green house gases
HST - hyperspectral tomography
IN – Ice nuclei
LAS - Laser absorption spectroscopy
LIF – Laser-induced fluorescence
MICC - Manchester Ice Cloud Chamber
MRI – Magnetic resonance imaging
NIR - Near infrared
PCA- Principal Component Analysis
PLIF – Planar laser-induced fluorescence
POD–Proper Orthogonal Decomposition
TDL – Tunable diode laser
TDLAS – Tunable diode laser absorption spectroscopy
TDM-Time-division multiplexing
UNFCCC - United Nation Framework Convention on Climate Change
UV- Ultraviolet
VCSEL - Vertical cavity surface emitting laser
WDM - Wavelength-division multiplexing

LIST OF NOMENCLATURE

A	Integrated absorbance/ area under the absorption peak.
c	Speed of light in vacuum ($c=2.99792458 \times 10^8 \text{ m s}^{-1}$)
C	Concentration (mol cm^3)
C_{ppm}	Concentration (ppm)
d_i	State-independent degeneracy factor
d_s	State-dependent degeneracy factor
ΔE	Change in energy
E_2, E_1	Higher energy, lower energy
E_i''	Lower-state energy of the transmission (cm^{-1})
E_s	Energy of state
$g(\bar{\nu} - \bar{\nu}_0)$	Normalised line shape function (cm)
g_l	Statistical weight in lower state
g_u	Statistical weight in upper state
h	Planck constant ($6.62606876 \times 10^{-34} \text{ J s}$)
\hbar	Reduced Planck's constant ($\frac{h}{2\pi}$)
$I_0(\bar{\nu}), I_t(\bar{\nu})$	Incident intensity, transmitted intensity at wavenumber ($\bar{\nu}$)
k	Boltzmann's constant (J K^{-1})
L	Absorption path length (cm)
N_A	Avogadro' constant ($6.022 \times 10^{23} \text{ molecules mol}^{-1}$)
n	Moles (mol)
N	Number density (molecules cm^{-3})
n_l	Number density in lower state
n_u	Number density in upper state
n_t	Total Number density
P	Pressure (Pa)
$Q(T)$	Partition function of the absorbing molecules at temperature (K)
$Q(T_0)$	Partition function of the absorbing molecules at reference temperature (K)
R	Ratio of two line strengths
R	Ideal gas constant ($8.314 \text{ m}^3 \text{ Pa K}^{-1} \text{ mole}^{-1}$)
S_{lu}	Line strength of normalised transition from lower to upper energy level
$S(T_0)$	Line strength at reference temperature at ($\text{cm}^{-1} / \text{molecules cm}^{-2}$)
$S(T)$	Line strength at temperature T ($\text{cm}^{-1} / \text{molecules cm}^{-2}$)
T	Temperature (K)
T_0	Reference temperature (K)
Δt	Time electron spends in energy level
$ u_{lu} $	Transition dipole moment
λ	Wavelength
$\bar{\nu}$	Wavenumber

ν_{lu}	Frequency of transition (cm^{-1})
$\bar{\nu}_0$	Peak centre
ν	Frequency of photon
V	Volume (m^3)
w	Full width at half maximum
y_0	Offset

ABSTRACT

Laser absorption spectroscopy and tomography of gas flows
Doctor of Philosophy (PhD) · James Foo · The University of Manchester
December 2016

This research focuses on developing optical sensing systems for 2D and 3D spatial monitoring of temperature and concentration distribution profiles of complex or reacting gas flows. Non-invasive, species specific and sensitive nature of monitoring allows spatial information to be extracted from harsh environments with poor physical access, allowing validation of computational models or process monitoring. This is suitable for processes like combustion engines or sealed atmospheric cloud chambers.

A novel line-of-sight (LOS) Tunable Diode Laser Absorption Spectroscopy (TDLAS) system using a preselected laser diode centred at 7212.88 cm^{-1} was first designed to monitor the change of relative humidity (water vapour concentration) during an expansion process within the Manchester Ice Cloud Chamber (MICC), operating from atmospheric pressure, down to 0.7 atm. The experimental results were validated with an Aerosol Cloud Precipitation Interaction Model (ACPIM) simulation, feasible for tomography applications.

The MICC shares similar combustion monitoring challenges such as minimal optical access or reactive gas flows. The TDLAS system developed for the MICC was then used as a foundation design for a TDLAS tomography setup capable of conducting temporal two-dimensional (2D) and three-dimensional (3D) concentration and temperature imaging. This system uses the principle of two-line thermometry, centred within the near infrared (NIR) region of 7181.93 cm^{-1} and 7179.8 cm^{-1} . The laser was divided into 4 simultaneous parallel beams using a 1×4 fiber coupler (4 LOS). Using a motorised platform, the beams were projected at 0.5° interval, from 0° to 179° angle within 3.6 s, around the exhaust of two asymmetrical shaped flame burners. A total of 360 projection slices comprised of 1440 integrated absorbance data were used per tomogram reconstruction. By solving for the spatial distribution of temperature first, the concentration distribution of water vapour could be then calculated.

Reconstruction algorithms (Filtered Back Projection, Fourier Slice Reconstruction and Direct Fourier Reconstruction (DFR)) were compared using a range of criteria. The DFR method was selected as the best method at 700 zero padding, with a spatial in-plane resolution of 1-2 lp/cm, pixel resolution of 128 by 128, thermocouple temperature validations of $\pm 5^\circ\text{C}$ and a relative mean error performance of 8.12%. The concentration could not be validated due to the lack of a mass spectrometer.

3D volumetric monitoring results took 36 seconds to complete, and was constructed using 10 interpolated parallel, 1 cm height interval spaced tomograms. Independent vertical slices along the x-axis and y-axis could also be extracted. The temporal results were also successfully conducted and consisted of a quick succession of 16 experiments at a temporal resolution of 0.28 frames per second.

A tomographic system that performs 3D and 2D temporal sensing was successfully developed and validated. Although 3D work was conducted using planar imaging or hyperspectral tomography, no work has been conducted so far using NIR TDLAS systems to date.

DECLARATION

No portion of the work referred to in the thesis has been submitted in support of an application for another degree or qualification of this or any other university or other institute of learning.

COPYRIGHT STATEMENT

- i. The author of this thesis (including any appendices and/or schedules to this thesis) owns certain copyright or related rights in it (the “Copyright”) and s/he has given The University of Manchester certain rights to use such Copyright, including for administrative purposes.
 - ii. Copies of this thesis, either in full or in extracts and whether in hard or electronic copy, may be made only in accordance with the Copyright, Designs and Patents Act 1988 (as amended) and regulations issued under it or, where appropriate, in accordance with licensing agreements which the University has from time to time. This page must form part of any such copies made.
 - iii. The ownership of certain Copyright, patents, designs, trade marks and other intellectual property (the “Intellectual Property”) and any reproductions of copyright works in the thesis, for example graphs and tables (“Reproductions”), which may be described in this thesis, may not be owned by the author and may be owned by third parties. Such Intellectual Property and Reproductions cannot and must not be made available for use without the prior written permission of the owner (s) of the relevant Intellectual Property and/or Reproductions.
 - iv. Further information on the conditions under which disclosure, publication and commercialisation of this thesis, the Copyright and any Intellectual Property and/or Reproductions described in it may take place is available in the University IP Policy (see <http://documents.manchester.ac.uk/DocuInfo.aspx?DocID=487>), in any relevant Thesis restriction declarations deposited in the University Library, The University Library’s regulations (see <http://www.manchester.ac.uk/library/aboutus/regulations>) and in The University’s policy on Presentation of Theses
-

ACKNOWLEDGEMENTS

I would like to thank Dr Philip Martin for his supervision. I have learnt much from him, not just in the discipline of science, but also in life as a person. His generosity with his time and his continual support was undoubtedly the reason I could complete this process. My PhD experience would have been very different without his guidance.

I would also like to thank my progress examiner, Dr Patricia Scully, for being so kind with her encouragement and generating new ideas for my work. Her kindness has always made me feel welcome in a land far away from home.

To Dr Paul Connolly, Dr Christopher Emersic and Emma Simpson, for allowing me to see past my own research field by collaborating with them and introducing to me their work at the Manchester Ice Cloud Chamber.

My thanks to all my office colleagues, Xu Shao Jun, Dr Paul Coffey, Dr Adam Higginson, James Thomson for enriching my life. To Dr Alex Grosch and Dr Yunchul Byun for teaching me so much in my first 2 years of my PhD, not just in theory but also in auxiliary research skills and attitude that every scientist needs. To Ali Arafeh and David Knox for helping me out in my experiments and sharing their knowledge and gear so unselfishly.

I would also like to thank Dr Martin Hehn, my motivator and friend, for always pushing me to try new research methodologies and techniques, even when I was not always comfortable or willing. Also to my good friend, Dr Michael Moulin-Ramsden for always encouraging me and supporting me, especially in the last few months of completion.

To my mother, I want to thank especially for her love and believing in me. Without her support, I would have never completed this thesis. To my father, I would like to express my upmost gratitude for his wisdom and providence. The precious opportunities and resources that have been presented to me would neither been possible nor available without him.

To Damian Callaghan, for all his understanding and faith in me.

1 INTRODUCTION

There are pressures to improve the efficiency and performance of combustion engines due to environmental legislation centred on anthropogenic climate change and commercial competitiveness for more efficient designs. This thesis focuses on designing an optical absorption tomography system, specifically Tunable Diode Laser Absorption Spectroscopy (TDLAS) tomography system, to monitor the spatial changes of both temperature and concentration of gaseous water in the exhaust of two asymmetrically placed mixed-fuel burners.

The thesis begins with the set up of a line-of-sight (LOS) near infrared (NIR) tunable diode laser absorption spectroscopy (TDLAS) system to monitor rapid changes of gaseous water (changes of relative humidity) in the Manchester Ice Cloud Chamber (MICC). Although the MICC is not a combustion system, the physical constraints of the MICC (temperature, pressure and optical access) are similar to a combustion engine. It also demonstrates the potential applicability of the tomography system beyond the combustion industry.

Using the LOS TDLAS system (both physical and software design) as a starting foundation, coupled with an original fan beam TDLAS tomography system within the research group, a 3D and temporal tomography system is developed. Comparisons of suitable reconstruction algorithms for the beam geometry of this system were also conducted.

3D and temporal experiments were conducted and validations using physical phantoms were conducted and verified with a thermocouple for temperature measurements. Simulations were carried out using digital phantoms for quantitative analysis on the system, measuring its signal to noise ratio as well as the relative mean errors of the reconstruction algorithm employed.

1.1 Aims and objectives

The primary aim of this thesis was to design an optical absorption tomography sensing system, which could perform both 3D and temporal studies. This was achieved in two stages as detailed in Section 1.1.1 and Section 1.1.2.

1.1.1 Designing a line-of-sight laser system to monitor relative humidity

Researchers working at the Manchester Ice Cloud Chamber (MICC) focus on the study of cloud microphysics, in particular, the formation of clouds in the presence of aerosols. The goal is to study the suppression of ice nucleation in the presence of anthropogenic aerosols (ammonium sulphate) and naturally occurring aerosols (Snomax or mineral salts). Their work employs a variety of instrumentation to study parameters like particle size and concentration, ice particle concentration as well as relative humidity of gaseous water. However, their pre-installed chilled mirror hygrometer that samples for relative humidity does not keep up with the rapid changes of the pressure and temperature during expansion processes, which simulates a cloud parcel rising up into the air.

Therefore, the first section of the thesis focuses on developing a line-of-sight (LOS) near infrared (NIR) tunable diode laser absorption spectroscopy (TDLAS) system to monitor rapid changes of gaseous water (changes of relative humidity) in the MICC.

The objectives with regards to the MICC experiments were therefore:

- To design an in-situ laser absorption system and control program to perform non-invasive monitoring of water vapour concentration in the chamber during operation.
 - the system should be able to detect changes in relative humidity every second, with temperatures ranging from 0 °C to -20 °C and pressures from atmospheric pressure down to 70 kPa.
- To validate the TDLAS results with the chilled mirror hygrometer when there are no rapid change of conditions within the MICC.

1.1.2 Designing a 3D and temporal tomography system

The second half of the thesis focuses on further developing the LOS TDLAS system into a tomography system. First, the design concept was developed from an existing fan-beam tomography system where criteria and requirements were drawn up. The minimum basic tomography system requirements involved being able to measure 2D spatial changes of temperature and water concentration over time. For aim for this work, that the system must be capable of executing 3D reconstructions and carry out temporal monitoring temperature and concentration changes. The projection geometry as well as a suitable reconstruction algorithm were also decided at this stage.

Next, a near-infrared (NIR) TDL laser that was compatible with two-line thermometry temperature measurements was selected to detect water produced from the combustion of two asymmetrically placed mixed-fuel burners. The 2D tomography algorithm was combined with LOS results to recover spatial temperature and water concentration distribution of the combustion exhaust.

The objectives with regards to the tomography experiments were therefore:

- To create a design framework to guide the construction of a tomography system. This framework should include potential challenges (from original fan beam system) as well as desired features or capabilities (3D and temporal imaging).
- To be able to compare and evaluate various reconstruction methods, both qualities of the image reconstructions and quantitatively of the numerical values determined within the reconstructed image.
- To explore 3D diagnosis of the space above the burners and to construct the changes of temperature and concentration with the additional dimension of height above the burners.
- To execute temporal measurements of temperature and concentration of the combustion exhaust within 5 seconds per tomogram (0.2 fps).
- To resolve images for objects which are at least 4 cm apart (0.25 lp/cm)
- To validate methods and ensure reproducibility of measurements

1.2 Thesis outline

Chapter 2 lays out the relevant literature review of optical imaging techniques commonly used for gas monitoring, primarily but not exclusively centred around combustion applications. The two main branches of optical imaging discussed here, planar imaging and tomographic techniques. Two tomographic modalities are further sub-divided into Classical Absorption Tomography (CAT) and Absorption-Based Non-linear Tomography (ABNT). Finally variations of tomography work conducted using 3D tomography and multiplexing are discussed. The identification of the gap in published literature and how the research in the thesis fills the gap is listed in the chapter summary.

Chapter 3 touches on the theory associated with the nature of research in this thesis, beginning with absorption spectroscopy and the conversions between common units of water concentration. The tomography reconstruction algorithms suitable for Tunable Diode Laser Absorption Spectroscopy (TDLAS) tomography and the working principles of key equipment are also discussed.

Chapter 4 is about developing a TDLAS line-of-sight (LOS) monitoring system in the Manchester Ice Cloud Chamber (MICC). It begins with the context of cloud formation study of the MICC team, their main research goals and the existing equipment setup. This is followed by the design of a TDLAS system for LOS monitoring of relative humidity during an expansion process inside the MICC. The results are presented, with validations and comparison of the experiment with a simulation of an expansion process.

Chapter 5 focuses on the concept, design and development of a 3D and temporal tomography system. It begins with discussion of the original fan-beam projection tomography system of the author's research group and the results and limitation of this system, before building a design framework of the improved tomography system. The final design of a new tomography system is developed from the foundations of the LOS monitoring system in the MICC and the design framework from the fan beam system. Details and measurements of the set up as well as the data analysis of that system are also discussed.

Chapter 6 focuses on the MATLAB implementation of the reconstruction algorithms, namely Filtered Back Projection (FBP), Fourier Slice Reconstruction (FSR) and the Direct Fourier Reconstruction (DFR) method. These methods are each validated with thermocouple readings (physical phantoms) for accuracy and digital simulations are used for quantitative comparisons. Discussions of various forms of resolutions are also discussed here. The DFR method was chosen from the various comparisons for future experiments.

Chapter 7 discusses the results from the tomography experiments. The results of both 3D reconstructions as well as the temporal reconstructions are presented, followed by a discussion on spatial resolution by changing the number of projections. The optimised zero padding approach is also discussed here, followed by the reproducibility of the system.

Chapter 8 concludes the thesis with the design and development highlights of the tomography system, conclusions on the results achieved and the challenges faced as well as further work and recommendations.

2 LITERATURE REVIEW

2.1 Chapter overview

The aim of this research was to develop a novel optical absorption tomography diagnostic system to study the temporal and three-dimensional (3D) spatial temperature and water concentration distribution. Currently, the primary drive of such research is for combustion applications. This chapter is to help provide context and gap analysis for this research.

As this research is on designing a tomography imaging system, the literature review will be centred on imaging modalities suitable for reactive gas flows. Section 2.2 provides the context for the importance of monitoring combustion processes (the most common drive for developing and employing optical imaging techniques). There are two main types of imaging techniques, planar imaging as introduced in Section 2.3.1 and tomographic imaging. Within tomographic imaging, it is further sub-divided into two categories; Classical Absorption Tomography (CAT) discussed in Section 2.3.2.1 and Absorption-Based Nonlinear Tomography (ABNT) in Section 2.3.2.2. Finally 3D tomography and multiplexing to simultaneously monitor multiple species is presented in Section 2.4.

2.2 Optical imaging techniques for combustion

In 1992, The United Nations Framework Convention on Climate Change (UNFCCC) was formed in the recognition that the anthropogenic rise of greenhouse gases (GHG) were posing a threat and became a concern to humankind.[1] There had been observable changes in our climate over the course of the last few decades. A linear trend was observed from 1880 to 2012 showing a global average increase of 0.85°C of the Earth's surface temperature.[2]

This climate change was affected by the unprecedented increment of greenhouse gases (GHGs) and aerosols in the atmosphere such as carbon dioxide (CO_2), methane (CH_4) and nitrous oxide (N_2O). Carbon dioxide, the fastest growing GHG is the largest single contributor to radiative forcing. Over 70% of increased GHG count belongs to carbon dioxide emissions, mainly contributed by the combustion of fossil fuel and industrial processes. Understanding combustion efficiency via combustion imaging allows improvements to performance efficiency as well as reduction in the formation of these pollutants. [2]–[6]

There are always new challenges facing combustion processes, including improvement of efficiency, reliability as well as adaptability to new fuel sources. Coupled with the increasingly tightening of environmental legislations and competitive pressures, the drive to monitor and understand the combustion process is ever present. [7]–[16]

In order to fully understand or monitor combustion processes requires the determination of chemical species concentrations, flow dynamics, chemical reaction kinetics and heat and mass transfers. Temperature is a key parameter to determine in this analysis. This information allows better performance

evaluation (efficiency or exhaust emissions), higher process understanding (increased knowledge of physical and chemistry process which leads to better process designs) as well as better process control during operation. [17]

Generally, conventional direct methods of investigating combustion parameters are not well suited because combustion devices tend to be turbulent in nature. Intrusive use of physical probes or extraction of samples may affect the process by interrupting the fluid flow or are simply inconvenient due to the slow response time. Even with the presence of sophisticated and comprehensive models to predict combustion behaviour, these models cannot be applied with confidence without validations using experimental observations. [18]–[26]

Optical imaging techniques have been developed over the last few decades and have proven to be advantageous due to their non-invasive measurement capabilities. Optical imaging techniques can also perform spatial measurements instead of traditional point measurements thus providing more detailed information. These advantages have made optical imaging techniques superior to traditional methods[27].

2.3 Categories of optical imaging techniques

There are generally two forms of optical imaging techniques, planar and tomographic imaging. An image measured using the planar technique typically depicts a direct singular view from the direction of the radiation source whilst an image produced using the tomographic method is typically a 2D cross section of a volumetric body [28].

Section 2.3.1 discusses planar imaging, which consists of illuminating the investigated plane within the flow field by a light source and capturing the signal with a 2D array detector.

Section 2.3.2 discusses tomographic imaging, which on the other hand employs multiple line-of-sight (LOS) measurements to reconstruct scalar fields. These LOS measurements are collected through lateral projections at different angles. A further sub-division of absorption spectroscopy based tomographic imaging techniques that would also be discussed; classical absorption tomography (CAT) in Section 2.3.2.1 and absorption based non-linear tomography (ABNT) in Section 2.3.2.2.

2.3.1 Planar imaging

Planar imaging has the ability to obtain 2D profile information on temperature [29]–[33], velocity [34]–[38] and mixture fractions [39]–[41]. If sequential projections are carried out in parallel planes, volumetric information can also be extracted [42], [43].

Examples of planar imaging techniques includes Mie scattering [44], Rayleigh scattering [29] and particle imaging velocimetry (PIV) [45]. Laser-induced fluorescence (LIF) [46], is another well establish method for monitoring flow parameters such as temperature, velocity and even pressure.

In LIF, a selected species is excited from the ground to an excited electronic state by a photon of the required energy. When the molecules relax directly back to the ground state, they emit characteristic radiation called fluorescence. The LIF technique functions by probing into either one-photon absorption processes for species like OH, CH, NH or NO or two-photon

absorption processes like O, H, N or CO. A variation of LIF, planar laser-induced fluorescence (PLIF) [47]–[50] enables the measurement of 2D species distributions, gas temperatures and flow velocities by creating a laser sheet instead of a beam. These 1D and 2D visualizations are extracted using linear diode-array detectors and 2D detectors (CCD cameras) respectively. [12], [18], [51]–[59]

An example [18] was the study of water vapour from combustion fluorescence at 417 nm. This was investigated using two-photon excitation using a KrF excimer laser centred at 248 nm shown in Figure 1. Two detection modes were used in the example with the aid of beam shaping lens to create a laser sheet. The first method involved the detection of fluorescence from the cell using a CCD camera with the aid of a Nikon lens and colour glass filters. The second method involves the collection of water vapour emissions that were lens-focused onto a spectrograph. Spectral overlaps were reported from hot oxygen molecules, which resulted in the use of narrowband detection. Quenching effects appeared to be prevalent in the studies conducted, which decreased the signal with time. Quenching occurs when the excited molecular states depopulates via collisions with other molecules in the system, resulting in a reduction in signal strength and therefore potentially a problem for 2D imaging. [18], [23], [60], [61]

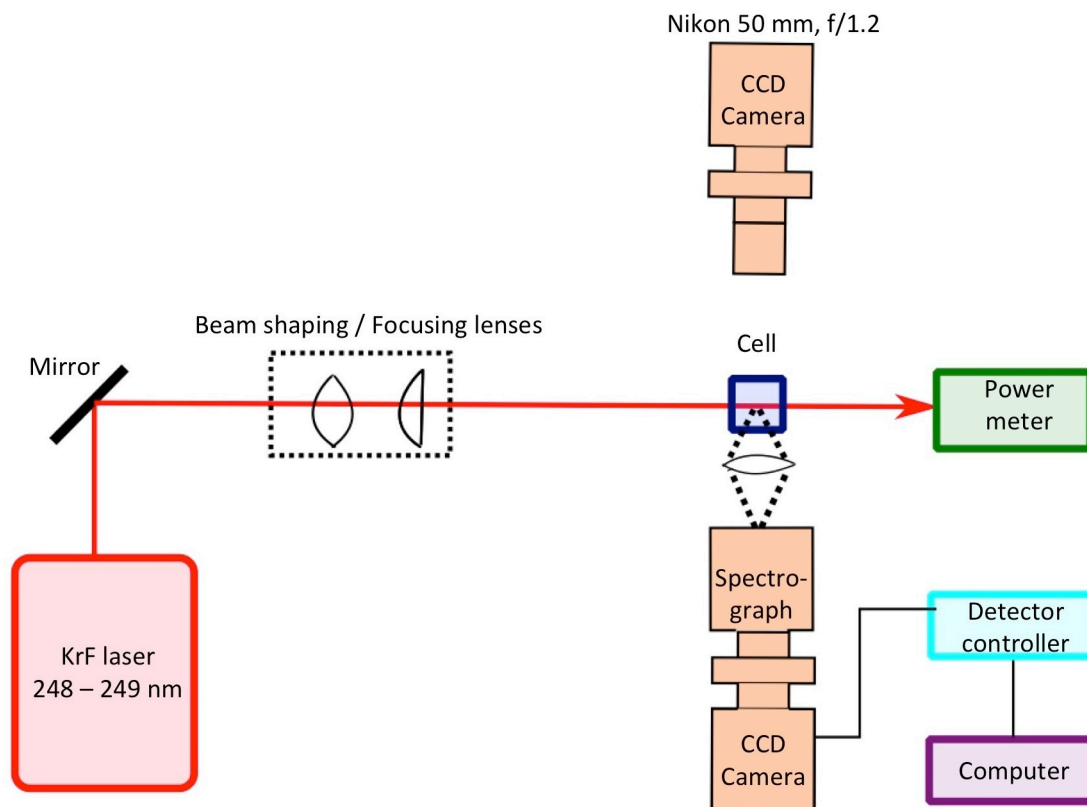


Figure 1 Simplified example of a PLIF experimental setup.[18]

In general, planar imaging techniques produce high temporal and spatial resolution data [47], [62]–[66] benefitting the study of flow regimes which are turbulent and harsh in nature [67]–[71]. However, they tend to suffer from the requirement to have high levels of optical access, which is difficult in most monitoring for combustion engines without major redesigns or converting them

into optical combustion engines. Due to their high costs, they are also impractical in most implementations due to the harsh operating environments.

2.3.2 Tomographic imaging

Tomographic absorption spectroscopy (TAS) uses the absorption or extinction coefficients of absorbing species of multiple transitions to reconstruct information on temperature and species concentration [72]. Examples of popular tomographic imaging includes using tomographic X-ray imaging of fuel mass distributions [73], [74] and the use of particle image velocimetry (PIV) for 3D velocity measurements of particles [42], [75], [76].

However, this thesis focuses on another form of tomographic modality that involves coupling absorption spectroscopy with tomography to recover temperature and species concentration spatial profiles.

TAS, using tunable diode lasers (TDL), has been used previously for tomographic applications. The growth of TDL was due to the applications in the telecommunication industry, which has extensive investment in research and development of near infrared (NIR) technology. The widespread use of a matured technology has driven down the cost of TDL technology, making it a cost effective method of species diagnostics. [77]–[84]

TAS using TDL has been developed in several industrial process applications with examples such as the detection of signals in high pressure or temperature fuel cells or gas turbine engines. Other uses include the measurement of temperature and species concentration in high-speed flow scenarios such as oxygen within a shock tube or used as a diagnostic tool for combustion and exhaust species in industry, laboratory flames or for open path monitoring in petroleum refineries. [24], [85]–[88]

TAS using TDLAS generally requires easier optical integration with combustion engines due to its compatibility with optical fibre technology and spatial optical access requirements [89]. This increases its span of deployment opportunities, equipment architecture flexibility and simplicity. Either direct or wavelength modulated (WM) over a narrow spectral range, tunable diode laser spectroscopy is capable of high sensitivity and molecular specificity with minimal interference from other transitions due to the high spectral resolution. [77]–[84] Species specificity here refers to the absorption spectra where individual species are uniquely identifiable and distinguishable from one another [59], [90]. Table 1 summaries additional research of TDLAS for both H₂O and CO₂, the primary products for complete combustion.

Table 1 Sample TAS TDL research conducted on H₂O and CO₂

Target species	Detectors	References
H ₂ O	InGaAs, Ge	[72], [91]–[94]
CO ₂	InSb, InAs	[95], [96]

To exploit the NIR region where TDL lasers are well developed, the NIR spectra of the main products of complete combustion are shown in Figure 2. It can be seen that H₂O lines are well distributed throughout the NIR region, significantly more than CO₂, with much stronger line intensities. This provides the user a large selection of commercially available laser diodes to choose from

that are capable of accessing strong H₂O lines. Stronger lines enable better signal to noise ratios and facilitate easy detection in a short single pass path length.

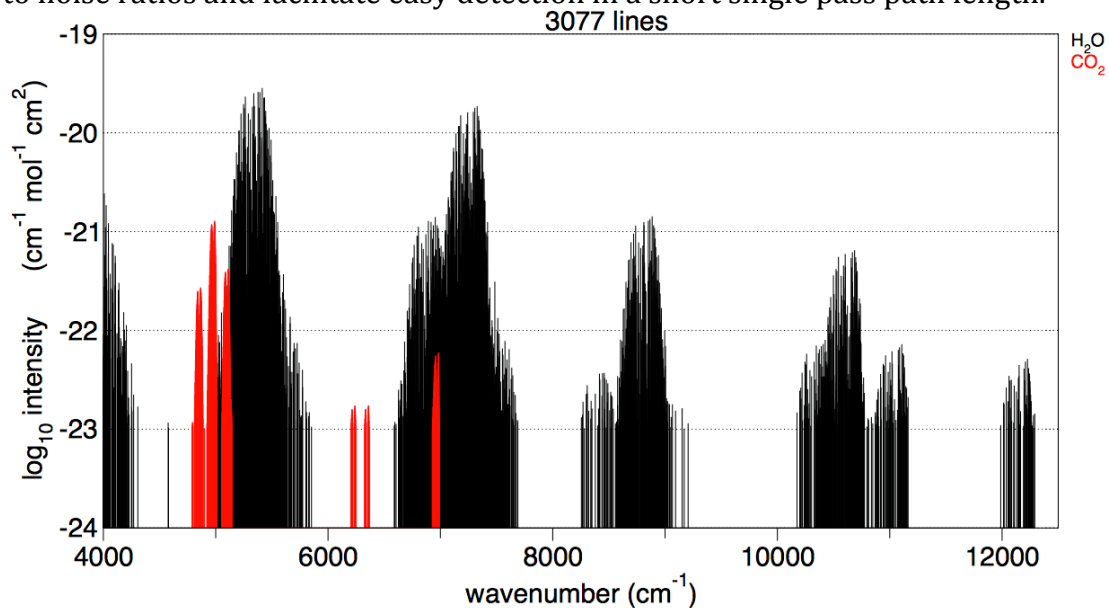


Figure 2 NIR line list for H₂O and CO₂, at room temperature based on HITRAN 2012 and extracted from www.spectralcalc.com.

TAS comes in two sub genres and will be discussed with case studies in Section 2.3.2.1 (CAT) and Section 2.3.2.2 (ABNT).

2.3.2.1 Classical Absorption Tomography (CAT)

The origin of CAT resides in the medical discipline (nuclear magnetic resonance imaging (MRI) and X-ray tomography, for example) and later expanded its use into other disciplines like geophysics, oceanography, as well as chemical engineering [97]–[100].

CAT consists of projecting through the investigative space from the peripherals of the system at various angles and using these projections to construct sinograms. These sinograms are then post-processed to recover the spatial distributions of temperature and species concentration [72].

The post-processing involves using the projections allocated in the sinograms as linear equations to create an equation system, and for this system to be well posed, a large number of equations/projections are required. Therefore, if insufficient optical access were available, the amount of projections/equations would create an ill-posed equation system. [101]–[103]

There are generally three geometric configuration of CAT, ranging from parallel beams, fan-beams and irregular beams. Parallel [104] and fan-beam [105] configurations are classed as regular beams, where the beams are equiangular and the beams equidistantly spaced. The other irregular beam configuration tends to be more practical in application with combustion engines because it maximises the optical access of the engine with minimal retrofitting as well as providing good spatial sampling of the investigated area [106], [107]. This however comes at a cost of experimental complexity [108]–[111].

CAT demonstrations on laboratory flames include using TDLAS to monitor axisymmetric burners to produce profiles of both temperature and CO₂ concentration [95], [112] and similarly to recover temperature and

concentration H_2O profiles in a premixed methane/air flame [72]. Other work includes demonstration on a steady, non-reacting flow of methane and argon [113]; mean methane concentration in an off-axis turbulent methane-air free jet [114]; and temperature and sodium atom concentration in turbulent burnt gases [115].

Practical applications of tomographic instrumentation have been developed extensively, for example, on the measurements of hydrocarbon fuels in Manchester in automotive engines [108], [109], [116], [117]; and the measurement of hydrocarbon concentration in fuel/air mixtures of a model gas turbine combustor [118]

Although advances in CAT have been towards combustion engines and laboratory flames, it has been found beneficial in other areas such as to better understand the chemical vapour deposition process by monitoring the spatial distribution of both temperature and water species in a coating process [93]. Larger scale applications have also been attempted by the measurement of atmospheric CO_2 over a volcanic site [96]. This versatility in size of deployment and application areas makes this a promising research field to pursue.

An example case of CAT is depicted in Figure 3 on a TDLAS fan beam optical tomography system conducted by Kasyutich on the study of spatial temperature and concentration of water over two heaters.[93]

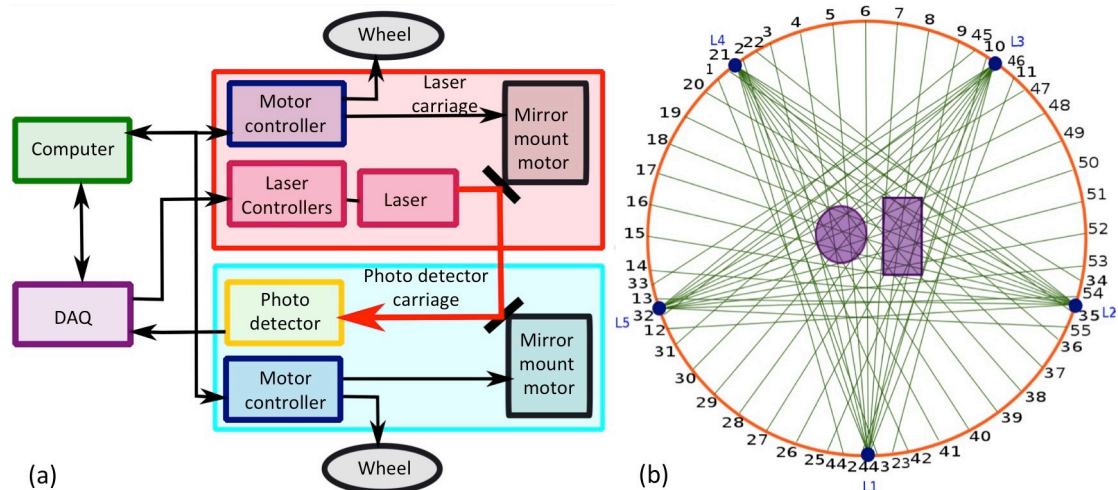


Figure 3 (a) Simplified example schematic of fan beam optical tomography setup. (b) Distribution of laser projections (green) in 5 ‘fans’ of 11 projections over two heaters (purple).

It consists of a laser carriage and a photo detector carriage as shown in the schematic in Figure 3 (a) and with the aid of motors, the carriages rotate around a circular boundary, shown in orange in Figure 3 (b). These motors control both the wheels of the carriages as well as the mirror mounts, which in turn control the angle of the laser beam. The laser carriage stops at 5 points on the circle, and with the aid of the turning mirror, the projections are swept in a fan-like shape that is detected by the photo detector carriage on the other side of the circle. A total of 55 projections were used in the study. These are illustrated in Figure 3 (b). Using the algebraic reconstruction technique (ART), the temperature and concentration profiles of water could be reconstructed above the heated plates using a primary absorption line at 7185.6 cm^{-1} and a weaker absorption line at 7185.394 cm^{-1} [93].

2.3.2.2 Absorption-Based Nonlinear Tomography (ABNT)

CAT with TDLAS uses a large number of projections, and a wavelength scan creates well-posed system of equations. ABNT on the other hand, makes use of the large amount of spectral information per projection to cover the lack of projections.

To achieve this, ABNT uses broadband laser sources where simultaneous sampling of different species at different wavelengths could be achieved [119]–[122]. Frequency-multiplexing laser diodes is also another option of accessing and detecting multiple wavelengths and species for ABNT [123]–[130].

ABNT allows for more practical implementations of projection geometry in combustion engines as it could employ fewer projections which may be beneficial when the optical access is limited. This means less retrofitting into the physical engines, which promotes the use of the more pragmatic irregular projection geometry. [131]–[133]

Another benefit of ABNT is the rich spectral information gathered during data acquisition provides a high immunity to experiment generated noise [132], [134] which improves its performance in harsh experimental scenarios [135].

An example of ABNT is hyperspectral tomography (HST). This utilises laser wavelength multiplexing to scan rapidly over a wide spectral range, of the order of 100 nm. [132], [136]–[139]

The use of HST has been demonstrated in several applications. One of them is the use of imaging in an aero-propulsion engine for temperature distribution, as well as the concentration of water vapour under high-speed flows. Another use is a similar diagnostic in an isooctane fuel homogeneous charged compression ignition engine. [140], [141]

CAT is essentially an inverse problem, where the results (absorption) are used to calculate the causes (spatial combustion parameters), using a set amount of information to solve for a set amount of unknowns. For HST to be utilised, the standard tomography inversion problem needs to be changed into a minimization problem. The goal is to minimise the difference between all the projections and wavelengths involved contributing to the spatial temperature and species concentration profiles. [132], [142]

Li et al reported that a comparison of reconstructions using HST and a two-wavelength tomography technique yielded similar results at only 20 % of the projections required under the traditional route. The technique has been validated with good performance of overall mean relative reconstruction errors below 3% and the maximum standard deviation below 1%.

However, this superior performance comes at a cost of an increased computational time of approximately 10 hours on an average personal computer for a 10 by 10 grid cell image. [13], [132], [143]

2.4 3D tomography and multiplexing

2.4.1 3D tomography

There are typically two methodologies for creating 3D imaging. The first and most commonly used method is to create a series of 2D images at different

levels and to interpolate between the levels. Although frequently employed in the medical industry, Wajman et al [144] argue that this particular method involves an additional level of assumptions and approximation and described this method as a “2.5D” reconstruction. The second method considers the direct acquisition of 3D detection from the start and reconstructing without any form of interpolation.[6], [144], [145]

A variety of 3D studies include using chemiluminescence tomography to obtain 3D distributions of combustion radicals or flame profiles with the aid of CCD (charge-coupled device) cameras[146]–[149] and the progression of using electrical modality tomography from 2D tomography to 3D studies. [150], [151]

Another study involves expanding the use of hyperspectral tomography not only for improving computational time but also to perform studies for 3D diagnostics with the aid of Proper Orthogonal Decomposition (POD). [143] POD, also more commonly known as Principal Component Analysis (PCA), focuses on performing dimension reduction and retrieving low dimensional descriptions of the process. The goal of this dimensionality reduction is to reduce the number of variables for consideration and consequently the computational cost.[143], [152]

The use of POD in the case of Cai et al reduced the number of variables by 4 times, but also found that the parameter bounds were much better controlled. The reduction of performance time was down to only 18% of the original computational runtime. With POD, the use of hyperspectral tomography can move closer towards temporal reconstruction and easily adapted to multiple 2D slices stacked close over each other, creating a 3D image.[143]

Among most of the studies conducted, there were a larger number of methods that apply the “2.5D” method, especially when optical tomography is concerned, while other 3D studies were carried out using electrical modality tomography. However, there have been minimal studies conducted using TDLAS optical tomography to perform volumetric tomography studies.

2.4.2 Multiplexing

Multiplexing was briefly mentioned in Section 2.3.2.2 and in this section, multiplexing is further discussed.

One of the benefits of using tunable diode lasers is the fact that the laser system can be multiplexed to monitor multiple gas species simultaneously. Unlike using free-space laser diodes where the laser beam is transmitted directly from source to detector through the medium (air or vacuum for example), the laser beam is first directed through optical fibres before transmitting through the medium into the detector. This allows easier manipulation of the beam, such as beam steering (curves or bents) without mirrors or division into multiple sources. There are two common methods of multiplexing, time-division multiplexing (TDM) and wavelength-division multiplexing (WDM).

For a dual laser TDM scenario for example, where the lasers are multiplexed into a single source and are timed to transmit alternatively through the gas cell with the other kept below current threshold (current too low to lase) as depicted in Figure 4 (a). As the detector is synchronised with the lasers' current sweeps, it allows identification of the laser signal by recorded time Figure 4 (b). This configuration required minimum additional equipment, simplifying the physical equipment setup.[153], [154]

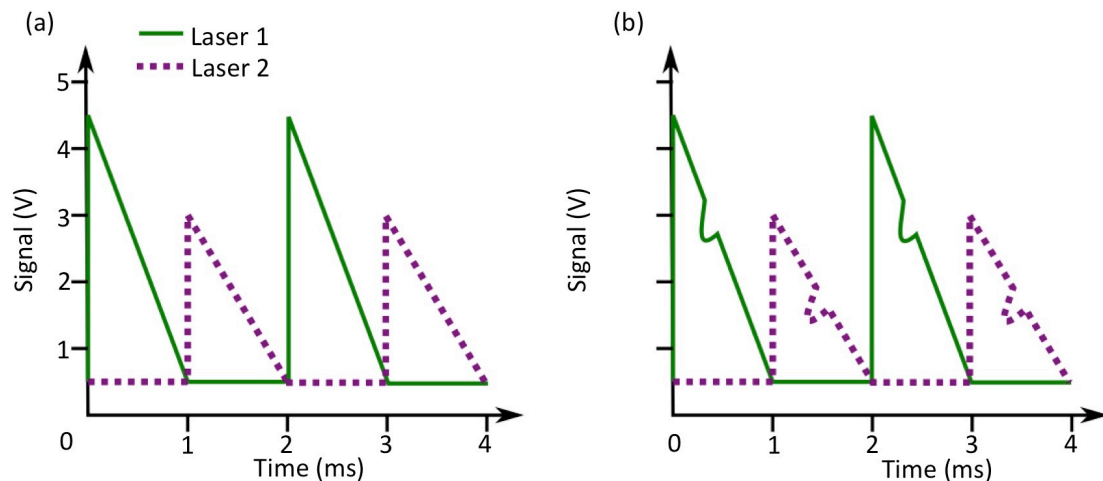


Figure 4 (a) Current ramps of Laser 1 and 2. (b) Photodetector signal with both laser's attenuation signals.

Using a similar dual laser scenario, the WDM setup starts with combining the laser output with a fibre combiner before being transmitted simultaneously through the gas cell. As the two different laser transmissions at different wavelengths leave the gas cell, they are separated with the use of a diffraction grating. The sample laser sweeps of both lasers is shown in Figure 5 (a) and the individual detector readings in Figure 5 (b). [155], [156]

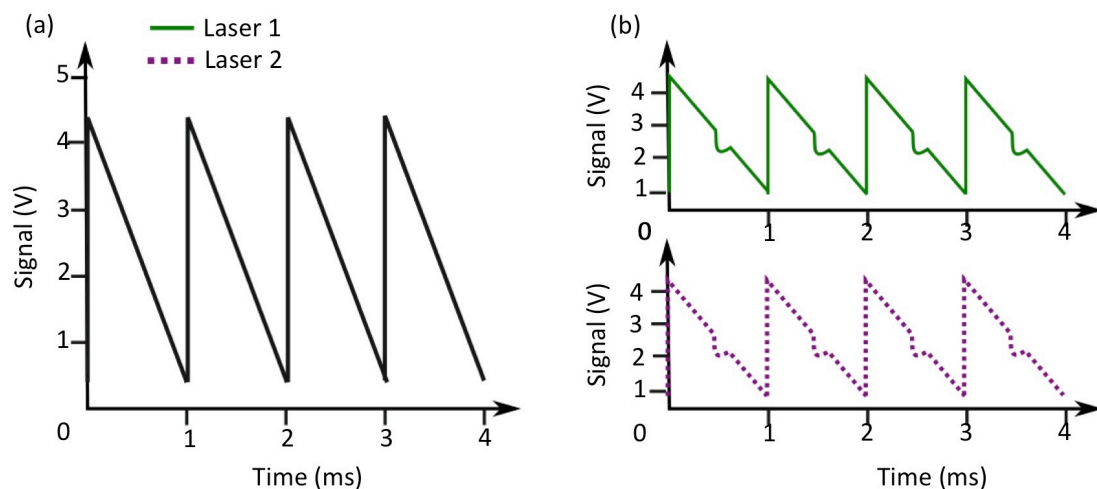


Figure 5 (a) Current ramp of both Lasers 1 and 2. (b) Photodetector signals, each with individual laser attenuation signal.

A multiplexing setup contains an output that continuously cycles through a set number of spectrally narrow wavelengths that correspond to a set of spectroscopic features. It is a cost effective and versatile way of monitoring a range of species at once without massive changes to the internal setup of a process like the addition of equipment or the presence of additional optical access. [154]

Multiplexing combined with tomography not only allows the reconstruction of the temperature of the probed field, but also the reconstruction of multiple chemical species concentration of a particular process, providing a clear insight of chemical species interaction during reaction.

[155] Multiplexing several lasers together effectively increasing the total amount of wavelength probed, allows the user to have access to multiple species to monitor. Many studies on multiplexing have been carried out, including the simultaneous measurement of both H₂O and O₂ [155] and the measurement of the efficiency of a combustion system with post-combustion species like combustion fuels, soot, CO, CO₂ and H₂O [116], [157]–[160]

2.5 Chapter summary

Planar imaging techniques on its own cannot create cross sectional profiling of flow parameters unless combined with tomographic techniques. Even though they benefit from high spatial and temporal resolutions, they suffer from high cost and require a large degree of optical access, rendering it impractical for many practical applications of combustion monitoring.

ABNT is a practical way of monitoring combustion engines because it benefits from high signal to noise ratio due to its rich spectral data. It also requires a significantly smaller number of projections, making it a practical solution to combustion monitoring due to minimal retrofitting for optical access. However, ABNT suffers from a long processing time.

CAT using TDLAS benefits from high molecular specificity and sensitivity, and could be generally adapted for multiple species analysis with the use of multiplexing. Work that has been conducted on laboratory flame 2D tomography work is listed in Section 2.3.2.1. There are also several examples of 3D work conducted, however most consist of only using planar imaging techniques (3D-PIV or 3D chemiluminescence for example) or ABNT (3D hyperspectral tomography). However, minimal research work has been conducted so far using TDLAS for 3D CAT to date.

3 THEORY

3.1 Chapter overview

This chapter describes the relevant theory required for the research conducted. In Section 3.2, the theory associated with absorption spectroscopy is discussed. This is the primary modality of measurement for average line of sight temperature and concentration in an absorption path. A brief discussion of unit conversion is presented in Section 3.3 so that concentration results could be easily applied in different studies in their respective conventional units. Different tomography algorithms used in this thesis are introduced in Section 3.4, which is key to calculating spatial distribution of temperature and concentration. Finally, relevant theory on equipment used is discussed in Section 3.5.

3.2 Near infrared absorption spectroscopy

Spectroscopy is the study of the interaction of electromagnetic waves and matter, and in this thesis the focus is on the absorption of water vapour in the near-infrared NIR region of the electromagnetic spectrum. The vibrational energy of a water molecule in the NIR region could be quantized as energy levels, and can transit in energy level with a finite amount of energy. Transition energy, ΔE , is expressed in Equation 1. The energy of transition occurs by the absorption/emission of a photon, relating to the frequency and intensity of the radiation. The wavenumber ($\bar{\nu}$) is the number of waves in 1 m of distance, is also commonly used interchangeably with wavelength (λ). [161]

$$\Delta E = E_2 - E_1 = h\nu = \frac{hc}{\lambda} = hc\bar{\nu} \quad \text{Equation 1}$$

Where:	ΔE	Energy of transition
	E_2, E_1	Higher energy, lower energy
	h	Planck constant ($6.62606876 \times 10^{-34} \text{ J s}$)
	c	Speed of light in vacuum ($2.99792458 \times 10^8 \text{ m s}^{-1}$)
	λ	Wavelength (cm)
	ν	Frequency of photon
	$\bar{\nu}$	Wavenumber (cm^{-1})

Considering 3 Cartesian location coordinates of x-axis, y-axis and z-axis per atom in a molecule and N the number of atoms in the molecule, the total number of degrees of freedom is 3N. For a non-linear, tri-atomic molecule like water, the amount of freedom is 3N - 6 (fundamental vibrations) = 3 allowed internal vibrational modes. The fundamental vibrations are made up of 3 axes of rotational motions so that the degrees of freedom for that rotation is 3, summing up to 6.

For the water molecule to be infrared active, there is a requirement for a change in the electron dipole moment during vibration as shown in Figure 6.

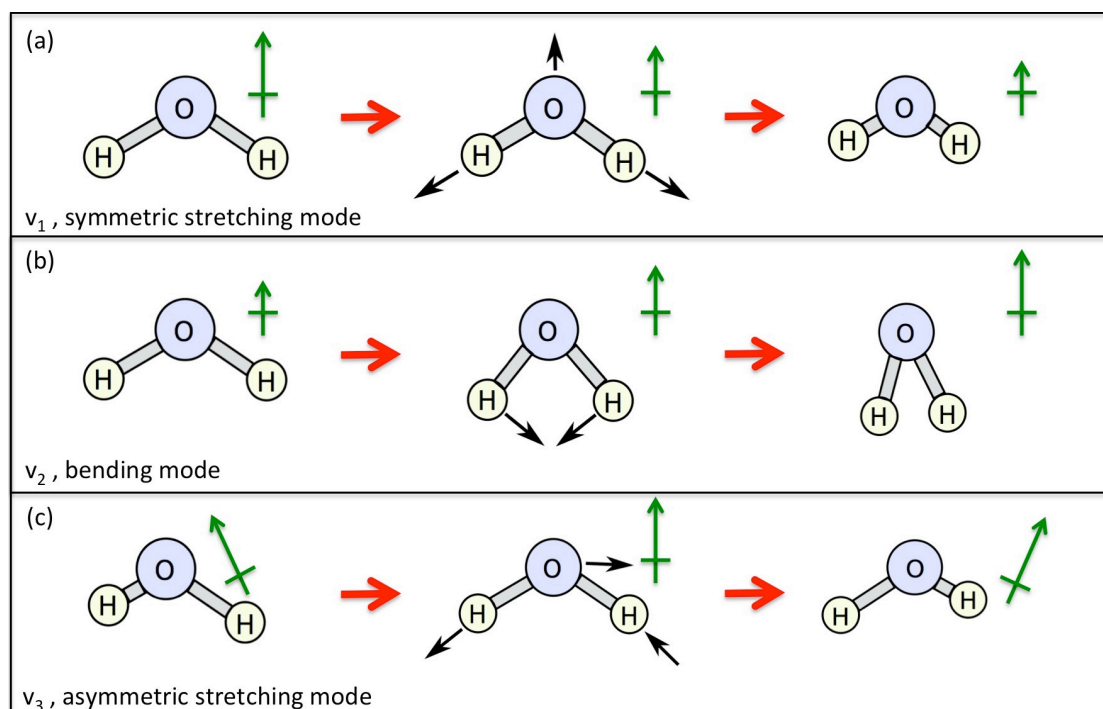


Figure 6 The change in dipole moment (shown in green) produced by different vibration (a) for v_1 , (b) for v_2 , (c) for v_3 of the water molecule.[161]

The NIR region lies within $0.78 \mu\text{m}$ to $2.5 \mu\text{m}$ in wavelength, or 12800 cm^{-1} to 4000 cm^{-1} in wavenumber. Absorption bands in the NIR region are usually classified as overtone or combination bands as depicted in Figure 7. A fundamental vibration occurs when the molecule is excited from the ground state by 1 quantum ($v = 0$ to $v = 1$). An overtone occurs when the molecule is excited by a quantum level greater than 1 (the first overtone is $v = 0$ to $v = 2$ and the second overtone is $v = 0$ to $v = 3$). A hot band transition consists of movements from level 1 to higher vibrational levels ($v = 1$ to $v = 2$).[161]

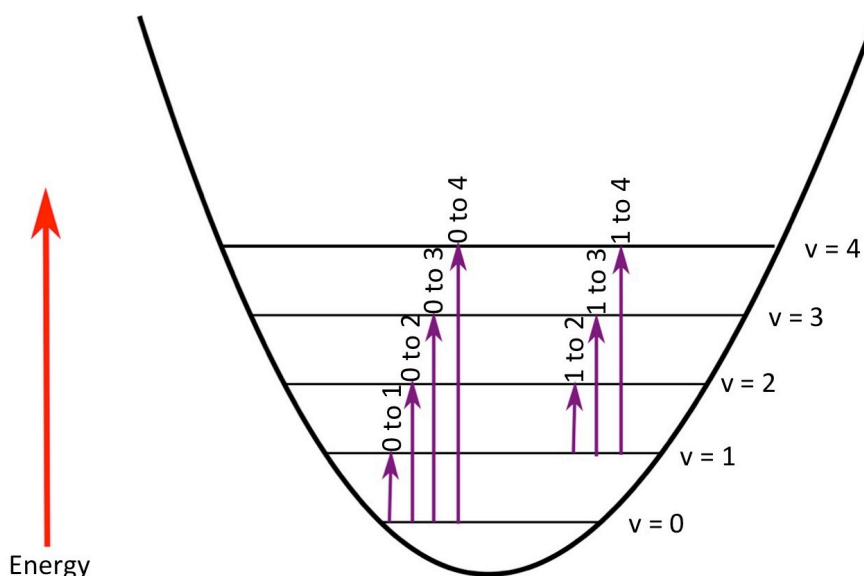


Figure 7 Vibrational levels and the types of transitions.

The absorption features of H₂O in the NIR region are shown in Figure 8. The TDL used in the thesis is shown as well, depicting the use of combination band ($\nu_1 + \nu_3$).[162]. Although having the appearance of thin lines, these absorption features are not truly monochromatic (single wavelength) but exist as broad peaks. The factors that influence peak broadening include its natural line width, Doppler and pressure broadening.

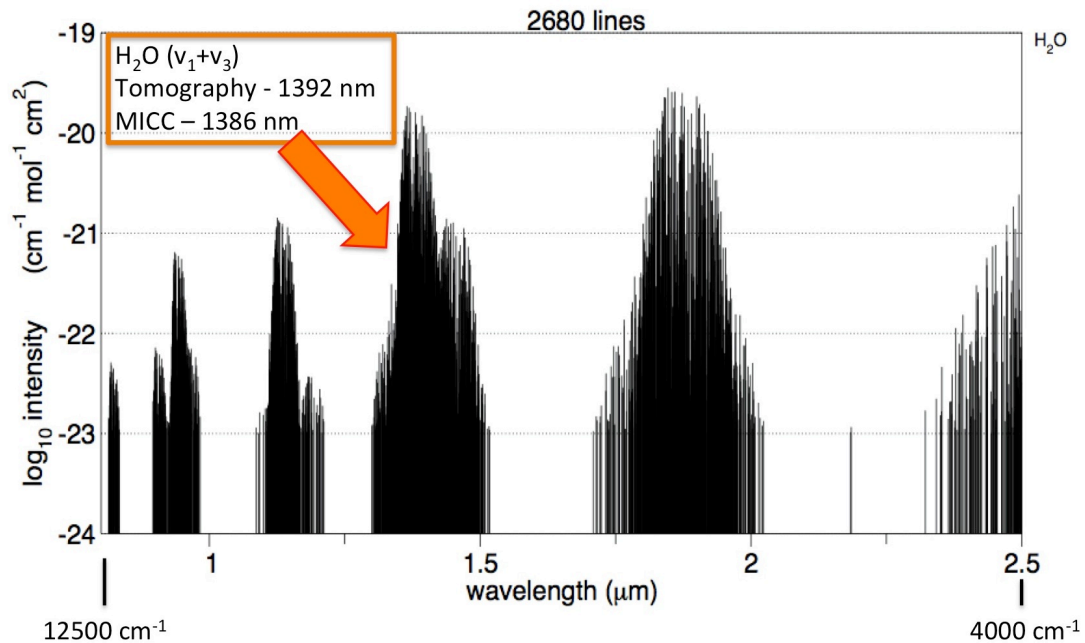


Figure 8 NIR line list for H₂O at room temperature with the lasers utilised in research shown. Based on HITRAN 2012 line list obtained from www.spectralcalc.com.

3.2.1 Line broadening

The characteristic of the peak is shown in Figure 9 (a), where the maximum intensity I_0 will be located at central wavelength $\bar{\nu}_0$. Two half maximum intensity $\frac{I_0}{2}$, are located at $\bar{\nu}_1$ and $\bar{\nu}_2$ respectively. The distance between $\bar{\nu}_1$ and $\bar{\nu}_2$ is termed Full Width at Half Maximum (FWHM). The locations of the line kernel and wings are also depicted in Figure 9(a), where the peak centre at $\bar{\nu}_0$ is called the line kernel and the wings of the peak are located to the left of $\bar{\nu}_1$ and the right of $\bar{\nu}_2$.

Unlike Equation 1 where E_1 and E_2 are exact, due to the Heisenberg's uncertainty principle shown in Equation 2 and depicted in Figure 9 (b), it is more realistic for E_1 and E_2 to correspond more closely to ΔE_1 and ΔE_2 . [161], [163], [164]

$$\Delta E_i = \frac{\hbar}{\Delta t} \tag{Equation 2}$$

Where: \hbar Reduced Planck's constant ($\frac{h}{2\pi}$)
 Δt Time in energy state

The natural line width is built on the model of the damped oscillation of an excited atomic electron. As the amplitude of the electron's oscillation decreases gradually, the frequency of the emitted radiation is no longer sharp compared to a constant oscillation electron.

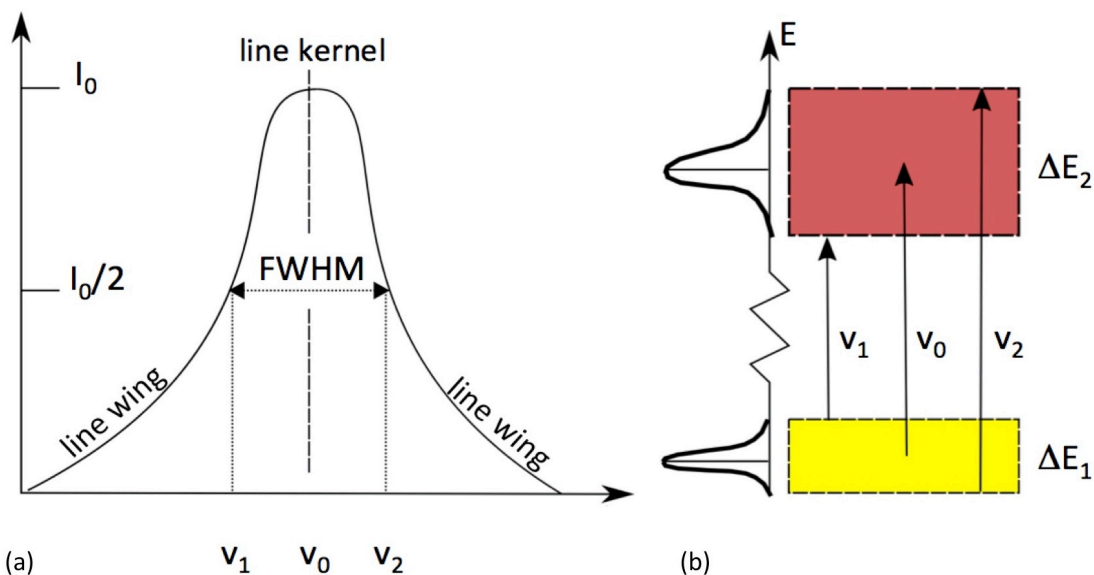


Figure 9 (a) The characteristics of an absorber peak (b) The uncertainty principle is depicted in the shaded area of ΔE_1 and ΔE_2 .

The Fourier transform of the dampening oscillation profile shown in Figure 10 (a) produces the frequency distribution profile in Figure 10 (b), which is also known as the normalized Lorentzian profile and could be expressed in Equation 3. The normalised line shape function is normalised such that the area that is integrated over the range of wavelength is unity (equal to 1). [165]

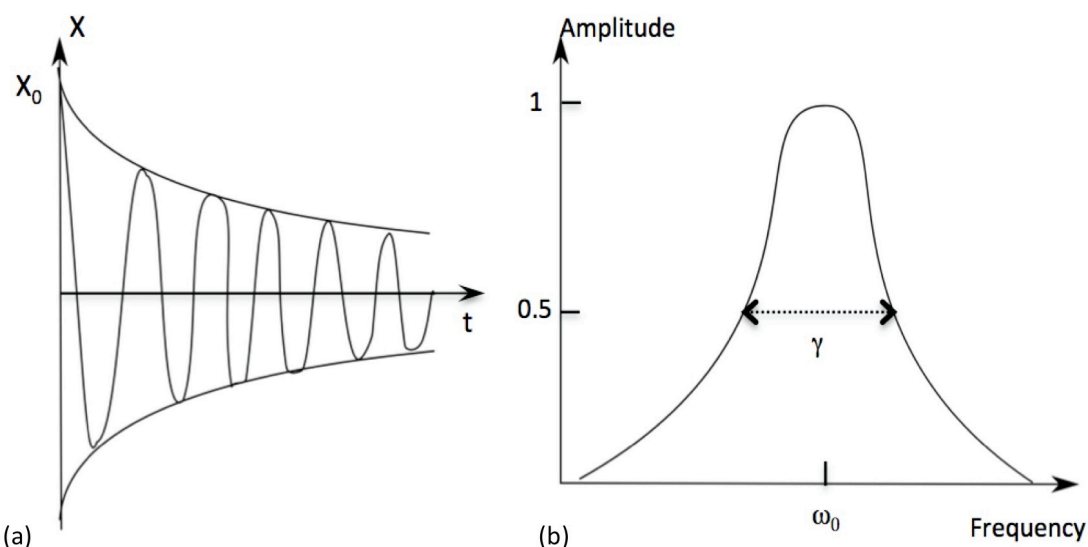


Figure 10 (a) The damped oscillation profile, where X_0 is the initial amplitude, decreasing as time (t) is increased (b) The normalised frequency distribution profile of the damped oscillation after being Fourier transformed. γ is the damping constant ω_0 while is the frequency no damping.

$$y = y_0 + \frac{2A}{\pi} \frac{w}{4(\bar{\nu} - \bar{\nu}_0)^2 + w^2} \tag{Equation 3}$$

Where: y_0 Offset
 A Area under the peak
 w FWHM
 $\bar{\nu}_0$ Peak centre

Molecules or atoms colliding with each other cause collision or pressure broadening. These collisions cause deformations in the outer electron shells creating a broadening effect. Increasing the pressure shortens the distance in between molecules, increasing the rate of collisions. These collisions shorten the lifetime the molecules spend in the upper energy state, thus causing line broadening. Collisions between the same species, water molecules in this context, is termed self-broadening. When collisions occurs with different species, then it causes foreign-broadening. Pressure broadening can also be described by a Lorentzian profile.

Another broadening effect on gases is Doppler broadening. This is caused by thermal motion of the absorbing molecules, shifting the central frequency of the molecular emission with an additional element of velocity. Doppler broadening as depicted in Equation 4 can often be expressed as the Gaussian function shown in Figure 11.[165]

$$y = y_0 + \frac{Ae^{-\frac{4\ln(2)(\bar{\nu} - \bar{\nu}_0)^2}{w^2}}}{w\sqrt{\frac{\pi}{4\ln(2)}}} \tag{Equation 4}$$

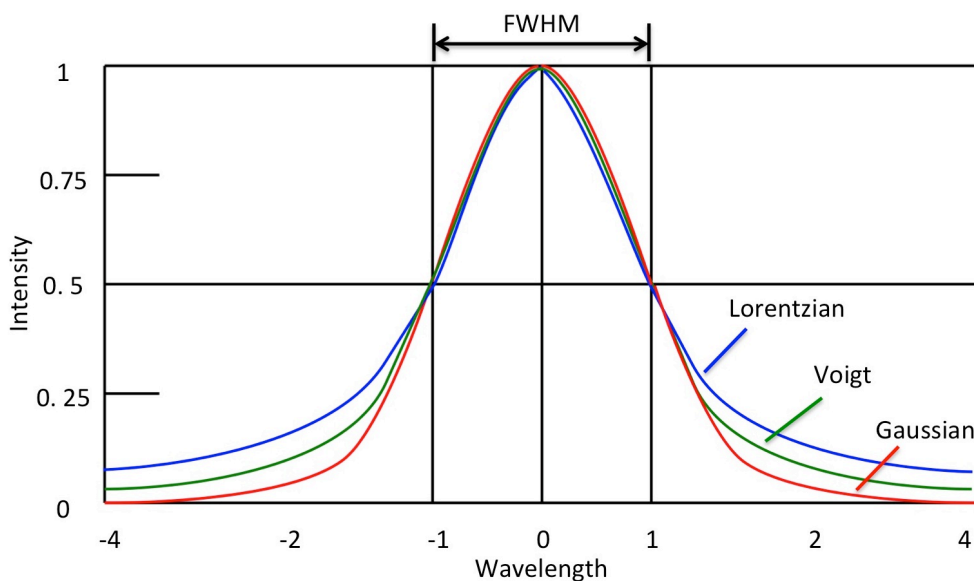


Figure 11 The comparison of the Lorentzian line profile with the Gaussian line profile.

However, there are certain situations where a convolution of the Lorentzian and Gaussian profile yields a more accurate peak fitting. This convolution of two profiles is called the Voigt profile. However, a pseudo-Voigt function, which is a close approximation to a Voigt function, shown in Equation 5 can be used. The addition of one more fitting parameter m_u is the profile shape factor and ranges from 0 to 1. This is useful in situations where the peak shape changes from Lorentzian to Gaussian with time due to pressure change.[165]

$$y = y_0 + A \left[\left(m_u \frac{2}{\pi} \frac{w}{4(\bar{\nu} - \bar{\nu}_0)^2 + w^2} \right) + \left((1 - m_u) \frac{\sqrt{4 \ln 2}}{\sqrt{\pi} w} e^{-\frac{4 \ln 2}{w^2} (\bar{\nu} - \bar{\nu}_0)^2} \right) \right] \quad \text{Equation 5}$$

3.2.2 Beer-Lambert Law and Two-line thermometry

The principle of absorption spectroscopy involves sending a beam of radiation from a source through a cell containing the absorbing medium and onto a detector as shown in Figure 12. The Beer-Lambert law for weak absorptions can be applied for the measurements of water vapour in this thesis and expressed in Equation 6.[93]

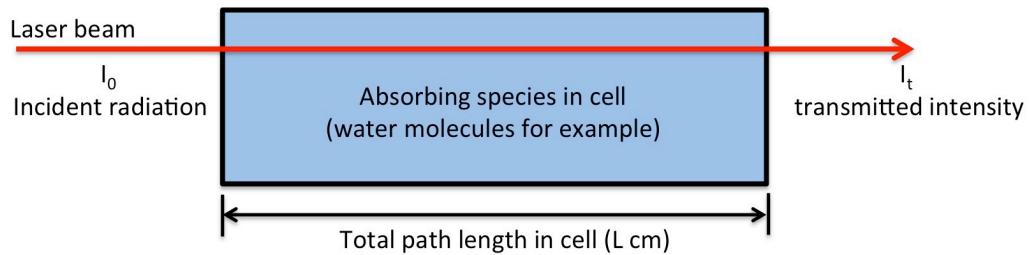


Figure 12 The depiction of absorption process with a sample cell of length L .

$$I_t(\bar{\nu}) = I_0(\bar{\nu}) \exp(-S(T)g(\bar{\nu} - \bar{\nu}_0)NL) \quad \text{Equation 6}$$

Where:	$I_0(\bar{\nu}), I_t(\bar{\nu})$	Incident intensity, transmitted intensity at wavenumber ($\bar{\nu}$)
	$S(T)$	Line strength at temperature T ($\text{cm}^{-1}/\text{molecules cm}^{-2}$)
	T	Temperature (K)
	$g(\bar{\nu} - \bar{\nu}_0)$	Normalised line shape function (cm)
	N	Number density (molecules cm^{-3})
	\bar{L}	Absorption path length (cm)

Under the conditions of uniform distributions of temperature and concentration, the number density of the absorber could be extracted from the integrated absorbance using Equation 7.

$$A = \int_{-\infty}^{\infty} \ln \left(\frac{I_0(\bar{\nu})}{I_t(\bar{\nu})} \right) d\nu = NS(T)L \int_{-\infty}^{\infty} g(\bar{\nu} - \bar{\nu}_0) d\nu \quad \text{Equation 7}$$

Where: A Integrated absorbance or area under the absorption peak

The line strength Equation 7 could be derived by considering a two-level energy system with a lower level (l) and an upper level (u) shown in Equation 8. [82], [93][166], [167]

$$S_{lu} = \frac{8\pi^3}{3hc} \nu_{lu} \frac{n_l}{n_t} \times \left[1 - \frac{g_l n_u}{g_u n_l} \right] \times \left\{ \frac{1}{g_l} |u_{lu}|^2 \right\} \quad \text{Equation 8}$$

Where: S_{lu} Line strength of normalised transition from lower to upper energy level
 n_l Number density in lower state
 n_u Number density in upper state
 n_t Total Number density
 g_l Statistical weight in lower state
 g_u Statistical weight in upper state
 $|u_{lu}|$ Transition dipole moment
 ν_{lu} Frequency of transition (cm^{-1})

The line strength is also known as the transition probability, which is dependent on the population difference between the lower and upper level. The Boltzmann distribution of states shown in Equation 9 is used to describe the temperature dependency of the population distribution of the molecules in their allowed quantum states and can be substituted into Equation 8 at thermal equilibrium at temperature T . [82], [93][166], [167]

$$\frac{n_l}{n_t} = \frac{g_l \exp \left(\frac{-E_l}{kT} \right)}{Q(T)} \quad \text{Equation 9}$$

Where: T Temperature (K)
 k Boltzmann's constant
 E_l Energy of lower state
 $Q(T)$ Total internal partition function with respect to temperature

The line strength is temperature dependent because the Boltzmann factor is temperature dependent. The temperature is the factor that controls the

amount of energy the particles have to cross the activation energy barrier. As HITRAN uses a reference temperature of 296 K, the line strength $S(T)$ needs to be adjusted with respect to the line strength at the reference temperature. This is shown in Equation 10.[82], [93], [166], [167]

$$S(T) = S(T_0) \frac{Q(T_0) T_0}{Q(T) T} \exp \left[-\frac{hcE''}{k} \left(\frac{1}{T} - \frac{1}{T_0} \right) \right] \times \left[1 - \exp \left(-\frac{hcv_0}{kT} \right) \right] \times \left[1 - \exp \left(-\frac{hcv_0}{kT_0} \right) \right]^{-1} \quad \text{Equation 10}$$

Where:	$S(T_0)$	Line strength at reference temperature at ($\text{cm}^{-1}/\text{molecules cm}^{-2}$)
	$Q(T)$	Partition function of the absorbing molecules at temperature (K)
	$Q(T_0)$	Partition function of the absorbing molecules at reference temperature (K)
	E''	Lower-state energy of the transmission (cm^{-1})
	k	Boltzmann's constant (J K^{-1})

The total internal partition function shown in Equation 9 and Equation 10 is given by the sum of all states, like electronic, vibrational and rotational shown in Equation 13. [168]-[170]

$$Q = d_i \sum_{\text{all states}} d_s \exp^{-hcE_s/kT} \quad \text{Equation 11}$$

Where:	d_i	State-independent degeneracy factor
	d_s	State-dependent degeneracy factor
	E_s	Energy of state

For convenience, calculated partition functions have been organised for convenient rapid recall in the form of a third order polynomial expression in T as shown in Equation 12.[168]

$$Q(T) = a + bT + cT^2 + dT^3 \quad \text{Equation 12}$$

Where:	a, b, c, d	Polynomial coefficients of partition function within a given temperature range
--------	--------------	--

The partition function shown in Equation 12 utilises the low and medium temperature range coefficients shown in Table 2 for H_2^{16}O . The temperature for low ranges from 70 K – 500 K and medium ranges from 500 K to 1500 K. [168]

Table 2 The coefficients for the partition function of H₂¹⁶O. (Low and medium temperature range). [168]

	a	b	c	d
Low	-4.44	0.27678	1.25 × 10 ⁻³	4.89 × 10 ⁻⁷
Medium	-9.43	0.81903	7.40 × 10 ⁻⁵	4.24 × 10 ⁻⁷

The temperature must be known before the line strength can be calculated from Equation 10. In the absence of temperature measurements from conventional instrumentations like thermocouples, the average temperature across the absorption path length could still be calculated using the two-line thermometry technique. Two-line thermometry can be used to find the path-averaged temperature of the gas cell if two transitions are monitored simultaneously under the same mole fraction, pressure and path length.

For the two-line thermometry technique to work, at least two transitions are required within a singular measurement. The two-line thermometry measures two transitions simultaneously under the same pressure, mole fraction, path length and temperature. The temperature can be recovered by finding the ratio of the two integrated absorbance of two transitions. From Equation 13, the ratio of both A₁ and A₂ can be reduced to the ratio of S₁ and S₂ as a function of a specific temperature. By rearranging Equation 13, the temperature could be recovered using Equation 14.[82], [93]

$$R = \frac{A_1}{A_2} = \frac{S_1(T)}{S_2(T)} = \frac{S_1(T_0)}{S_2(T_0)} \times \exp \left[-\frac{hc}{k} (E_1'' - E_2'') \left(\frac{1}{T} - \frac{1}{T_0} \right) \right] \quad \text{Equation 13}$$

Where: R Ratio of integrated absorbance

$$T = \frac{\left(\frac{hc}{k} \right) (E_1'' - E_2'')}{\ln \left(\frac{A_1}{A_2} \right) + \ln \left(\frac{S_2(T_0)}{S_1(T_0)} \right) + \left(\frac{hc}{k} \right) \left(\frac{E_1'' - E_2''}{T_0} \right)} \quad \text{Equation 14}$$

The number density can then be determined from the Beer-Lambert Law in Equation 7 after the temperature is recovered using the two-line thermometry technique.

3.2.3 Line selection process

There are several criteria to aid consideration of water spectral line selection. [82], [171], [172] The first criterion to consider is to decide which spectral region to target for the absorption of water molecules. To fully exploit the TDL technology due to telecommunication advancement, the spectral region chosen would have to be within the region telecommunication of 1.25 to 1.65 μm. This region possesses a range of absorption bands, namely the ν₁ + ν₃, 2ν₁ and 2ν₃. The spectrum closer to 1.3 μm is dominated by the 2ν₁ band overtone transitions. As it moves higher than 1.35 μm, the stronger combination band transition of ν₁ + ν₃ holds more influence.[24], [82], [173][174] By working

within this spectral region, it ensures a wide selection of diode lasers and single mode optical fibres.

The second criterion is that the absorption strength of the selected lines must also enable a good signal-to-noise ratio of absorption spectra without being optically thick. The range used by Liu et al was that the absorbance must be within 0.9 to 1.[174]

The third criterion involves the use of absorption spectra to be isolated enough from nearby strong H₂O and CO₂ features to prevent interference and identity uncertainty during analysis.

The fourth criterion involves selecting line pairs with sufficient temperature sensitivity between their ratios to enable sensitive temperature measurements. A recommendation from Zhou et al [172] suggested that the difference of the lower state energy of the two lines were to be more than 700 cm⁻¹ as shown in Equation 15.

$$|\Delta E_1''| = |E_1'' - E_2''| \geq 700 \text{ cm}^{-1} \quad \text{Equation 15}$$

3.3 Unit conversions

The concentration shown in Equation 16 could be derived with the use of Avogadro's constant and rearranging Equation 7.

$$C = \frac{A}{S(T) \cdot L \cdot N_A} \quad \text{Equation 16}$$

Where:	C	Concentration (mol cm ⁻³)
	N_A	Avogadro's constant (6.022 × 10 ²³ molecules mol ⁻¹)

Percentage relative humidity is the preferred unit of measurement for the concentration of water vapour in the MICC. To calculate this, the ideal gas law shown in Equation 17, is used to first determine the total number density of all molecules in the chamber. The environmental conditions are considered to obey the ideal gas law, where the assumptions are that the kinetic energy of the molecules are proportionate to the temperature of the gas and that there are no intermolecular forces acting between the gas molecules. [175]

$$PV = nRT$$

Equation
17

Where:	P	Pressure
	V	Volume
	n	Moles
	R	Ideal gas constant (8.314 m ³ Pa K ⁻¹ mole ⁻¹)
	T	Temperature

The percentage relative humidity could be calculated by multiplying the partial pressure with the calculated saturation pressure as shown in Equation 18.

$$RH = \frac{p_{H_2O}}{p_{sat}(T)} \times 100\%$$

Equation
18

Where:	RH	Relative humidity (%)
	p_{H_2O}	Partial pressure of water (hPa)
	p_{sat}	Saturation pressure (hPa)

The saturation pressure could be calculated using the Arden Buck equation, which is an empirical correlation between saturation vapour pressures for moist air as shown in Equation 19. The partial pressure could be calculated using the Dalton's law, which states that the total pressure is the summation of all the partial pressures of its individual species in the system, shown in Equation 20.[176], [177]

$$p_{sat}(T) = 6.1121 \exp \left(\left(18.678 - \frac{T}{234.5} \right) \left(\frac{T}{257.14 + T} \right) \right)$$

Equation
19

$$p_{H_2O} = \frac{N_{water}}{N_{total}} \times p_{Total}$$

Equation
20

Where:	N_{water}	Number density of water (molecules cm ⁻³)
	N_{air}	Number density of air (molecules cm ⁻³)
	p_{Total}	Total pressure (hPa)

Converting the concentration to parts per million (ppm) could also be performed using the ratio of partial pressure to Equation 21.

$$C_{ppm} = \frac{p_{H_2O}}{p_{Total}} \times 10^6 \quad \text{Equation 21}$$

Where: C_{ppm} Concentration (ppm)

3.4 Tomographic algorithm

The discussion so far assumes that the temperature, concentration and pressure of the absorption path are uniform. In the scenario where there is a varying temperature and species concentration across the absorption path, tomography can be used to detect the variation in parameters, not just across the absorption path, but across the 2D spatial distribution as well.

Tomography involves dividing the two-dimensional (2D) optical plane of measurement into a grid of cells. The cells of the grid will be individually allocated an (x, y) coordinate. There are various methods of employing tomographic techniques, typically chosen based on equipment architecture layout and resources and which projection geometry best complements the physical layouts. Examples of common reconstruction algorithms are Filtered Back Projection (FBP), Fourier Slice Theorem and the Algebraic Reconstruction Tomography (ART).

The reconstructions used in this thesis focus on the reconstruction of the integrated absorbance of water. The reconstructed image will be comprised of grid cells or pixels, and the assumption used is that the temperature, pressure and concentration of water are uniform in each cell/pixel.

3.4.1 Filtered Back Projection (FBP)

Firstly a definition of terminology is required. A singular beam from laser source to detector across the optical plane is a line integral. This optical plane where the measured objects are located is termed the space domain and is a two-dimensional function $f(x, y)$. The rays or line integrals shown in Figure 13 are defined by its unique equation based on the angle (θ) in relation to the object of measure as well as its coordinates as shown in Equation 22. These line integrals are also represented as functions of (θ, t) . [110]

$$x \cos\theta + y \sin\theta = t \quad \text{Equation 22}$$

Typically, FBP works by emitting a set amount of laser beams in a parallel fashion at an arbitrary θ_i and repeating the same process at θ_{i+1} and so on. A combination of laser rays or line integrals from t_1 to t_n at a set angle θ_i will form

a singular parallel projection represented by $P_{\theta}(t)$ in Figure 13, where t is the location of the line integral along an arbitrary line on θ . [110]

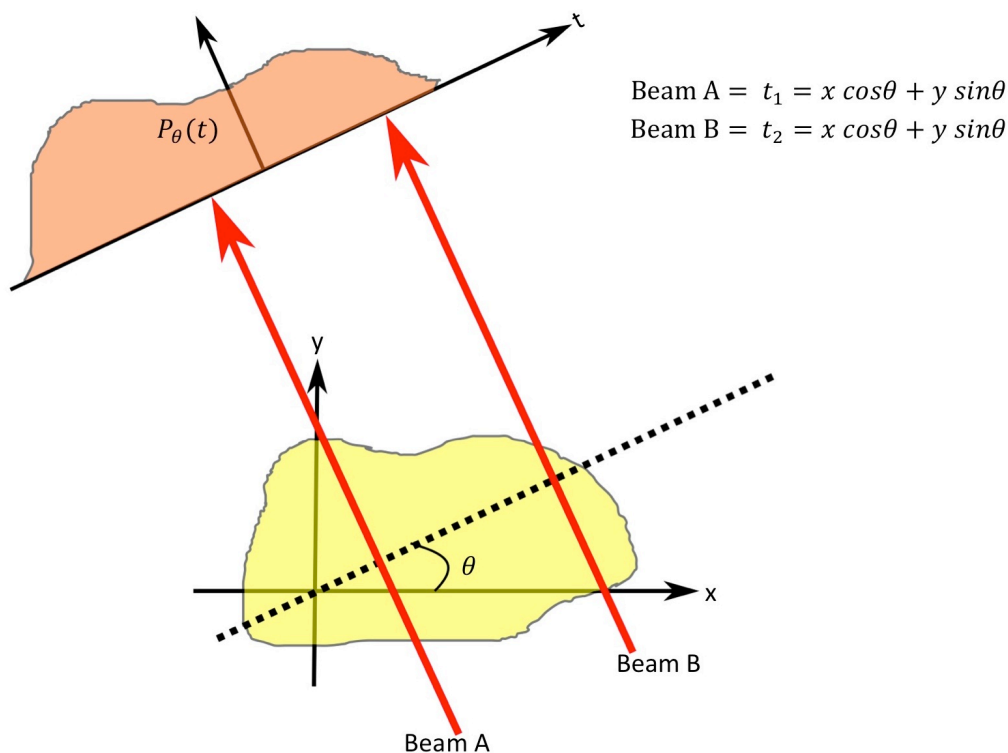


Figure 13 Example of object in 2D function (x, y) with individual line integrals forming a Radon Transform.

The function $P_{\theta}(t)$, also known as the Radon transform of the measured optical plane $f(x, y)$ can be expressed in Equation 23 and Equation 24, where s is the intensity of the line integral. [110]

$$P_{\theta}(t) = \int_{(\theta,t)line} f(x, y) ds \tag{Equation 23}$$

$$P_{\theta}(t) = \int_{-\infty}^{\infty} \int_{-\infty}^{\infty} f(x, y) \delta(x \cos\theta + y \sin\theta - t) dx dy \tag{Equation 24}$$

Typically at this point, an impulse function filter is multiplied to the individual radon transforms and back-smearred onto the image via their respective projection angle. The filter is used to counteract the blurring that occurs from back 'smearing' of the data back into the image. [110]

It is worth noting at this point that the Abel transform is also commonly used to study combustion. The Abel transform is actually a special case of the Radon transform, which is used when the interference is symmetrical in shape and that the line-of-sight integrals are all at the same angle. However in many industrial applications, this is rarely the case and therefore the Radon transform is used and all the experiments conducted in this research feature asymmetrical heating/combustion configurations. [178]

3.4.2 Fourier Slice Theorem

Figure 14 depicts the use of the Fourier Slice Theorem (FST) to transform information from the space domain into the frequency domain. The FST is executed by performing a 1D Fourier Transform of a parallel projection and by allocating it to a 2D Fourier transform of the original optical plane measurement area. A standard way of depicting a 2D transform of any object, F , is shown in Equation 25, where u and v are the axes in the frequency domain. [110]

$$F(u, v) = \int_{-\infty}^{\infty} \int_{-\infty}^{\infty} f(x, y) e^{-j2\pi(ux+vy)} dx dy \tag{Equation 25}$$

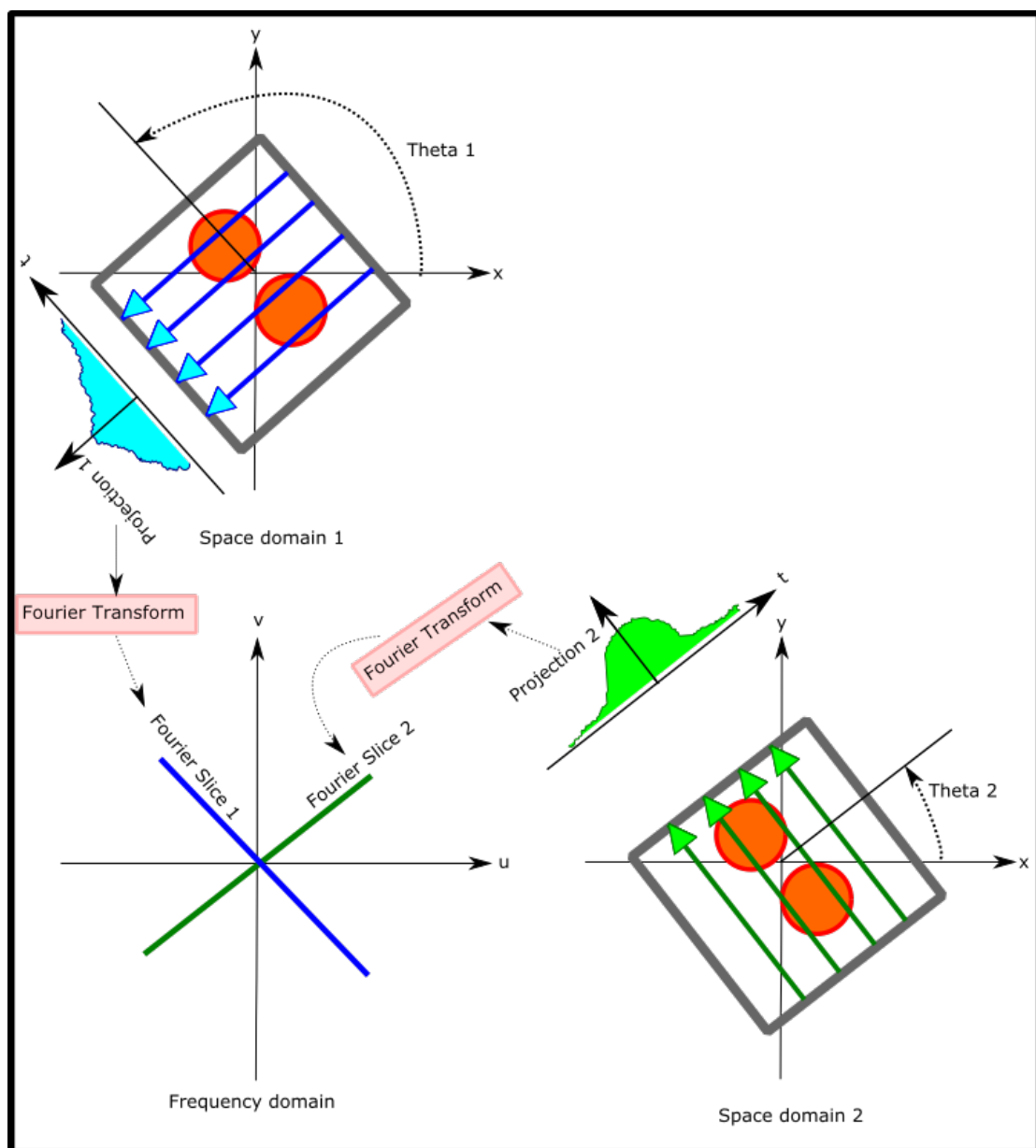


Figure 14 The translation of projection slices from the space domain to the frequency domain Fourier slices via Fourier Transform.

So the Fourier transform for a projection $P_\theta(t)$ at an angle θ is Equation 26.

$$S_\theta(w) = \int_{-\infty}^{\infty} P_\theta(t) e^{-j2\pi w t} dt \quad \text{Equation 26}$$

In reference to Equation 23, $f(x, y)$ could also be expressed as $f(t, s)$ as shown from their relation in Equation 27 and Equation 26 could be rewritten as Equation 28. [110]

$$\begin{bmatrix} t \\ s \end{bmatrix} = \begin{bmatrix} \cos\theta & \sin\theta \\ -\sin\theta & \cos\theta \end{bmatrix} \begin{bmatrix} x \\ y \end{bmatrix} \quad \text{Equation 27}$$

$$S_\theta(w) = \int_{-\infty}^{\infty} [f(t, s) ds] e^{-j2\pi w t} dt \quad \text{Equation 28}$$

The 2D transform shown in Equation 29 could be achieved by transforming Equation 28 using Equation 27.

$$S_\theta(w) = \int_{-\infty}^{\infty} \int_{-\infty}^{\infty} f(x, y) e^{-j2\pi w(x \cos\theta + y \sin\theta)} dx dy \quad \text{Equation 29}$$

3.4.2.1 Computer implementation

The Fourier transform could be implemented by a FFT (Fast Fourier transform) function, by band-limiting the Fourier transformed slices. A bandlimited Fourier transform assumes components over a certain frequency to be negligible (zero) and suitable for a FFT algorithm to be a good approximate to the Fourier transform in Equation 29. [110]

Filters are used to suppress the high frequencies, which tend to be observation noises. These filters are usually convoluted to the projection slices, either in the spatial domain or in the frequency domain. [110]

Zero padding consists of adding a trail of zeros to the projection slices and this will decrease the step size/ cell size of the data points in the Fourier domain. Adequate zero padding reduces the overall formation of artifacts caused by interperiod interference present in the reconstruction images by producing smoother individual spectrums. [110]

3.4.3 Algebraic Reconstruction Technique (ART)

ART is usually best implemented where the projections are not evenly distributed over 180° or 360° or it is not physically possible to measure a large number of projections. Similar work was based on fan beam projection using Algebraic Reconstruction Tomography (ART) [93] and was chosen because it suited that particular equipment architecture as it only had one laser source and detector, which made acquiring large volumes of projections time consuming. [110]

ART is achieved by first superimposing a grid on the image $f(x, y)$ as depicted in Figure 15, where each cell in the grid are assumed uniform in pressure, temperature and concentration. The projection (p_i), that is transmitted across the image is given a set width, and a single projection is expressed in Equation 30. The ratio of area within each cell that is exposed to the passing projection is given by w_{ij} , which is depicted as the purple rectangle within points ABCD shown in Figure 15. Each cell is the accumulation of the total impact each projection have on it, where the impact of a projection not touching the cell is 0. The value of each cell, f_j can then be calculated via iteration with Equation 31. [110] A threshold value is typically used between the latest and previous iteration to stop the iteration process, which in this thesis is set at 1% [93].

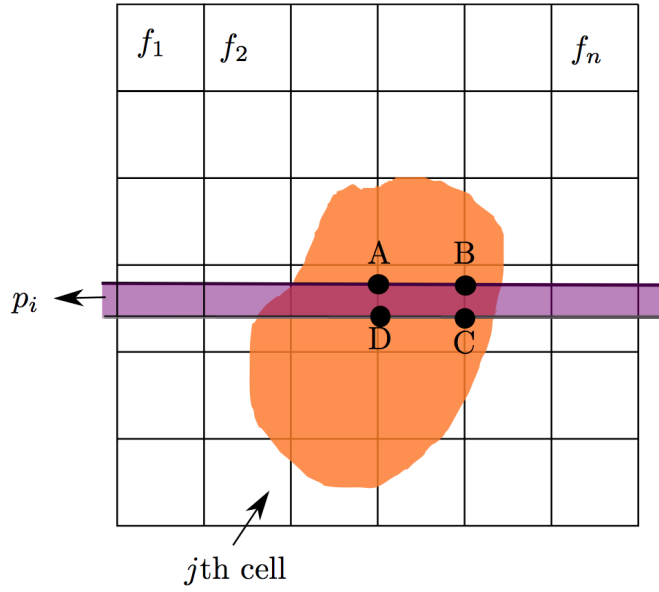


Figure 15 Superimposed grid over object, with the ratio of cell exposed to passing projection located within points ABCD.

$$p_i = \sum_{j=1}^N w_{ij} \times f_j \quad , \quad i = 1, 2, \dots, M \tag{Equation 30}$$

Where:

p_i	i^{th} Projection
N	Total number of cells
w_{ij}	Ratio of cell j exposed to the projection
f_j	Constant value inside the cell j
M	Total number of projections

$$f_j^{(k+1)} = f_j^{(k)} + \lambda \times w_{ij} \times \frac{p_i - \sum_{l=1}^N f_l^{(k)} \times w_{il}}{\sum_{l=1}^N f_l^{(k)} \times w_{il}^2} \tag{Equation 31}$$

Where:

λ	Relaxation parameter
k	Iteration step number

3.5 Key equipment theory

3.5.1 Distributed feedback (DFB) diode semiconductor laser

A typical laser consists of three main components, the active medium, the energy pump and the optical resonator. The active medium is used to amplify the incident electromagnetic wave. The energy pump is used to deliver energy into the active medium for populating energy levels until population inversion occurs.

Population inversion can occur when a deviation from thermal equilibrium occurs. A typical lower level always has a larger population than a higher level in thermal equilibrium state and no accumulation may occur in this state as shown in Figure 16 (a). A population inversion occurs when the higher level contains a higher population than the lower level as shown in Figure 16 (b).

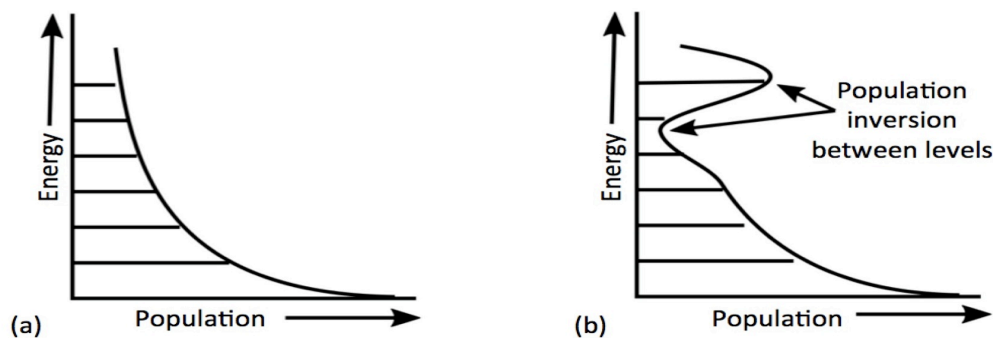


Figure 16 (a) The population distribution for energy levels at thermal equilibrium (b) Population inversion occurs at higher level

A semiconductor laser consists of two terminals, p and n, with a junction between the two terminals. The n-type (n-terminal), also known as the conduction band, is usually doped with impurities such as phosphorous to increase the conductivity of the semiconductor. The p-type (p-terminal), also known as the valence band, is doped with impurities such as gallium to create deficiencies of valence electrons or holes for recombination. This is shown in Figure 17 (a).

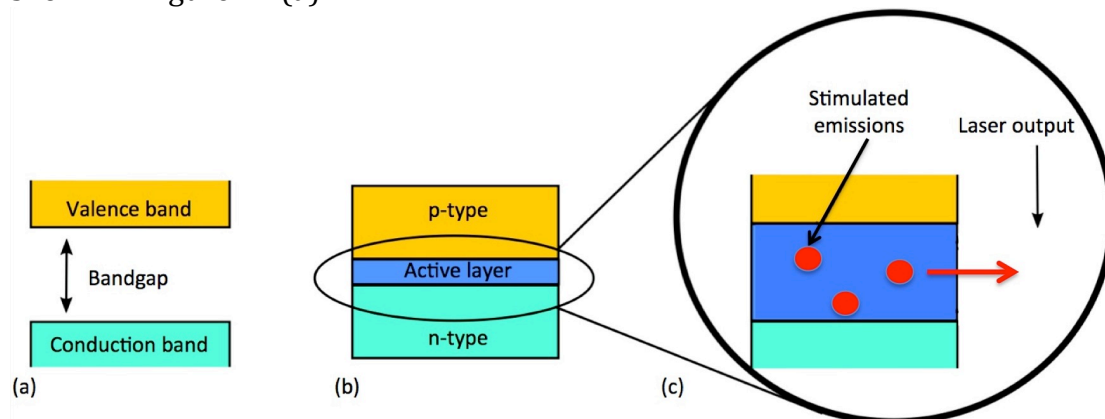


Figure 17 (a) The bandgap between the semiconductor terminals. The conduction band or the n-type, contributes the free electrons while the valence band, the p-type, contains valence electrons or the holes for recombination. (b) The layout of the semiconductor diode laser (c) Depiction of stimulated emission in the active layer.

When the n terminal has a negative voltage and the p terminal a positive voltage, a forward direction electric current is sent through the p-n terminals causing the electrons and holes within the p-n junction to recombine. This is also termed forward biasing. This recombination process emits energy in the form of electromagnetic radiation as shown in Figure 17 (b) and Figure 17 (c). The energy difference or bandgap between the energy levels of the electrons and holes produces light of a specific wavelength. This is dependent on the composition of the semiconductor material.

The standard binary compounds are GaAs and InP, which have a fixed bandgap and therefore emitted wavelength. However, adding additional elements changes the lattice constant and bandgap, thus changing the emitted wavelength. InGaAsP diodes were used in this research, which are typically used for telecommunications. The forward electric current must first be higher than a certain threshold current before emission of radiation occurs. The type of semiconductor diode determines this current threshold. The electric current threshold is exceeded when the radiation field in the p-n junction becomes intense enough for the induced-emission rate to exceed the radiation-less electron-to-hole recombination rate.

A distributed feedback (DFB) laser utilises the Bragg grating shown in Figure 18 (a) to reduce the spectral width of the laser and allow it to only emit one mode or wavelength. This is shown in Figure 18 (b), where the grating reflects portions of stimulated photons back to the active layer, thus the term 'feedback'. The reflection occurs throughout the active medium, which gives the term 'distributed'.

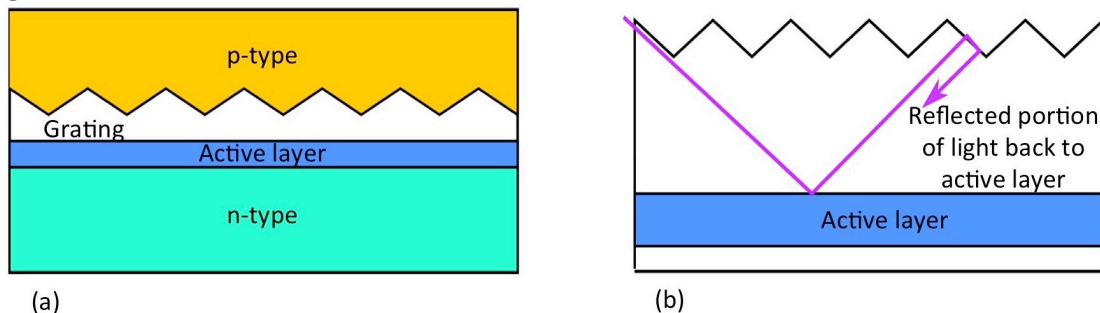


Figure 18 (a) The layout of a DFB laser (b) The reflected portions of stimulated photons from the grating.

3.5.2 Fibre Optics

Fibre optics are primarily used for telecommunication purposes as transmission channels, carrying light beams through the fibre via total internal reflection. An optical fibre consists of an inner central dielectric core of high refractive index, n_1 , while being cladded by a secondary material of slightly lower refractive index, n_2 to allow light to be transmitted through the fibre as shown in Figure 19. [179], [180]

SiO_2 is commonly used for both core and cladding, but the core is usually doped with a secondary component to change its refractive index. Examples of oxides used to increase the refractive index are TiO_2 , GeO_2 and Al_2O_3 . Light propagated through an optical fibre suffers from mild attenuation due to minor losses but most modern fibres have improved significantly, with as low as 20dB loss per km. [179], [180]

There are typically two kinds of optical fibre, single mode and multi-mode fibres. Single-mode fibres typically consists of smaller cores of $9\ \mu\text{m}$, with lower attenuation and are designed for single transmission of wavelength. Multimode fibres on the other hand are thicker in the core and commercially available at $50\ \mu\text{m}$ and $62.5\ \mu\text{m}$. They support multiple wavelengths but suffer from higher attenuation of light. The claddings are usually at $125\ \mu\text{m}$. [179]–[181]

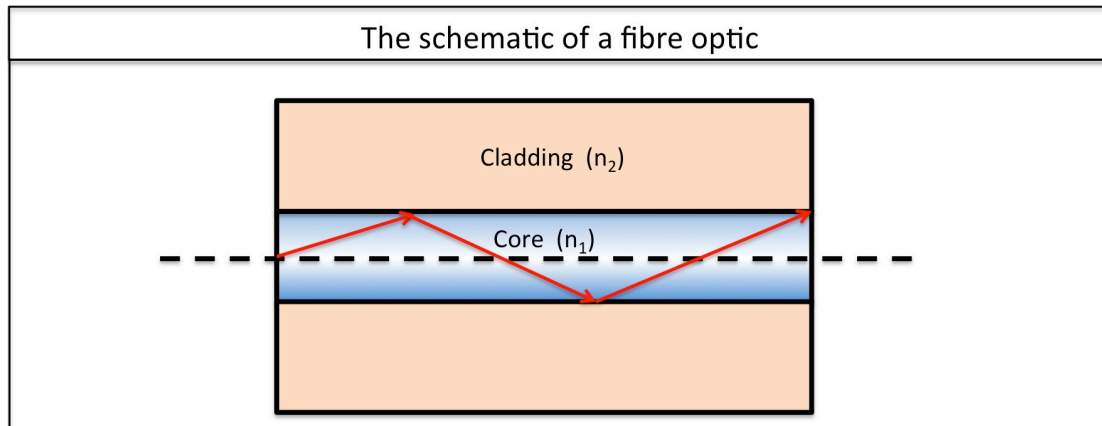


Figure 19 Schematic of a fibre optic, with the core wrapped by the cladding. The light propagating through the core is shown in red.

3.6 Chapter summary

The chapter summarises the relevant theory required for the average line of sight measurements using TDL. The tomography algorithms that were used in this thesis have also been discussed to calculate the varying spatial temperature and concentration distribution of water vapour in the optical plane. The working principles of key equipment used during the research have also been discussed.

4 TUNABLE DIODE LASER (TDLAS) LINE OF SIGHT (LOS) MONITORING IN ICE CLOUD CHAMBER

4.1 Chapter overview

In this chapter, the research focuses on setting up a TDLAS system in the Manchester Ice Cloud Chamber (MICC). There are 3 ice cloud chambers to the authors knowledge, the AIDA chamber in Karlsruhe, Germany[182], the MRI in Tsukuba, Japan[183] and the MICC in Manchester UK. The use of TDLAS systems as hygrometers has only been done so in AIDA but not below atmospheric pressures.

It is a novel idea in incorporating a TDLAS tomography system for 2D, 3D or temporal imaging for an ice cloud chamber to study the spatial distribution of water vapour concentration during cloud formations. However, before the tomography system is considered, a single line-of sight (LOS) TDLAS system needs to be designed to test its diagnostic capabilities in the chamber. The design of this TDLAS system and its associated programs also serves as a starting point for future tomography work detailed in this thesis.

The background and the reason for conducting the experiments at the MICC is introduced in Section 4.2. Section 4.3 details the TDL equipment for LOS monitoring, as well as the associated acquisition and fitting programs, that were designed and written by the author to be retrofitted onto the existing MICC. The results of TDLAS monitoring, together with calibrations and validations are discussed in Section 4.4. Finally, challenges and future work are summarised in Section 4.5.

4.2 Background on suppressed Snomax immersion freezing

One of the most devastating outcomes from climate change is the increased frequency of extreme weather events. The Earth's climate is largely determined by the solar radiation entering and leaving the atmosphere.

The radiation budget depicted in Figure 20 is seen as a balancing act between the incoming shortwave solar radiation from the sun and the outgoing longwave terrestrial radiation emitted from Earth and its atmosphere. A tipping in either direction of the radiation budget would have a role in the overall climate change. [184] Over the years, anthropogenic activities have altered the state of equilibrium, which is one of the causes of climate change. Aerosols affect the climate in two ways; the first involves the direct absorption of radiation in the atmosphere while the second affects the climate indirectly through cloud-aerosol interactions. Although the majority of aerosols are naturally occurring (dust or volcanic ash for example), it is the anthropogenic aerosols that are of concern here. Aerosols resulting from human activities usually occur from fuel combustion, and a rise of sulphate aerosols could be seen since the industrial revolution. [5], [185]–[187]

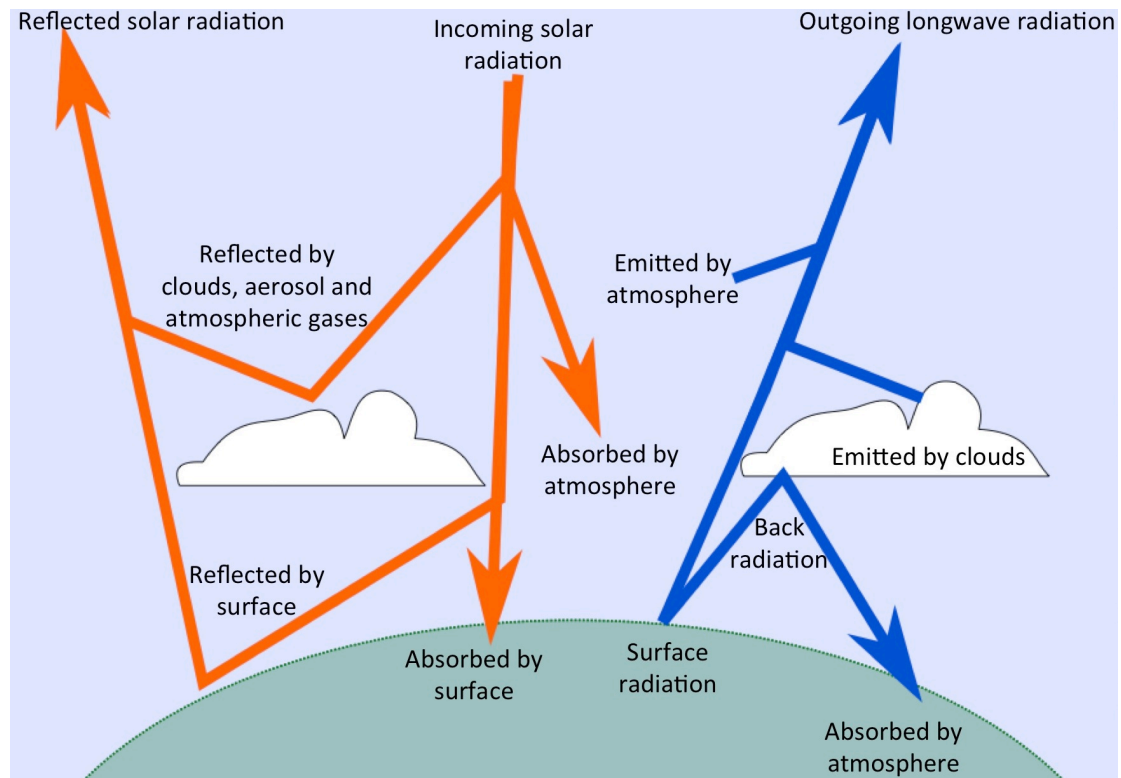


Figure 20 The radiation budget of incoming solar radiation and outgoing longwave radiation.[2]

The presence of these sulphate aerosols affects the climate in several ways. It has a direct role in reflecting the incoming solar radiation. Indirectly, they create clouds with smaller droplet sizes, making the clouds more reflective to incoming solar radiation (cloud albedo effect where net cooling is created). By reflecting incoming solar radiation from either the direct or the indirect manner, the general trend of aerosols cooling the Earth is opposite to the rising effects of GHG. However, unlike GHG, the effects of aerosols are more regional in impact. While there are suggestions that the cooling effect of aerosols could alleviate GHG warming effects, there are high levels of uncertainties.[5], [188], [189]

It is estimated that 69% of global precipitation involves ice formation. Ice glaciation begins as ice nucleation, wherein heterogeneous freezing, requires the presence of ice nuclei (IN) like mineral dusts and bacteria. As the ice crystal grows through collisions and coalescence of nearby water droplets and ice particles, it becomes large enough to fall as precipitation. These ice precipitation particles melt as they fall, becoming rain as they hit the ground. It is hypothesized that the presence of cloud condensation nuclei (CCN) like ammonium sulphate will inhibit the formation of ice within the cloud by competing for water vapour in the air, resulting in suppressed immersion freezing where there is less condensed water to freeze. [190]–[192]

Immersion freezing occurs when the air is cooled to dew point and the relative humidity is raised to a 100%. When this happens, two processes occur. The first occurs when the water vapour condenses onto the CCN to form a cloud droplet. Precipitation occurs via the coalescence process (action of colliding droplets with each other) by forming large enough droplets before falling. The falling droplets continue to grow as they continue to collide with other droplets during its fall. The second process involves the ice nucleation process where

water vapour is condensing onto the ice crystal. The ice crystal grows into a snow crystal when the rate of condensation is higher than the rate of evaporation[188], [193]–[195].

The researchers working at the MICC studying the expansion simulation conducted in the ice cloud chamber are supposed to simulate a parcel of air rising adiabatically as it would in the atmosphere. It is conducted with the addition of ice nuclei (IN) inside the air, and varied with and without the presence of anthropogenic cloud condensation nuclei (CCN).

Based on a cloud parcel model, Aerosol-Cloud-Precipitation Interaction Model (APCIM)[196], the presence of CCN suppresses the freezing of IN due to the higher competition of aerosols for water molecules. The goal of the experiments was to validate the hypothesis model of suppressed IN freezing in the presence of CCN particles. Snomax was used as the source of IN, which is a commercially available protein based ice nuclei (IN) and ammonium sulphate was used as CCN.

However, to study this process successfully, an instrument is required to measure the changes in relative humidity of gaseous water in the air inside the chamber. As the chamber is sealed during experiments, the rate of diminishing gaseous water is directly related to the rate of ice nucleation. This allows the comparison of ice nucleation rate at different conditions.

Currently, a chilled mirror hygrometer is used to monitor the relative humidity in the chamber. This instrument however does not keep up with rapid changes in relative humidity, which occurs during an expansion process. Therefore the work described here focuses on designing a TDLAS system and validating its results in measuring the rapid changes of relative humidity inside the chamber.

The TDLAS line of sight setup and its associated programs create a fundamental step in developing a future tomography system.

4.2.1 Details of the experimental site

The expansion process is conducted in the MICC, which is a 10 m high stainless steel tube of 1 m in diameter, spanning across 3 floors as shown in Figure 21. The pressure sealed chamber, accessible at each floor is enclosed within a temperature controlled cold room that could each be reduced to $-55\text{ }^{\circ}\text{C}$ to reduce the effect of ambient temperature on the structure and its content.

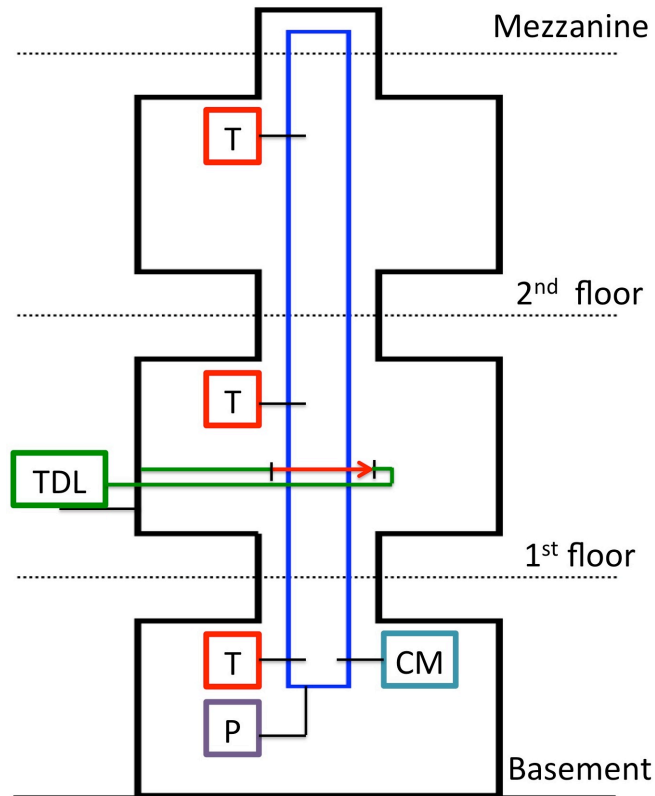


Figure 21 Schematic of the MICC. The locations of the temperature probes (T) are listed in red, pressure probes (P) as grey, chilled mirror as (CM) and the TDLAS system (TDL) as green.

The aerosols that are fed into the chamber are premixed with ambient air in the Manchester Aerosol Chamber (MAC) before being fed into the chamber. The MAC is an 18 m^3 Teflon bag suspended by a mobile frame. A filtration system capable of removing all particles and trace gases is used to filter the ambient air before being fed into the MAC. The filtration system consists of 3 types of filters, namely Paurafil/charcoal mix, charcoal and HEPA. The IN, Snomax power, was prepared as a solution by mixing 0.402 g of dried Snomax power with 250 ml of $18.2\text{ M}\Omega$ deionised water. The final concentration of the IN solution is 1.6 mg/ml . A sonic bath was used to facilitate mixing of the Snomax, which is insoluble in water. The CCN used for the experiments was ammonium sulphate, was prepared from an aqueous salt solution of ammonium sulphate at solute mass concentration of 0.01% . Depending on the aerosol requirements of the experiment, the corresponding solutions are atomised and passed through diffusion dryer before mixing with the filtered ambient air in the MAC. The aerosol-air mixture in the MAC is delivered into the chamber via a pipe nozzle. The chamber was left to equilibrate with the cold room via an open porthole

located at the base of the chamber. The air of the cold room was allowed to enter the chamber and once the temperature of the air inside the chamber equilibrated with the air of the cold room, the porthole would be shut. The experiments conducted would always begin at atmospheric pressure and -13 °C.

For the expansion process to occur, high power pumps are used to evacuate the chamber. This expansion process will reduce the pressure from atmospheric pressure down to approximately 0.7 atm, while cooling the air down from -13 °C to approximately -17 °C. A variety of instruments were used to measure different parameters within the chamber. Examples of parameters monitored included particle concentration, particle size distribution, and aerosol and droplet size distribution.

The pressure is monitored by a pressure probe located at a sampling port at the base of the chamber. The temperatures were monitored across the chamber using thermometers at 8 sampling points inside the inner chamber walls. The thermometers were platinum resistance and were calibrated to measure temperature down to approximately -30 °C. A chilled mirror hygrometer (MBW Calibration Ltd LX-373) located at the bottom of the MICC was used to monitor the relative humidity with the assistance of an air sample line.

4.3 TDL equipment and setup design

This section details the TDL setup that was designed by the author for the MICC research team to be retrofitted onto the pre-existing MICC setup. The author was involved in the design and equipment selection process unless otherwise stated. Several points were considered during the setup design phase.

- Most of the equipment, including the laser, its controllers and computers should be kept outside the chilled room due to the low temperature (-13 °C). This allows the operator to work comfortably at the computer, as well as provide optimum working conditions (within room temperature) for the laser diode itself.
- Optical access needs to be installed for the laser to pass through the chamber.

The TDL setup was designed to be located in the middle of the 3 floors and away from the chilled mirror as shown in Figure 21. The rationale to locate the TDL setup away from the chilled mirror in the basement was space constraints in the basement and to include another point of measurement of relative humidity away from the existing chilled mirror in the lower chamber.

The TDL setup spans through the external area outside the cold room into the internal area of the cold room on the first floor. The area outside the cold room is exposed to atmospheric conditions as depicted by the orange dashed line of Figure 22, while the second area depicted by the blue dashed line depicts the cold room at atmospheric pressure but chilled down to a desired temperature.

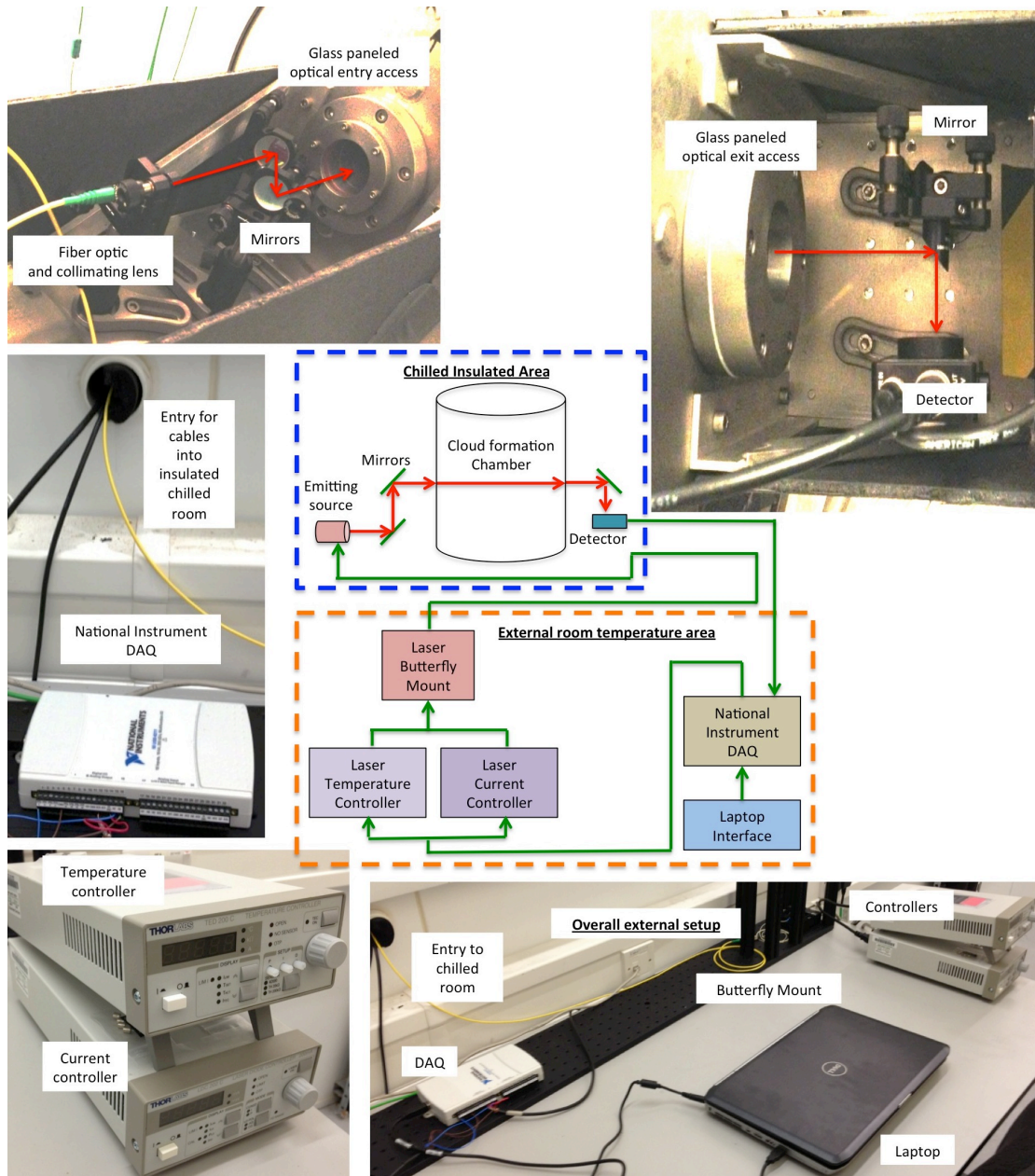


Figure 22 Schematic and relevant photos of the equipment setup.

The external room in Figure 22 hosts the majority of the equipment involved, which consists of the laptop, a data acquisition board, the laser controllers as well as the laser and its mount. This allows the user to operate the program comfortably outside the chilled room and keep the chilled room sealed during experiments. This allows the assumption that the chilled room condition stays constant throughout the experiments in terms of both humidity and temperature.

A hole was drilled into the wall of the chilled room and used as a portal for both entering and exiting electrical cables and fibre optics cables. Insulating foam was wrapped around the cables to seal up the excess gap in the hole. The end of the laser diode was fed through this hole into the internal chilled room, which also contains other optical components like mirrors to redirect the laser beam. The detector was also located inside the internal room as well.

The enlarged view of the chilled room from Figure 22 can be seen in Figure 23, which shows the schematic of the laser arrangements, inclusive of the length at different zones of the laser path.

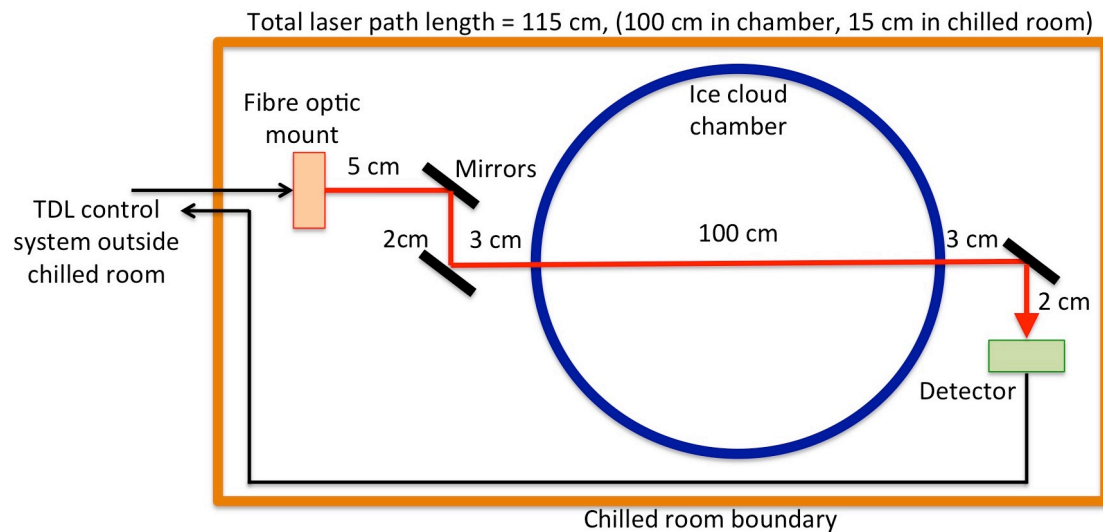


Figure 23 Schematic of laser path length and location of key equipment. The red arrow depicts laser path, while black arrows depict fibre optic cables.

The fibre optic end, coupled with a collimating lens (Thorlabs F230APC-1310), was fed into the chilled room and mounted onto a kinematic mount (Thorlabs KM100T) with the aid of an adapter (Thorlabs AD11F) as shown in Figure 23.

The laser beam was directed through a calcium fluoride window panel constructed for this purpose, into the chamber with the help of two adjustable mirrors (Thorlabs PF05-03-M01) mounted onto kinematic mounts (Thorlabs KM100CP/M). The laser beam traverses 1 m across the chamber, and exits from a similar calcium fluoride window panel and was directed onto an InGaAs switchable gain photodetector with 2 mm diameter (PDA10CS-CS) with the help of an off-axis 90° parabolic mirror (Thorlabs MPD129-M01). Calcium fluoride was used because it provides good transmission in the NIR. The windows were also wedged to prevent optical interference effects.

All laser optics and detectors were mounted on 50 mm long, 12.7 mm diameter optical posts (Thorlabs TR50/M) and secured with 30 mm high post holders (Thorlabs PH30/M). These optical posts were placed onto customised pre-drilled stainless steel 1 cm thick breadboards, which were then attached outside of the optical access areas of the chamber.

The laser diode, which was made available prior to the author's introduction to the project, was a factory pre-assembled 10 mW distributed feedback (DFB) pigtail fibre optic coupled laser with a FC/APC connection (NLK1E5EAAA). It was centred at 7220 cm⁻¹ (1.38512 μm) with a possible deviation of ± 1 nm. The laser diode had a conservative working range between 7210 cm⁻¹ and 7224 cm⁻¹ as shown in Figure 24.

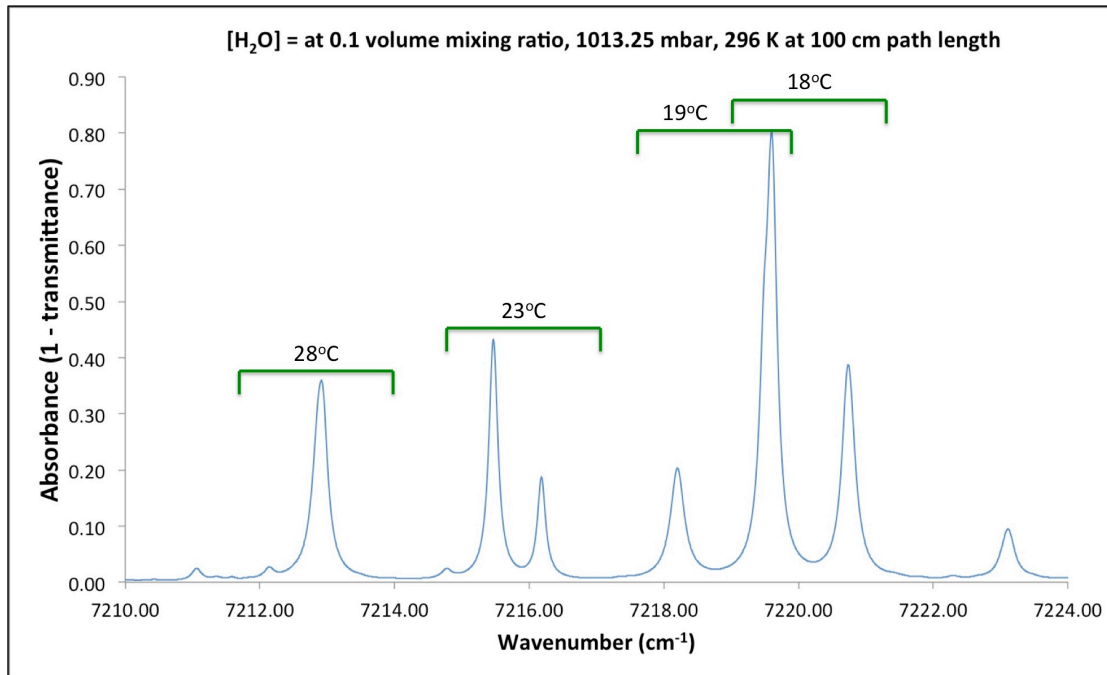


Figure 24 The simulated H₂O absorption spectra at 296 K accessible by the laser at different laser temperatures. Extracted from HITRAN 2012 from www.spectralcalc.com.

The laptop running LabVIEW is used to control the data acquisition board (DAQ) (National Instruments 16-bit NI USB 6211). The interface used in the laptop was a customised LabVIEW program, similar to the example shown in Appendix 11.2. The DAQ was used to either send commands to the laser controllers or to receive information from the photodetector. The DAQ transmits a signal to the current controller (Thorlabs LDC 202C) to tune over a range of current values, which corresponds to a wavenumber scan. The temperature controller (Thorlabs TED 200C) was used to control the laser temperature as shown in Figure 24. The forward voltage from the controllers was directed to the 14-pin butterfly laser mount (Thorlabs LM14S2).

The modulation input waveform applied to the laser diode current driver is shown in Figure 25 in red. A specific voltage corresponds to a specific bias current and the laser diode lases at a particular wavelength. By applying this voltage modulation waveform, the laser diode bias current was increased linearly in the shape of the voltage ramp, and the corresponding wavenumber targeted by the laser was also linearly increased in relation to the time and pattern of the input voltage waveform.

The modulated waveform was rapidly swept at 100 Hz, with a single sweep lasting a total of 200 μ s with 200 data points. Averaging was done for each spectrum, and for each averaging cycle, consisting of 5 spectra amounting to a total time of 1000 μ s and 1000 data points. Each cycle was averaged and the resulting spectrum of 200 points per cycle lasting 1000 μ s as depicted in Figure 25.

The conversion to relative wavenumber will not be discussed in detailed here as a sample demonstration can be seen in Chapter 5.2.3 As the pressure may fluctuate between atmospheric and lower pressures, a pseudo-Voigt function shown in Equation 5 in Chapter 3.2.1 was used to fit the each of the peaks in the spectrum.

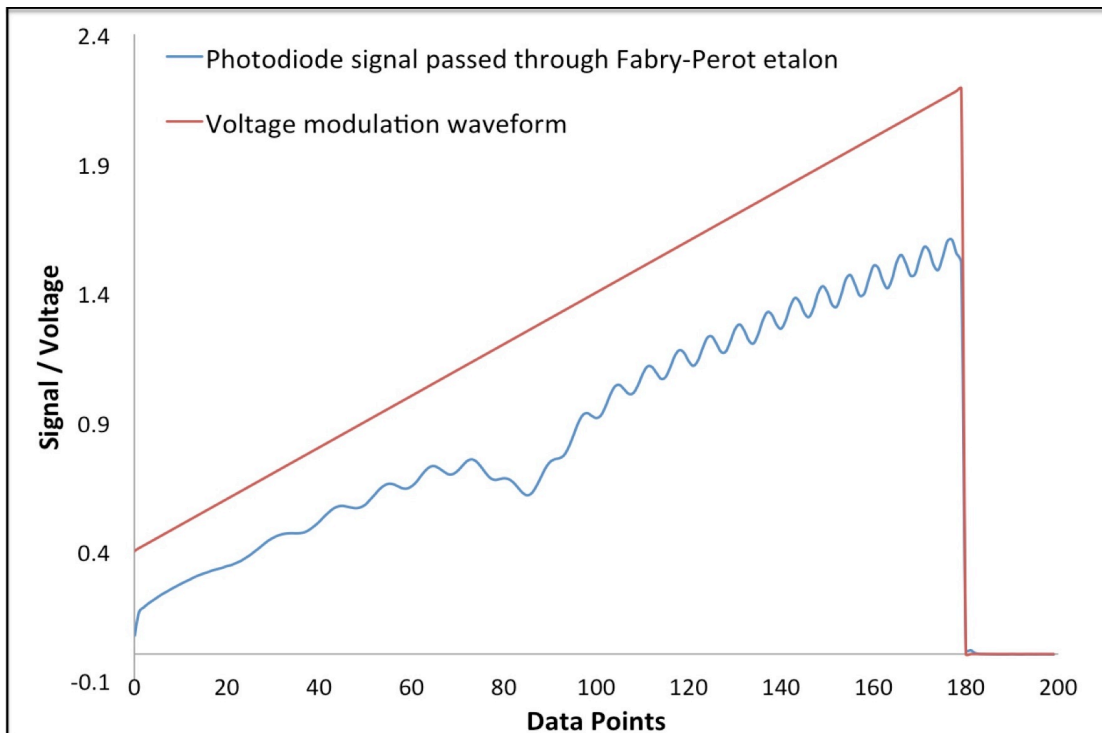


Figure 25 Voltage modulation waveform used for tuning the laser wavenumber is shown in red. The blue signal represents the signal acquired at the end of the photodetector with the laser passing through a Fabry-Perot etalon.

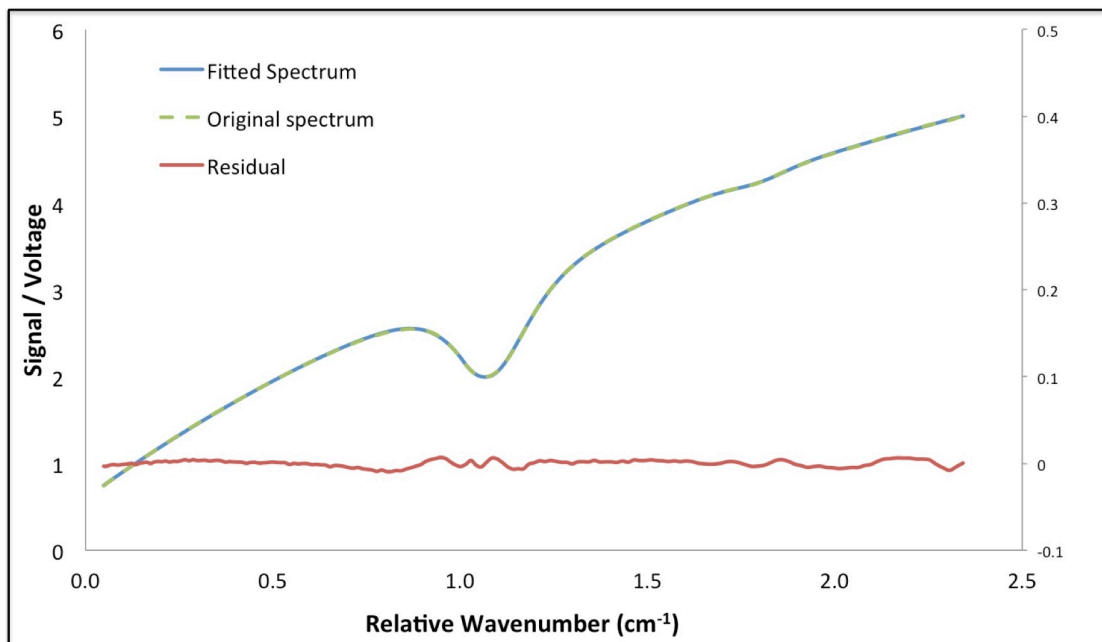


Figure 26 A transmission fitting of a sample experimental spectrum. The experimental spectrum is in dashed green, the fitted spectrum is blue and the residual of the fit is in red (secondary y-axis).

Only lines with line strength larger than a threshold of 1×10^{23} were used for the peak fitting shown in Figure 26. There are a total of 4 of these lines present are either centred near 7212.88 cm^{-1} or 7212.14 cm^{-1} as shown in Figure 27.

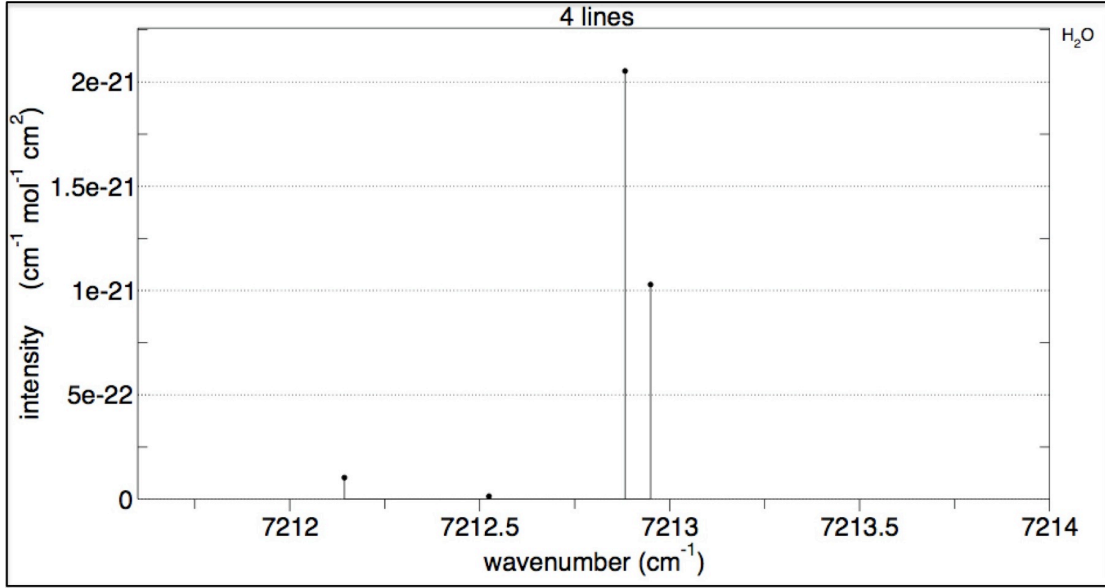


Figure 27 Line strengths above threshold deemed significant enough to contribute to peak fitting process. Extracted from HITRAN 2012 at room temperature from www.spectralcalc.com.

The peak convolution of the 4 pseudo-Voigt peaks in Figure 26 was used to fit the transmission spectrum as shown in Equation 32. The residual was calculated by subtracting the fitted spectrum over the original experimental data.

$$\begin{aligned}
 I_v(\nu) = & (I_{0\nu} + I_{1\nu}\nu + I_{2\nu}\nu^2 + I_{3\nu}\nu^3) \\
 & \times \exp \left(- \sum_{i=1}^4 A \left[\left(m_u \frac{2}{\pi} \frac{w}{4(x-x_c)^2 + w^2} \right) \right. \right. \\
 & \left. \left. + \left((1 - m_u) \frac{\sqrt{4\ln 2}}{\sqrt{\pi}w} e^{-\frac{4\ln 2}{w^2}(x-x_c)^2} \right) \right] \right)
 \end{aligned}
 \tag{Equation 32}$$

The standard deviation (*SD*) of the residuals is shown in Equation 33, where *n* is the number of residual samples. The standard deviation of experimental data over the fitted spectrum was calculated to be approximately around 1.339×10^{-5} .

$$SD = \sqrt{\frac{\sum \text{residuals}^2}{n - 2}}
 \tag{Equation 33}$$

The unit conversions to convert number density to relative humidity were covered in Chapter 3.2.3.

4.4 Results

4.4.1 Calibrations and validations

The laser path from the laser source to the detector as shown in Figure 23 was a total of 115 cm. The laser path within the MICC was 100 cm and 15 cm of the laser path length was outside the MICC (but within the cold room), which means the absorption of water molecules includes those of the chilled room enclosure. Therefore it is important to remove the number of absorbing water molecules before processing the relative humidity of the MICC.

To do this, several assumptions are laid out.

- The parameters of the MICC were allowed to equilibrate with the chilled room by leaving the bottom porthole open.
- During the calibration process, the temperature and pressure of the chilled room are the same as inside the MICC.
- The distribution of water vapour during calibration is assumed homogeneous.
- The concentration of water vapour in the chilled room stays constant after the porthole has been shut and the experiment is being carried out in the MICC.
- The temperature of the chilled room stays constant throughout the experiment.
- If the peak shape of water vapour absorption in chilled room is different from the peak shape of water absorption inside the MICC due to a difference in temperature and pressure, it is assumed negligible, as the difference is small.

The calibration steps of the TDL readings are described in Figure 28. During this calibration process, the condition of the chilled room was equivalent to the MICC and the condition of the chilled room stays constant throughout the experiment after the MICC porthole was closed.

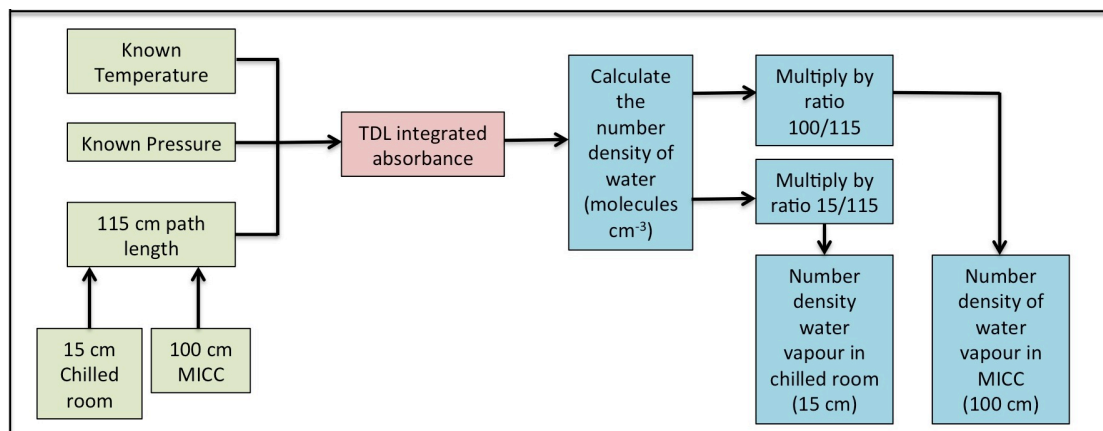


Figure 28 The known parameters are shown in green. The integrated absorbance data from the calibration is shown in red and the number density calibration process shown in blue.

Based on the conditions of the chilled room at -15 °C, and the pressure at 0.98 atm, the total number density of the recorded water vapour is 2.12×10^{17} molecules cm^{-3} . This corresponds to 1.84×10^{17} molecules cm^{-3} for the MICC (100 cm path length) and 2.76×10^{16} molecules cm^{-3} for the chilled room (15 cm path length). The corresponding total integrated absorbance value is 0.009398, 0.00817 for the MICC and 0.001226 for the chilled room. Table 3 summarises the information above.

Table 3 Comparison of number density and integrated absorbance values of water during calibration process

	Total	MICC	Chilled room
Number density (molecules cm^{-3})	2.12×10^{17}	1.84×10^{17}	2.76×10^{16}
Integrated absorbance	0.009398	0.00817	0.001226

As it was assumed that the number density of water vapour, as well as the temperature and pressure of the chilled room does not change during the experiment, it was assumed that the integrated absorbance could be used as 0.001226. During the course of the expansion process, pressure and temperature fluctuates, but absorbance is additive and the peak shape of A_{Total} is a convolution of A_{MICC} and $A_{Chilled\ room}$ as shown in Equation 34.

$$A_{Total\ of\ 115\ cm} = A_{MICC\ of\ 100\ cm} + A_{Chilled\ room\ of\ 15\ cm} \quad \text{Equation 34}$$

It was also assumed that during peak fitting, the difference in peak shape exhibited by $A_{Chilled\ room}$ is negligible as the value is small with respect to A_{MICC} . With this assumption, the values of the TDL were calibrated and used for in situ monitoring of relative humidity. A validation process shown in Figure 29 was also conducted using the pre-installed chilled mirror hygrometer located at the bottom floor of the MICC as shown in in Figure 21.

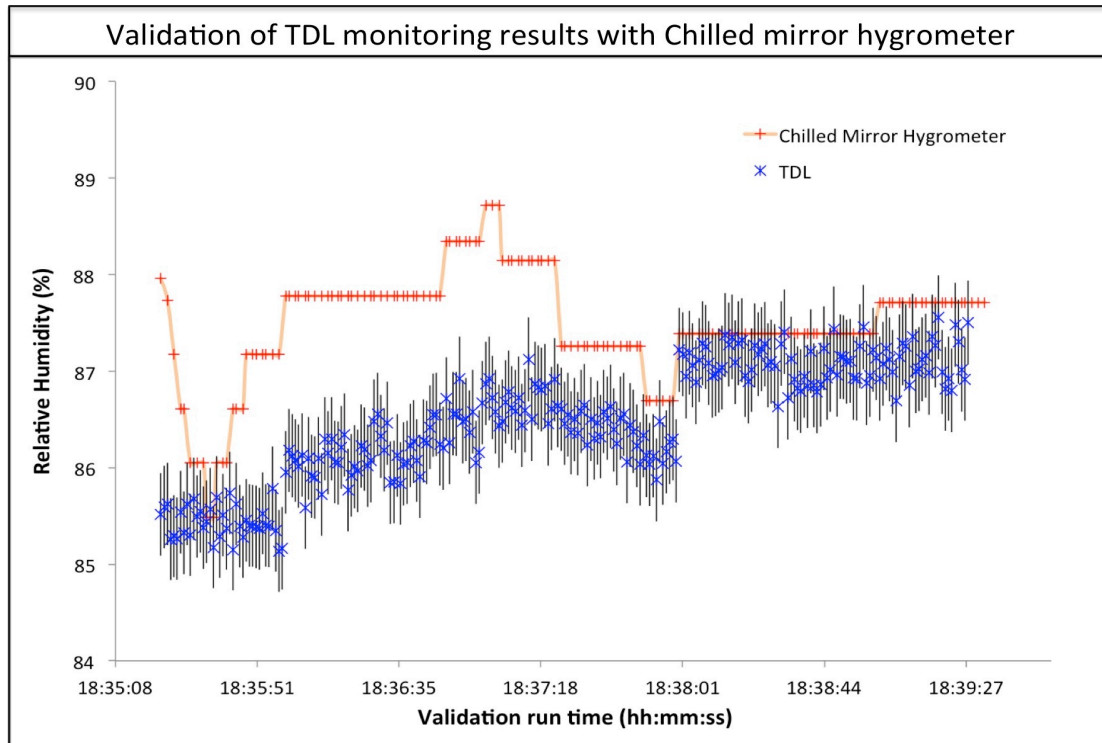


Figure 29 Comparison of the chilled mirror hygrometer sampling against the TDL sampling at constant pressure of 0.99 atm and at similar temperature.

The validation process was conducted over a stable period without any form of expansion, as the hygrometer was incapable of tracking rapid changes in relative humidity. The pressure in the MICC was constant throughout and was held at 0.99 atm. However, the temperature distribution in the MICC was not as homogenous and the area around the chilled mirror measured approximately 15.2 °C, with a range of $\pm 0.2^\circ\text{C}$.

The TDL measurements were recorded simultaneously, and the temperature taken from the nearest thermocouple located above the TDL station inside the chamber shown in Figure 21 was consistently higher by approximately 0.3 °C. The averaged standard deviation of peak fitting of the TDL was 0.000368, which correlates to approximate $\pm 0.4\%$ of fluctuating relative humidity.

The measurement of relative humidity between both methods were close, with similar trends. The relative humidity recorded using the TDL system seems to be consistently lower than the hygrometer. This could be due to the fact that the temperature and concentration of water vapour were not fully homogenous, as shown in the area of the TDL with consistently slightly higher temperature.

From this, it is concluded that the TDL could record the change in relative humidity faithfully.

4.4.2 Comparison of TDLAS monitoring with simulation

The monitoring of the expansion process was meant to study its trend with its ACPIM cloud parcel simulation shown in Figure 30 performed by Simpson in the MICC research group.

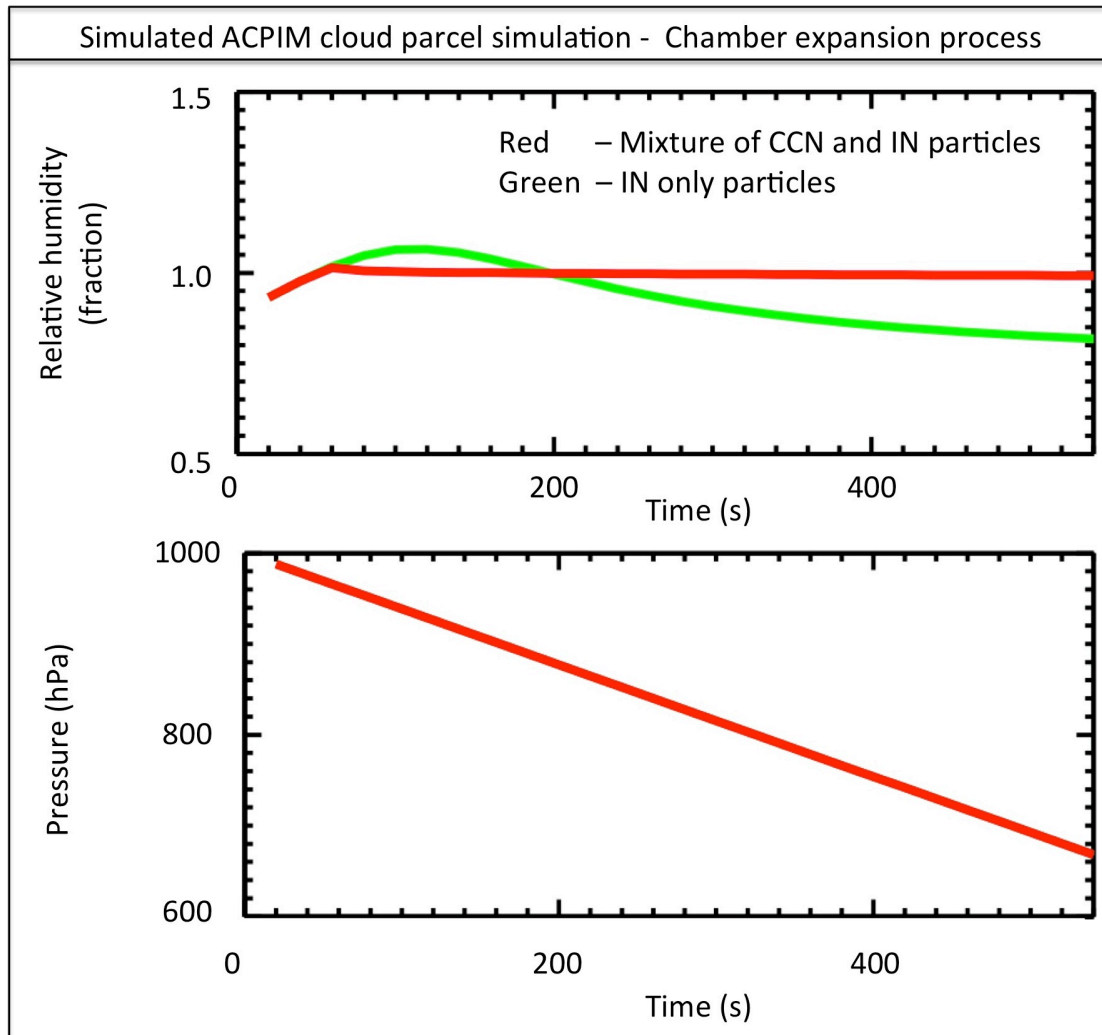


Figure 30 Taken from E. Simpson’s first year PhD report, the simulation of the cloud parcel with the relative humidity of 2 separate scenarios at the same expansion speed. The first scenario, marked in green involves only IN particles, where super saturation occurs, of which the relative humidity of water falls as ice crystals are formed. The second scenario, marked as red involves the mixture of CCN and IN particles, and does not form any ice crystals as the relative humidity did not decrease and stayed at saturation throughout. [197]

The initial starting pressure of the simulation begins at 1000 hPa and involves a pump speed of -1.23 hPa s^{-1} for the expansion to occur in the chamber. The total run time of the simulation was 540 s. The simulation was conducted in two separate scenarios, the first involves only IN particles in the MICC, comprising of 1 cm^3 of Snomax with a mean diameter of 80 nm. The second scenario consists of aerosol mixture content, which was comprised of aerosol mixture of 1000 cm^3 ammonium sulphate (CCN) with a mean diameter of 50 nm and 1 cm^3 of Snomax with a mean diameter of 80 nm.

From Figure 30, scenario 1 shown in green depicts the relative humidity reaches supersaturation before a steady decline. This was due to the formation of ice particles and the freezing of the water vapour droplets, thus a decline in the gaseous phase. Scenario 2 as shown in red, depicts the increase of relative humidity to saturation point, but stays saturated throughout. This is correlated with having no ice formation.

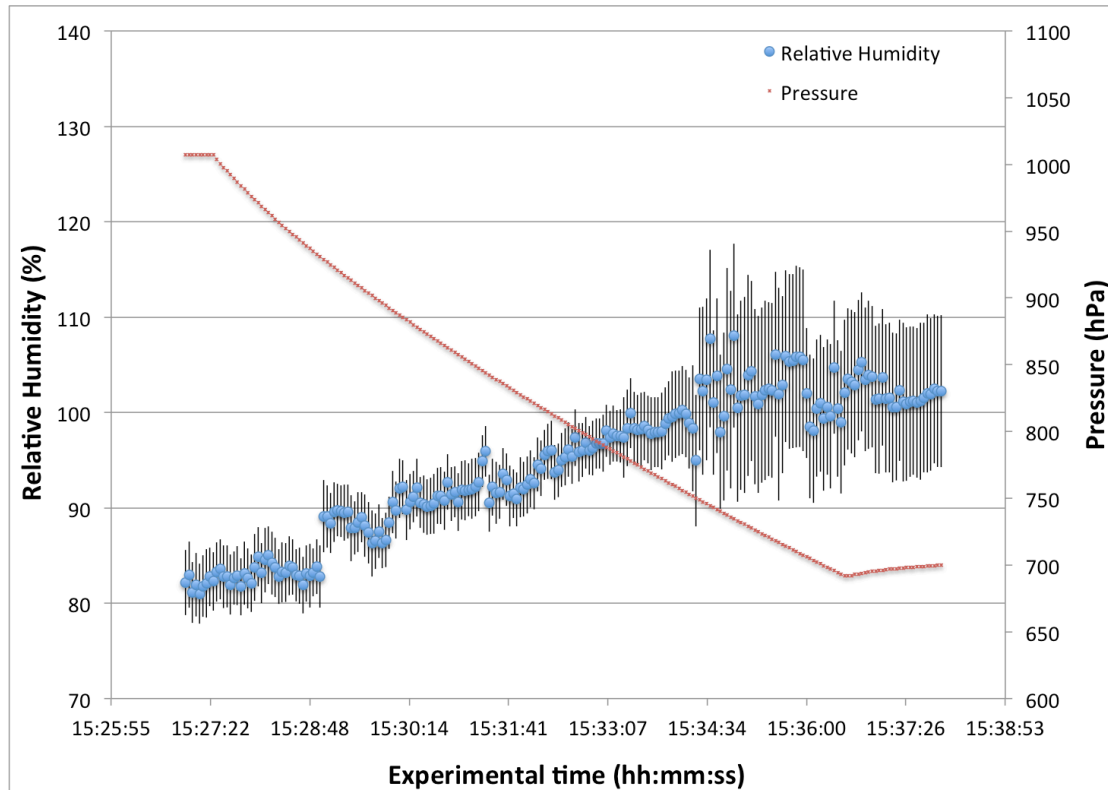


Figure 31 The monitoring of relative humidity change per time with error bars (blue). The red dots mark the decrease of pressure over time.

The experiment conducted and shown in Figure 31 depicts the simulation of scenario 2, with the same aerosol mixture of 1000 cm^3 ammonium sulphate (CCN) with a mean diameter of 50 nm and 1 cm^3 of Snomax with a mean diameter of 80 nm.

The trend in the relative humidity matched the cloud parcel simulations of increasing in relative humidity as pressure was decreased. The relative humidity reached 100 % and fluctuated around 100% whilst the simulation models the relative humidity to remain consistently at 100%. The experimental trend matched the simulation model, where the presence of CCN particles suppressed the freezing capabilities of water, resulting in a lower/no formation of ice crystals. This was due to the fact that CCN competes with IN with available droplets of water.

The standard deviation of the peak fitting at 1000 hPa increased from an average of 0.0008 to an average of 0.0016 for peak fittings at 700 hPa. It could be seen that the standard deviation of the peak fitting stays consistently around $\pm 3.2 \%$ relative humidity from atmospheric pressures to approximately 750 hPa. However, the standard deviation error increases to approximately $\pm 7.9 \%$ relative humidity once it was lower than 750 hPa. This may be due to the possibility of icing of the optical access, which may inhibit partial optical access.

The relative humidity provided 1 measurement per second during the expansion process, which was the requirement as that was what the hygrometer failed to do.

4.5 Chapter summary

There are several challenges faced in the experiment that could be overcome in the future. The first was fogging/condensation of the portholes during rapid changes in temperature that may obscure optical access of the laser. The experiments carried out did not encounter major issues with obscured optical access during decreasing pressure. This was because the temperature of the chamber decreases with decreasing pressure. However, condensation does occur during the warming up of the chamber, but there are no records of condensation or fogging of portholes that was drastic enough to block all optical access of the laser. However, during repeated cycles after the chamber has been subjected to multiple warming and cooling; condensation that have previously occur may cause icing of the optical portholes.

Theoretically, the MICC was built to withstand low pressures, from atmospheric down to 200 hPa. However, significant flexing and contraction does occur and the pressure was only decreased down to approximately 700 hPa. Even though the MICC would be able to withstand 700 hPa without any movements of the chamber structure, a small amount of contraction and shifting could still be detected. This may cause misalignments of laser, resulting in poorer signal to noise ratio.

An in-situ TDLAS system and its associated operating and analysis programs were designed to monitor changes in relative humidity in rapidly changing conditions, something the pre-installed chilled mirror hygrometer could not perform. The TDL monitoring system was calibrated and validated under stable conditions with the chilled mirror hygrometer and yielded similar results. As the distance between the hygrometer and TDL system was a floor apart, the results were considered acceptable and within reason. The design of the TDLAS system and its programs were used as a design foundation for the tomography chapters discussed in this Chapter 5.

The experiments conducted were successful in the monitoring of the suppressed formation of ice crystals with Snomax in the presence of ammonium sulphate. It matched simulated results of the ACPIM cloud parcel simulation.

5 OPTICAL TOMOGRAPHY CONCEPT DESIGN AND DEVELOPMENT

5.1 Chapter overview

This chapter focuses on the design progression of the equipment architecture for a new tomography system. Firstly, the concept of optical tomography is introduced as a fan beam tomography system designed by Kasyutich [93]. Description of the original system, new developments, analysis, results and challenges of that system are described in Section 5.2. Based on the challenges of the first system, coupled with new requirements, a design framework was crafted. The iterations of equipment design were discussed and the final setup is introduced in detail in Section 5.3. The chapter summarises in Section 5.4.

5.2 Fan beam optical tomography system

The author first began tomography by further developing a fan beam optical tomography system designed initially by Kasyutich [93]. The equipment architecture of the fan beam system is first briefly described (Section 5.2.1) followed by the developments made to the original system in (Section 5.2.2).

The decisions on line peak selection as well as analysis will also be shown in (Section 5.2.3). The result of a sample experiment is presented together with its validation in (Section 5.2.4.5) and its challenges in (Section 5.2.5).

5.2.1 Equipment architecture of fan beam tomography system

The experimental setup shown in Figure 32 depicts two separate carriages, one carrying the laser emitter (laser platform) and one carrying the photodetector (photodetector platform), moving along a white circular optical rail. This rail facilitated the manoeuvring of the laser and photodetector platforms and served as an imaginary system boundary.

Two heaters placed in the centre of the rail were used to create inhomogeneous temperature and water molecule spatial distribution. The heaters were both different in shape as well as temperature setting for an asymmetrical variation. The circular plate heater was set at a lower temperature setting, while the rectangular coil at a higher temperature setting.

The laser platform was positioned at five equally spaced points (L1 to L5) on the circular rail marked by the blue dots in Figure 33. In each position, the laser was swept from left to right through a set radius in a series of 11 spaced beams, forming a projection fan. As the laser beam swept for each successive beam position, the photodetector platform on the other side of the rail moved in sync with the laser beam location. Each laser projection (green lines) was also allocated a number in the figure which indicated the order it was recorded, from 1 to 55, from the first to last projection respectively.

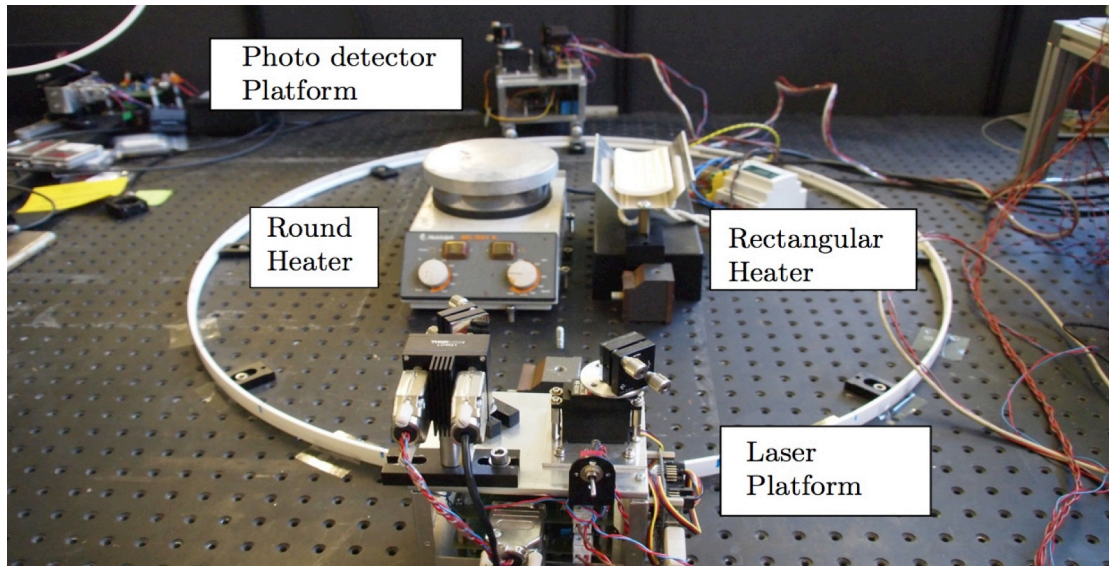


Figure 32 Photo of fan beam tomography system setup.

Orange – Optical rail to facilitate the maneuvering of platforms, as well as functioning as an imaginary boundary

Blue dots – Laser platform resting locations (numbered L1 to L5)

Green lines – Laser optical paths (numbered 1 to 55)

Purple objects – Positions and shapes of heaters. Heaters set at different temperature settings to create an asymmetrical temperature interference

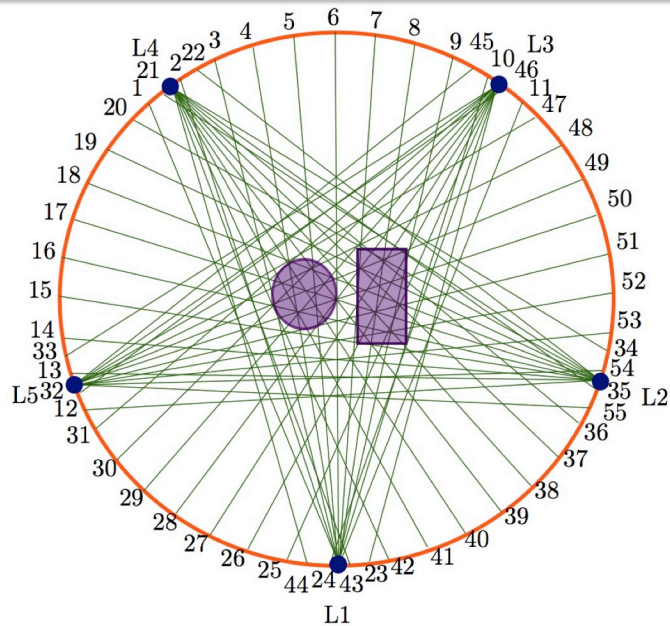


Figure 33 Diagram and description of fan beam system.

To facilitate the laser sweep per projection fan, mirrors were installed on each platform to redirect the beam to its desired path. The laser platform had two mirrors as shown in Figure 34. The first of the two mirrors (Mirror 1) located on the laser platform was fixed, mainly to redirect the beam from laser source to the rotatable scan mirror (Mirror 2). Mirror 2, the rotatable scan mirror re-directed the incoming laser beam across the optical plane into the photodetector. Mirror 2 on the laser platform moved in a clockwise manner and thus created a left to right fan beam projection sweep.

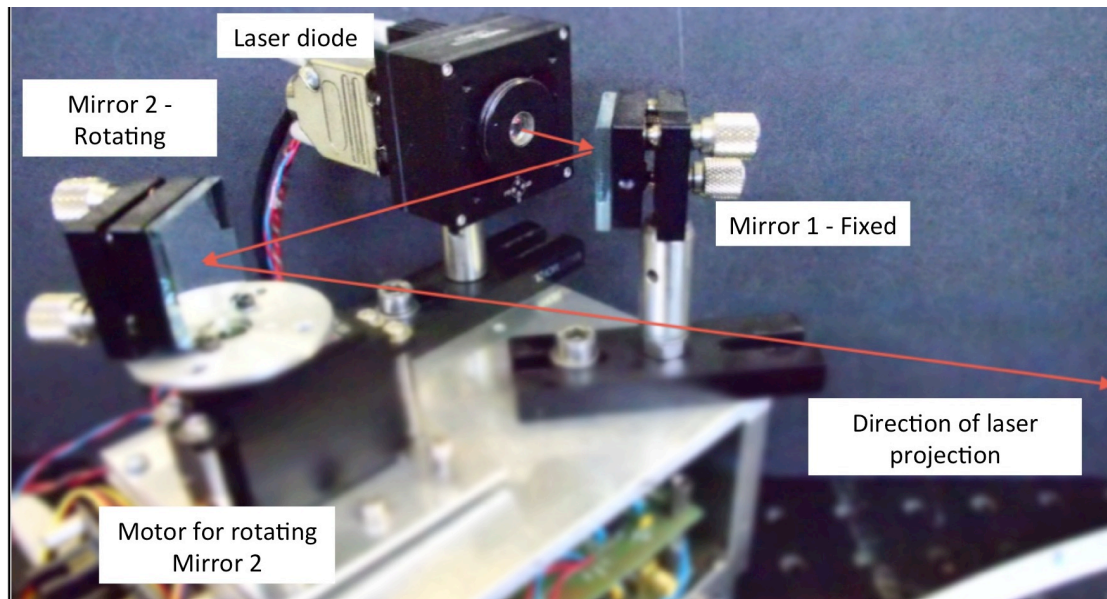


Figure 34 Example of laser projection travelling from source and directed by mirrors on the laser platform.

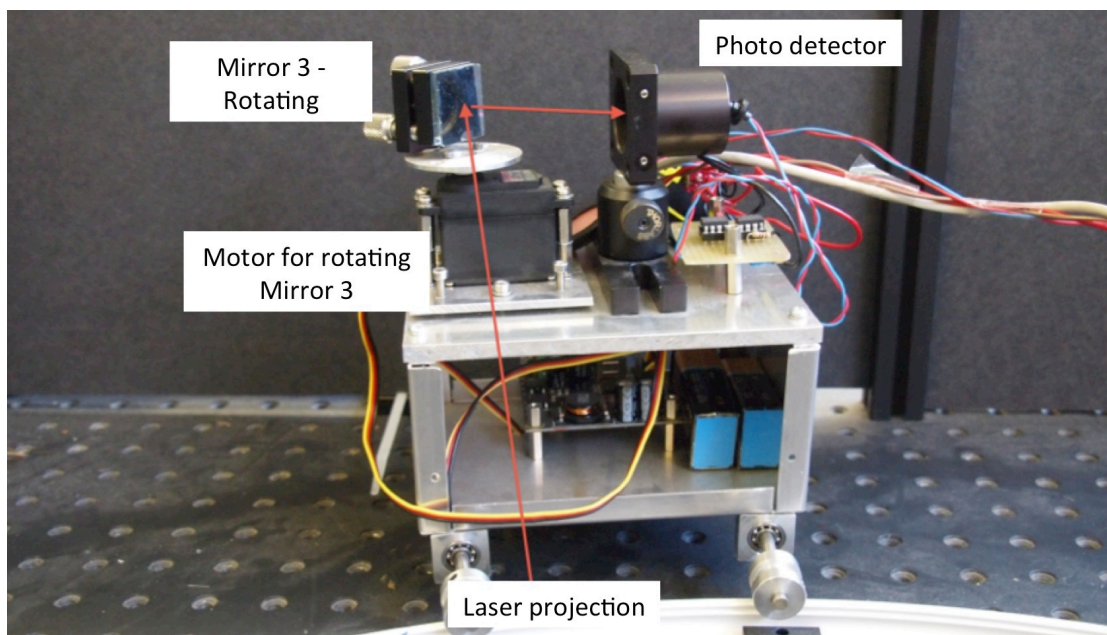


Figure 35 Example of laser projection being directed by mirror into the photodetector on the detector platform.

To accommodate the clockwise laser sweep, the photodetector platform shown in Figure 35, moved along the rail in an anti-clockwise manner. The mirror (Mirror 3) located on this platform was also controlled by another rotating motor, tuned to redirect the incoming laser projection into the photodetector regardless of the incoming laser angle.

The circular heater on the left was located at $(-7.5, 0)$ and the rectangular heat on the right was located at $(8, 0)$. The surface of the circular heater was located 3.5 cm below the optical plane and the surface of the rectangular heater was located 2 cm below the optical plane.

A LabVIEW program operating on a laptop controlled the setup via a National Instrument data acquisition card (DAQ). Servomotor printed circuit

boards (PCB) with detailed information are tabulated in Table 4. The total experimental time for all 55 beams to be acquired was approximately 160 s, excluding the movement of individual carriages and alignments. This is further discussed in Section 5.2.5.

Table 4 Details of fan beam tomography equipment setup

Laser Platform	
Diode Laser	Centred at 1392 nm 10 mW Eblana Photonics EP1392-DM NIR DFB TDL, with beam diameter approximately 2 mm. Threshold current at 15 mA, maximum forward current at 120 mA, operating temperature from -5 to 70 °C. Mode-hop free tuning.
Current Controller	Thorlabs (LDC205C)
Temperature Controller	Thorlabs (TED200C)
Servomotor 1	HITEC (HS-322HD), for adjusting mirror angle
Servomotor 2	HITEC (HSR-1422CR), for wheeling the platform around the rail
Mirrors	2 Al coated mirrors, one fixed and the other rotating
DACQ	National Instruments 18 bit (USB-6281)
PCB	Phidgets (PhidgetAdvancedServo-1061), for controlling the servo motors
Detector Platform	
Photodetector	Thorlabs (PDA10CS-EC), InGaAs switchable gain detector
PCB	Phidgets (PhidgetAdvancedServo-1061), for controlling the servo motors
Servomotor 3	HITEC (HS-322HD), for adjusting mirror angle
Servomotor 4	HITEC (HSR-1422CR), for wheeling the platform around the rail
Other components	
Circular rail	97 cm in diameter
Heater 1 (circular)	Heidolph (MR3001K), stainless steel heating plate, 14.5 cm in diameter
Heater 2 (rectangular)	CERIX (HTE500W), ceramic heating plate of 5.5 by 12 cm, controlled by temperature controller CAREL (IRDRW2000)

5.2.2 Developments to original publication

The LabVIEW program controlling the setup was further developed such that peak fitting was conducted in real-time. This aided a more simplified post experiment analysis where only the reconstruction program was used (Previously, a post-experiment MATLAB peak fitting was used followed by a MATLAB reconstruction program)

The updated laser used was centred around 7178 cm^{-1} (1392 nm) with a range from 7155 cm^{-1} to 7185 cm^{-1} This allowed a larger selection of peaks to access compared to the original publication which used 7185.6 cm^{-1} and a weak

absorption line at 7185.394 cm^{-1} [93] The wavenumber sweep range of the updated laser was also larger by 2 cm^{-1} , allowing a wider range of transitions per sweep to be measured.

5.2.3 Waveform modulation, Peak selection and Analysis

The modulated waveform is depicted in Figure 36 in green. Using a similar modulation method discussed in Section 4.3, a single cycle of wavenumber tuning consisted of sweeping the current linearly up a ramp for the first $800 \mu\text{s}$ of which the current was dropped below the laser diode operational current bias threshold value for another $200 \mu\text{s}$. The laser was not lasing during these last $200 \mu\text{s}$ of the cycle. The modulated wavelength at different laser temperatures corresponded to a different range of wavelength sweep as shown in Figure 37.

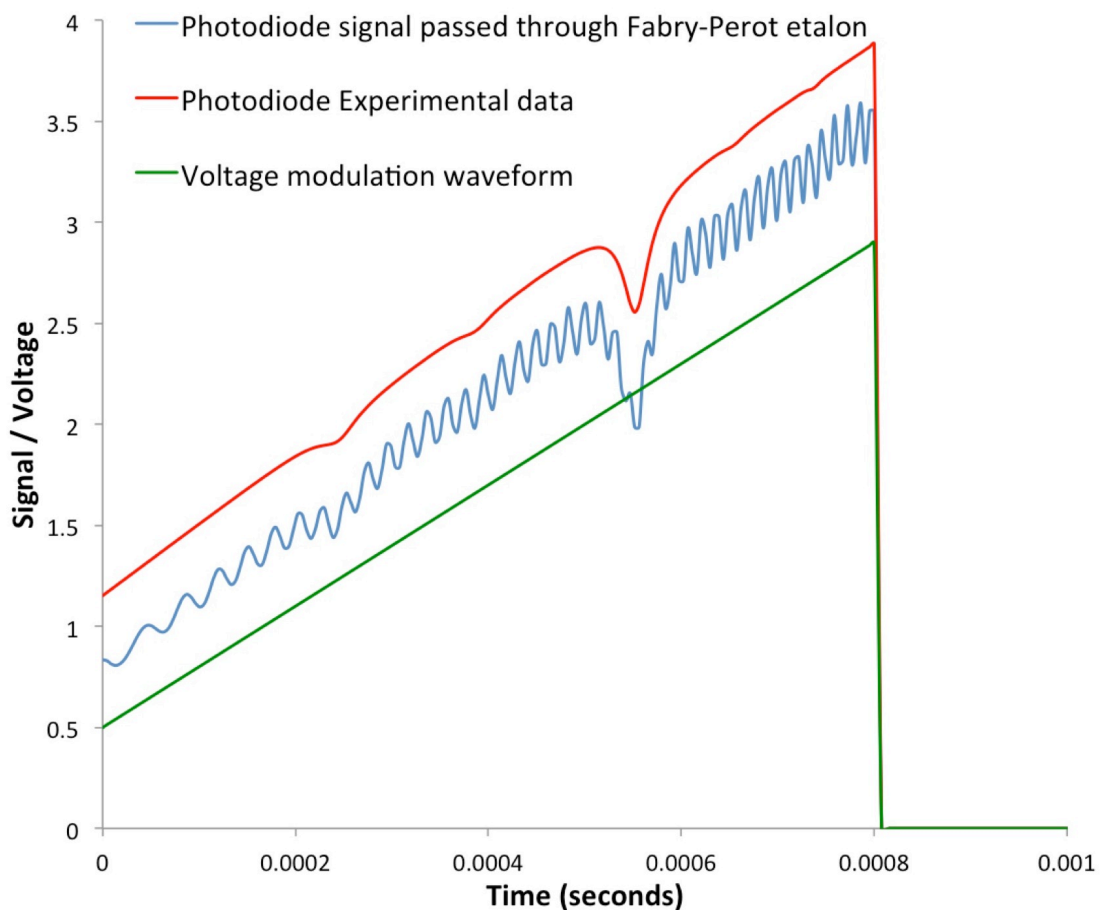


Figure 36 Voltage modulation waveform used for current ramping of laser. The photodiode output is given in red and the same signal passed through a Fabry-Perot etalon is shown in blue.

The laser was swept for a total of 1000 data points per cycle and averaged over 5 times within that cycle to form a spectrum of 200 data points. This allowed a total of 100 spectra to be acquired per 1 second, or inversely 10ms to acquire 1 spectrum. Therefore the rate of spectrum sampling may not be higher than 100 Hz. The rate of photodiode data acquisition was set at maximum frequency of 100 kHz.

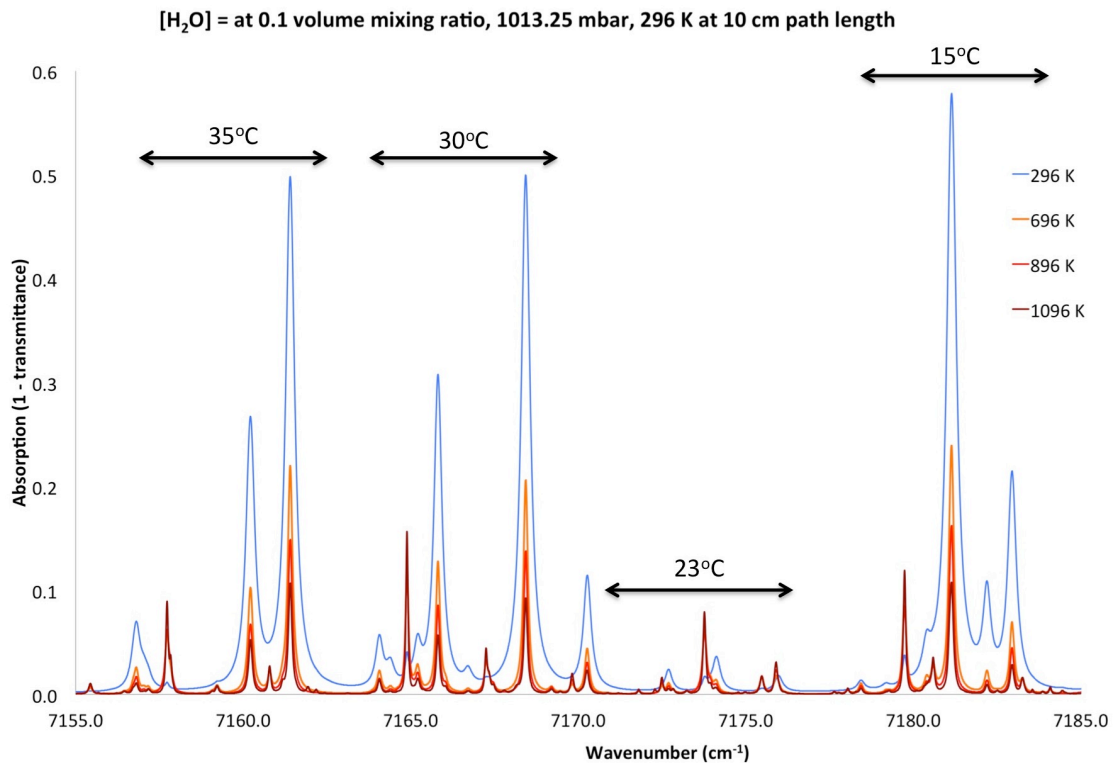


Figure 37 Simulated H₂O absorption spectra at four different temperatures (296 K, 696 K, 896 K, 1096 K) using HITRAN 2012 at different laser operating temperatures (15°C, 23°C, 30°C, 35°C). Obtained from www.spectralcalc.com.

Typical removal of background atmospheric water concentration was carried out using dual beam measurements, where two spectra were simultaneously recorded and divided, improving the detection limit of the system [198]. However, this was not feasible due to the constraints of the data acquisition board (insufficient ports) and the lack of additional splitters/detectors.

The background concentration however, was taken into account by performing peak and background fitting across the range of wavelengths covered (shown in red in Figure 36). This allowed the detection of changes with the integrated absorbance of water against the background.

The averaging was performed to enhance the signal to noise ratio (SNR)/interference ratios and reduced the level of noise and errors. As the signal was present in each spectrum, their final contributions to the final averaged spectrum were cumulative. However, because the noise from the detectors was random, it was cancelled out as the averaging number increased. Theoretically, an averaging of 100 could reduce the relative error by two orders of magnitude [199], however in this scenario, speed and data acquisition space conservation was more important than SNR. In some cases where there was initially a weak signal, a double-beam laser noise cancellation could be conducted where a beam is divided into a signal and reference beam. The signal beam is used for data acquisition while the reference beam is used for blanking purposes. The reference beam (noise) is deducted from the signal beam results at the end [200].

The signal to noise ratio was calculated from the average height of the signal divided by the average peak to peak height of the noise (in this case background detector noise).

$$SNR = \frac{\textit{Average signal power}}{\textit{Average background noise}} = \frac{2.4522}{0.00048} = 5108.75$$

Due to the high power of the laser (even after splitting it by 4), the signal was strong as shown in Figure 36 and produced a good SNR value of 5108.75. Any form of further averaging for further improvement to SNR was considered negligible.

The selection of which spectral region to capture depended on several criteria, from the sensitivity of the peak ratios to temperature change, how densely packed the region is with peaks as well as its signal to noise ratio. Figure 38 and Figure 39 are zoomed in versions of Figure 37.

The region accessible at a laser temperature of 35°C is shown in Figure 38 and contains a convoluted peak of inverse temperature trend identified as 1a. It also contains 2 other peaks of good absorption values over 0.2. It also has a low complexity peak density with only 3 primary peaks. However there is a difficulty in capturing the full region accurately due to peak drifting from efficient temperature control within this region during the experiment. This is because it takes significant energy to raise the laser temperature above typical room conditions of approximately 23°C and maintain a constant 35°C without any additional heat sink. The peak drifting results in wings being chopped off on either ends of the extreme peaks as the desired peaks are located very close to the end boundaries of the laser sweep.

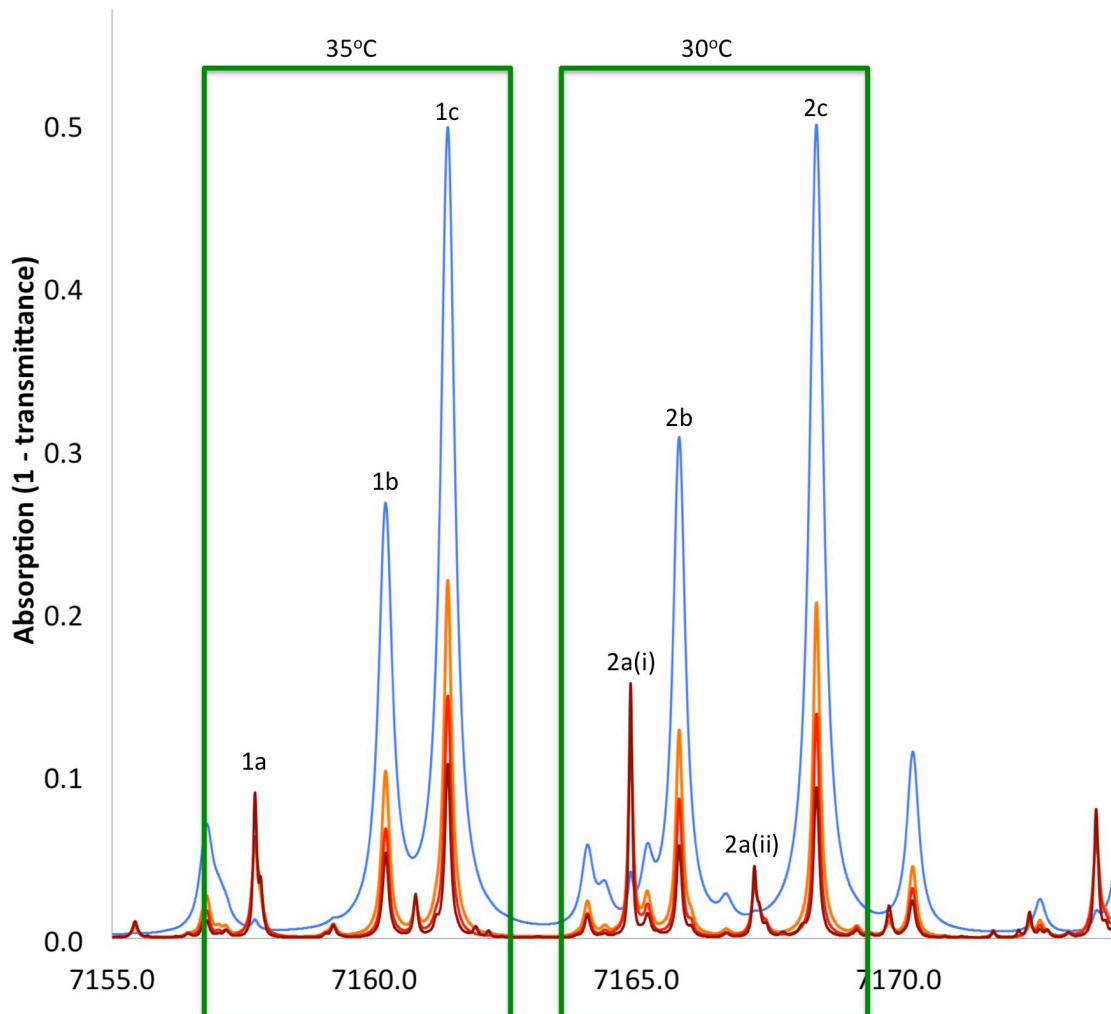


Figure 38 Zoomed in portion of Figure 37 for regions of wavelength accessible by laser at 30°C and 35°C.

The region accessible at 30°C as shown in Figure 38 benefited from having two peaks (2a(i) and 2a(ii)) that could be used with the two-line thermometry technique. However, 2a(ii) has low absorption values and 2a(i) might be preferred due to higher signal to noise ratio. This region is also fairly complex with regards to the peak density (total of 7 primary peaks). Although the complexity is not an issue with the actual spectrum fitting process, it loses its appeal when there are other easier and ‘cleaner’ regions to choose from. It would also increase the length of time required to fit the spectrum (detrimental to a live analysis program) due to its complexity. The extreme right wing of peak 2c may also be cut off during the data acquisition process due to minor peak drifting during experiments, albeit less pronounced than 35°C (again due to the lack of additional heat sinks). Based on this reasoning, this region was discarded from the selection process.

The region accessible at 23°C as shown in Figure 39 contains 3 ‘a’ peaks, but all of the peaks suffer from weak absorbance values, with every peak lower than 0.1. Due to the poor signal to noise ratio of this region, this region was not considered for experiments.

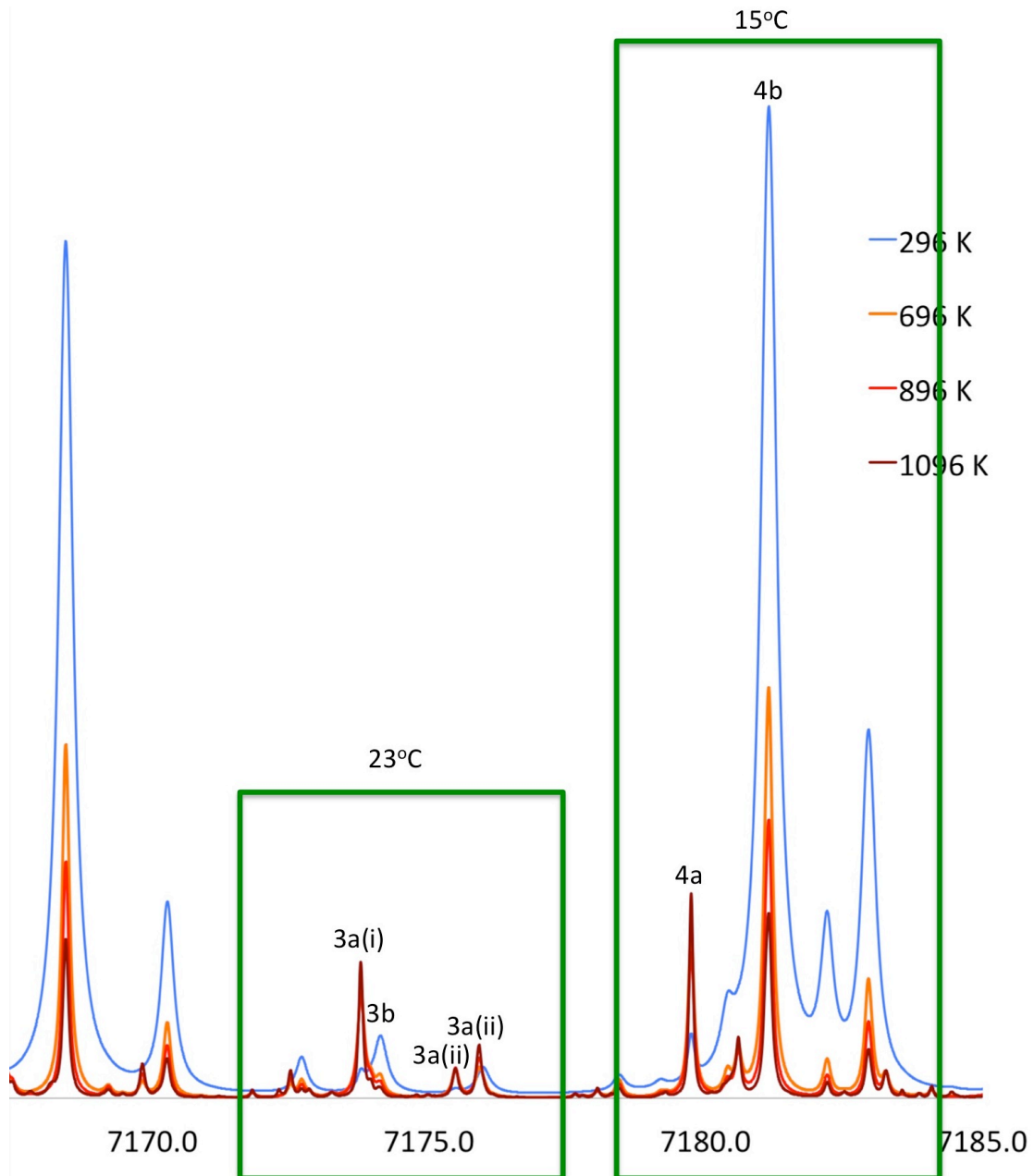


Figure 39 Zoomed in portion of Figure 37 for regions of wavelength accessible by laser at 15°C and 23°C.

The final region accessible at 15°C is shown in Figure 39 contains 5 primary peaks. It also contains peak 4b, which exhibits the highest absorbance value. Peak 4b also shows good inverse trends with peak 4a at good signal to noise ratio. With a moderate peak density of 5 primary peaks, they are also easily captured within the range of a laser current sweep. This region was chosen for analysis using the DFB diode laser, and the range accessible under laser temperature of 15°C corresponds to 7179 cm^{-1} to 7184 cm^{-1} .

The relationship between line strengths of peaks 4b (7181.93 cm^{-1}) and 4a (7179.8 cm^{-1}) as a function of temperature, as well as their ratio, is depicted in Figure 40. They are calculated from Equation 13 and Equation 14 in Section 3.2.2. The ratio as a function of temperature can be described as a polynomial order-3 equation given in Table 5.

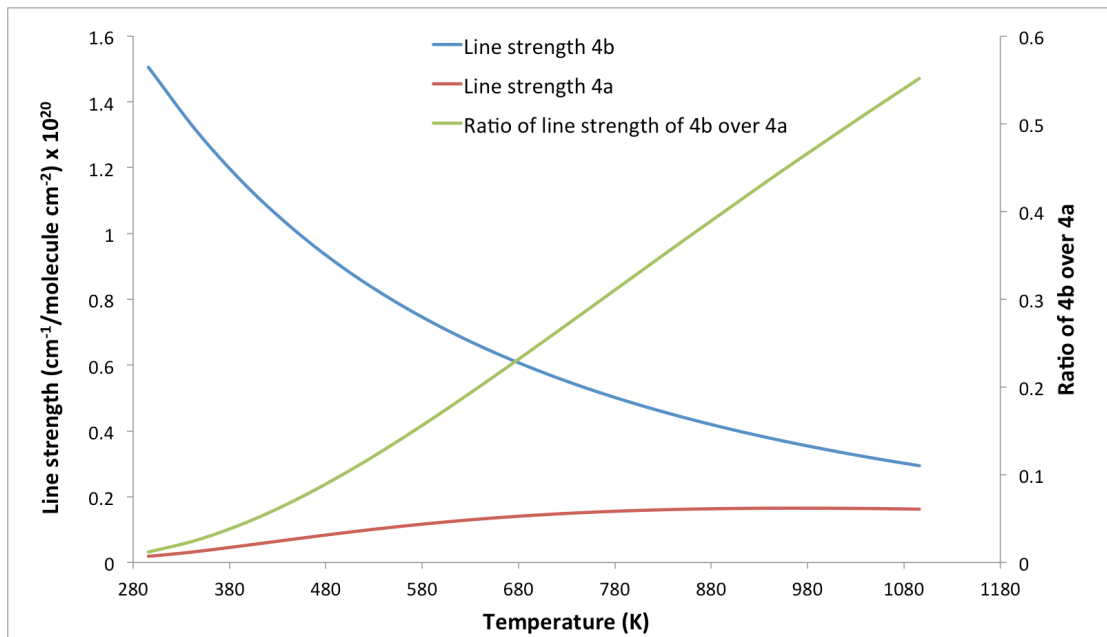


Figure 40 Depicts the changes of line strength of peaks 4b (blue) and 4a (red) with temperature (left vertical axis). The ratio of the two line strengths as a function of temperature is shown in green (right vertical axis).

Table 5 Parameters of polynomial relationship between line strength ratios as a function of temperature.

x^3	x^2	x^1	x^0
-6.83×10^{-10}	1.66×10^{-6}	-5.31×10^{-4}	3.94×10^{-2}

A sample photodetector output is shown in red back in Figure 36. This is recorded for the wavenumber sweep over a cluster of H₂O peaks accessible at laser temperature of 15°C, between 7179 cm⁻¹ to 7184 cm⁻¹. The ambient temperature was 22°C, a pressure of 1 atm and 57% relative humidity with total laser path length of 37 cm. The laser path travelled through undisturbed from source to detector in the laboratory and was assumed to be of uniform temperature and concentration of water molecules.

A Fabry-Perot etalon was also inserted in between the laser and photo detector wavelength and its photodetector output could be seen in blue in Figure 36. This etalon-influenced signal was later used to convert the time x-axis of a photodiode signal to relative wavenumber shown in Figure 41 using Equation 35.

$$\bar{\nu} = (k_0 + k_1t + k_2t^2 + k_3t^3) \quad \text{Equation 35}$$

Where: k_0, k_1, k_2, k_3 Parameters of the polynomial equation
 t Time or Data points

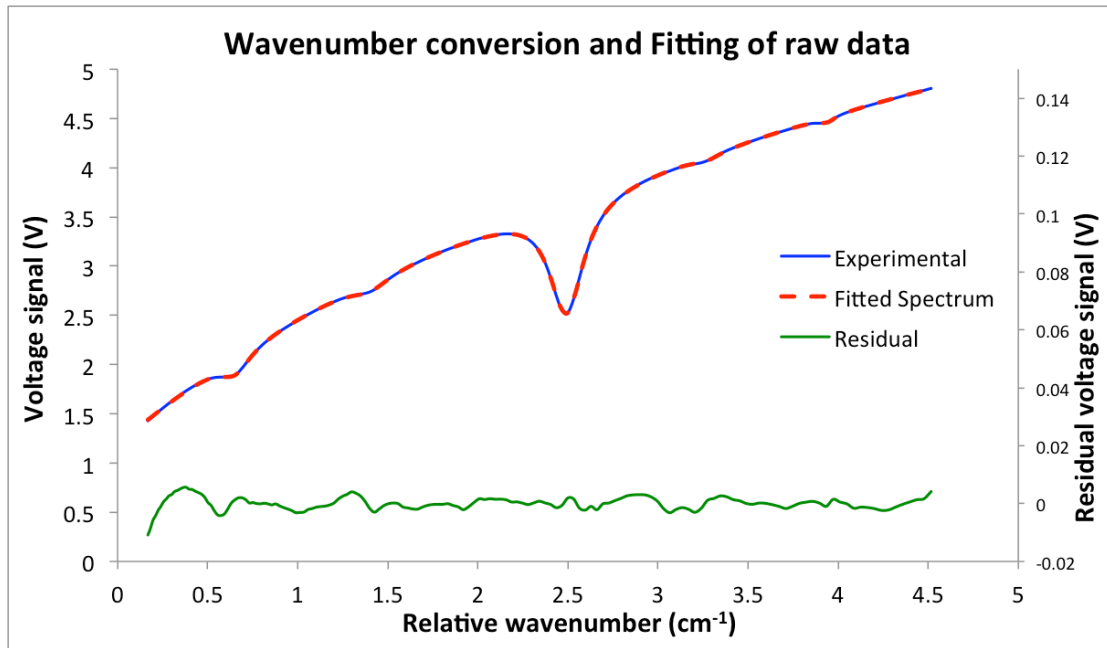


Figure 41 Fitting of a sample spectrum after wavenumber conversion. The experimental spectrum is in blue, with the peak fitting in red dashes (both left vertical axis). The residual is in green (right vertical axis).

Turbulent flow of gases created during combustion or thermal gradients within the optical plane create refractive index gradients, which causes unwanted beam steering of lasers passing through it, or the defocussing of the laser beam to the detector. However, in situations where smaller combustion devices operating at or near atmospheric pressure, this phenomenon does not pose any significant problems [199]. This was confirmed for this work by the strong signal to noise ratios of the individual spectra as shown in Figure 41.

The polynomial relationship used to convert data points to relative wavenumber is shown in Figure 42 and the parameters of Equation 35 are shown in Table 6.

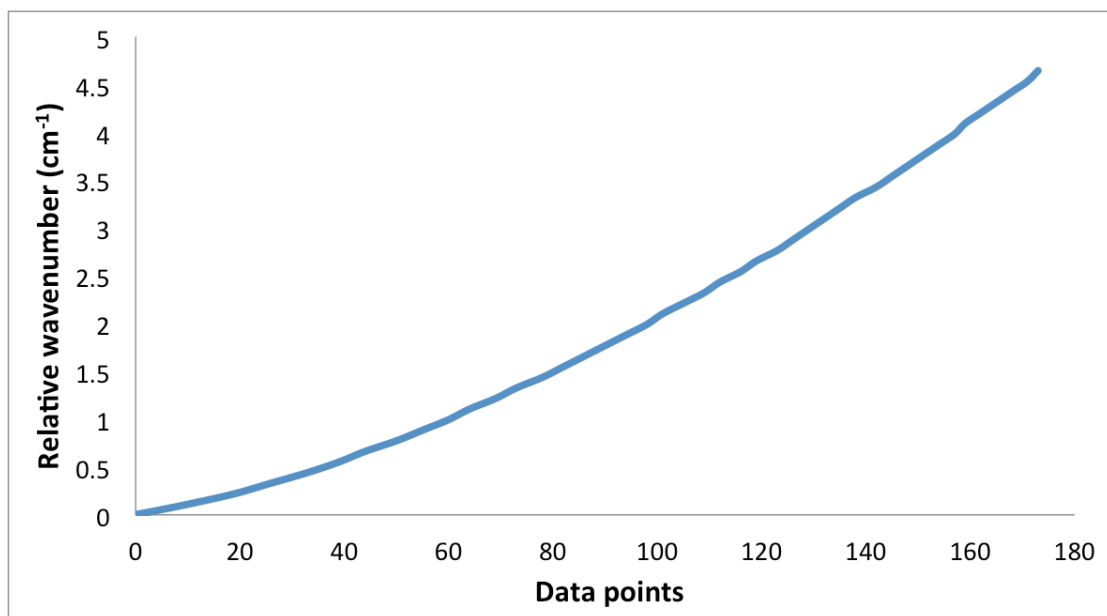


Figure 42 Relative wavenumber as a function of data points.

Table 6 Parameters of polynomial relationship between relative wavenumber as a function of data points.

k_3	k_2	k_1	k_0
-1×10^{-7}	0.0001	0.0106	-0.0111

As the experiments were carried out at room temperature under atmospheric conditions, the Lorentzian line shape function was used for the transmission fitting process. The spectra consisted of several peaks, so peak convolution was necessary as part of the transmission fitting. Line strengths within the investigated region that are above a set threshold of 10^{-23} ($\text{cm}^{-1}\text{molecules}^{-1}\text{cm}^2$) were used as part of the convolution process. Any lines with their strength below the threshold value were assumed to be negligible in contributing to the peak shape. Within this spectral range, there were a total of 9 lines used for convoluted fitting as shown in Figure 43. The transmission fitting was also multiplied by a base line fitting, which is a 3rd order polynomial to accommodate the curved behaviour produced by the laser current ramp as shown in Equation 36.

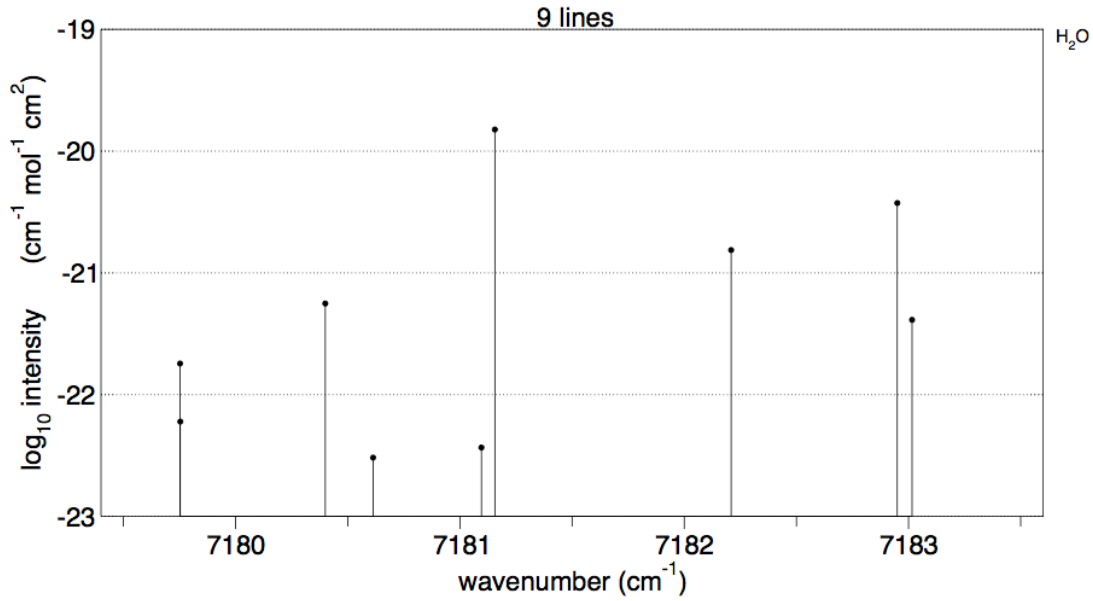


Figure 43 Line strengths above threshold deemed significant enough to contribute to peak fitting process. Extracted from HITRAN 2012 at room temperature from www.spectralcalc.com.

$$I_v(\bar{\nu}) = (I_{0\bar{\nu}} + I_{1\bar{\nu}}\bar{\nu} + I_{2\bar{\nu}}\bar{\nu}^2 + I_{3\bar{\nu}}\bar{\nu}^3) \times \exp\left(-\sum_{i=1}^9 \frac{2A_i w_i}{\pi(w_i^2 + 4(\bar{\nu} - \bar{\nu}_{0i})^2)}\right) \quad \text{Equation 36}$$

The residual of the line shape in Figure 41 was also calculated to see the goodness of fit, and a typical standard deviation (SD) of fit is approximately 0.00223, calculated from Equation 37, where n is the total number of residual points.

$$SD = \sqrt{\frac{\sum residuals^2}{n-2}} \quad \text{Equation 37}$$

The reconstructed spatial distributed integrated absorbances of a sample fan beam tomography experiment were analysed using ART discussed in Section 3.4.3 to recover the temperature spatial distribution. The reconstruction program worked by separately analysing the integrated absorbance from each peak. Each peak was reconstructed individually using MATLAB 2013 to form its own integrated absorbance grid of 50 by 50. Each cell in the grids was assumed uniform and suitable to apply the two-line thermometry technique discussed in Section 3.2.2. The two grids were divided over each other (Grid of peak 4b over 4a) to create a singular grid which was referenced to its temperature values using Figure 40.

To confirm that the laser operating at 15 °C was exhibiting the same wavenumber range as shown in Figure 37, a simulation was extracted using HITRAN 2012 database and compared with experimental data at the same conditions as shown in Figure 44.

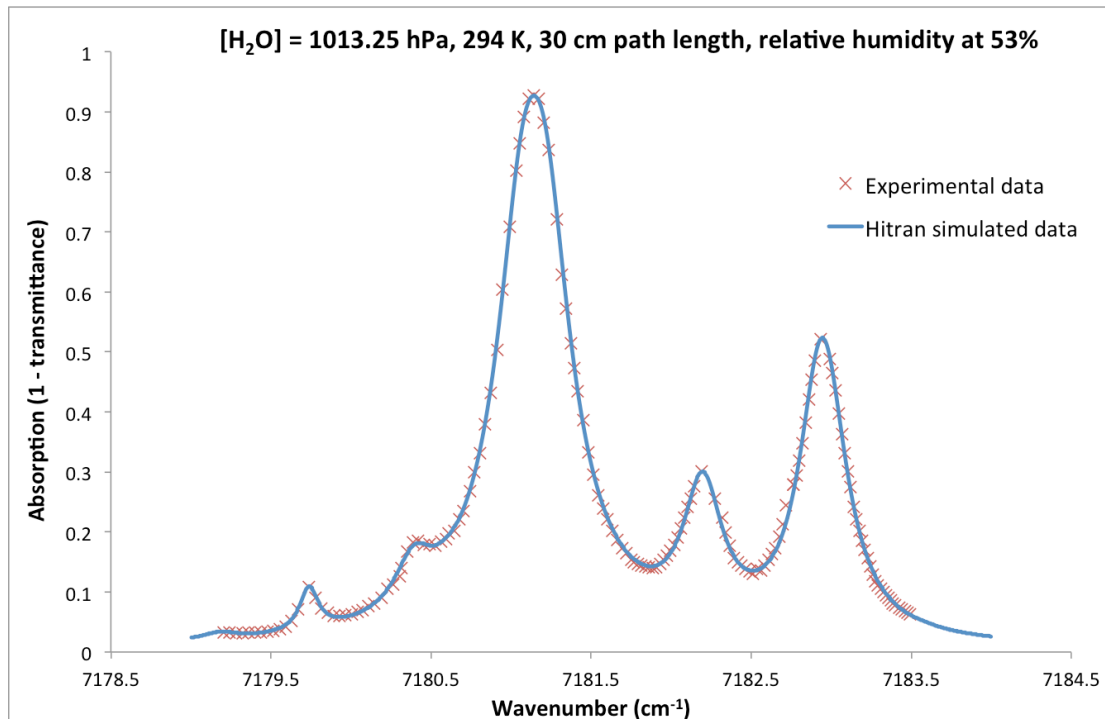


Figure 44 Laser operating at 15 °C wavenumber sweep from 7179.2 cm⁻¹ to 7183.4 cm⁻¹ in comparison to HITRAN 2012 data simulated at identical experimental conditions. Simulation data obtained from www.spectralcalc.com.

For the laser to operate at 15 °C, the temperature controller works by cooling the laser diode down, and the ease of control was dependent on its normal operating temperature and room temperature. At a typical room temperature of 23 °C, there was a slight deviation of wavenumber sweep range (from a lack of precise temperature control). This was typically ±0.25 cm⁻¹ from the minimum or maximum sweep indicated in Figure 44. For better temperature control precision, a larger heat sink attachment could be attached to the laser mount. However, the range per wavelength sweep covers the targeted water

lines adequately and does not affect the analysis even with $\pm 0.25 \text{ cm}^{-1}$ wavelength deviation.

5.2.4 Results of fan beam tomography experiment

The experiment was conducted at ambient temperature of 296 K with relative humidity at 42%. A K-type welded tip/glass fibre thermocouple was used for validation of the experiment. The circular heater on the left was set to heat up to 400 K. However the thermocouple measurement of the heater surface stabilised at only 360 K. The rectangular heater on the right was set to operate at 450 K. However the thermocouple reading on the heater surface read only 430 K. The integrated line-of-sight absorbance of H_2O centred at 7181.93 cm^{-1} of the experiment is shown in Figure 45, where it was arranged by fans of 11 beams each, totalling up to 55 beams per experiment.

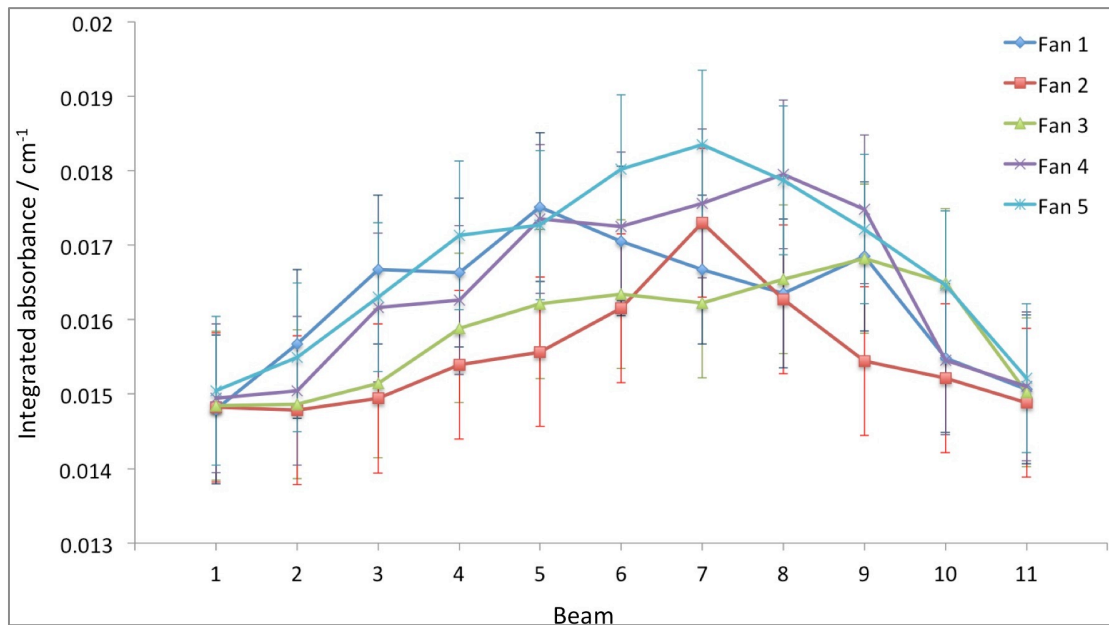


Figure 45 Line-of-sight of H_2O integrated absorbance at 7181.93 cm^{-1} at ambient temperature of 296 K and relative humidity of 42%.

The results of Figure 45 were reconstructed using ART and depicted in Figure 46 (a) that is validated by thermocouple sampling on the optical plane shown in Figure 46 (b). The thermocouple validation consisted of sampling with a thermocouple on a 25 by 25 imaginary grid superimposed onto the optical plane. They were then linearly interpolated via MATLAB to a 128 by 128 grid. The temperature reconstructions, using ART and thermocouple readings are presented as 3D visualisations of a 2D spatial distribution for easier comparisons. It can be observed that the ART reconstruction matches well with the thermocouple validation.

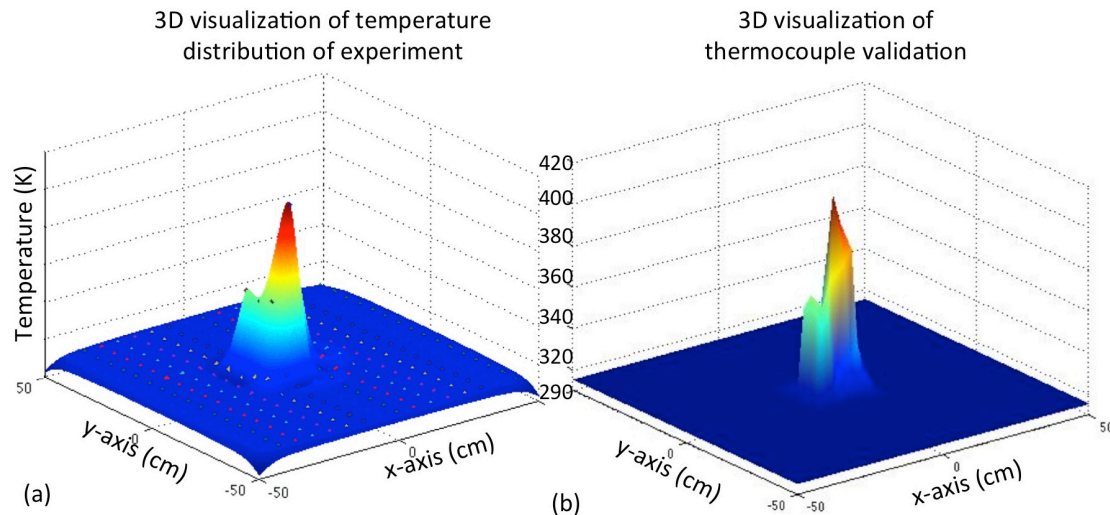


Figure 46 (a) Experiment results of 3D visualisation of 2D temperature spatial distribution over the two heaters. (b) Thermocouple validations of the experiment at the same heater settings and configuration.

The spatial distribution of water concentration could now be recovered using the Beer-Lambert law and the number density converted to its desired unit as discussed in Section 3.3. However the main purpose of this section was to demonstrate the concept of an optical tomography system and to aid the design of a new system.

5.2.5 Challenges

There were several challenges that this setup encountered during operation.

- The design was only capable for 2D data acquisition

Although the height of the laser diode and photo detectors could be adjusted, the rotating mirrors were mounted directly onto fixed height motors, rendering it incapable of performing 3D experiments.

- The long overall measurement time rendered temporal experiments unsuitable

The design of the fan beam tomography prototype had a theoretical optimum experimental time of 160 s, which included the optimum movement time of the various mechanical components. However there were several practical challenges that lengthened the overall experimental time.

The motors of the carriage wheels used in the experiment were programmed to travel at a set distance upon activation. However the motors exhibited a range of movement response and had high tendencies of not responding as expected. This lack of accurate response meant an additional fine-tuning of the stopping positions of the carriages, lengthening the overall experimental time by approximately 7 minutes.

As different parts of the setup were resting independently on different parts of the table surface, it was important that the surface is flat. An uneven

surface creates a skewed optical plane, as well as creating secondary problems such as projection misalignments. These misalignments forced the user to perform fine-tuning of mirrors during the experiment to correctly realign the laser beams into the detector, adding approximately another 10 minutes to the measurement time.

Because the design of the original prototype involved two wired carriages to circle around the heaters for data acquisition, the cables tend to tangle up when the carriages start circling around the heaters. The tangled cables generally have to be repositioned during the experiment to allow smooth carriage movements, increasing the overall experimental time by approximately 1 minute.

The overall time added to the original experimental time is approximate, and varies from experiment to experiment and is averaged based 14 experiments. The total average measurement time is approximately 21 minutes or 1240 seconds, rendering this system unsuitable for temporal experiments.

5.3 Design of temporal and 3D tomography system

The design framework was created based on the challenges of the previous fan beam system and new goals. This is followed by an introduction to the design iteration, before the final design is described in detail.

5.3.1 Framework and direction of tomography algorithm

- Framework based on previous challenges

The new design needs to be able to conduct 3D tomography. With the temperature interference being a three dimensional effect, it is attractive to not just study a 2D slice, but extend the experiment to study the effects of temperature with height as well.

The design should also work towards executing temporal experiments and in order to do that, the total experimental time should be reduced significantly. The target per tomogram measurement is less than 3 seconds, which would be an approximately 400% improvement to the fan beam system. Although it is ideal to aim for an even lower measurement time, 3 seconds was allocated for any physical limitation of moving components of the new system. To achieve this temporal goal, the projections should be pre-aligned from source to detector, to remove the need for individual alignments during the experiment and to remove the risk of misalignments all together. The optical plane should also be independent of the surface, and be consistent regardless of resting surface irregularities.

Finally the design needs to consider the movement of the laser sources and detectors, as well as the restrictions the cables might pose. Entanglement of cables should be considered and adjustment not required during experiment.

- Framework based on new criteria

As well as building the new design framework to address the challenges that the first prototype faced, several other considerations were also added based on changes of the experimental needs.

The heaters that were used were replaced with mixed fuel burners because the burners can reach higher temperatures compared to the heaters, as well as produce water vapour from the combustion process and was therefore more realistic. The change in heat source provides the experiment a wider range of temperature interference as well as providing additional water concentration interference to the optical plane. Due to safety reasons, there was also a need to make special considerations that the construction materials are able to handle close proximity to open flames. That would also extend to materials that are located in the area above the flame to be non-flammable and have a high melting point. For example, plastic frames and gears were substituted with metal whilst fabric ropes substituted with spun metal cables.

Metal construction tubes were also made available within the laboratory and it was desirable to have them repurposed. This determined that the setup would be more suitable for parallel beam configuration.

The original prototype consisted of several independent components, such as carriages that housed the laser and detector, as well as requiring a separate optical rail that was resting on the surface to guide the carriage movement. It was attractive to keep the whole system singular, compact and mobile so that the system could be moved from location to location easily. This allows the experiment to be easily moved and conducted in a variety of places. This is beneficial for any potential collaboration with other departments.

- Direction of tomography algorithm

Algebraic Reconstruction Technique (ART) was used to reconstruct data from the fan beam tomography system because it was a suitable solution to fan beam geometry. The projection geometry of a system is usually based on the space and equipment available, which comprises a single laser source and detector in this case. However, with access to a new fibre optic splitter (1 to 4 splitter) and 4 new detectors, 4 simultaneous projections could be acquired at any one projection angle. There was also access to construction tubes that could be used as support and as frame beams.

It would then be natural to change the projection geometry from a fan beam style to a parallel beam style. The parallel beam style was more efficient compared to fan beam style by reducing the total movement of the system to just the rotation of the parallel projections along the peripheral boundary of the object of study.

However, it could also be argued that a fan beam projection could still be employed by creating fans of 4 beams and increasing the amount of fans to accommodate a decrease in beam density per fan. This could be easily done for emitters that produce light in sheets, or smaller emitters that could be housed closely together to create a single location emitting at several angles. However due to the space constraints of the larger fitting equipment available, a fan beam configuration was not considered.

Due to the parallel beam configuration, the filtered back projection (FBP) and Fourier slice theorem would then be a more suitable technique to analyse parallel beam data compared to ART.

5.3.2 Design iteration of 3D tomography systems

5.3.2.1 Initial iteration of 3D tomography system

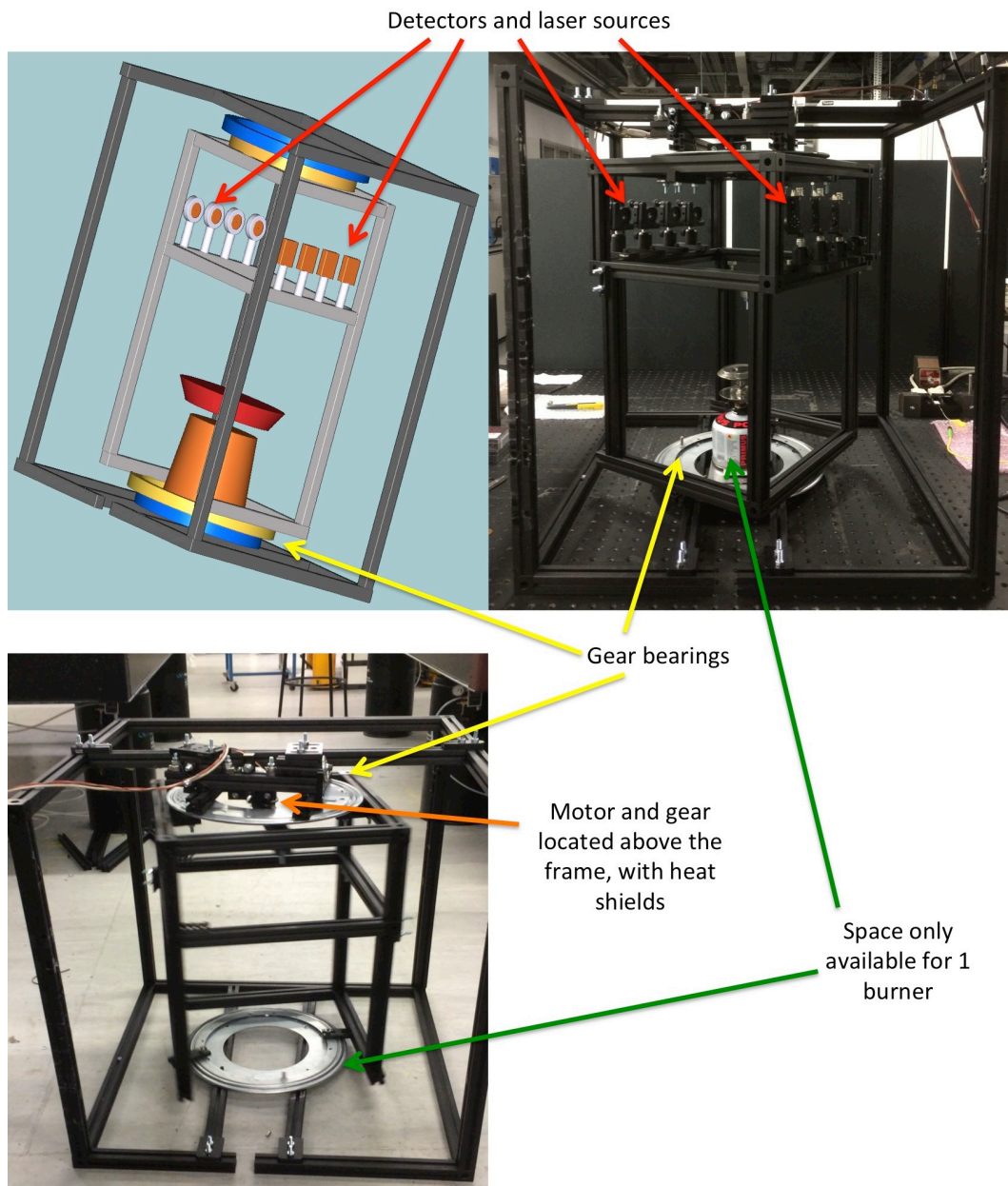


Figure 47 Various views and drawing of the first iteration of 3D tomography system.

The first design iteration is shown in multiple angles and drawing in Figure 47. This iteration used internal black-coated aluminium construction tubes as housing/frames to support the 4 detectors and 4 laser sources. The internal housing was sandwiched between two stainless steel gear bearings and attached to an external, larger black-coated aluminium housing. The gear bearings comprised of a rotatable component (yellow in drawing) and fixed component (blue in drawing), which allowed the internal housing to rotate either clockwise or anticlockwise independently from the external housing. The rotation direction is dependent on the motor attached to the top gear bearing. The burner was placed in the centre, and could be elevated via a laboratory jack.

However this iteration was discarded, as even though this design could be utilised for both temporal and 3D studies, there were problems with this setup.

- Damaged motor and gear

The motors ceased functioning correctly over time, and the gear to facilitate the rotation became misshapen due to the proximity of high heat radiation during 3D experiments. This occurred even when precautions were taken using a stainless steel heat shield attached to the gear and motor.

- There was only space for a singular heater.

The heater was placed on a laboratory jack that could facilitate the change in height of the flame, thus simulating a 3D study. However there was only space for a smaller laboratory jack, which could only accommodate a single burner. A false surface was constructed on top of the laboratory jack that could accommodate two burners, however it was discarded due to poor surface stability.

5.3.2.2 Final iteration of 3D tomography system

The detailed diagram of the final iteration of the tomography system is shown in Figure 48 with simplified annotation and alternative angles of the system shown in Figure 49. The main difference between the first and final iteration was that the motor and gears were now located at the bottom and beneath the flame source. A separate carriage for the burners was constructed for 3D studies and the rotation now pivoted on only a single gear bearing.

The setup consisted of three main sections, each defined by its own 'cage'. These three 'cages' were composed of 2.5 cm by 2.5 cm thick black construction rails. The rails were formed into general cuboid shapes of varying sizes with mild alteration to their individual shapes as shown in Figure 48.

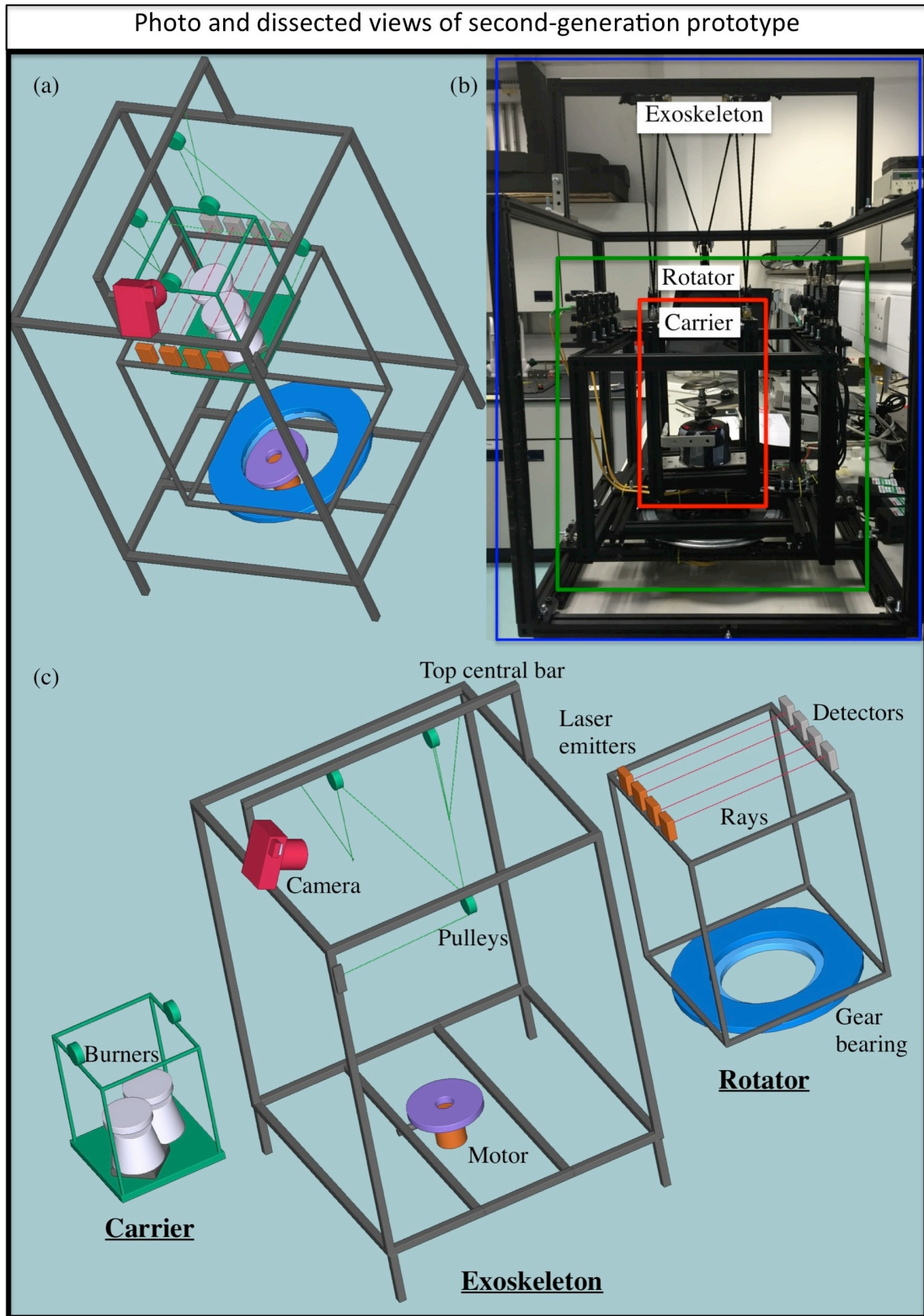


Figure 48 (a) Overall view of the full setup from the top. (b) The corresponding photo of the setup, with each primary section boxed out in blue (Exoskeleton), green (Rotator) and red (Carrier). (c) Exploded view of the setup, with each primary section removed for a clearer view of the individual segments.

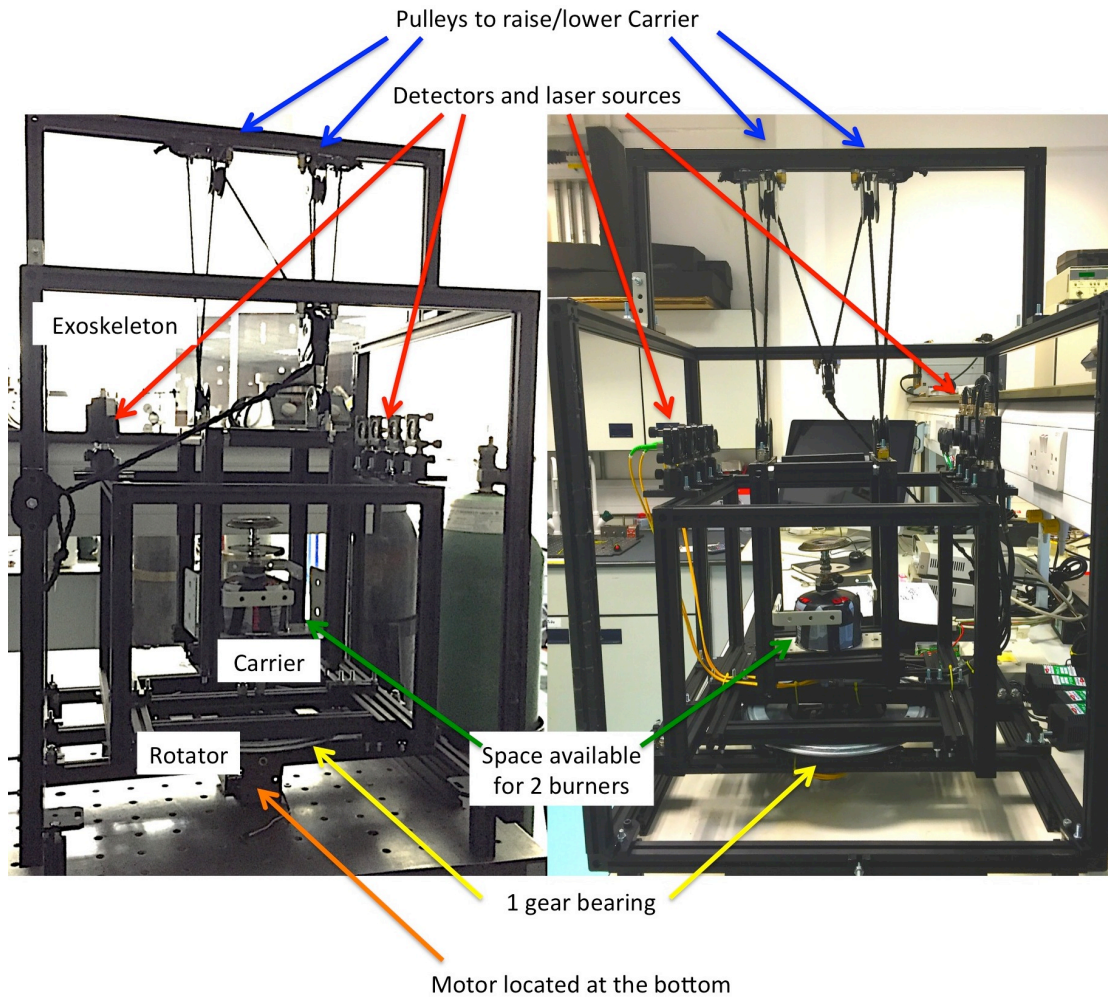


Figure 49 Alternative views of the final design, with simplified annotations of main components.

5.3.3 Equipment and setup design of temporal and 3D tomography system

5.3.3.1 Equipment and software details

With reference to Figure 50, the Exoskeleton which housed the two ‘cages’ was the largest, and had the dimension of 90 cm width by 90 cm depth by 100 cm height. A 90 cm long central bar supported by two rails of 40 cm high further extended the height. The Exoskeleton sat on four legs of each 10 cm in height. The Rotator that sat in the bottom half of the Exoskeleton had the dimension of 37 cm width by 37 cm depth by 60 cm height. Finally the Carrier, which was the smallest ‘cage’, had the dimension of 22 cm width by 22 cm depth by 28 cm height. The Exoskeleton also acted as a barrier to protect users from accidentally touching the moving components or heat source during operation.

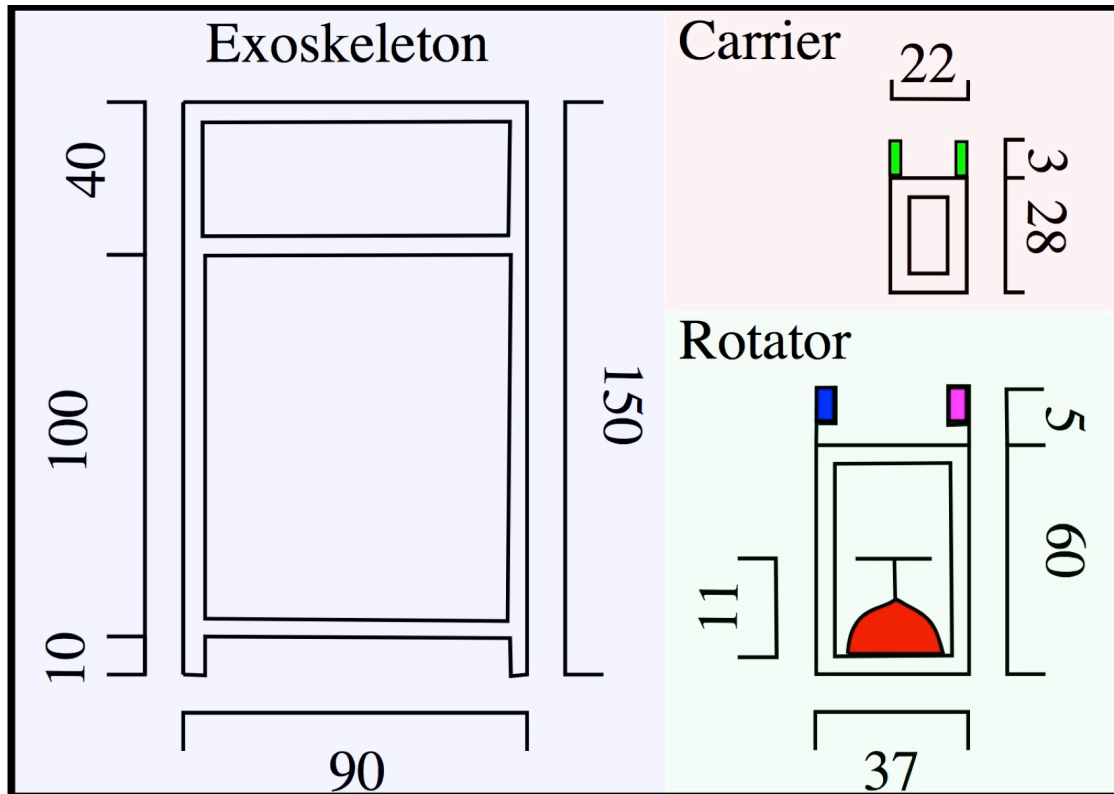


Figure 50 All the dimensions of the setup are in (cm). The Exoskeleton is located in the blue section, the Rotator in the green section and the Carrier in the red section. (Green Rotator section) The red object indicates the burner. The detector is the rectangle in blue and the laser source is the rectangle in purple. (Red Carrier section) The pulleys are indicated by the green rectangles.

The Rotator held the moving cage, which was located inside the bottom-half of the Exoskeleton. The Rotator sat on a 38 cm diameter circular bearing, which was made up of a stationary half and a rotating half. This circular bearing also had a hollow inner hole of diameter 28 cm as shown in Figure 48. The stationary half of the bearing was mounted at the bottom of the Exoskeleton to secure the bearing to a stationary object while the Rotator was screwed onto the rotating other half of the bearing.

The rotating half was connected to a motor from SpingRC (Sm-S4303R) located at the bottom of the circular bearing and fixed onto the Exoskeleton. This motor was connected via a cable to a printed circuit board (PCB) from Phidgets (PhidgetsAdvanceServo-1061), which was controlled directly from the laptop via LabVIEW and powered directly by Iso-Tech IPS-3303 bench power supply unit as shown in Figure 51. The 6 V motor (Sm-S4303R) with no load had a technical specified maximum rotational speed of 54 RPM. However, the motor behaved differently under additional load from the Rotator. With this current setup, the maximum rotation speed was 16.6 RPM, and the slowest speed at 5.7 RPM. This was calculated by using the fastest speed per single rotation during experiment to be at 1.8 s and the slowest speed to be at 5.2 s (lowest speed possible to break inertia from weight).

The same computer was also connected to an 18-bit data acquisition board (DAQ) from National Instruments (NI-USB 6281) to control actions or to receive information. The DAQ controlled the laser current controller (ThorLabs LDC 205C) and the temperature controller (ThorLabs TED 200C). These

controllers adjusted the current ramp and temperature of the distributed feedback (DFB) tunable diode laser from Eblana Photonics (EP1392-DM-B01-FA) mounted on to a butterfly mount from ThorLabs (LM14S2). The output of the laser diode was divided into 4 fibre optic emitters with the aid of a 1 × 4 fibre coupler from Topfibre tech (S/N AA002048). The single mode fibre optics were then fed through the bottom of the Exoskeleton through the central hole within the circular bearing and the bottom of the Rotator and finally mounted on top of the Rotator. Each of the fibre optic emitters was mounted on to a ThorLabs adjustable kinematic mount (KM 100) and a 5 cm ThorLabs optical post (TR50/M) with the aid of a ThorLabs adaptor (RMS11P). A collimating lens from ThorLabs (F230SMA-C) was also used to collimate the laser beams to a diameter of approximately 2 mm. The average beam diameter was approximately 1.5 mm and travelled along a path length of 37 cm. This created an imaginary circular boundary of 37 cm in diameter around the optical plane as the beams rotated around the periphery of the gas exhaust. The emitters were centred on the middle of the Rotator and placed 4 cm apart.

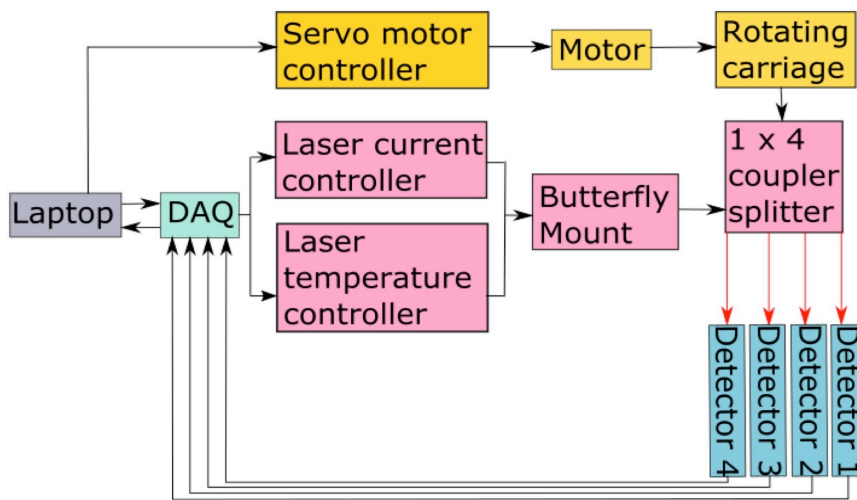


Figure 51 The schematic layout of the software control loop. The laptop is coloured in grey and signifies the main control interface. It communicates with the motor via LabVIEW through the servo motor controller PCB. The motor is then activated and moves the rotating carriage. The DAQ (teal) controls the rest of the equipment setup. The DAQ handles both output commands as well as input commands. The output actions are listed in pink and the input data receiving is in blue. The DAQ controls both the laser current and temperature controller, which is connected to the butterfly mount. The laser sitting on the mount will lase through a 1 x 4 coupler across the one side of the rotating carriage to the other end. The detectors will receive the signal and send it back to the laptop via the DAQ.

Four InGaAs switchable-gain photo detectors (ThorLabs PDA10CS-CS) with 2 mm diameter active area were aligned to sit across the four laser emitters and were also located 4 cm apart on top of the Rotator, as shown in Figure 52. The distance of 4 cm was the minimum distance possible, as space was required to accommodate the size and spacing of the detectors and fittings. Due to the lack of space, a parallel beam configuration was a more economical geometry to a fan configuration. This was also because the emitting sources do not come from a singular emitter, but from 4 emitters spaced side-by-side, 4 cm apart. As the length of the bar the detectors were sitting on was also space limited, this

created minimal angles of the fan beam and the complexities of this configuration severely outweighed the benefits.

The wired electrical and data cables were also similarly fed through under the Exoskeleton, through both the circular bearing and bottom of the Rotator. The detectors received the attenuated signals from the lasers and the data was fed back to the DAQ and then recorded on the computer via LabVIEW. The data of each detector were received by the DAQ simultaneously through multiple analogue channels on the DAQ.

The final section and cage is called the Carrier. This was the cage that held the burners that were lowered into the Rotator. It was fitted with two 3 cm diameter pulleys on the top. Two similar pulleys were also installed below the Exoskeleton central bar. Each of the individual pulleys on the Carrier was connected to the Exoskeleton central pulley with their individual rope. A final similar pulley was installed in the middle of the Exoskeleton front where both ropes were fed into to ensure equal force during height adjustment. The ropes once fed through the final pulley were tucked on the side of the Exoskeleton front hook.

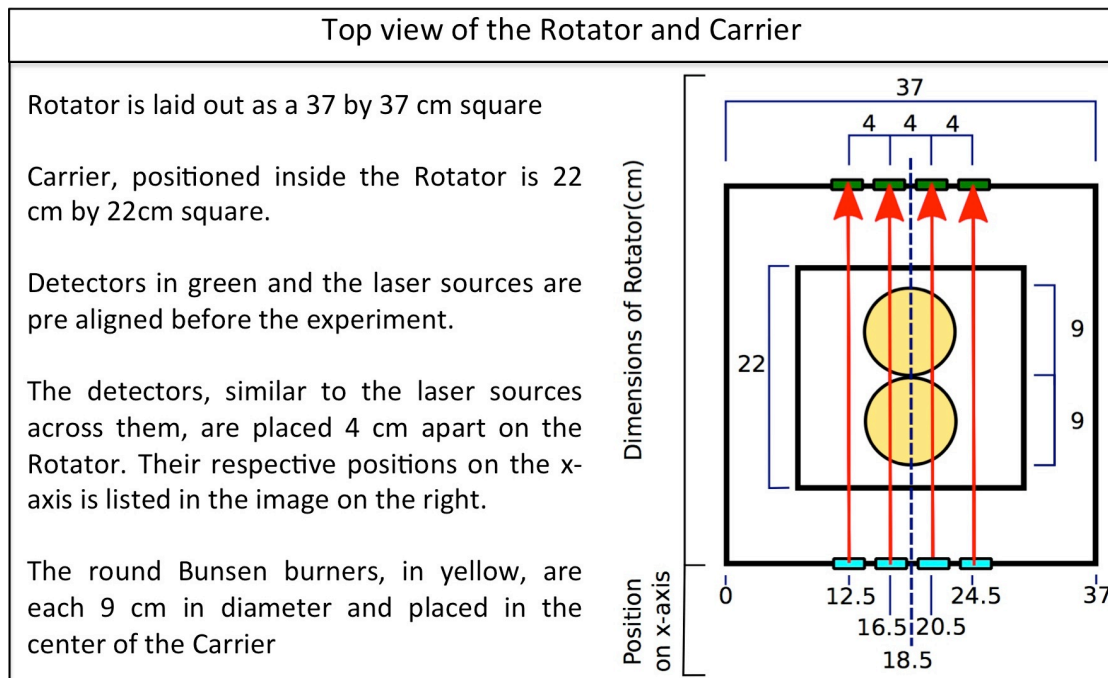


Figure 52 The dimensions of the image are provided in (cm). The Rotator is pictured as the outer black square while the Carrier forms the inner black square. The layout of laser source emitters (cyan rectangles) and photo detectors (green rectangles) are shown sitting on the Rotator. Four laser beams are shown as red. Two yellow discs located are located in the centre of the Carrier. The current layout of this arrangement is pictured at theta at 0 degrees. The locations of the laser source emitters and Rotator mid-point are located in the bottom of the figure in (cm). The mid-point of the rotator is 18.5 cm.

Based on Figure 52, it was clear that there was no beam projected through the middle of the burners (position 18.5 cm on the image). This meant that the information had to be interpolated by the beams at 16.5 cm and 20.5 cm. However, due to the physical constraints of the equipment and the carriage structure, this was the most suitable arrangement for maximising the data sampling.

A camera (Olympus E-P2 with a 14-42 mm zoom lens) was also attached to the central bar of the Exoskeleton to record throughout the course of the experiments. A program written using LabVIEW 2010 was used to control the laser and motor, as well as to receive the attenuated laser signals from the detector.

The detector received signals at a rate of 10 ms per spectrum as discussed in Section 5.2.3. However the Rotator does not stop for data acquisition at each projection angle, which meant that the recorded spectrum is actually not at a single projection angle, but at a range of projection angles. The size of the range of projection angle depends both on acquisition rate, as well as on the speed of rotation. Assuming that the acquisition rate was left constant at 10 ms, then the faster the speed of rotation, the larger the range of projection angle. At this point, assumption was made that this would not largely affect the results of reconstruction, but some blurring of the reconstructed image could be expected. This is discussed later on in the results section.

5.3.4 Burner details

Each burner consisted of a mixed fuel canister and mounted on top of it was the fuel delivery mechanism that was connected to a valve and a flat 9 cm diameter top where the flame exits along the circumference of the round metal plate. The fuel canisters were from Jetboil (Jetpower Isobutane / Propane fuel mix 100g). The total height of the burner, inclusive of the fuel canister was 11 cm. The composition of the mix fuel was unknown, but it is typical for these types of fuel to be approximately 20% to 30% weight Propane and the remaining to be Isobutane.

Each half of the burner plate was covered by aluminium foil (Reynolds Heavy Duty Foil) as shown in Figure 53. The purpose of the foil was to block part of the gas outlet, shown by the 1 cm thick perforated edge along the inner circumference of the plate from escaping, thus creating a non-symmetrical pattern for the flames when lit. Two burners were used during the experiments, resulting in two asymmetrical shapes formed from the flames.



Figure 53 The top view of the 9cm in diameter burner plate and the image of the fuel canister used. The perforated edge along the circumference is the holes where the gas exits from the gas canister.

Assuming that the actual area where the gas escapes (total surface areas of the gas holes) makes up 50% of the perforated area and the aluminium foil covers half of the perforation, the surface area of gas exhaust can be calculated from Equation 38.

$$\begin{aligned}
 \text{Area of perforation} &= 0.5 \times 0.5 \times (\text{Area of total plate surface} \\
 &\quad - \text{Area of non perforated plate surface}) \qquad \text{Equation 38} \\
 0.5 \times 0.5 \times (\pi 4.5^2 - \pi 4^2) &= 3.339 \text{ cm}^2
 \end{aligned}$$

The area of perforation (estimated gas exhaust area) was calculated to be approximately 3.339 cm^2 .

5.3.4.1 Steady state burning

The burners were adjusted in quick succession during the temporal experiments. To make sure that the burner was operating in steady state after each adjustment and before the next sequential image acquisition, a high frame rate video capture camera was used. The camera used was a 12 MP GoPro HERO4, recording video at 32 frames per second.

Sample frames were extracted from the video and examples shown in Figure 54. The burner was turned on at 2 full turns of gas notch and left to burn for 30 seconds before an adjustment of 1 gas notch higher (turned up to gas notch 3) was done. The burner was left alone for another 10 seconds to see any change in flame shape. The assumption being that steady state was attained once the visual shape of flame stays constant after gas notch adjustment.

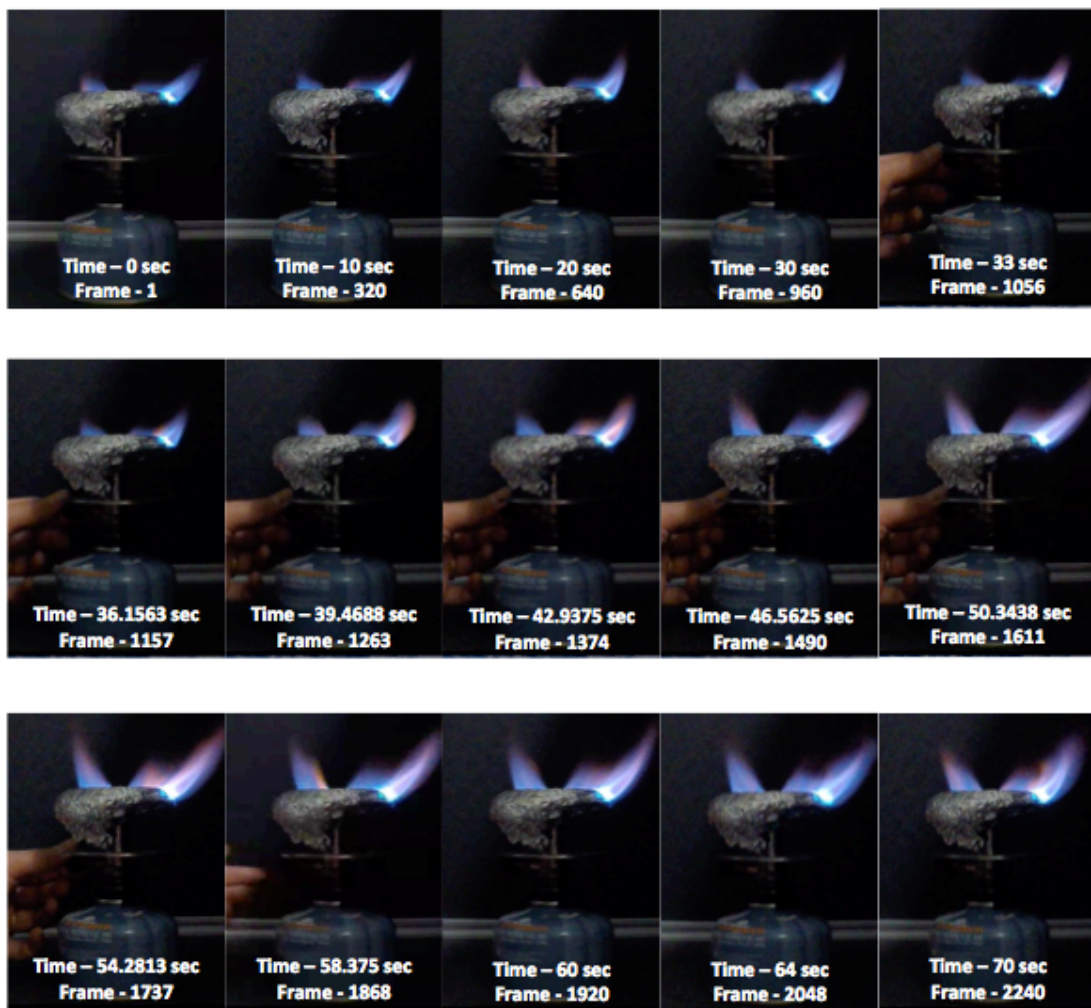


Figure 54 Selected frames from a video recording of the adjustment of a burner, from gas notch 2 to gas notch 3. Video was recorded using GoPro HERO4, 12 MP at 32 fps.

The burner was sampled from frame 1 to 960 (0 to 30 sec) as shown in Figure 54 and the flame was stable from visual inspection. The gas flow was slowly increased by 1 gas notch is shown from frame 1056 to 1737 (33 to 54.2813 sec). At frame 1868 (58.375 sec), there was no physical adjustment from this point with the burner (fingers could be seen moving away and no

longer in contact with the burner in this frame). No changes in flame pattern were observed from frame 1920 to 2240 (60 to 70 sec) and it was concluded that it only took 1.625 sec to reach steady state after adjustment (60-58.375 = 1.625 sec).

5.3.4.2 Adiabatic flame temperature

The adiabatic flame temperature was also calculated to provide an estimate of the maximum temperature the flame could achieve. The assumptions used for the calculations are as followed:

- For each canister, the lighter fuel dominated the fuel composition of the initial burning cycle and the heavier fuel dominated close to the end of the burning cycle. Each gas canister lasted approximately 30 minutes if the gas notch regulator was turned fully twice. Each experiment listed in this thesis was conducted with new gas canisters, and only lasted for the first few minutes of its 30 minutes burning cycle and it was therefore assumed that the primary fuel was the lighter fuel. In this case, propane was the lighter fuel at a density of 2.01 kg/m³ as compared to the heavier fuel of isobutane at 551 kg/m³.
- The combustion was assumed to be complete in the presence of excess air. This could also be inferred from Figure 54 where the flame burns predominantly blue, typical of complete combustion in a Bunsen burner (incomplete combustion tends to burn orange).
- The fuel escaped from the burner plate surface, along the perforated edge along the plate circumference. This was where the air mixes with the fuel.
- The air fuel ratio AFR was assumed to be 10:1 as the burner was operating in atmospheric conditions, although it is typical for the combustion within an engine to operate at significantly leaner conditions (higher AFR value of 14:1 have been used for diesel engines). A lower AFR value yields higher theoretical flame temperature calculations.
- As this is a theoretical flame temperature calculation, the fuel flow rate and other heat losses were not considered.
- Typical method for solving for adiabatic temperature involved using iterations via software (solvers on excel for example) to recover temperature-dependent specific heat capacity values. However, in this case, averaged specific heat values were used (using the average temperature of 573 K). This was because the changes between the specific heat values were not considered significant; the working temperature range for this burner was relatively small (from 296 K to 896 K).

The combustion of propane at 10:1 AFR is given in Equation 39.



Equation
39

The enthalpy of reaction is given in Equation 40 and could be calculated by using enthalpy of formation of combustion products and reactants, where O₂ and N₂ are 0 and omitted, as they are elements.

$$\Delta H^{\circ}_r = 3(\Delta H^{\circ}_{f,CO_2}) + 4(\Delta H^{\circ}_{f,H_2O}) - (\Delta H^{\circ}_{f,C_3H_8}) \quad \text{Equation 40}$$

Where: ΔH°_r Enthalpy of reaction
 ΔH°_f Enthalpy of formation

$$\Delta H^{\circ}_r = 3 \left(-393.51 \frac{kJ}{mol} \right) + 4 \left(-241.82 \frac{kJ}{mol} \right) - \left(-104.7 \frac{kJ}{mol} \right)$$

$$\Delta H^{\circ}_r = -2043.099 \frac{kJ}{mol} = -2043099 \frac{kJ}{kmol}$$

At this point, ΔH°_r is now also the exit state of the adiabatic flame temperature T_2 , which is also the summation of all the specific heat capacities of the combustion products multiplied by the change in temperature ΔT (from reference room temperature T_1). An average temperature of 573 K is referenced for each c_p .

$$2043099 \frac{kJ}{kmol} = \Delta T \{3(c_{p,CO_2}) + 4(c_{p,H_2O}) + 45(c_{p,O_2}) + 188.09(c_{p,N_2})\}$$

$$2043099 \frac{kJ}{kmol} = \Delta T \{3(46.64) + 4(14.98) + 45(15.95) + 188.09(35.95)\}$$

$$\Delta T = \left(\frac{2043099 \frac{kJ}{kmol}}{7679.4255} \right) = 266.05K$$

$$T_2 = \Delta T + T_1 = 266.05 + 296 = 562.05 K$$

The final adiabatic flame temperature is approximately 562.05 K, which was similar to experimental validations using a thermocouple (within regions of 400 - 800 K). However, as stated in the assumptions that the theoretical calculation of adiabatic temperatures varies with actual conditions as other factors affecting flame temperatures were assumed or not considered (inaccurate AFR assumptions, no consideration of surface area or other heat losses etc.).

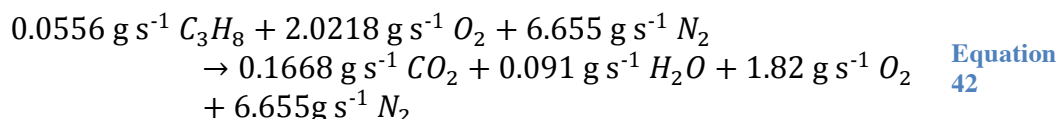
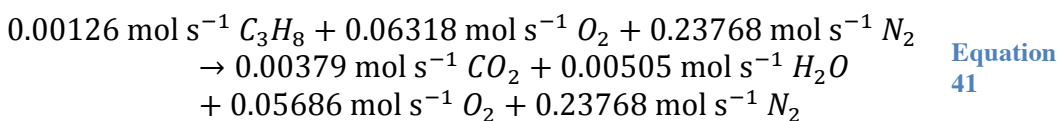
5.3.4.3 Mass and heat transfer

Based on an averaged total burning time per canister of 30 minutes (1800 seconds) for 2 fully notch turns, the flow rate can be calculated as follows.

$$\begin{aligned} \text{Total volume of gas canister} \div \text{time required for full discharge} \\ = \text{gas flowrate} \end{aligned}$$

$$100 \text{ g} \div 1800 \text{ sec} = 0.05556 \text{ g/sec}$$

Based on the stoichiometric balance shown in Equation 39 and the calculated gas flow rate, the flow rate in mol s⁻¹ and g s⁻¹ could be recalculated as shown in Equation 41 and Equation 42.



The energy of combustion for 1 mole of propane can be calculated in Equation 43 using only the reacting/produced species from Equation 39.



Where the bond dissociation energies stands for BDE:

$$\begin{aligned} [(2 \times \text{BDE}_{\text{C-C}}) + (8 \times \text{BDE}_{\text{C-H}})] + [(5 \times \text{BDE}_{\text{O=O}})] \\ \rightarrow [(3 \times 2) \times (\text{BDE}_{\text{C=O}})] + [(2 \times 4) \times (\text{BDE}_{\text{O-H}})] \\ + [\text{Energy of combustion}] \end{aligned}$$

$$\begin{aligned} [(2 \times 356 \text{ kJ}) + (8 \times 436 \text{ kJ})] + [(5 \times 498 \text{ kJ})] \\ \rightarrow [(3 \times 2) \times (803 \text{ kJ})] + [(2 \times 4) \times (467 \text{ kJ})] \\ + [\text{Energy of combustion}] \end{aligned}$$

$$\begin{aligned} [3488 \text{ kJ} + 712 \text{ kJ}] + [2490 \text{ kJ}] \\ \rightarrow [4818 \text{ kJ}] + [3736 \text{ kJ}] + [\text{Energy of combustion}] \end{aligned}$$

$$\text{Energy of combustion for 1 mol C}_3\text{H}_8 = 1864 \text{ kJ}$$

Based on Equation 41 where the molar flow rate was calculated, the energy of combustion can be determined.

$$1864 \frac{kJ}{mol} \times 0.00126 \frac{mol}{s} = 2.355 \frac{kJ}{s}$$

Using the enthalpy of combustion shown in Equation 44, the temperature of the heated air (combination of $1.82 \text{ g s}^{-1} \text{ O}_2 + 6.655 \text{ g s}^{-1} \text{ N}_2$ from Equation 42) can be estimated. An average of $C_{p_{air}}$ at 350 K was used.

$$\Delta H = mass_{air} \times C_{p_{air}} \times dT \quad \text{Equation 44}$$

$$2.355 \frac{kJ}{s} = 0.008475 \frac{g}{s} \times 1.008 \frac{kJ}{Kg K} \times (T_{final} - 296 K)$$

$$275.7 K = (T_{final} - 296 K)$$

$$T_{final} = 571.7 K$$

The final estimated temperature was 571.7 K, which was within the range of experimental thermocouple validations of 400 to 800 K. It also yields a fairly similar value to the adiabatic flame temperature of 562.05 K.

5.3.5 Satisfying the design framework

- Suitable for 3D tomography studies

To allow 3D volumetric studies, the optical plane was adjusted by moving the actual heat source itself instead of the optical plane, thus effectively distancing the flame distance from the optical plane. The Carrier started off at its lowest point via the pulley rope adjustment, and was raised by pulling the rope. Therefore the results taken were in fact inverted, where the lower Carrier position, the cooler the temperature of the tomogram would be. As the Carrier was raised higher, the heat source was closer towards the optical plane, and would thus register a higher temperature tomogram distribution.

- Suitable for temporal studies up to 1.8 seconds per tomogram

To prevent a skewed optical plane from uneven surfaces, the lasers and detectors were placed on the Rotator, which in turn was held and supported by the Exoskeleton. The actual optical plane was not be affected by resting surface irregularity due to the rigidity of the Exoskeleton structure.

To increase the speed of data acquisition, all the laser to detectors were all pre-aligned. This removed the need for secondary motions such as mirror movements to redirect laser paths. To maximise data coverage per angle without sacrificing time, the single laser source was also divided into 4 with the 1 x 4 laser coupler splitter.

The new setup solved tangled cable issues during the experiment by only having the Rotator performing 180 degrees rotation before returning back to the

starting position. The cables that were being fed through below the Rotator were all consolidated neatly together and then given sufficient slack to wind up for only 180 degrees before returning to their original positions. The given slack of the cables was also adjusted so that the maximum rotation angle was only up to 180 degrees to prevent over rotation per experiment cycle.

These improvements allowed the data acquisition per experiment to be reduced down to 1.8 seconds.

- Material choice

The primary materials used in the construction of the equipment structure were aluminium construction rails. Aluminium was chosen because there was a need to be non-flammable and be able to withstand high temperatures due to safety precautions. In the scenario of accidental knocking of the burners from the Carrier they would neither melt the structure nor set the structure on fire. Metal framework was chosen due to its high melting point and non-flammability. (The hottest parts of the structure during the experiment were found at the upper frames of the Carrier and at no point did the temperature exceed 60°C during normal operation).

The setup was designed to be moved around easily by dismantling the connections at the bottom of the setup, which included the USB servo motor controller cable to the computer, power cables to the photo detectors, the BNC lead cables connected to the DAQ as well as the primary fibre optic before the 1x4 coupler splitter. All of these cable connections were located at the same spot below the Rotator carriage and were neatly consolidated. This facilitated the easy detachment and the movement of equipment.

5.4 Contributions, Developments and Chapter summary

The equipment and software used in the line of sight TDLAS system designed for the MICC was used to update and further develop a fan beam tomography system within the group.

An updated fibre optic diode laser with an improved wavenumber range, centred at 7178 cm⁻¹ was used to update a free-space diode laser that relied on weaker water absorption lines 7185.394 cm⁻¹. The analytical programs were also updated to live peak fitting to reduce overall experimental time and processing time. Peak selections was conducted and selected based on the wavelength accessible by the new laser and a sample experiment with analytical procedures was conducted.

Basing on challenges faced by this fan beam tomography system and the new equipment available, a framework was created to guide the design to achieve both 3D and temporal measurement capabilities.

The first design iteration was introduced before detailing the final design of the setup, the rationales (material choice etc.) behind the finalised design and the tomography algorithm best suitable for this setup. The burners used were also described, depicting the method of blocking gas outlets to create asymmetrical flows, as well as the time required to reach steady state after adjusting the fuel flow.

6 IMPLEMENTATION, COMPARISON AND VALIDATION OF TOMOGRAPHY ALGORITHMS

6.1 Chapter overview and experimental conditions

This chapter focuses on demonstrating how to apply the reconstruction theory on experimental data. It first begins with priming the data (integrated absorbance from experiment) in Section 6.2 and arranging them in the order suitable for the reconstruction program. The use of filters and zero padding is located in Section 6.3. The sample walkthrough of each method: Filtered Back Projection (FBP), Fourier Slice Reconstruction (FSR) and Direct Fourier Reconstruction (DFR) are presented in Section 6.4, Section 6.5 and Section 6.6 respectively. These methods are then validated using a thermocouple and other techniques in Section 6.7. Additional simulations of the three methods are also discussed in Section 6.8 to calculate errors and standard deviation against simulated image. Finally a comparison of the methods is discussed in Section 6.9 and the chapter summarises in Section 6.10.

6.1.1 Experimental conditions

For the purposes of comparison, the same experimental data were used for the implementation of all three methods. The experimental conditions consisted of 360 projections, each at 0.5 theta / angle of projection step size. The duration to complete the measurements was 3.6 seconds (rotation speed of 0.139 RPM). The burner settings for back burner (A) were set at 5-notch opening and the front burner (B) at 3-notch opening. Each notch corresponded to a complete turn of the fuel flow regulator. The centre of the back burner (A) was located at (2, -4) on the spatial axis and the front burner (B) was located at (-1, 5).

The ramp filter was used as the standard for this chapter unless otherwise stated as this chapter focuses on the software implementation and comparisons of the different algorithms. When applicable, the zero padding was set at 700. Further discussion will be held later on the variation of filters. The peak ratio that was used in the MATLAB programs was the ratio of integrated absorbance of 7181.93 cm^{-1} (Peak 1) divided by 7179.8 cm^{-1} (Peak 2). The ambient lab conditions were recorded at 23 °C, 103.2 kPa and relative humidity of 53%.

6.2 Data priming

A sinogram is a compilation of projection slices as a function of theta or angle of projection of laser beams to the object scanned. Figure 55 (a) shows the laser beams transmitted across the object. The collection of integrated absorbances of a compiled projection slice (Radon slice) at that projection angle is shown in Figure 55 (b) and is expressed visually within the yellow box in the sinogram in Figure 55 (c) and fills up with projection slices at different

projection angles (from 0 to 179 degrees). The sinograms presented in the thesis are expressed as a 2D image as shown in Figure 55 (c), however they are expressed numerically in the program as a 2D matrix of integrated absorbance values down the column and angle of projection across the rows.

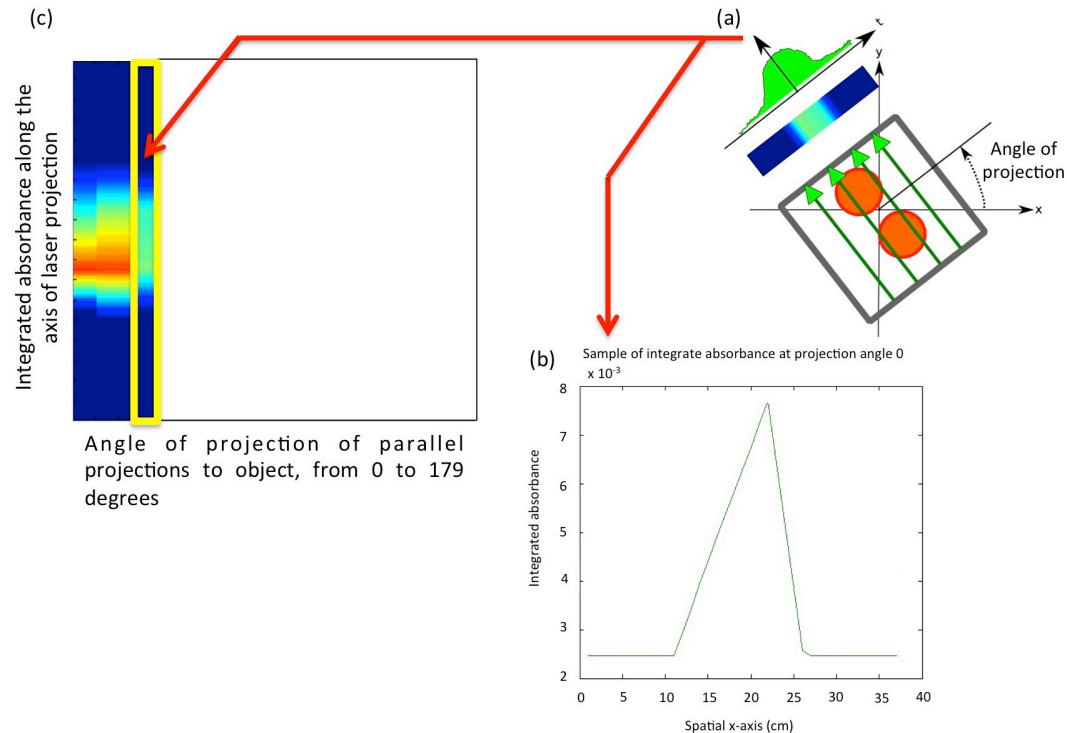


Figure 55 (a) A sample image of collected integrated absorbance through the laser beams along the angle of projection. (b) Compiled integrated absorbance along the angle of projection. (c) A compiled sinogram of each projection slice (Radon slice) at each projection angle of sampling.

From the experiment, there were 4 data (integrated absorbance values) per projection angle. These 4 data spaced 4 cm apart corresponded to the data acquisition of 4 detectors within a singular parallel projection. This was considered sparsely spaced, as the objects scanned were only 9 cm to 18 cm wide as shown back in Figure 52 in Chapter 5.3.3.

The sparse sampling within a projection slice was due to the physical space limitation of laser sources/detectors. Linear interpolation was carried out to improve the sparse data population of each slice. The first assumption was therefore that the difference between each sampled data was linear, and that if they were not linear, the number of projections due to a small theta step size would over-compensate for this inaccuracy. The data outside the 4 original data points was interpolated towards room conditions taken prior to the start of each experiment. The second assumption was that the laboratory was large enough, so that the room conditions were invariant with the effects of the flames and that the effects of the flames did not affect the extreme ends of each projection slice. A simple test of taking the temperature of the extreme ends of the spatial axis during the experiment with a thermocouple proves that this assumption is valid. These interpolated projection slices from each projection angle were used to build the final sinograms used in the reconstruction programs.

6.3 Filters and Zero padding

The use of filtering is a common post-processing technique for typical image processing. Generally a high pass filter allows values higher than a set point to pass while a low pass filter allows the value of a lower set point to pass. The uses of filters are highly dependent on the final objective, where a high pass filter increases the edging/sharpness whilst a low pass filter creates a smoother image.

Low pass filtering (Shepp-Logan, Hamming etc.) whilst smoothing the image by reducing noise and increases the signal to noise ratio, comes at a loss in spatial resolution, decreasing the level of numerical accuracy and accessible details within the image. A sample signal from Section 6.5 with associated example filters are shown in Figure 56, where it shows the various cut off points of the filters as the frequency moves towards 1 [201].

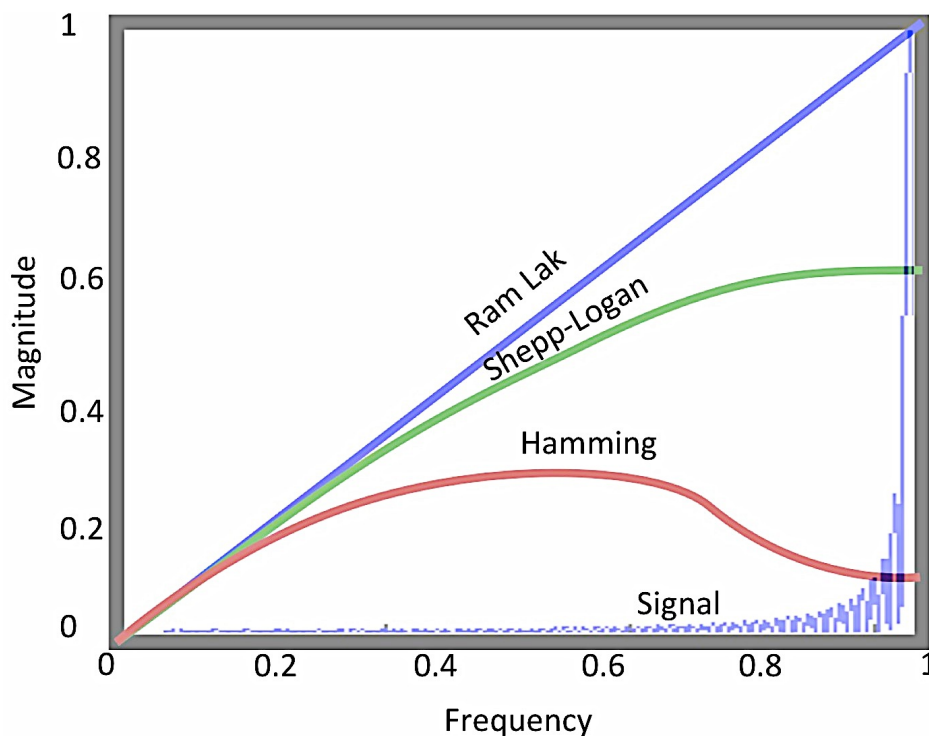


Figure 56 A sample Fourier transformed signal from Section 6.5 with different sample filters and their shape and cut off points.

The use of filters for tomography in other application areas such as medicine includes sharpening an X-ray image for detail clarity or smoothing filters used in standard photography for aesthetic purposes. Unlike these areas where the picture is analysed on face/aesthetic value, this thesis prioritises the numerical accuracy and correct distribution of information (shape) of the image. This is an important point to make, because by the very definition of a filter is that it removes certain portions of information prior/after the image reconstruction to improve the image. This makes the final image subjective to the choice of filter and the user, which is not the aim here. For the tomography system to be truly robust regardless of the scenario (user/data/image pattern), the filter recommended here is one that is created to safeguard from ‘obvious’ noise or artifacts and ignoring everything else in between. Examples of ‘obvious’

noise/artifacts in this thesis could be having random noise and unexpected temperature dips/spikes of $-30\text{ }^{\circ}\text{C}$ or $2000\text{ }^{\circ}\text{C}$ even though the expected temperature range within that image is known to be from $25\text{ }^{\circ}\text{C}$ to $700\text{ }^{\circ}\text{C}$.

A Ram-Lak filter (high-pass), shown in Figure 56, which ramps up to the maximum cut off frequency, was selected for this thesis even though it exacerbates noises at high frequencies. However, it does not filter information crucial to the image reconstruction's numerical accuracy. A decision between accepting noise to preserve reconstruction numerical accuracy was made here [202].

On the other hand, to increase the image quality without the heavy reliance of filtering, is to 'up sample' pre-existing data by zero padding. However, this technique can only be applied in Fourier transform-based techniques such as the Fourier Slice Reconstruction and the Direct Fourier Reconstruction.

Zero padding produces a smoother final image by decreasing the frequency intervals and thus improving the interpolated Fourier transform (also known as FFT interpolation). It is important to note that the purpose of zero padding is to smooth out the final image without the use of a filter. Zero padding does not improve spatial resolution because it does not add real information to the transform but simply adds a line of trailing zeros to the waveforms. The only way of improving spatial resolution is to acquire more data during the experiment [28], [203], [204].

6.3.1 Variation of zero padding

The original data was made up of four integrated absorbances within a sinogram slice of 37 cm long. The slice is bounded by the assumption that a set amount of distance from image centre is at room conditions. The interpolation between each known data creates a sinogram slice of total size of 145 data points with a distance of 0.25 cm step size between each data.

Figure 57 shows the effect of increasing the amount of zero padding on the final image reconstruction. Each image was reconstructed at a different final size with a different zero padding value, the individual images in Figure 57 had been cropped accordingly for comparison.

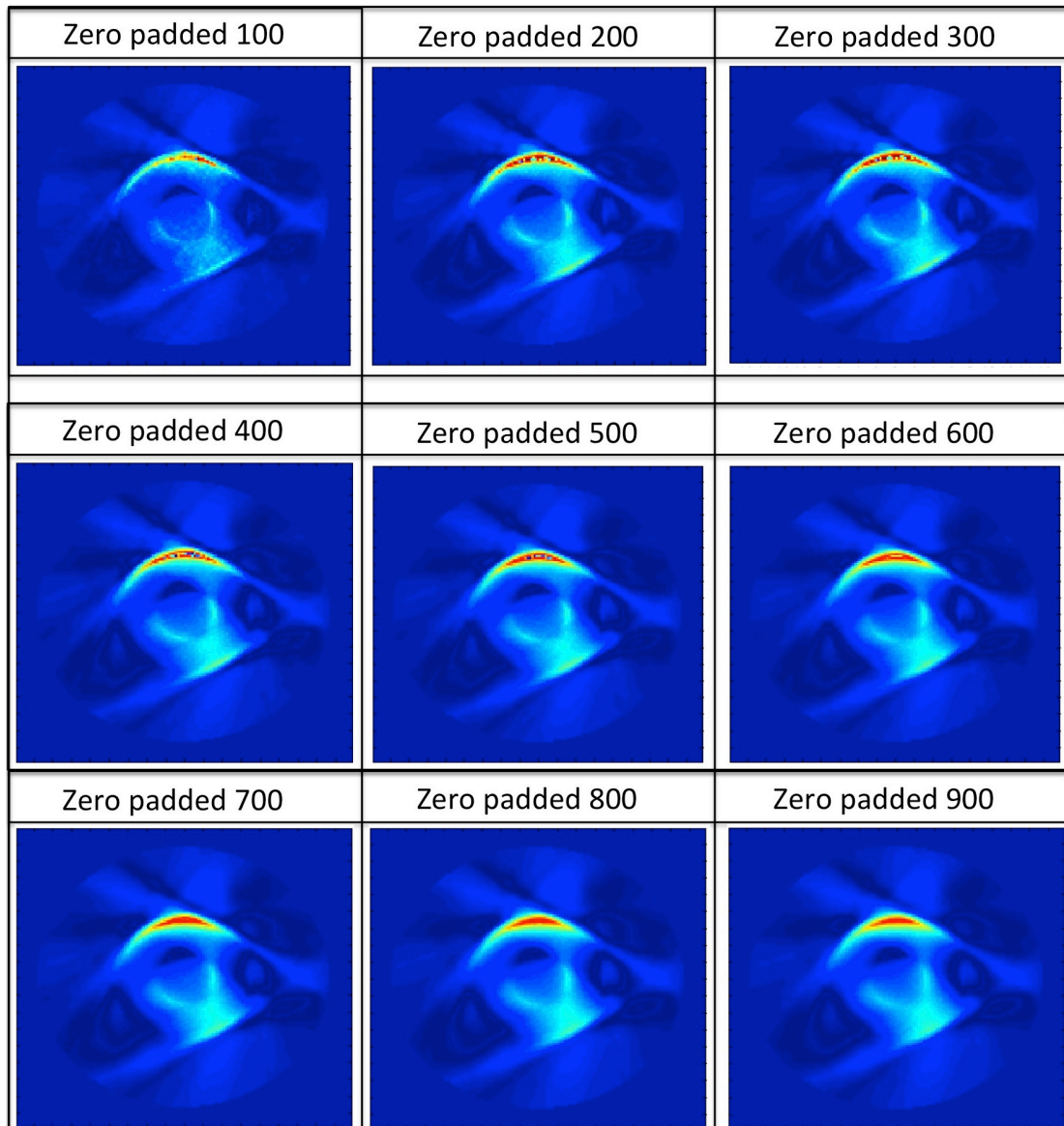


Figure 57 The effects of varying the degree of zero padding. The intensity of ‘salt and pepper’ noise could be seen diminishing as the degree of zero padding increases. No discernable improvement could be observed above zero padding of 700. However a trade-off over computational time occurs with the increment of zero padding.

A steady improvement of image smoothness can be seen in the reconstructed images as the value of zero padding increases. However it only improves up to 700, after which the improvements plateau. It is worth noting that the smoothness or increased pixel resolution could only be as good as the original data acquisition. Typical zero padding of original signals is normally between 2 to 4 times of the original signal, and in this situation, 700 is about 4 times the original size of the starting signal length[110].

Two enlarged samples of the varying amount of zero padded reconstructed images are shown in Figure 58. The zero padded - 300 depicts a larger amount of ‘salt and pepper’ noise in the final reconstruction, particularly at higher temperature zones. This seemed consistent with studies conducted by An et al[13], who showed that higher temperature zones tend to exhibit higher number of errors. An example of a sufficiently padded sinogram is the zero padded - 700 where there is no ‘salt and pepper’ noise present.

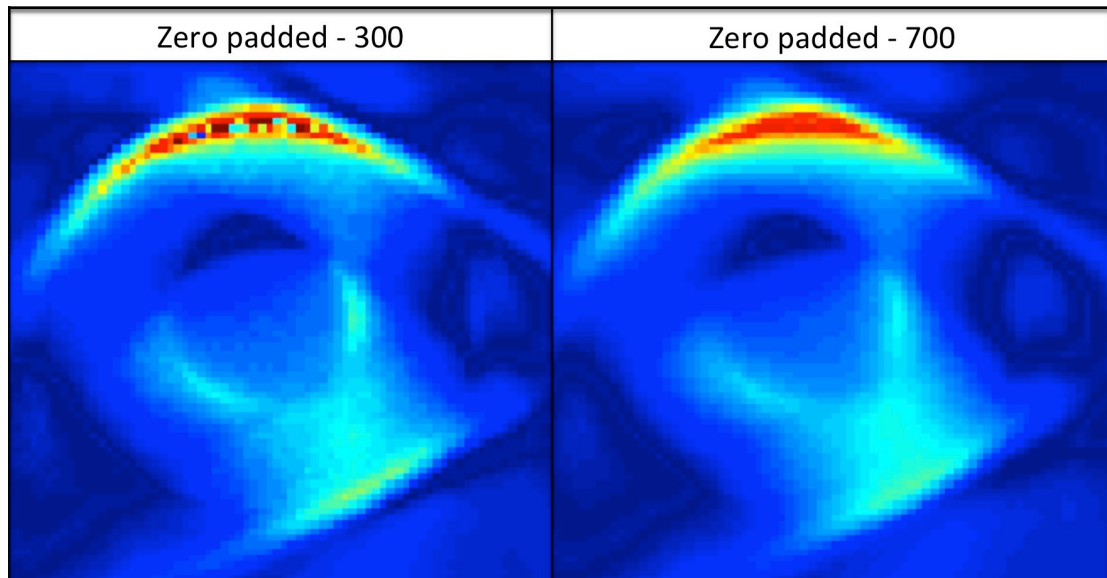


Figure 58 The sampled and expanded version of zero padded images as shown in the results section. Note that deficient zero padding creates ‘salt and pepper’ noise in the reconstructed image, more notably present in high temperature zones.

6.4 Filtered Back Projection (FBP)

The Filtered Back Projection method introduced in Section 3.4.1 is the simplest of the three methods studied, where individual projections at different angle of projections (thetas) to the measurement space are collected and filtered with a function before back-smearing the filtered projections to an initially empty image (matrix filled initially with zeros) at its respective angle.

There are generally two methods of executing this method as shown in Figure 59. The first approach is to reduce image blurring by multiplying each projection with a one-dimensional filter before back-projecting each projection onto the image. The alternative is to simply back-project each projection onto the image and then apply a two-dimensional filter to reduce the blurring in the image. The first approach was chosen for this thesis.

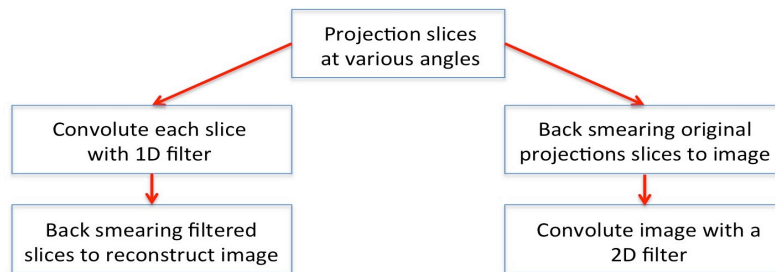


Figure 59 Methodology of programming pathways for applying the FBP technique in MATLAB

The procedure of the FBP MATLAB fitting program is shown in Figure 60 and the overall walkthrough is shown in Figure 61 where the major parts are further broken down for further discussion.

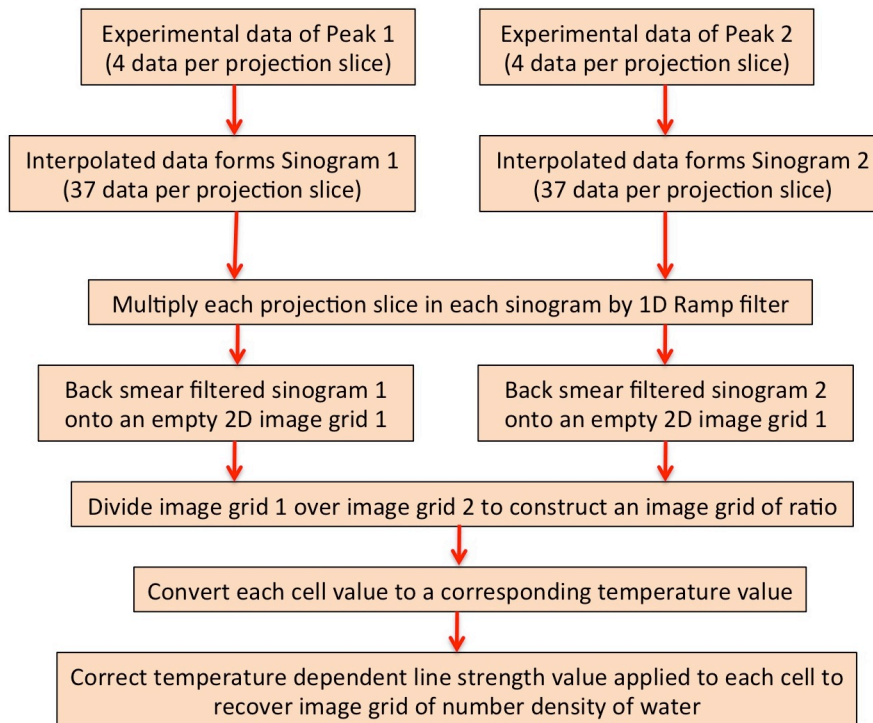


Figure 60 Flow chart of how the experimental data were primed for reconstruction and the procedures of the reconstruction procedures of FBP method.

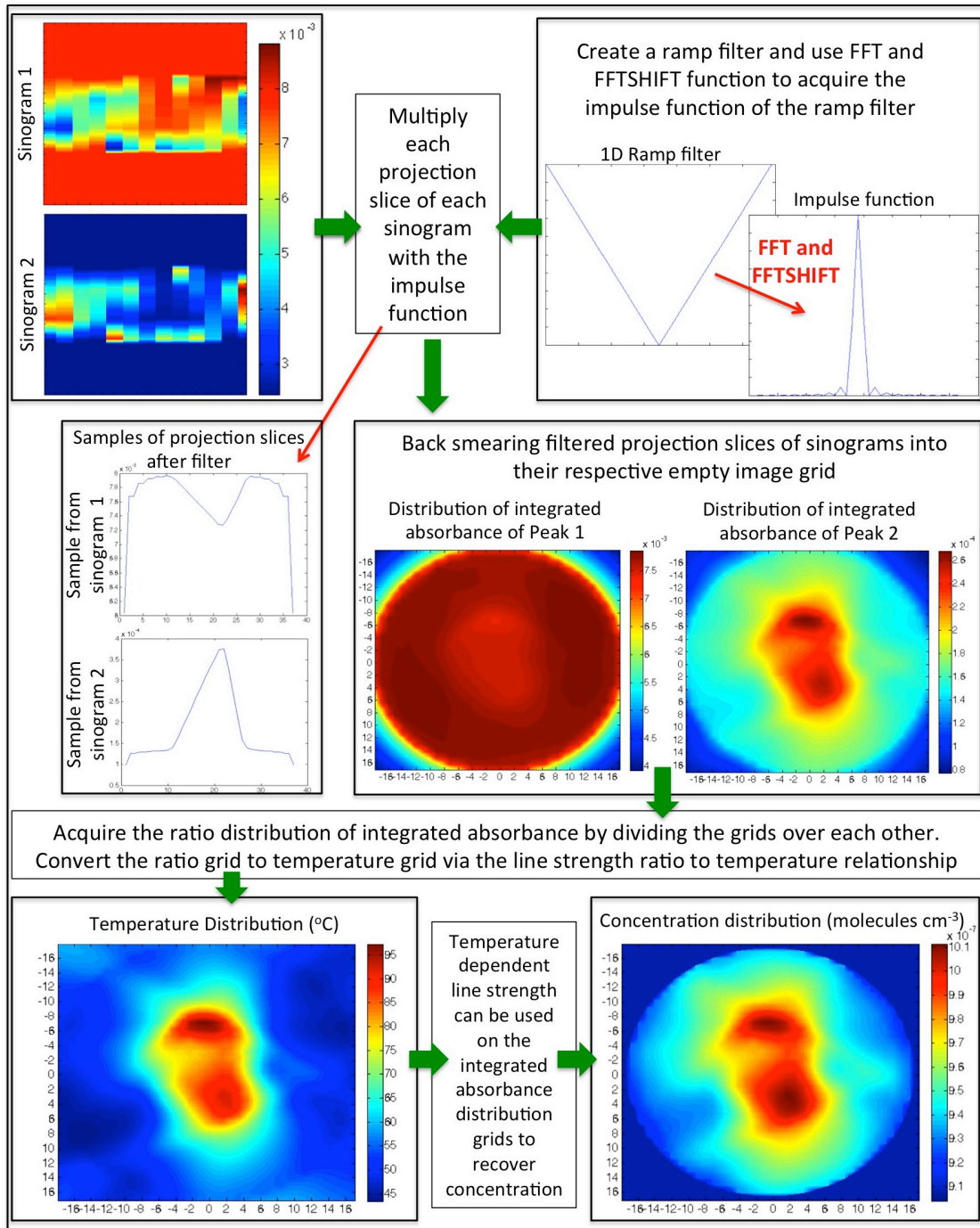


Figure 61 Walkthrough of MATLAB execution of the Filtered Back Projection method.

As there are two absorption peaks (2 sets of integrated absorbance per projection slice), two sets of sinograms were compiled. Each slice in both sinograms was linearly interpolated from 4 to 37 data, matching the length of the Rotator cage of 37 cm in length as shown in Figure 62.

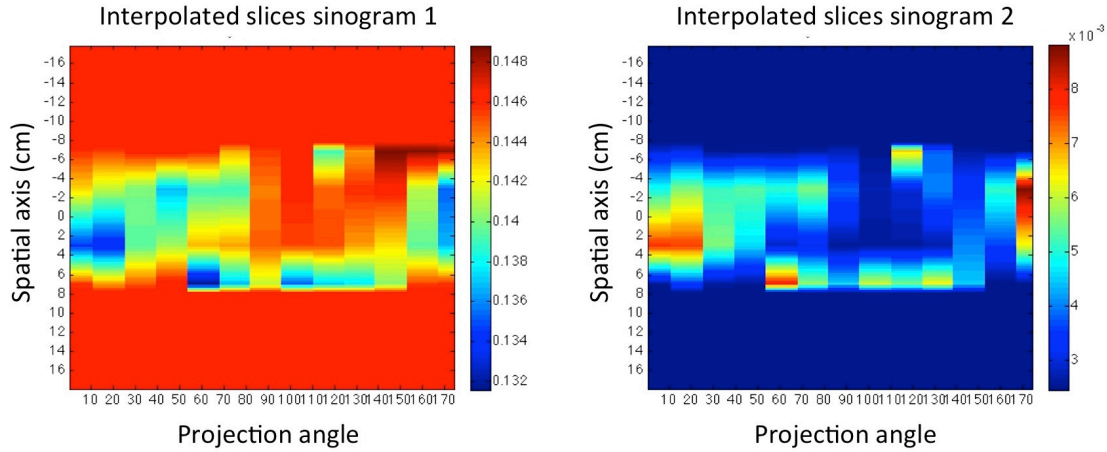


Figure 62 Sample sinograms of peaks 1 and 2. Peak 1 corresponds to 7181.93 cm^{-1} and Peak 2 corresponds to 7179.8 cm^{-1} .

The filtered back projection relies essentially on a filter and the ramp filter. This is shown in Figure 63. The ramp filter was transformed to an impulse function with MATLAB's FFT function as discussed earlier in Section 3.4.1, followed by an FFTSHIFT function to adjust the impulse function to the centre. The impulse function was convoluted with each projection in each sinogram. The filtered slices of each sinogram were then back smeared onto their corresponding empty cell grid to form two grid/ images of integrated absorbances.

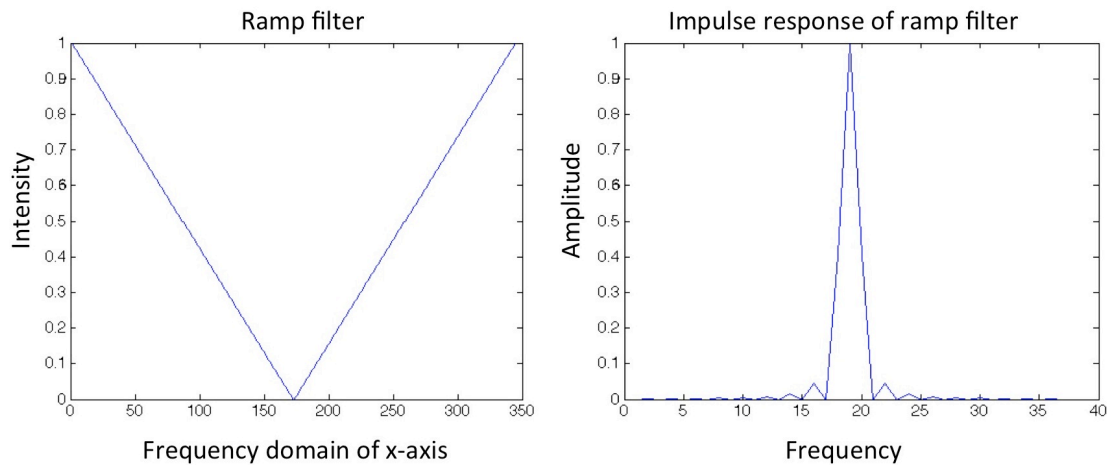


Figure 63 The ramp filter is shown in the left with its impulse function depicted on the left.

A non-averaged back-smearing of slices onto an image is traditionally done for purely imaging purposes and visual diagnosis as shown in Figure 64 (a), as the final image is formed via the contrast of values between neighbouring cells. This means that as long as the ratios of values within a grid are consistent, they will still construct the same image, on the assumption that the colour to number scale range are adjusted to the individual image. This is typically done in

most traditional image processing purposes as only the pattern of the final image is of importance, not the actual values of the cells.

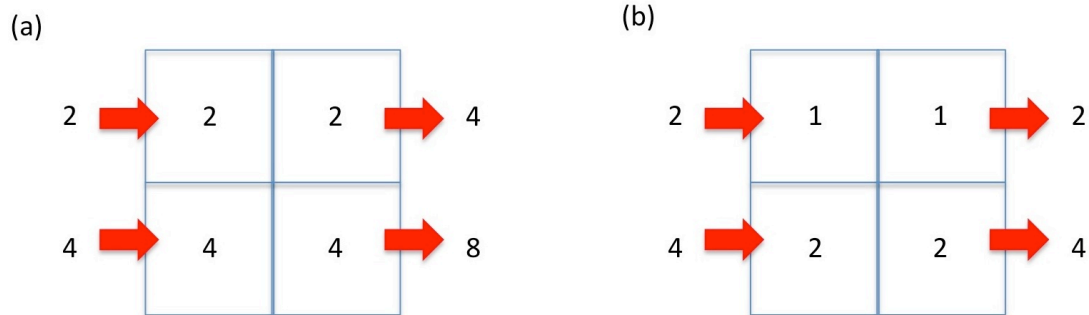


Figure 64 Example of the back smearing process. On the left (a), the integrated absorbance is not divided equally among the number of cells travelled, resulting in twice the amount of integrated absorbance at the end. On the right (b), the integrated absorbance is divided equally among the total amount of cells travelled, resulting in the correct final value coming out of the grid.

On the other hand, for correct visual reconstruction, as well as numerical accuracy, the individual integrated absorbances needs to be averaged with the number of cells it back smears, as shown in Figure 64 (b).

In Figure 65 for example, where both grids (a) and (b) are not numerically similar, grid (a) ranges from values 1 to 9 and grid (b) is exactly 3 times larger than grid (a) with a range from 3 to 27. However, when both grids are expressed as images, they look similar provided that the colour/contrast scales are used with respect to the numerical range of the respective grids. This leads to the third assumption where the total value of each filtered projection needs to be divided by the number of cells the projection passes. It is worth noting that this does not affect the overall pattern of the image constructed, only the physical values within that image.

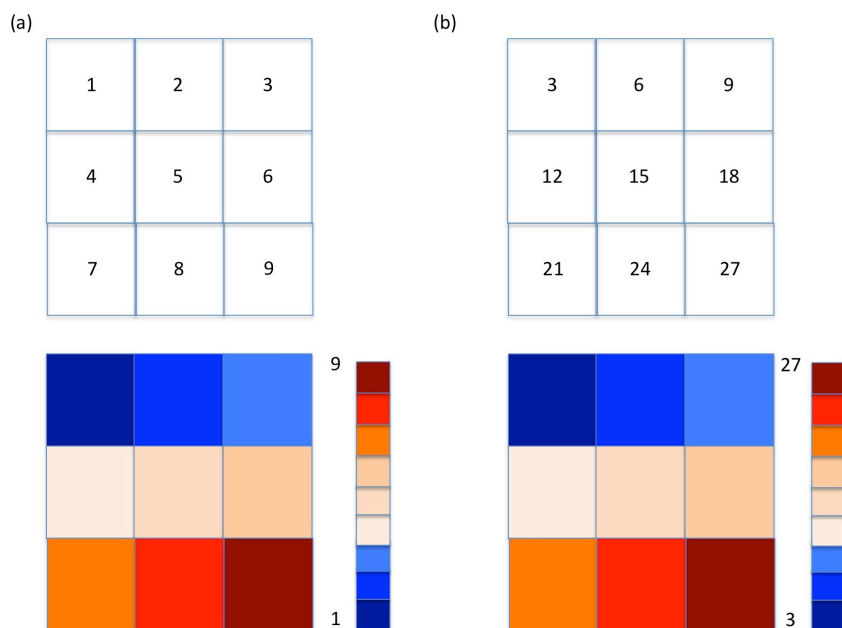


Figure 65 Comparison of two image grids. (a) Grid of arbitrary values, (b) Grid of values 3 times larger than grid (a). Both grids give the same image with respect to their number scale even though their values are different within each cell. This is due to the fact that the image is constructed based on the ratios each cell relative to their neighbours.

It is also important to note that because the final images are a convolution of multiple back smearing of projections, the individual cells in the final images need to be divided by the total number of smeared projections. For example, if there are a total of 180 projections back smeared over the image, then the final reconstructed image /grid needs to be divided by 180 to be numerically correct.

A total of two images of integrated absorbance will be created as each image represents the reconstruction from each absorption peak as shown in Figure 66.

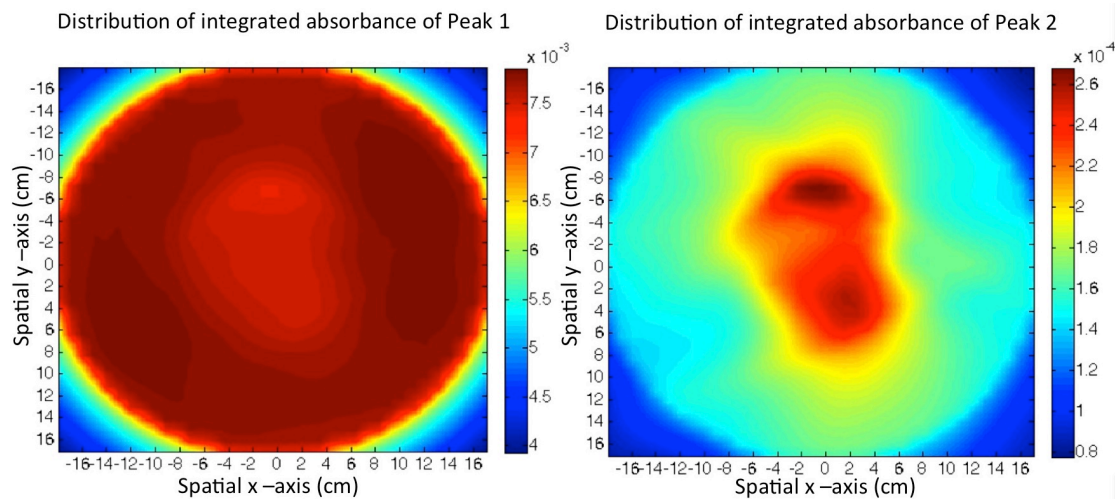


Figure 66 Comparison of sample experiment integrated absorbance distribution of two peaks. Even though the images look different at this point, once the correct temperature dependent line strength is applied to each cell with respect to their corresponding absorption peaks, the final concentration distribution will yield the same result.

As the absorption peaks chosen exhibit different behaviour with temperature as shown in Figure 66, so the distribution of integrated absorbance of both peaks will vary. At constant concentration, absorbance of Peak 1 decreases, shown as Peak4b in Figure 39, as the temperature is raised. This matches the general trend in the reconstructed image that the areas above flame locations are of a lighter shade. Absorbance of Peak 2, shown as Peak4a in Figure 39, increases with temperature, and can be seen in Figure 66 where the areas above the flames are of higher colour intensity. It is also worth noting that the contrasts of both images are different in Figure 66, (less distinct for Peak 1 than Peak 2). This was attributed to the fact that each peak reacts at a different rate to the same temperature change as shown in Figure 39 for the laser operating at 15 °C.

Although the concentration was not constant during the experiment, it was a good indicator of where the flame was present in relation to the spatial dimensions. This was a reasonable assumption as the amount of water vapour being released from combustion is assumed to be small in relation to the size of the room.

- Executing the two-line thermometry method to determine the temperature and concentration spatial distribution

The two grids of integrated absorbance distributions were divided by each other to achieve a grid of peak ratios, which allowed the corresponding temperature of each ratio number to be found using the two-line thermometry method. The ratio to temperature relationship was presented in Figure 40 in Chapter 5. The grids of recovered line strengths could then be applied to their respective cells in the original grids of the reconstructed integrated absorbances to retrieve the distributed grid of number density of water. The temperature and water concentration distribution are shown in Figure 67.

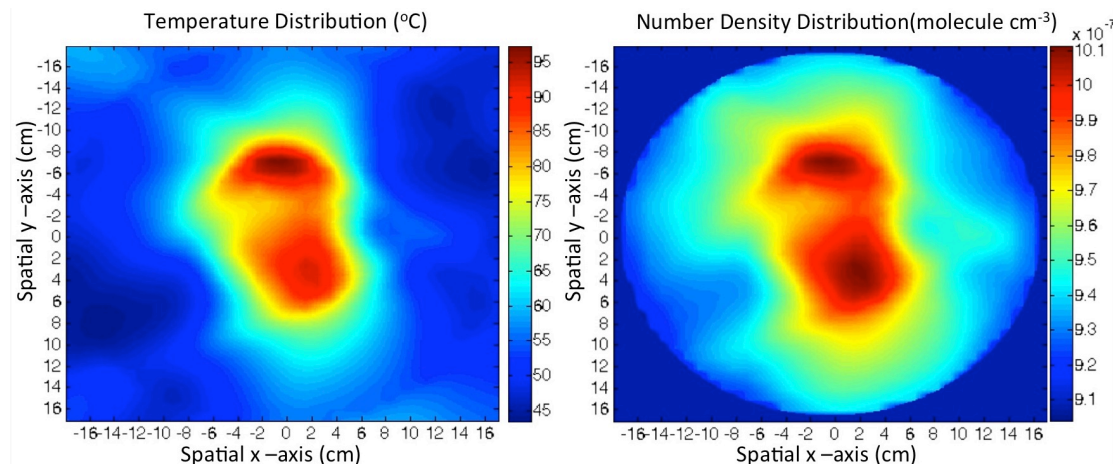


Figure 67 The reconstructed temperature and water concentration distribution using the FBP method.

6.5 Fourier Slice Reconstruction (FSR)

The Fourier Slice Reconstruction (FSR) is the second method studied and involves shifting between the spatial and frequency domain that was discussed in Section 3.4.2. There are two approaches to implementing the Fourier Slice Theorem, and the FSR is the first of the two methods. The other method is the Direct Fourier Reconstruction (DFR) method listed in Section 6.6.

The FSR method involves transforming each projection into the Fourier domain, filtering it, before conducting an inverse Fourier transform of that slice. It is then back-smearred onto the spatial 2D image. A flowchart is presented in Figure 68 as a summarised view to the implementation of the MATLAB program. The walkthrough of the program is also presented in Figure 69.

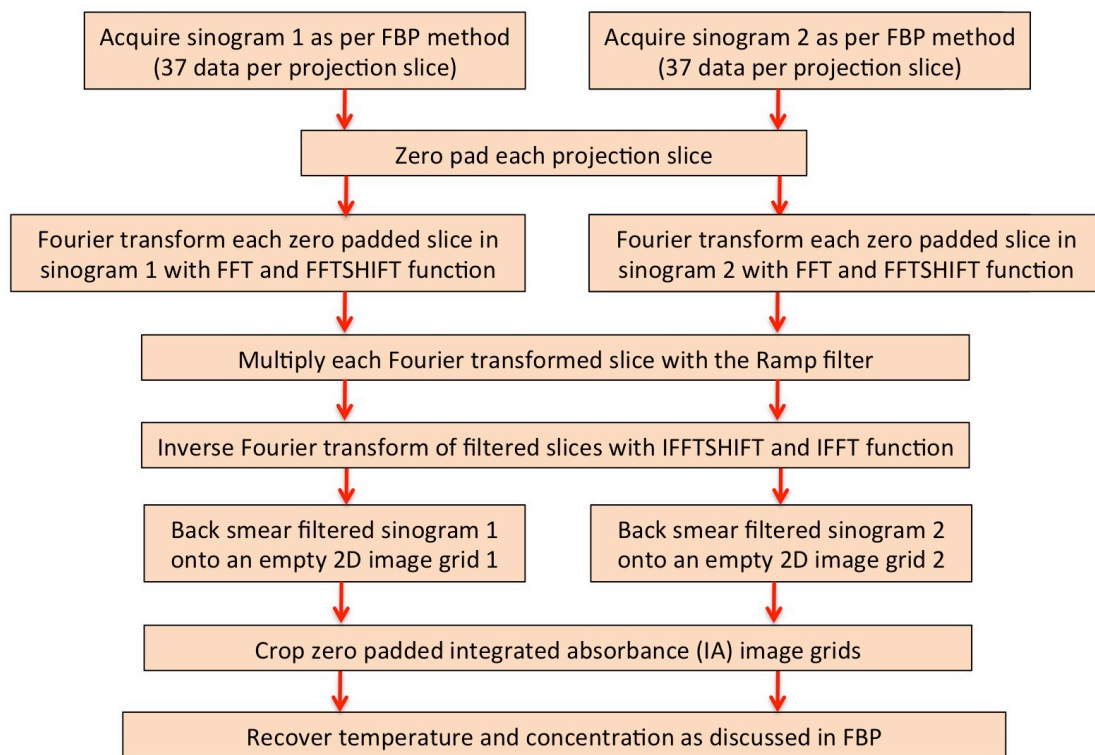


Figure 68 Flow chart of the procedures of the reconstruction procedures of FSR method.

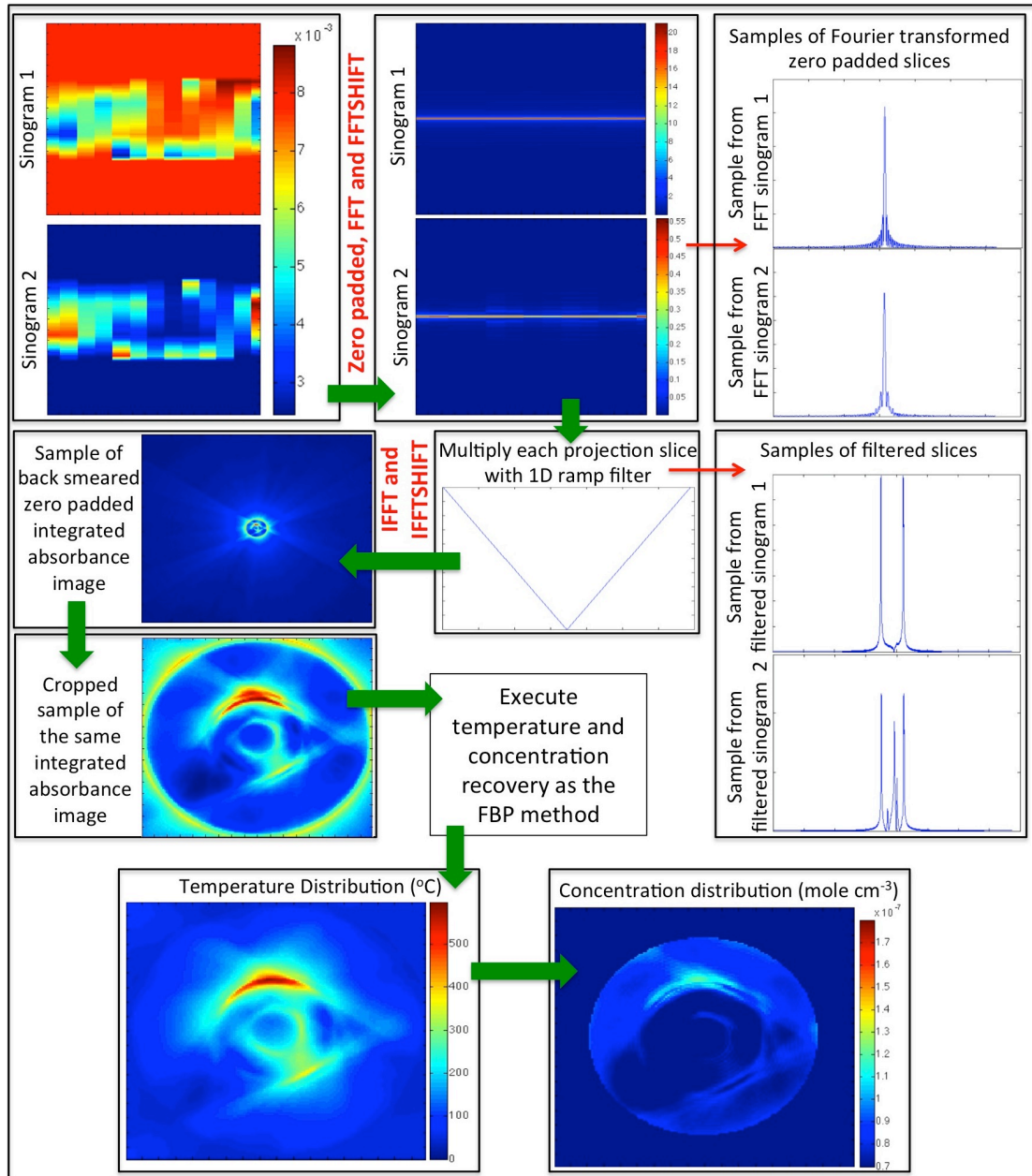


Figure 69 Walkthrough of MATLAB execution of the Fourier Slice Reconstruction method.

The initial sinograms were first zero padded to improve the final reconstruction quality. Using the fast Fourier transform functions FFT and then FFTshift to relocate the impulse function to the centre in MATLAB, each of the projection slices was individually transformed to form new sinograms as shown in Figure 70. A sample of the Fourier slice at theta 0 of each sinogram is shown in Figure 71 (a) and (b). These Fourier transformed slices were then convolved with a ramp filter shown previously in Figure 63 and their product sample is shown in Figure 71 (c) and (d).

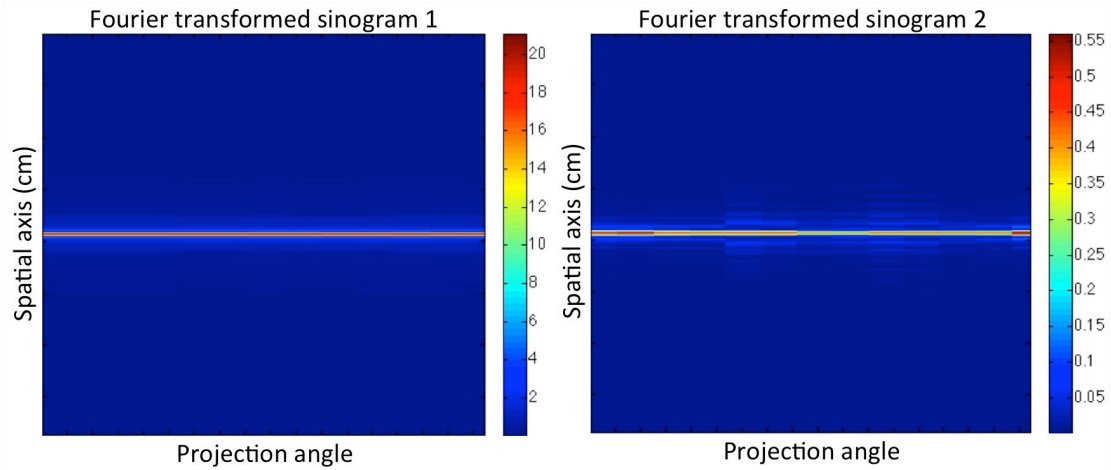


Figure 70 Fourier transformed sinograms as compared to previous sinograms in Figure 62.

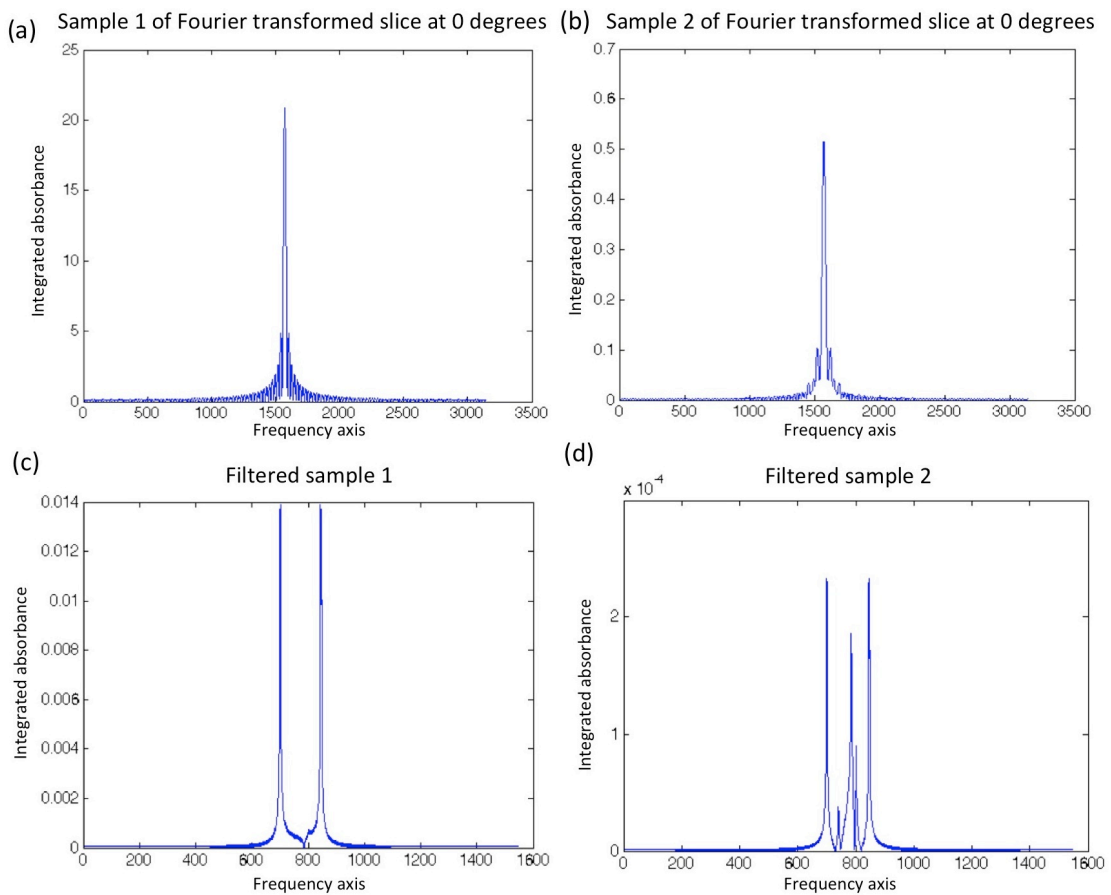


Figure 71 (a) Fourier transform projection slice sample of sinogram 1 at projection angle 0. (b) Fourier transformed projection slice of sinogram 2 at projection angle 0. (c) Filtered projection slice sample of sinogram 1 at projection angle 0. (d) Filtered projection slice sample of sinogram 2 at projection angle 0.

These filtered Fourier slices were then inverse Fourier transformed (IFFT and IFFTSHIFT) back to their original spatial domain information. Each of the filtered projection slices were then back smeared with respect to the projection angle back into an empty image grid to reconstruct images of integrated absorbance as shown in Figure 72. At this point, these images were larger due to the initial zero padded data. These zero padded data could either be removed prior to the back smearing or after the reconstruction. It was chosen in this

method to remove the zero padded data via cropping the final reconstructed image, as shown in Figure 73. The final steps in recovering temperature and concentration distribution shown in Figure 74 and have been omitted due to the similarity with the FBP method in Section 6.4.

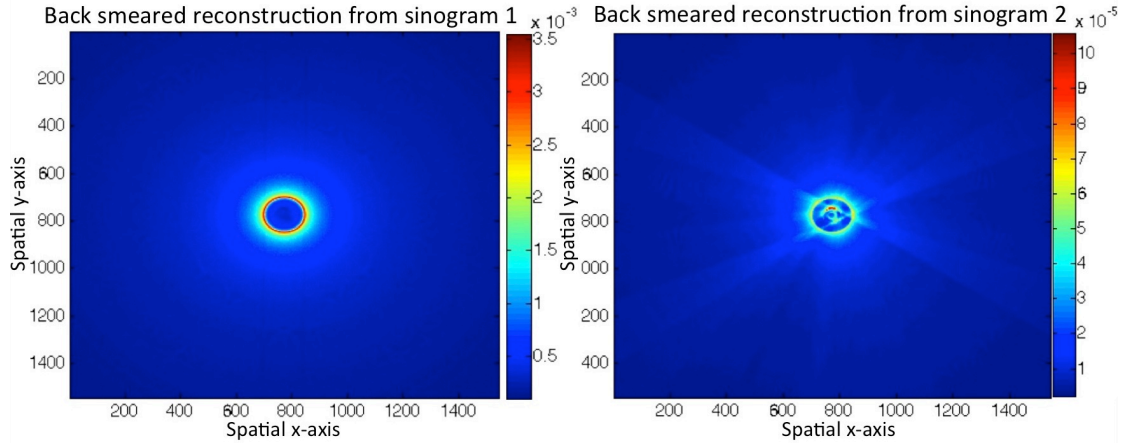


Figure 72 Back smeared reconstructed images of integrated absorbances of peaks 1 and 2.

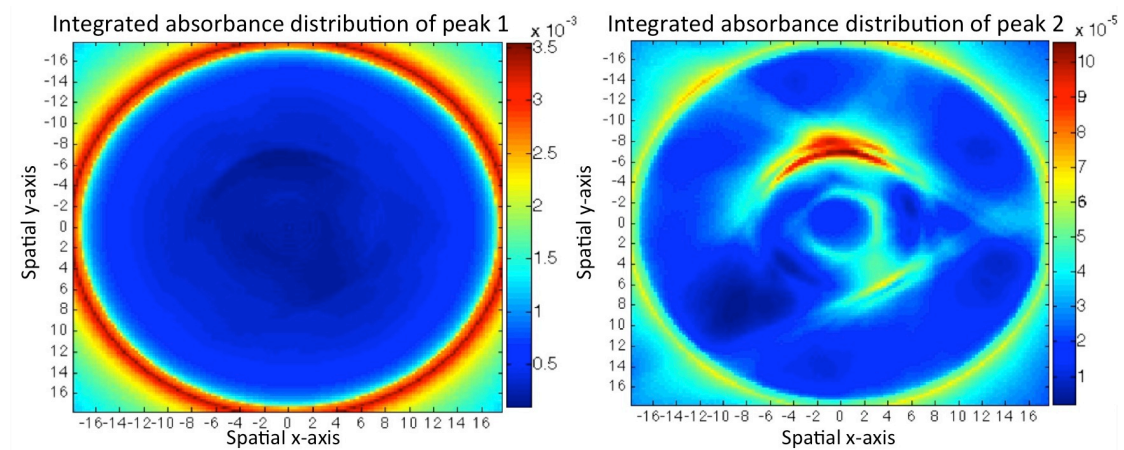


Figure 73 Cropped reconstructions of integrated absorbance distributions of peaks 1 and 2.

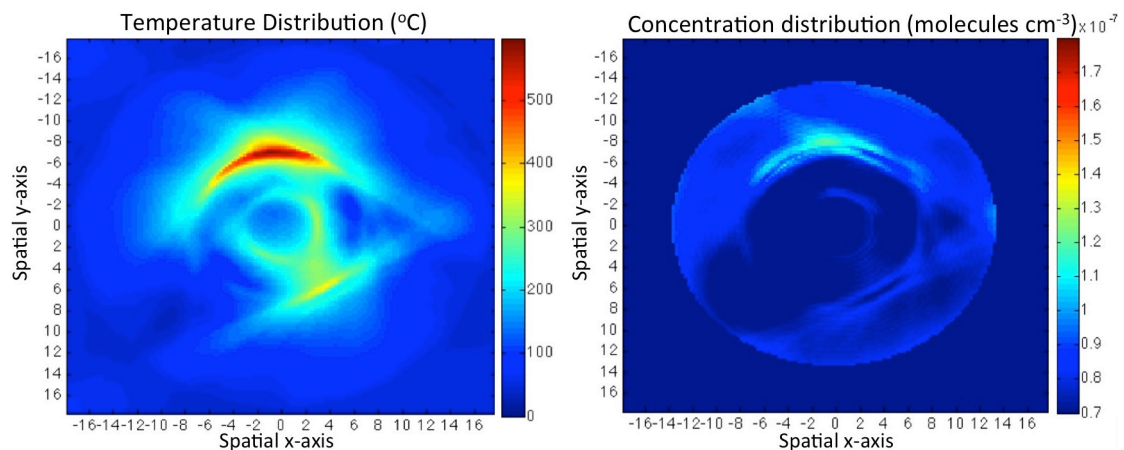


Figure 74 The temperature and concentration distribution sample images reconstructed by the FSR method.

6.6 Direct Fourier Reconstruction (DFR)

The Direct Fourier Reconstruction (DFR) is the last method studied and this involves shifting between the spatial and frequency domain and was discussed in Chapter 3.4.2. There are two methods of implementing the Fourier Slice Theorem, and the DFR is the second of the two methods. The other method is the Fourier Slice Reconstruction (FSR) method listed in Section 6.5.

The DFR method focuses on allocating the Fourier transforms of the projection slices onto the Fourier domain before conducting a 2D inverse Fourier transform directly back to a reconstructed spatial image. A flowchart is presented in Figure 75 as a summarised guide to the implementation of the MATLAB program. The walkthrough of the program is also presented in Figure 76.

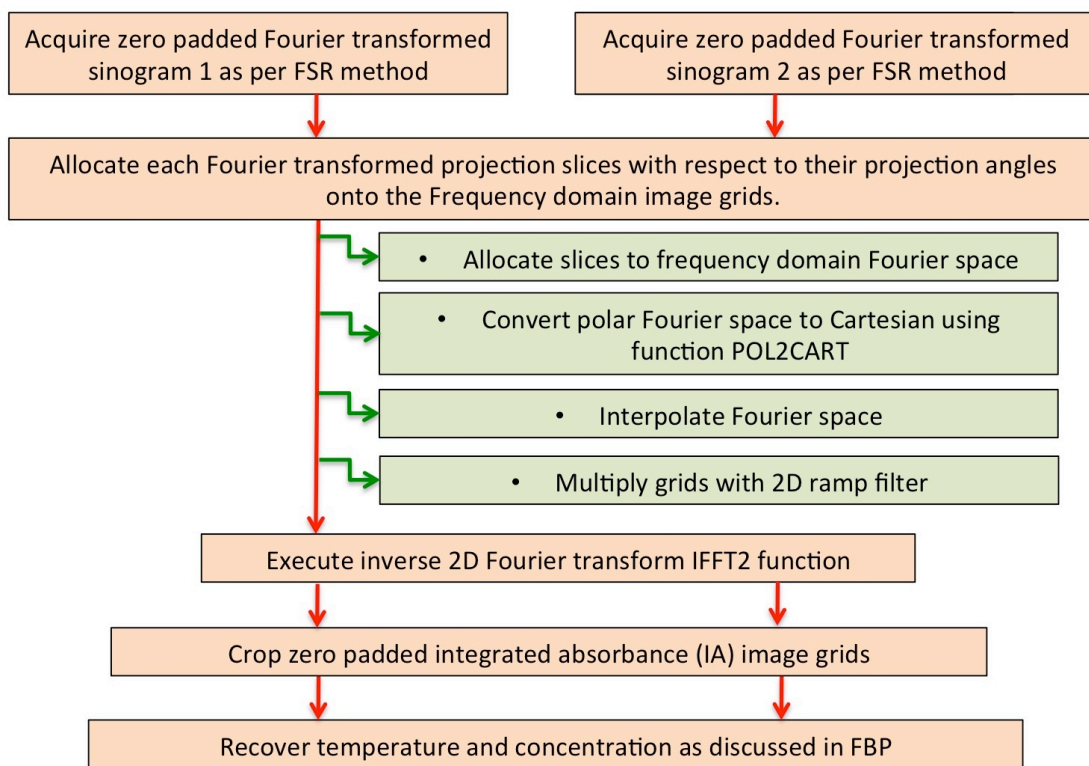


Figure 75 Flow chart of the procedures of the reconstruction procedures of DFR method.

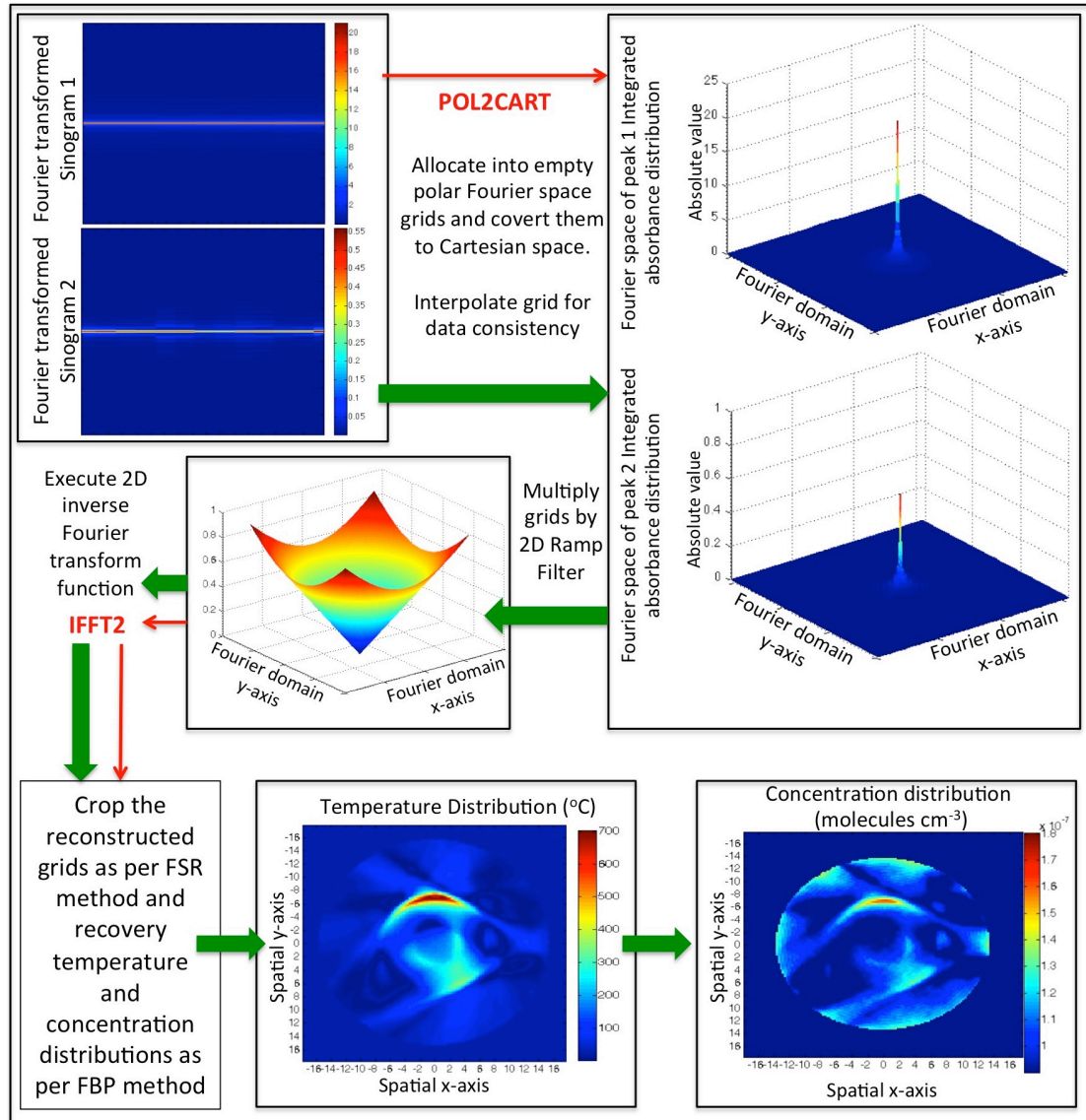


Figure 76 Walkthrough of MATLAB Direct Fourier Reconstruction implementation.

The zero padded sinograms were prepared as in the FSR method in Section 6.5 and shown in Figure 70. These Fourier transformed, zero padded slices were allocated onto the Fourier domain grids based on its angle of projection as shown in Figure 77. As the initial data sampling or the original sinogram is of a consistent length, the allocation of the Fourier transformed slices that were centred in the middle of the grid of the frequency domain grids will form a circular data pattern on a square grid (as shown as Polar Fourier space in Figure 77). This was converted to a Cartesian Fourier space using the MATLAB function POL2CART (as shown as Cartesian Fourier space in Figure 77). The Cartesian Fourier space was linearly interpolated for data smoothness and is presented in Figure 78. Filtering was carried out in the frequency domain and a 2D ramp filter was created for this purpose. A similar way of allocating the ramp filter into the frequency domain grid was done and can be seen in Figure 79.

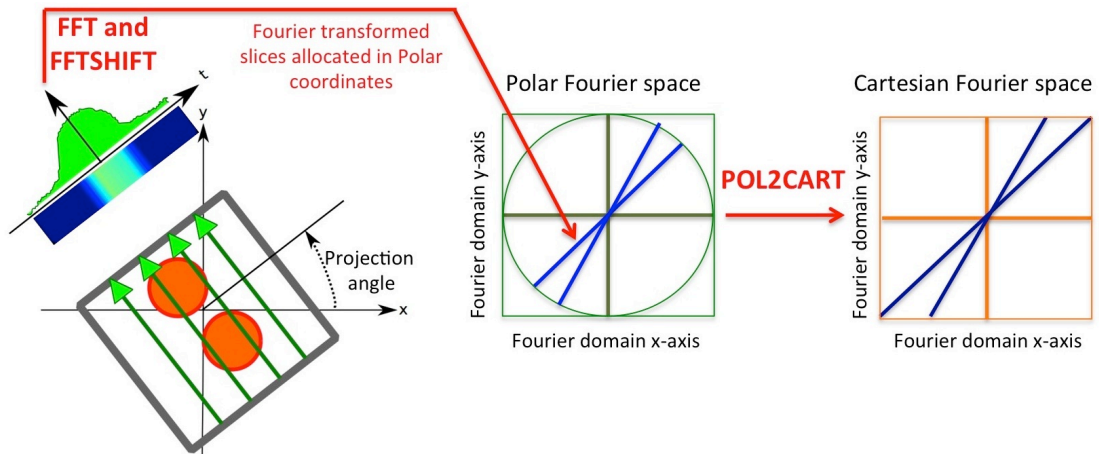


Figure 77 Example of how the spatial domain projection slices are converted to the frequency domain. The Fourier transformed slices are allocated to the polar coordinates in the frequency domain grid, and requires conversion to Cartesian distribution prior to interpolation.

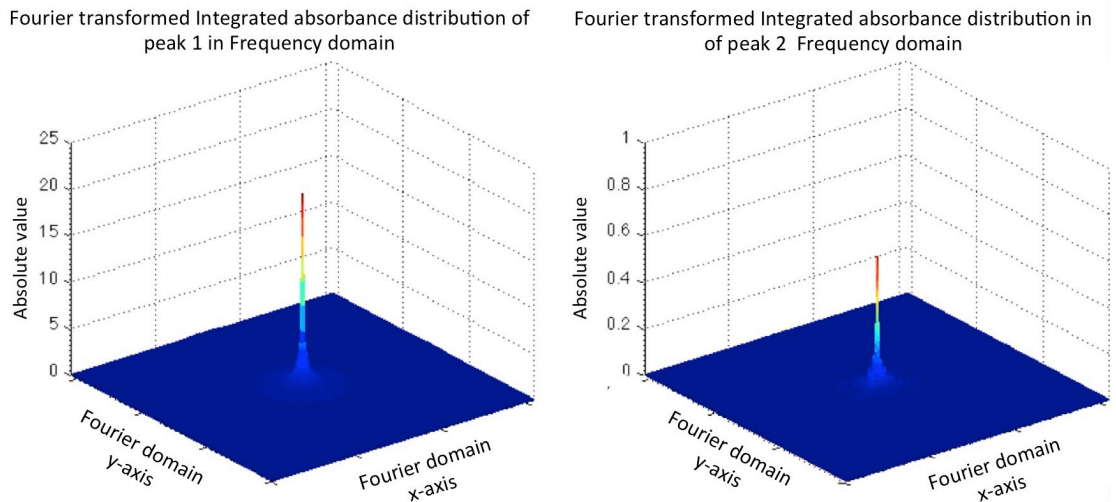


Figure 78 Allocated Fourier slices interpolated into the frequency domain of Peaks 1 and 2.

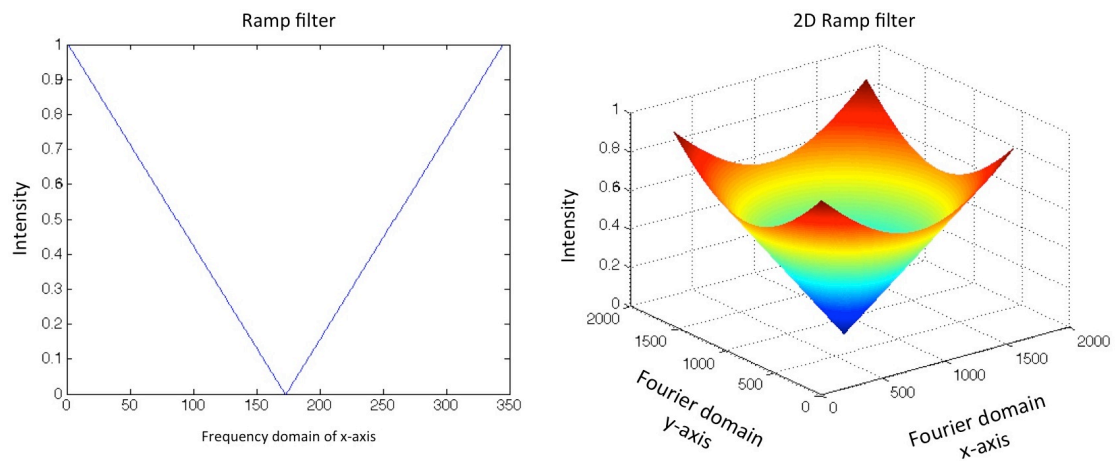


Figure 79 Conversion from a 1D ramp filter to a 2D ramp filter.

The DFR could now be executed immediately at this point. The in-built MATLAB function of IFFT2 (inverse fast Fourier Transform 2D) was used to convert the frequency domain grid back to the two grids of integrated absorbance distribution (spatial domain). Cropping of the integrated absorbance distribution can now be done, as well as the determination of temperature and concentration distribution, as described in the previous method stated in FSR in Section 6.5. The final reconstructions can be seen in Figure 80.

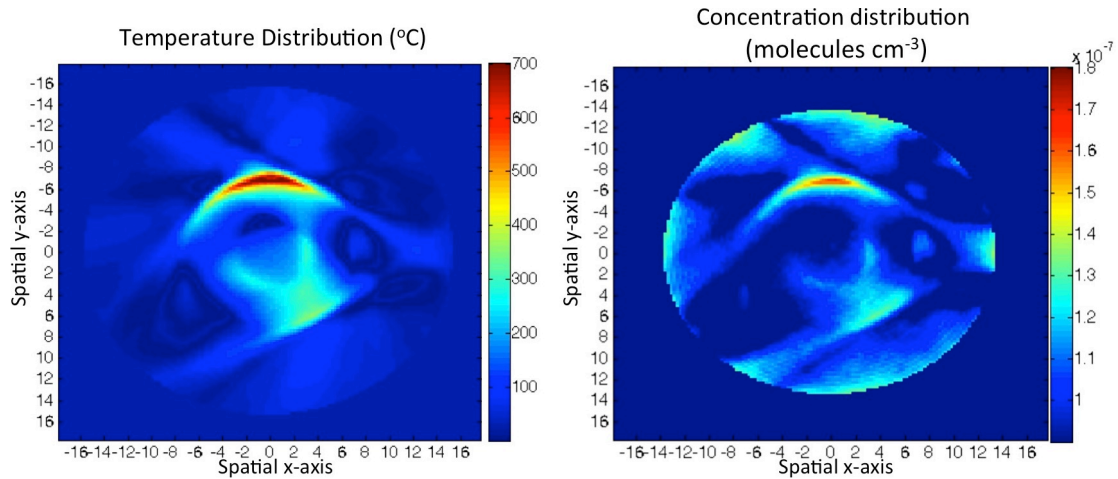


Figure 80 The temperature and concentration distribution sample images reconstructed by the DFR method.

6.7 Validations

6.7.1 Analysing the reconstructed image

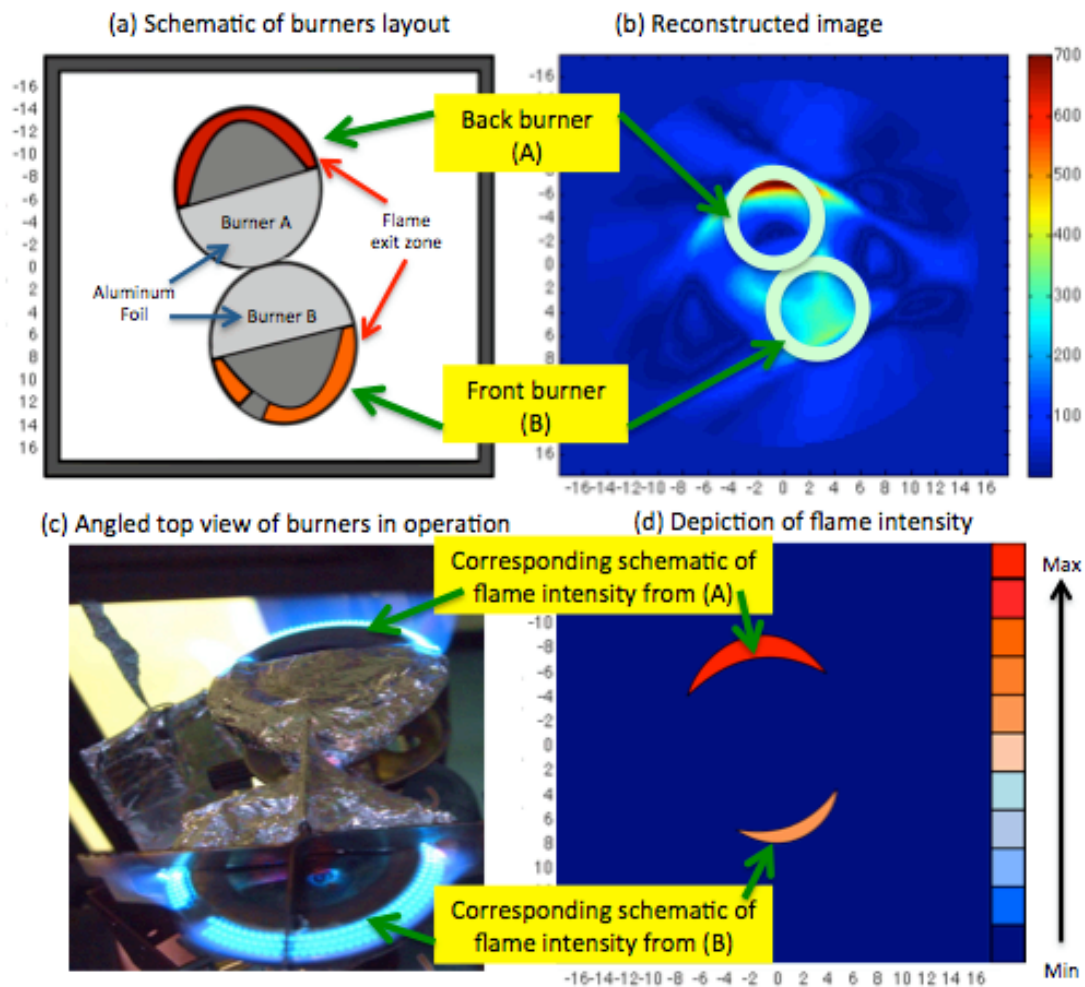


Figure 81 The correlation between the reconstructed temperature image with the schematics and photo of flame exit points of the burner. Burner 1 is the back burner, while Burner 2 is the front burner.

Figure 81 shows a schematic drawing of the burner layout with regards to the Rotator shown in Figure 81 (a) where the burners are placed front to back, with the aluminium foils touching each other creating an asymmetric pattern. An angled top view of the burners in operation is shown in Figure 81 (b). The picture was taken at an angle because the images were distorted from the heated air if the camera were placed directly above the setup.

It was essential that the thermocouple sampling be undertaken in the shortest time possible to ensure the flame intensity does not change throughout the thermocouple sampling.

The thermocouple images were constructed out of 10 by 10 grid cells, acquired on an average of 5 minutes. The reason for the crude sampling of the thermocouple was because it took too much time to create a denser thermocouple grid. The burner gas output fluctuates over time even at the same opening of the fuel regulator due to the decreasing pressure in the gas canister.

The lighter fuel also tends to burn first resulting in a change of fuel composition over time and thus affecting the intensity of the flame.

The cells were sampled individually using the thermocouple and executed by touching the tip of the thermocouple onto the optical plane. Guides were installed at the top and sides of the Exoskeleton to aid accurate placement of the tip of the thermocouple to the correct cells and distance away the burner surface. The optical plane was located 1cm above the surface of the burner plates.

As the thermocouple testing had to be executed quickly some shapes such as the curvature of the flame-heating patterns were lost in its representation as shown in Figure 81 (c). An observed image of the actual flame shape and location is drawn in Figure 81 (d) for easier comparison of heated areas.

The thermocouple sensor used for the validation process was Tenma 72-2065A. Its technical specification includes a measuring range between -50°C to 1300°C with an accuracy (non-inclusive of the thermocouple error) of $\pm 0.3\%$ of the final reading $+1^{\circ}\text{C}$. A type K nickel based thermocouple was used, however the accompanying alloy is unknown, but is usually either chromium or aluminium. The accuracy of this thermocouple is usually between $\pm 2.2^{\circ}\text{C}$ and $\pm 0.75\%$.

6.7.2 Validation using radon slices and thermocouple

The first validation test involved comparing the reconstructed image with the original experimental data. The second test involves the validation of the reconstructed temperature distribution with thermocouple sampling of the optical plane.

Typical theoretical validation or goodness of reconstruction involves extracting the x-axis values where y-axis = 0 cm and comparing the actual image with the reconstructed image.[205] However this was not possible as the actual data/spatial distribution was unknown. Therefore, another option was to use the available line- of-sight data at a chosen angle of projection, (theta at 0 degrees was used in this case). However, the line-of-sight data within each sinogram slice was populated by linear interpolation due to sparse data sampling per projection (Radon) slice as discussed earlier in Section 6.2. Therefore, the line of sight at theta 0 could only be used as a rough approximation of reconstruction goodness.

- Filtered Back Projection (FBP)

The FBP Radon slice validation is shown in Figure 82. Figure 82 (a) depicts the numerical comparison of the interpolated data of Radon slice at projection angle 0 of the original against the reconstructed version. The first point to note out of this comparison is shown in Figure 82 (b), that the areas outside the circle were considered inaccurate. This was because the data acquisition was only conducted inside the circle, and everything outside the circle was smeared data in the back-projection process. Therefore the further away from the central point of the x-axis in Figure 82 (a), the more errors it accumulated from the areas outside the circle. The information taken outside the red box is ignored for comparison.

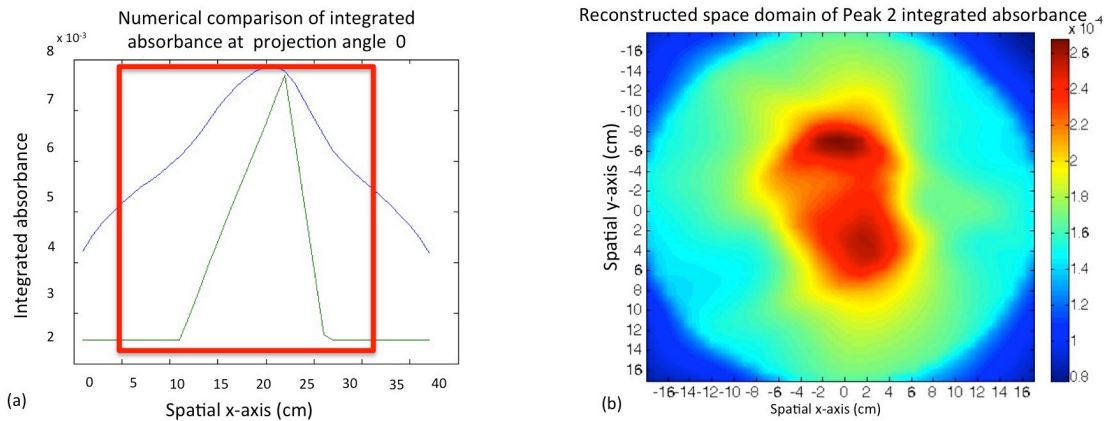


Figure 82 (a) The numerical comparison of experimental (green) integrated absorbance at radon slice of projection angle 0 with Filtered Back Projection method reconstructed (blue) integrated absorbance at radon theta 0. (b) The reconstructed integrated absorbance image of Peak 2 that was used for the validation process.

The trend of both original and reconstructed Radon slices in Figure 82 (a) appears to be similar, except that the reconstructed data lacks the sharpness the original data exhibits. The sharpness of the reconstructed image in Figure 82 (b) also seems to exhibit this blurring, labelled as “dishing”, which is typical of this method if executed on known phantoms. [205] The maximum temperature reconstructed from filtered back projection was 98°C, under the expected maximum temperature of 710°C from the thermocouple readings as shown in Figure 83.

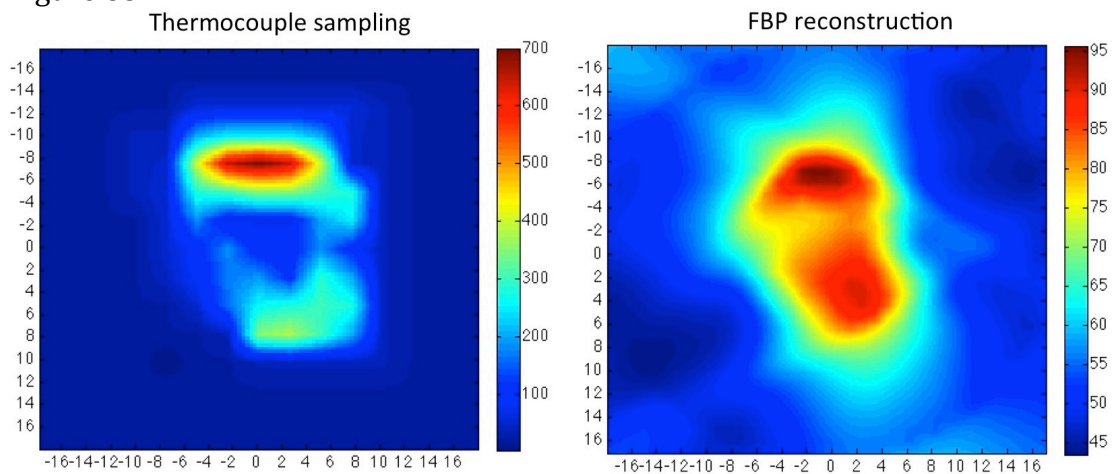


Figure 83 Comparison of thermocouple sampling of the optical plane with FBP reconstruction presented in (°C). Note the difference in temperature scale of both images.

○ Fourier Slice Reconstruction (FSR)

Using the same numerical comparison on the FSR method shown in Figure 84 (a), the Radon slices yields much closer values between original and reconstructed data as compared to the FBP method shown in Figure 82 (a). There is an increased sharpness of the image constructed in Figure 84 (b), which could also be seen in the more angular trends shown in the numerical comparison Figure 82 (a).

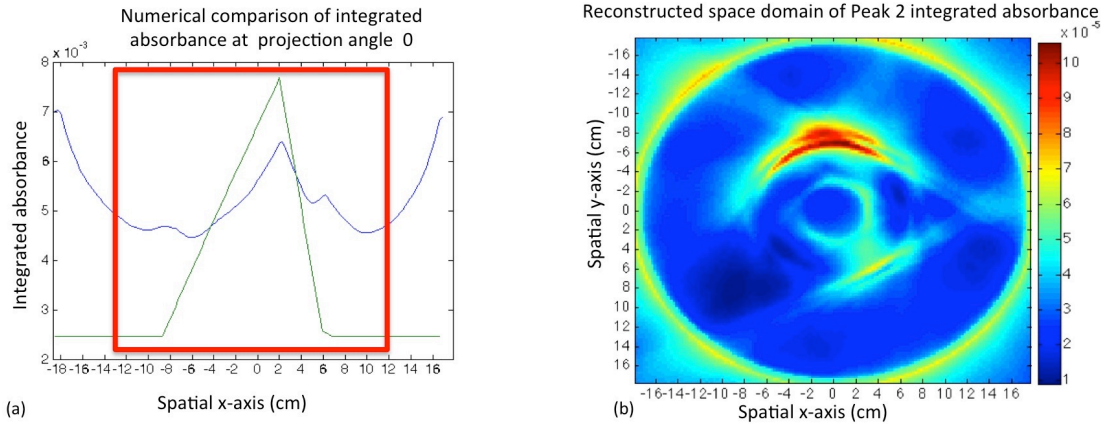


Figure 84 (a) The numerical comparison of experimental (green) integrated absorbance at radon at theta 0 with Fourier Slice Reconstruction method reconstructed (blue) integrated absorbance at radon theta 0. (b) The reconstructed integrated absorbance image of Peak 2 that was used for the validation process.

The original and reconstructed Radon slices are still not a close fit as shown in Figure 84 (a), and it might have been attributed to the back-projection process still used in this method. The maximum temperature of reconstructed image was a closer match to the values of thermocouple sampling. The maximum temperatures reconstructed at 590 °C while the thermocouple validated temperature sampled at 710°C as shown in Figure 84. Although the image pattern produced by the FSR method is much sharper than the FBP, and matches the thermocouple and visual heat trends, the quantitative values are still not accurate and differ from thermocouple validation by 120°C.

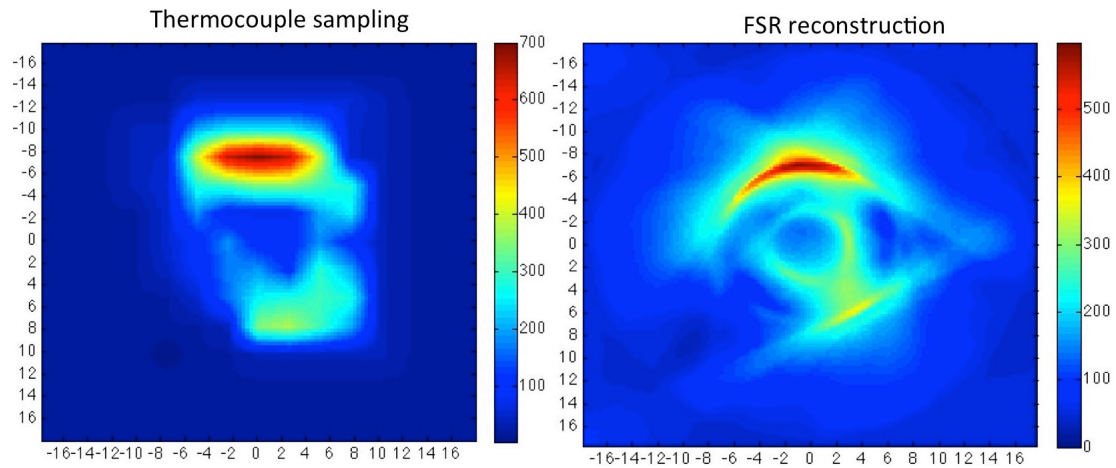


Figure 85 Comparison of thermocouple sampling of the optical plane with FSR reconstruction presented in (°C). Note the difference in temperature scale of both images.

○ Direct Fourier Reconstruction (DFR)

The comparison of Radon slices of the original experimental data and reconstructed by the DFR method yields the closest to the original experimental values compared to the previous methods as shown in Figure 86 (a). Figure 86 (b) also seems to exhibit the least amount of flaring and vertical artefacts apparent in Figure 82 (b) and Figure 84 (b).

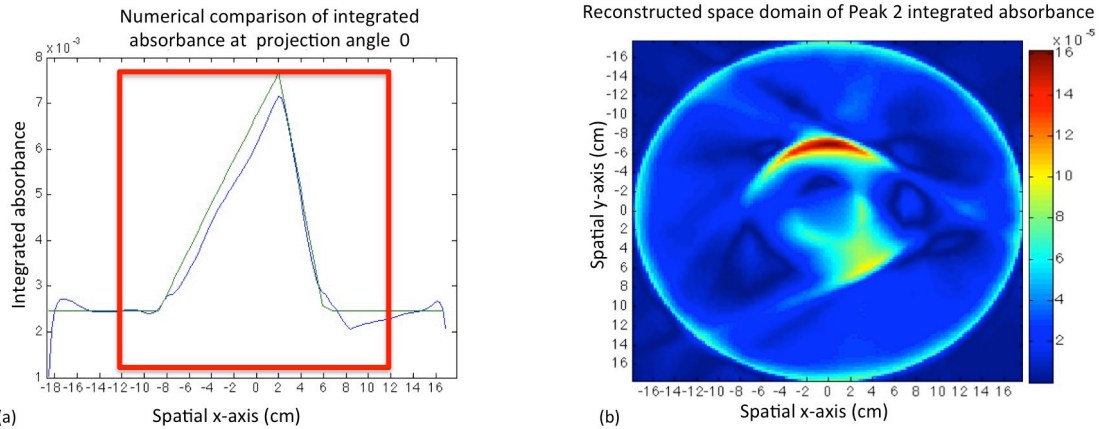


Figure 86 (a) The numerical comparison of interpolated (green) integrated absorbance at radon slice of projection angle 0 with Direct Fourier Reconstruction method reconstructed (blue) integrated absorbance at radon theta 0. (b) The reconstructed integrated absorbance image of Peak 2 that was used for the validation process.

The thermocouple validation of the DFR is the closest to the validated maximum temperature spike of reconstructed 705 °C to the expected thermocouple readings of 710°C as shown in Figure 80. The small temperature difference may be attributed to a small error in reconstruction as well as a change in temperature output from the burners during the 5 minutes of thermocouple validation.

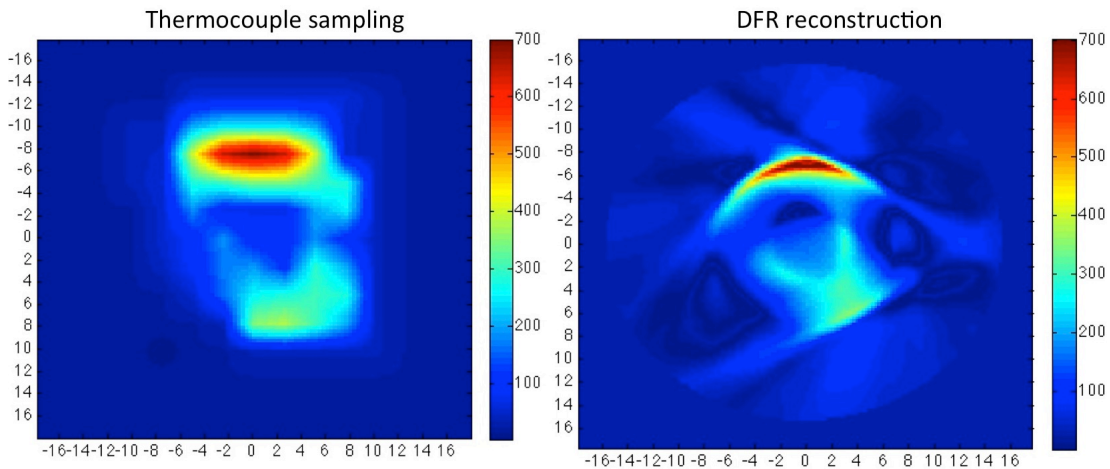


Figure 87 Comparison of thermocouple sampling of the optical plane with DFR reconstruction presented in (°C). Note the difference in temperature scale of both images.

6.7.3 Phantom validations

Each burner surface was individually covered with aluminium foil to create an asymmetrical effect during image reconstruction. In addition, they were placed back to back (with foil portions touching each other as shown in photographs on the extreme right column in Figure 88) to increase the variation of shapes formed. The locations of the burners were highlighted in translucent red rings in both thermocouple samplings and the DFR reconstructions. A schematic simulation of the flame pattern with a colour code is included beside each photograph to improve clarity of flame shape and intensity.

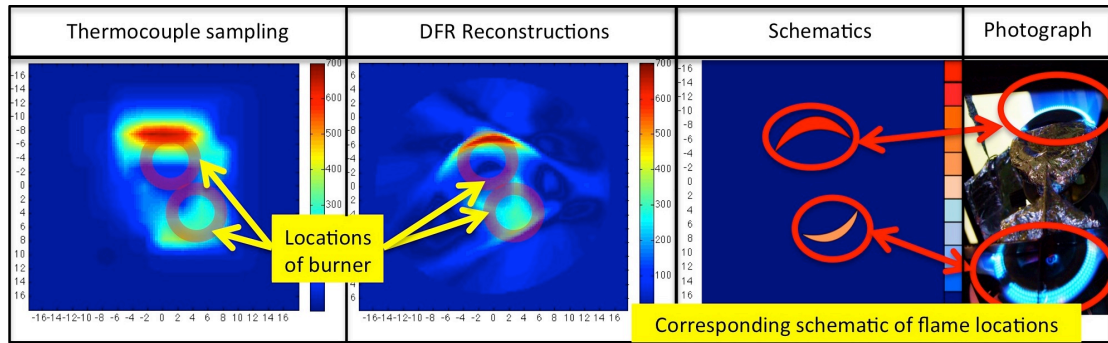


Figure 88 Depiction of flame patterns via photograph and schematic, compared to thermocouple sampling with image reconstructions for a sample scenario.

Each scenario in Figure 89 shows a different configuration. Scenario A depicts both burners activated, with the back burner set at notch 4 and front burner set at notch 2. Scenario B shows the back burner set at notch 3 with front burner at notch 0. Scenario C shows the back burner at notch 0 and the front burner at notch 4. Each of the scenarios were spaced 1 hour apart to prevent residual heat from a burner which is turned off but still radiating heat from the previous experiment.

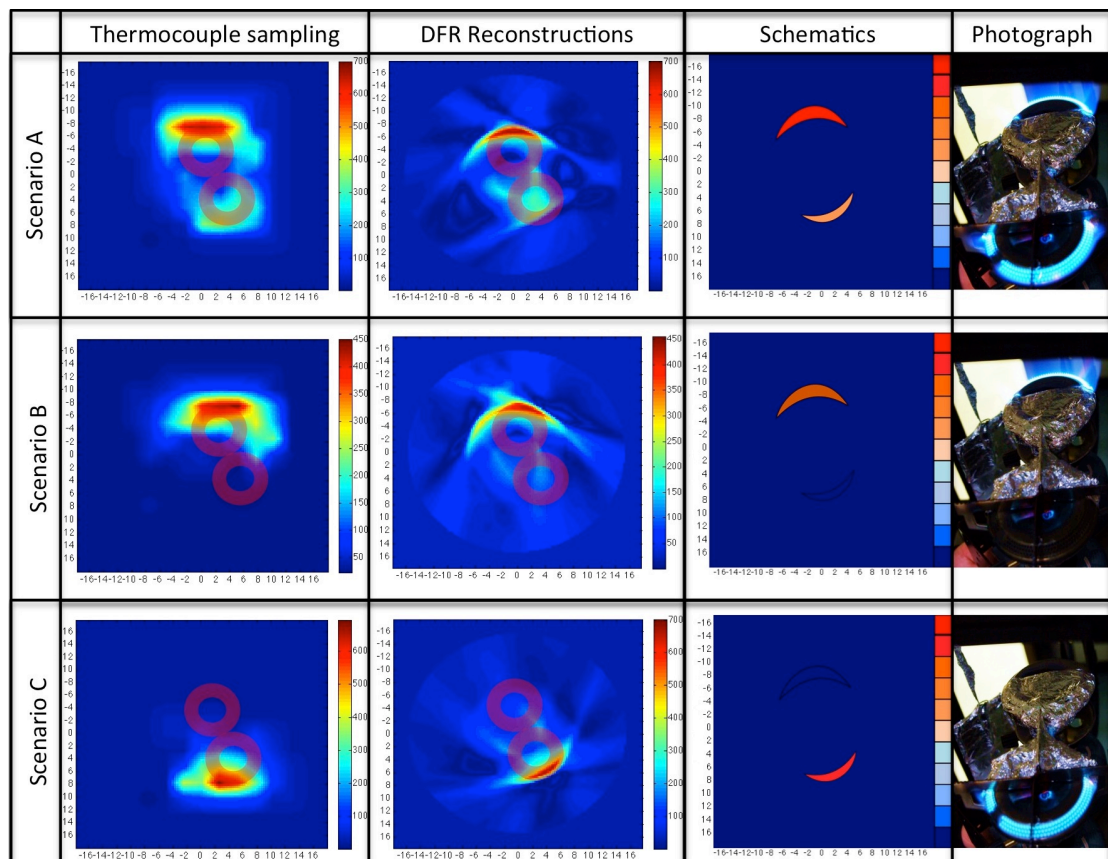


Figure 89 Three different scenarios with different flame patterns. Scenario A depicts both burners in operation, B with the back burner in operation and front burner off and C with back burner off and front burner in operation.

Thermocouple validations were provided for each flame variation scenario, constructed from a 10 by 10 grid using a thermocouple. They were used to compare and confirm with the image reconstructions in terms of flame

locations, presence/absence as well as temperatures. Thermocouple validations were sampled with only 100 cells (10 by 10) for speed to minimise the time interval from experiment and validations, the spatial resolution of the validation is crude and could only depict the generic locations and provide maximum temperatures of the flames.

The reconstruction results were generated using the DFR algorithm with 700 zero padding. For each scenario, the temperatures were also within $\pm 5^{\circ}\text{C}$ of the thermocouple validations. As seen in Figure 89, for each flame scenario, the image was reconstructed faithfully with regards to both flame locations and its temperature.

6.8 Simulations of varying data sampling conditions

Spatial resolution depicts the amount of information the reconstructed image holds from its original counterpart. The spatial resolution is dependent on many factors, from the reconstruction algorithm to projection geometry. However in designing this system based on the available equipment, many parameters such as geometry, laser-scanning frequency, distortions of studied space and measurement time are either limited or pre-determined. However, a simulation can be carried out by increasing the spatial resolution of the reconstructed image by increasing the density of data acquisition. Here, these simulations were focused on calculating the standard deviations and relative mean errors, which were not possible to do in the actual experiments.

- Simulation based on experimental data sampling conditions

First, a simulated image was created, comprised of a 37 by 37 grid cell configuration, totalling up to 1369 pixels as shown in Figure 90 (a) and labelled as Phantom. The primary background value used was 0.0171, which corresponds to 300 K and shown in dark blue. Two simulated heated blocks of different size were placed inside the Phantom. The first smaller heated phantom block was 18 pixels large and is shown in teal. It was set at ratio value 0.0343, corresponding to 480 K. The second larger heated phantom block in red made of 48 pixels was set at ratio value 0.0573, corresponding to 560 K. To imitate experimental conditions, the sinogram slices for the 3 methods have been altered to sample exactly as the laser configuration of the tomography setup shown in Section 6.1, where only 4 available data per projection slice, and bounded to room conditions on the extreme ends of the slice. Similar linear interpolation was also conducted. The number of projection slices were set at 360, which was 0.5-degrees step size.

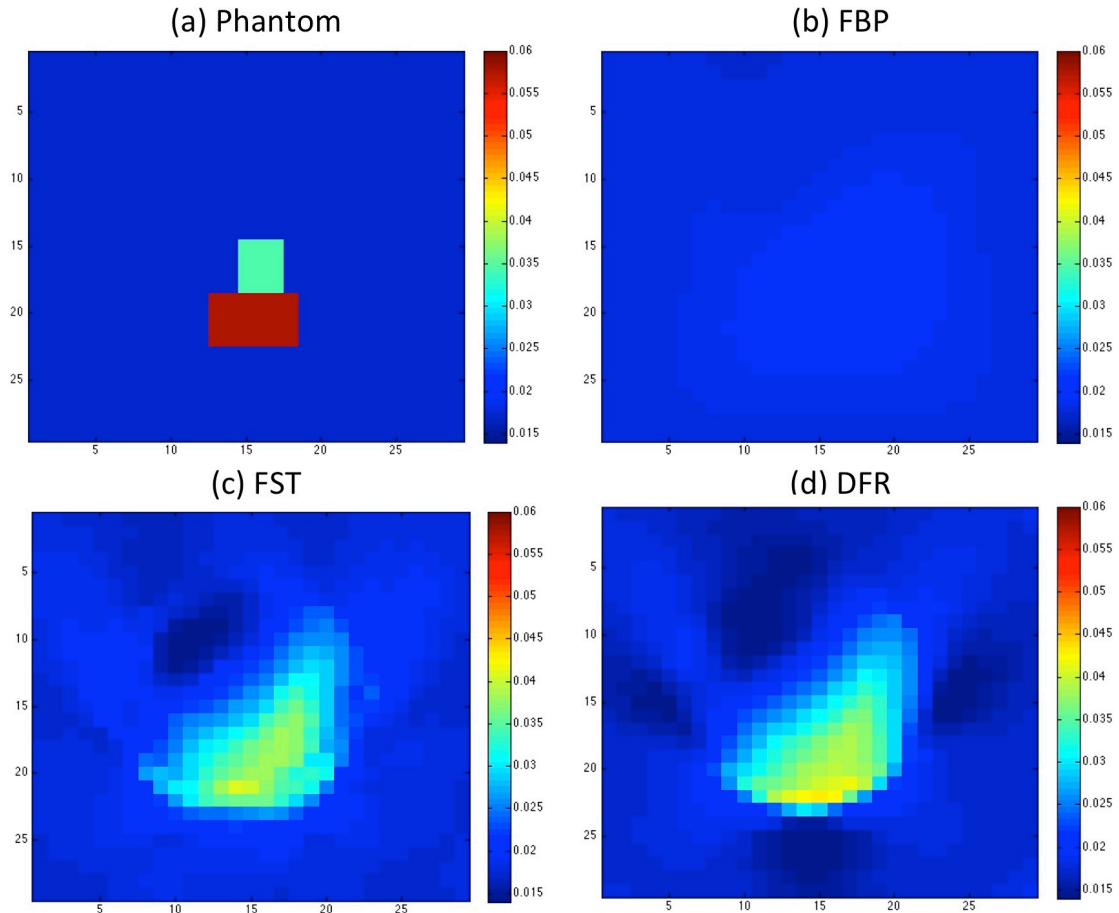


Figure 90 The comparison of reconstruction methods with a Phantom image. The reconstruction methods are based on sampling the original Phantom under experimental conditions of 4 known data per projection slice.

The first observation of the interpolated reconstructed images in Figure 90 was that the images were significantly blurred with respect to the Phantom. The FBP method in Figure 90 (b) suffered from blurring of the image consistent with this method with highly suppressed values, similar to the discussions in Chapter 6.4. The relative mean errors similar to what An et al[13] measured were also calculated, and the mean relative error of the FBP method was 13.78% with an SD of 0.009.

Both FSR and DFR shown in in Figure 90 (b) and (c) respectively, yielded similar reconstructed images. The two methods also had suppressed values in the heated blocks, although closer to the Phantom image compared to FBP. The overall image mean relative error of the FSR is 10.96% with a SD of 0.0085 while the overall image mean relative error of the DFR is 8.12% with a SD of 0.0066.

- Simulation based on densely packed data sampling conditions

In this scenario, the number of beams per projection slice was increased to 55 and spaced 0.68 cm apart. Using the same number of projections, the reconstructed image of the simulated Phantom could be seen in Figure 91. It can be seen that the FBP in Figure 91 (b) reconstruction still suffers from suppressed values and blurring, a resulting consequence from the back-smearing process. This process forces the higher valued pixels to be smeared across its

neighbouring cells, causing the supposedly low value pixels to be numerically larger, and the supposedly high value pixels to be numerically suppressed.

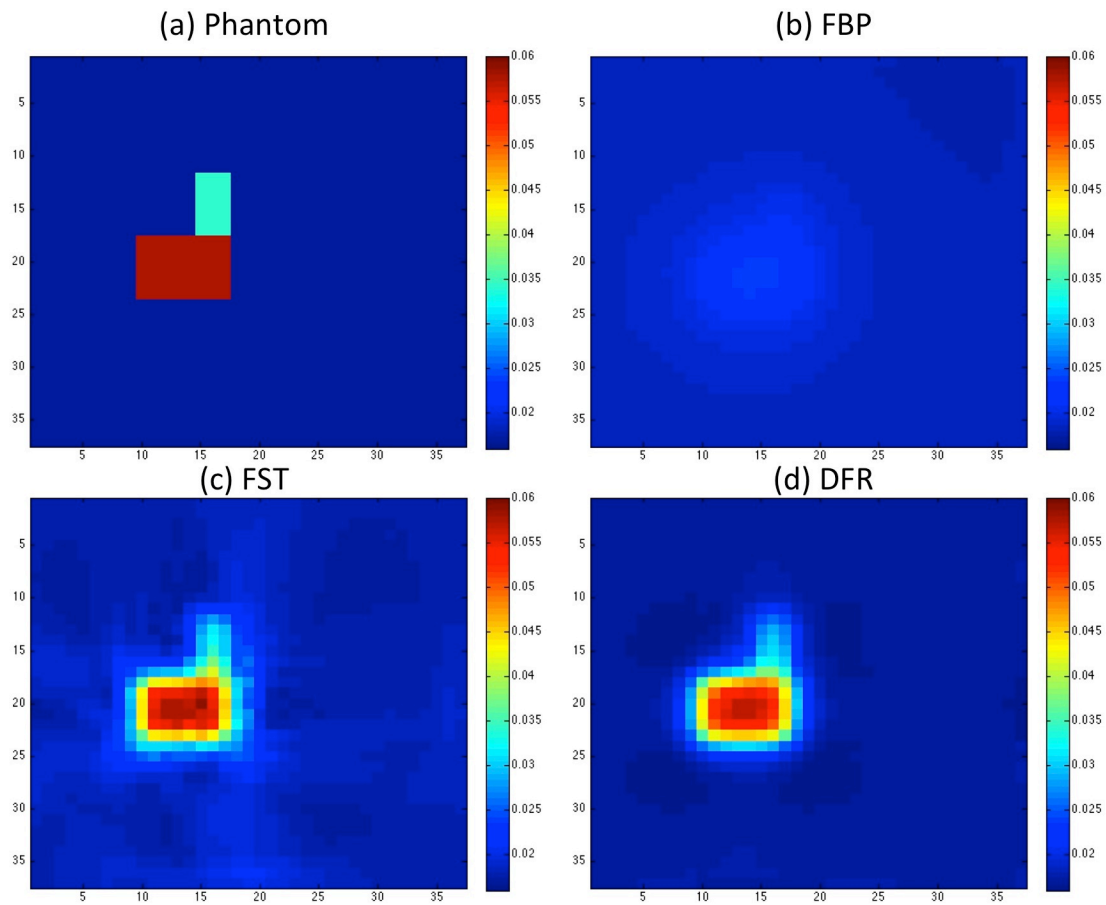


Figure 91 The comparison of reconstruction methods with a Phantom image. The reconstruction methods are based on full sampling of the original Phantom, and have a data-sampling ratio of 55 data to 37 cm per radon projection angle. The ratio to colour representation scale is set to be the same for direct value comparison.

The FSR and DFR, shown in Figure 91 (c) and (d) respectively, produced reconstructed images similar to the original Phantom, numerically and visually. It was noticeable that both reconstructed methods still yielded a blurred image, albeit significantly sharper than the FBP method. It was also noted that the FSR method in Figure 91 (c) generated a noisier image than the DFR method, with noise significantly present in the surrounding background of the heated blocks.

The pixel-by-pixel standard deviation (SD) was calculated for each of these methods and FBP was calculated with a SD of 0.0069, FSR with a SD of 0.0033 and finally DFR with a SD of 0.0028.

The mean relative error of each method was also calculated. The FBP method performed the worst, as expected of the suppressed reconstructed image with an overall image relative mean error of 8.2%. Both FSR and DFR reconstructions indicated faithful reproduction of the original Phantom, with FSR's overall image relative mean error of 5.9% and DFR at 1.3%. The difference in relative mean error is expected between FSR and DFR because of the noisier background in the FSR reconstruction.

It is worth noting again at this point that the FBP reconstruction shown in Figure 91 (a), if displayed with its own colour contrast scheme; would yield a similar image to the other two as shown in Figure 92.

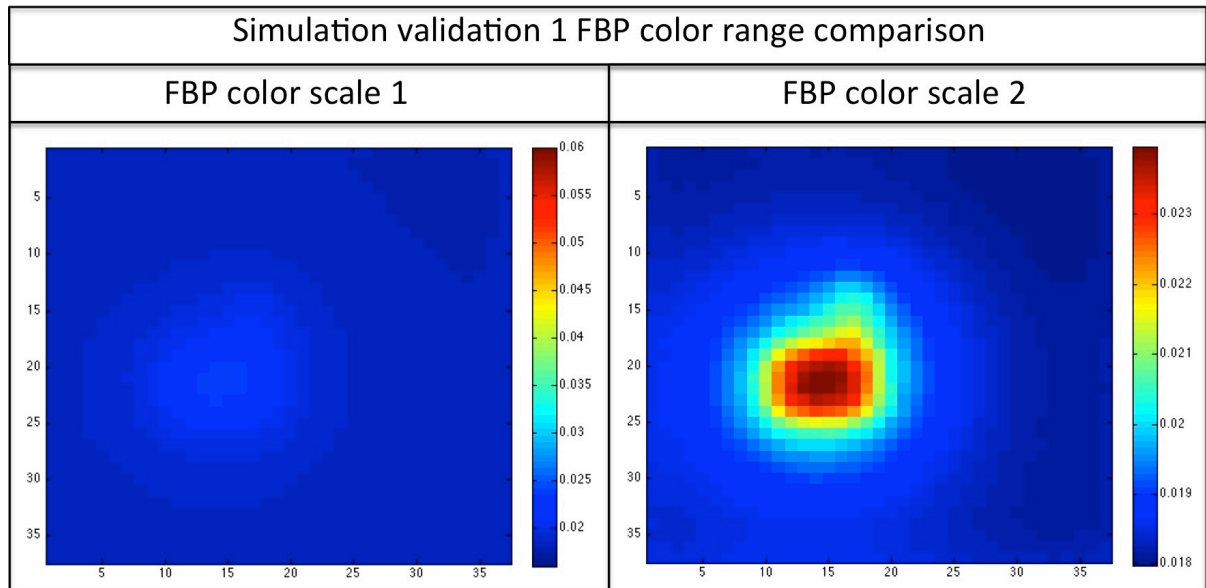


Figure 92 Both (a) and (b) depicts the same exact Filtered Back Projection reconstructed image, with a different ratio to colour representation scale. In (a), the ratio value to colour scale is consistent as Figure 91, while in (b) is set with respect to contrast base on its own variation in numbers within the image.

The FBP method was the fastest reconstruction method with a sinogram input of 360 projections with 55 data per projection slice; the reconstruction took an average of 3 s for complete reconstruction. On average, 70% of the reconstruction time was spent on the back smearing process. The FSR was the slowest method of reconstruction, taking an average of 54 s for a complete reconstruction. Dissecting the program, the time it took for the back smearing process was approximately 50 % of its total reconstruction time. This would make sense as this method requires heavier manipulation of matrix data, from zero padding and executing Fourier transforms. There was also more data to back smear per slice due to the zero padded slices. The DFR took an average of 41 seconds to complete. The reason the completion time was shorter than the FSR may be due to the fact that instead of the back smearing process, it makes use of physically allocating values of the projection slices to the pre-allocated empty grid.

6.9 Comparison of methods

Three methods of reconstruction (Filtered Back Projection (FBP), Fourier Slice Reconstruction (FSR) and Direct Fourier Reconstruction (DFR)) were studied for several scenarios of thermocouple validation. The outcomes of the three scenarios were fairly constant throughout.

Firstly, the FBP reconstruction was sufficient for detecting a blurred image of the original image, without achieving accurate numerical values, in this instance, temperature.

It could be argued that other popular and conventional filters like the Ram-Lak or the Shepp-Logan could be used to sharpen the image instead of simply using the ramp filter. However, unlike conventional situations where the sharpness of an image is the primary concern, equal attention is required to reconstructing the image with numerically correct cells as well. With that in mind, the simplest filter was used to ensure that the final numerical distributions of the image had not been over filtered and that numerical values were sacrificed for visual smoothness.

Next, the FSR method yielded sharper images than the FBP but produced a certain amount of blurring as compared to DFR. The supposedly high value pixels were still numerically suppressed. It was suspected that the reason why it was still reconstructing lower than expected temperatures was because back-smearing process was still part of its reconstruction protocol. A large number of artefacts were noticed that formed near the corners of the burner flame locations. The artefact streaks circled in green in Figure 93 were commonly identified as beam hardening, usually present in areas of high attenuation.

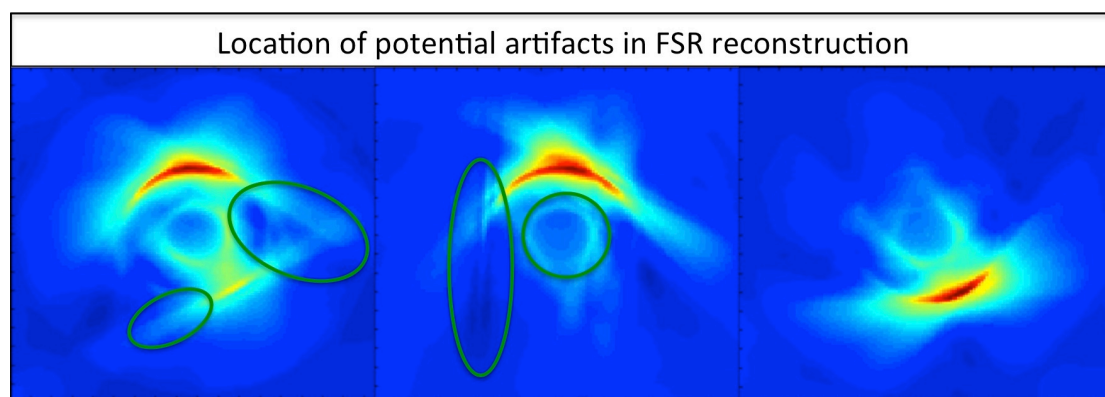


Figure 93 Sample of streaks of artefacts known as beam hardening, circled in green. The last image is left untouched for uninhibited viewing.

Finally the DFR performed the best in the validation test, giving approximately $\pm 5^{\circ}\text{C}$ of the thermocouple validation. It exhibited the sharpest image out of the three methods, which may be attributed to the fact that back smearing is not involved within its reconstruction protocol.

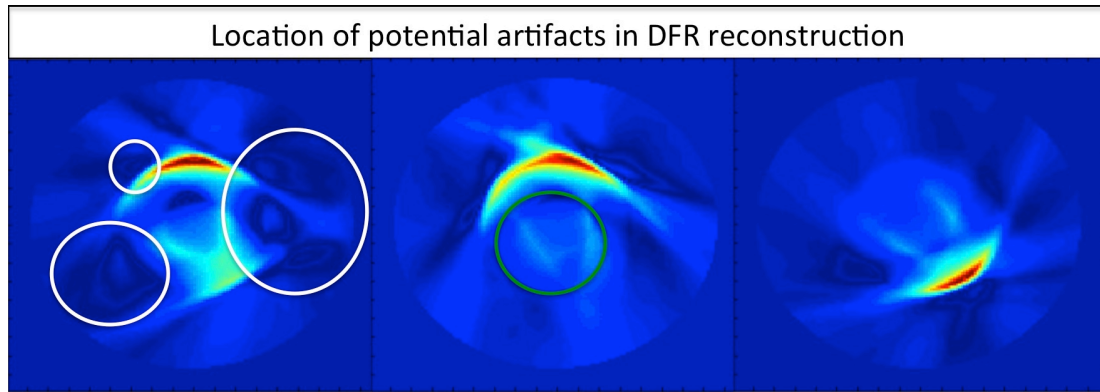


Figure 94 Sample of potential helical artefacts are circled in white. Sample of streaks of artefacts known as beam hardening are circled in green. The last image on the right is left untouched for uninhibited viewing.

The DFR method did yield several different potential artefacts as shown in Figure 94. The green circle marks the presence of streaks or beam hardening. However the effect of beam hardening seems less severe than the FSR method. There were however, also presences of ring-like structures formed in the reconstruction, circled in white. It was unclear whether these were artefacts or the reconstruction of heating pattern swirls. If they were artefacts, they might be classed as helical artefacts, caused by rapid change between the z-axis. This could be justifiable as with a high temperature output from the burners, the effects of convection currents would be very dominant in the area of study, causing a rise in these forms of artefacts.

6.10 Chapter summary

A summary of the comparison findings is compiled in Table 7. The DFR method achieved the sharpest image and the closest reconstruction to thermocouple validation. Even though there was the presence of some beam hardening artefacts and potential helical artefacts, the DFR was selected as the best method to carry out further tomography experiments.

Table 7 Summary table of reconstruction method comparison

Parameters	FBP	FSR	DFR
Blurriness	Very blur	Mild blur	Sharp
Numerical comparison of Radon transform	Bad match	Bad match	Good match
Ideal densely sampled simulation Standard Deviation test	0.0069	0.0033	0.0028
Experimental sampled simulation Standard Deviation test	0.0090	0.0085	0.0066
Ideal densely sampled simulation relative mean error test	8.2%	5.9%	1.3%
Experimental densely sampled simulation relative mean error test	13.78%	10.96%	8.12%
Reconstruction time	3 seconds	54 seconds	41 seconds
Temperature average difference from thermocouple	-529°C	-116°C	±5°C
Artefacts	None observed	Beam hardening	Beam hardening, potential helical

The discussion of the three reconstruction procedures for Filtered Back Projection (FBP), Fourier Slice Reconstruction (FSR) and Direct Fourier Reconstruction (DFR) were carried out, followed by a comparison of method validation using simulations and thermocouple measurements. Based on the summary comparison table, the method best suited to process the experimental reconstruction was the Direct Fourier Reconstruction method.

7 3D AND TEMPORAL TOMOGRAPHY RESULTS

7.1 Chapter overview

This chapter focuses on presenting the results of 3D and temporal experiments. In Section 7.2, the results of 3D reconstructions were initially presented as 2D measurements across the height axis. These slices were interpolated into a 3D matrix to be repackaged as 2D image slices as a function of height, moving along the x-axis and y-axis. The result of the temporal experiments (2D experiments with time) is presented in Section 7.3. Finally, the resolution of the images is discussed in Section 7.4 and the repeatability in Section 7.5.

7.1.1 Experimental conditions

Unless otherwise stated, the experimental conditions were conducted as stated in Section 6.1.1 and analysed using the Direct Fourier Reconstruction method, with a theta step of 0.5 degrees using 360 projections. The amount of zero padding was set at 700.

7.2 3D reconstructions

There are situations where 3D spatial information is more beneficial to a study compared to a 2D plane. Recreating the spatial distribution of desired parameters within a 3D volume of an environment could lead to more straightforward diagnoses such as the direct imaging of particular hot spots. The objectives of the 3D reconstruction was to extend the detection capabilities of the system by plotting temperature and concentration distribution within a 3D boundary.

Tomography used in medical applications often uses multiple 2D slices to diagnose a broken fracture by moving down the length of an arm, the vertical movement of the equipment setup will similarly mirror this process. There are two options of movement in the z-axis, the first where the observed space moving through a stationary optical plane, the other where the optical plane moves along the stationary observed space. In this instance, the decision to moving the optical plane was chosen based on the equipment architecture.

The experiment was conducted at 10 optical plane height levels with a step size of 1 cm between levels. The experiment begins at the optical plane being 1 cm above the burner plate surface depicted in Figure 95 (a). After the initial measurement was taken, the Carrier was lowered by 1 cm for another set of data acquisition until the last optical plane height depicted in Figure 95 (b). This motion is inversely representative of the optical plane being raised in steps of 1 cm above the object of study. Figure 95 (c) shows the process of the Carrier moving downwards, thus creating the difference in optical plane and a variation of the z-axis.

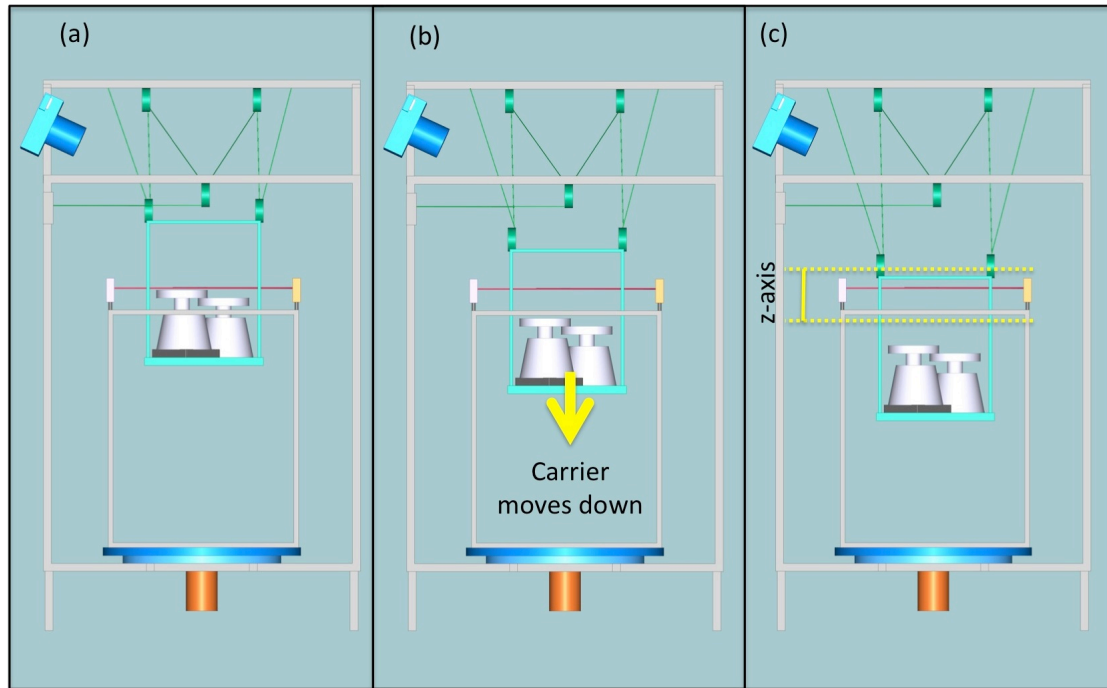


Figure 95 Visual representation, not drawn to scale, of how the Carrier moves down a stationary optical plane instead of the optical plane moving around the object of study. (a) The Carrier at position 1 (optical plane 1 cm above burners). The red line depicts the position of the stationary optical plane. (b) The Carrier moves down, thus lengthening the distance from the optical plane. (c) The z-axis that is shown here represents the total distance between first and final position of the carrier with respect to optical plane to flames.

The assumptions of the 3D experiment:

- To maintain constant flame intensity, the experiment was completed in less than 2 minutes and assumed that the gas output and flame intensity was constant within the experimental period. Flame intensity variation with time is discussed further in Section 7.5.
- The step size of 1 cm per measurement level was sufficiently small and to assume that there is a linear relationship between each slice. The changes of temperature in between each slice were deemed predictable enough to use linear interpolation.

The 3D experiment was conducted at an ambient temperatures of 19.3 °C, pressure of 101 kPa and a relative humidity at 87%.

The 2D reconstructions at varying height were also stacked on top of each other as shown in Figure 96. A larger view of the individual slices can be seen in Appendix 11.1. View-1 in Figure 96 shows all 10 slices stacked together, with each slice set at 75% transparency to simulate how it may look as a translucent volumetric space. View-2 in Figure 96 opens up the slices to show a clearer depiction of each slice. The maximum temperatures created by each burner in each slice have also been marked out. As expected, the bottom slice, which is closest to the flame, registered the highest temperature and decreases as the slices move further away from the flame.

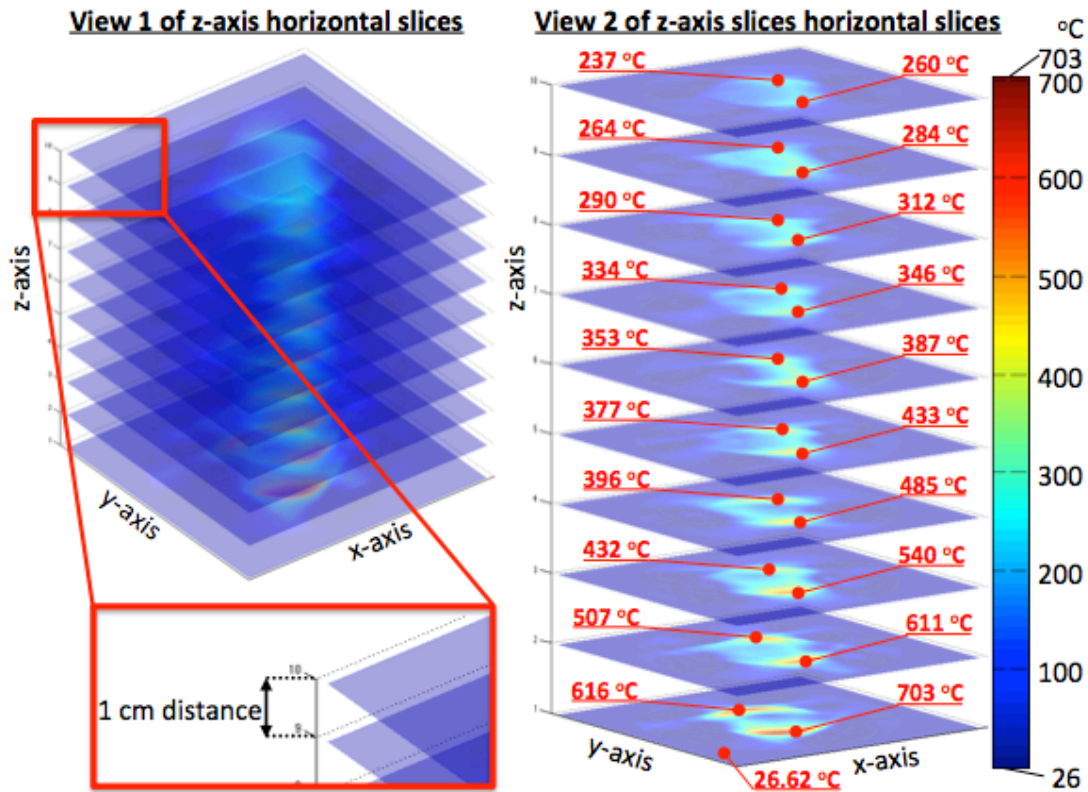


Figure 96 The individual reconstructed temperature slices vertically spaced 1 cm apart shown in 2 views. The slice at the bottom is the slice closest to the flames, which registers higher temperatures. View-1 depicts a tighter configuration of 75% transparent slices to simulate a translucent volume. View-2 shows similar 75% transparent slices with the perspective set to z-axis priority, with the maximum temperatures and locations by the two burners marked out.

The gaps between the slices in Figure 96 were linearly interpolated to form a 3D matrix, representing an imaginary volumetric space shown in Figure 97. Linearly interpolated vertical slices along both x-axis and y-axis can be generated from this 3D matrix, simulating the motion of vertical slices being measured as demonstrated in Figure 97.

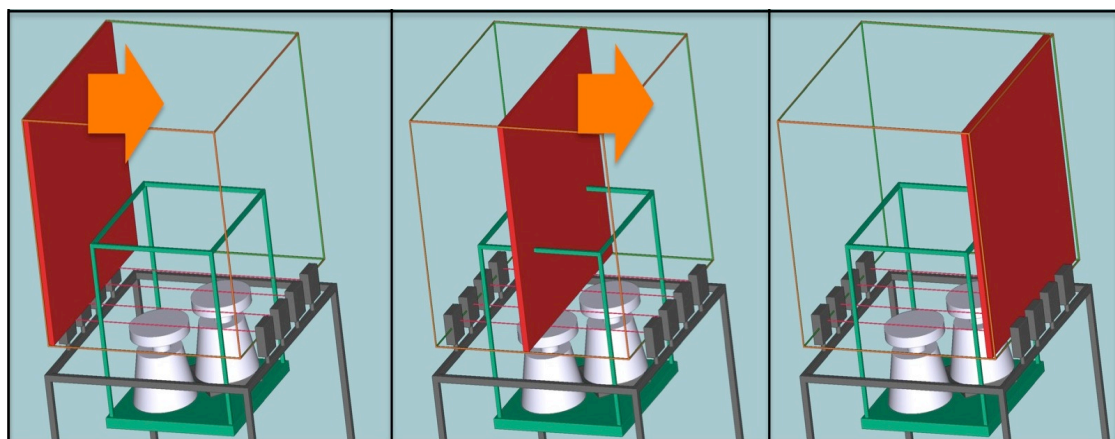


Figure 97 Visual representatives of the locations of vertical slices (shown in red) moving across the x-axis within the 3D boundary shown via the orange cuboid.

These vertical slice images were interpolated using MATLAB function of interp2 and were scaled with a factor of 4 using the “linear” method. Figure 98

represents the full range of the temperature vertical slices along the x-axis, from the left to right, x-axis (-17 cm) to x-axis (17 cm).

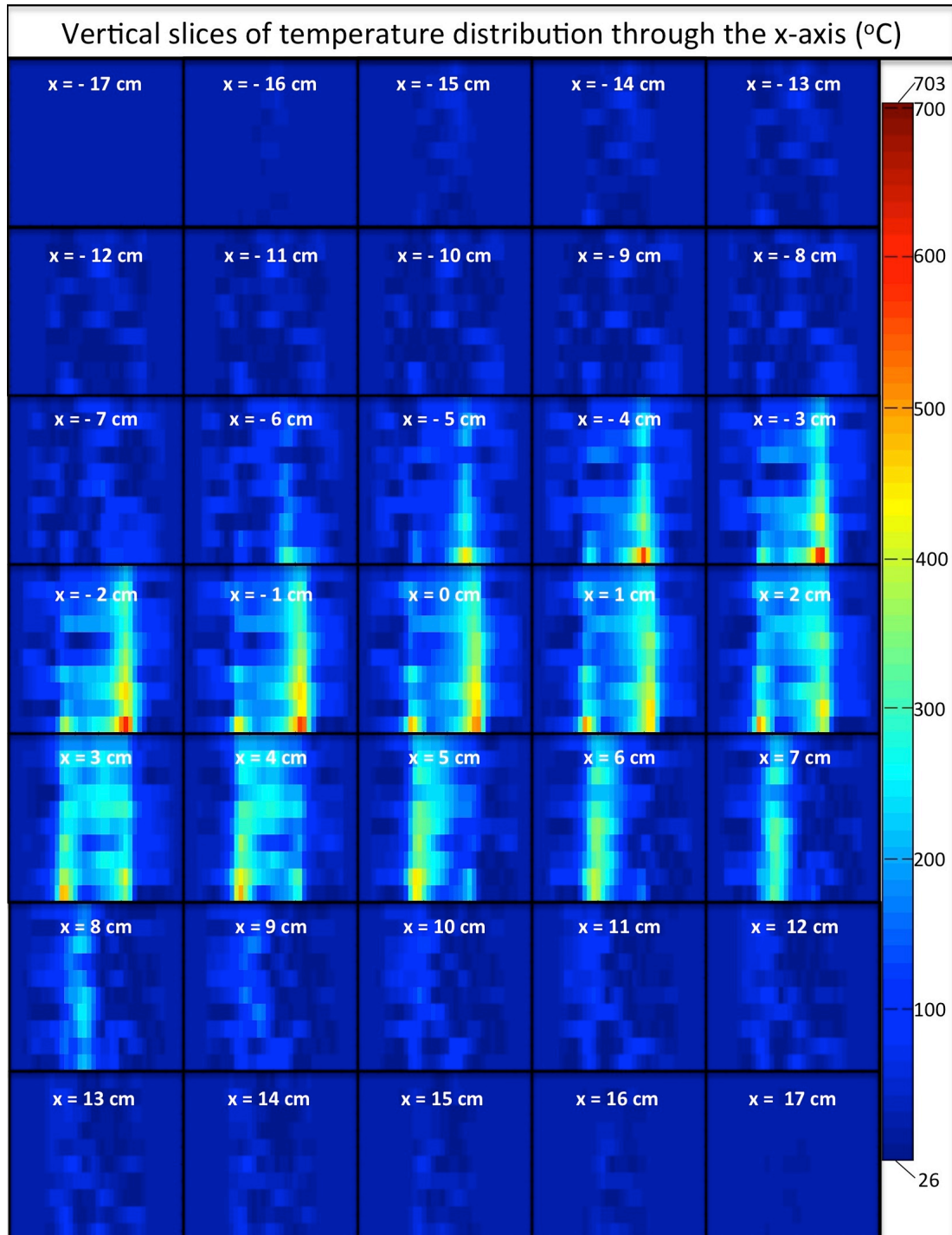


Figure 98 Individual vertical slices of interpolated temperature with respect to the x-axis, from -17 cm to 17 cm. Note that vertical slice of x-axis at -18 cm and 18 cm were omitted from this figure.

The full range of the vertical temperature slices down the y- axis of the volumetric block is shown in Figure 99.

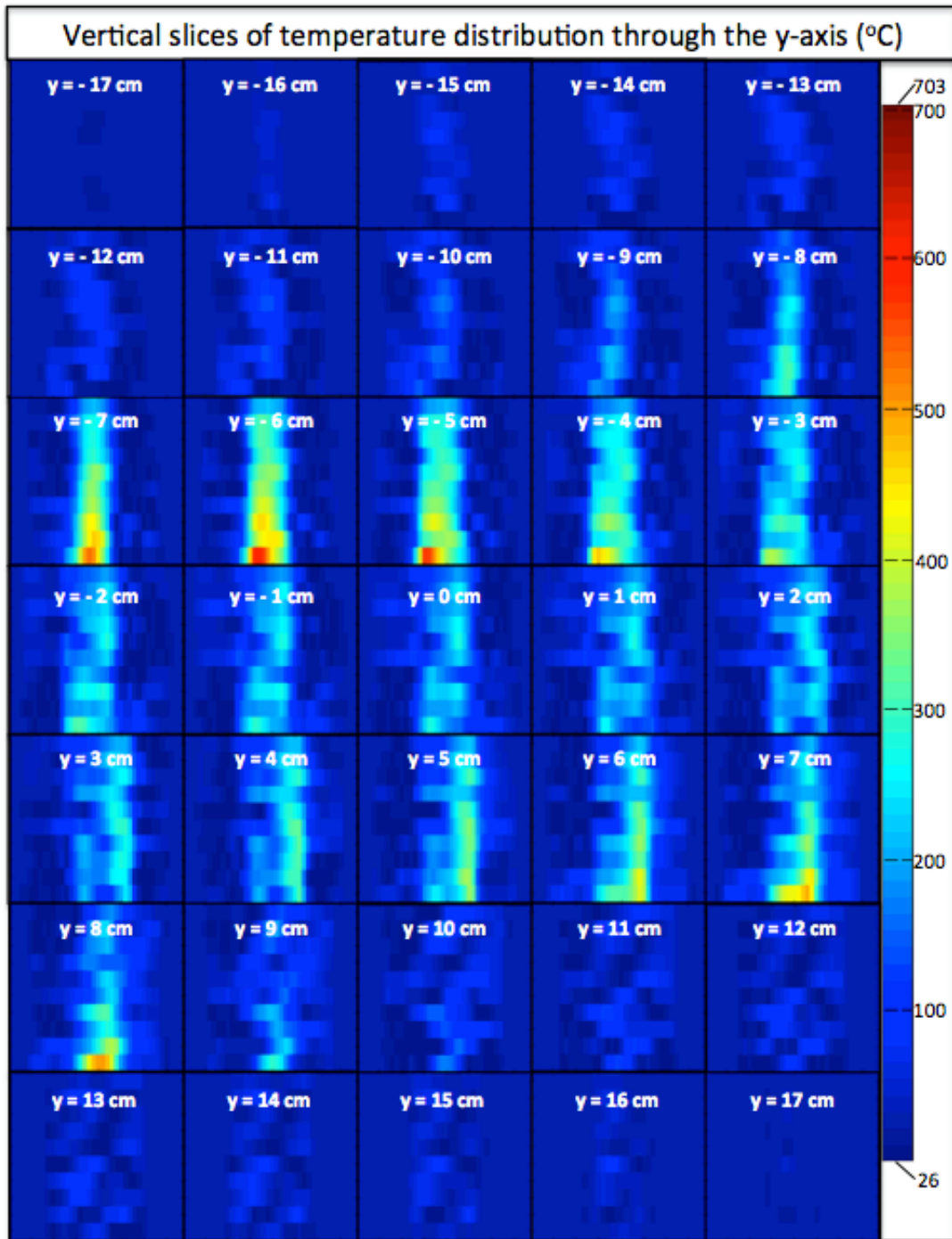


Figure 99 Individual vertical slices of interpolated temperature with respect to the y-axis, from -17 cm to 17 cm. Note that vertical slice of y-axis at -18 cm and 18 cm were omitted from this figure.

Figure 100 shows a simple comparison of vertical slices that are presented with respect to both x-axis and y-axis above the base horizontal slice (the horizontal slice closest to the flame). In Figure 100, 6 sample slices were extracted with respect to the dominant axis of study at -12.5 cm, -7.5 cm, -2.5 cm, 2.5 cm, 7.5 cm and 12.5 cm. Note that the information in the vertical slices was different depending on the axis of study. An enlarged comparison of sample slices at -7.5 cm, 0 cm and 7.5 cm are shown in Figure 101 and Figure 102.

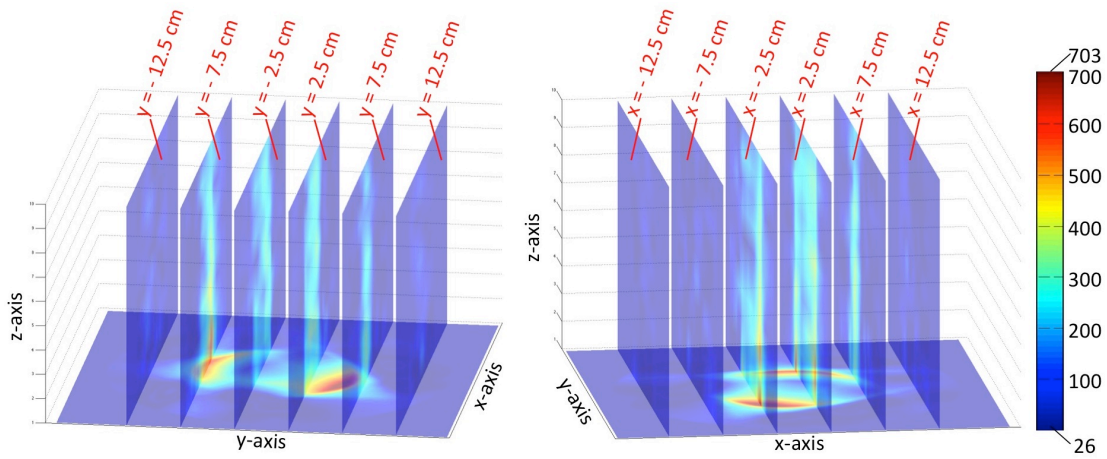


Figure 100 Sample of vertical temperature slices moving along the x-axis.

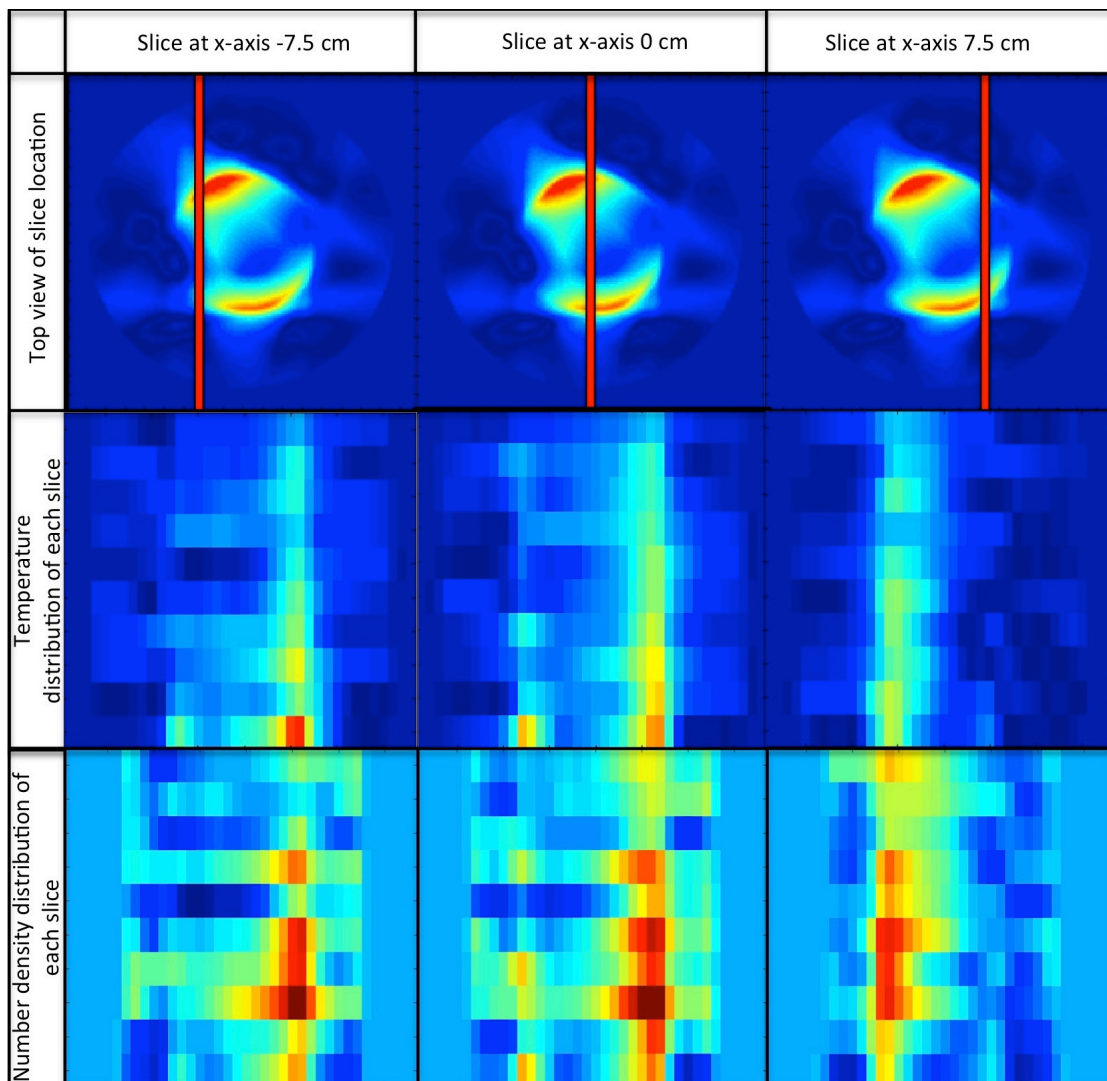


Figure 101 The location of the vertical slices is each shown on the top row as a red line superimposed on the bird eye view of the bottom most z-axis plane. The temperature and concentration vertical slices are individually shown below their slice location.

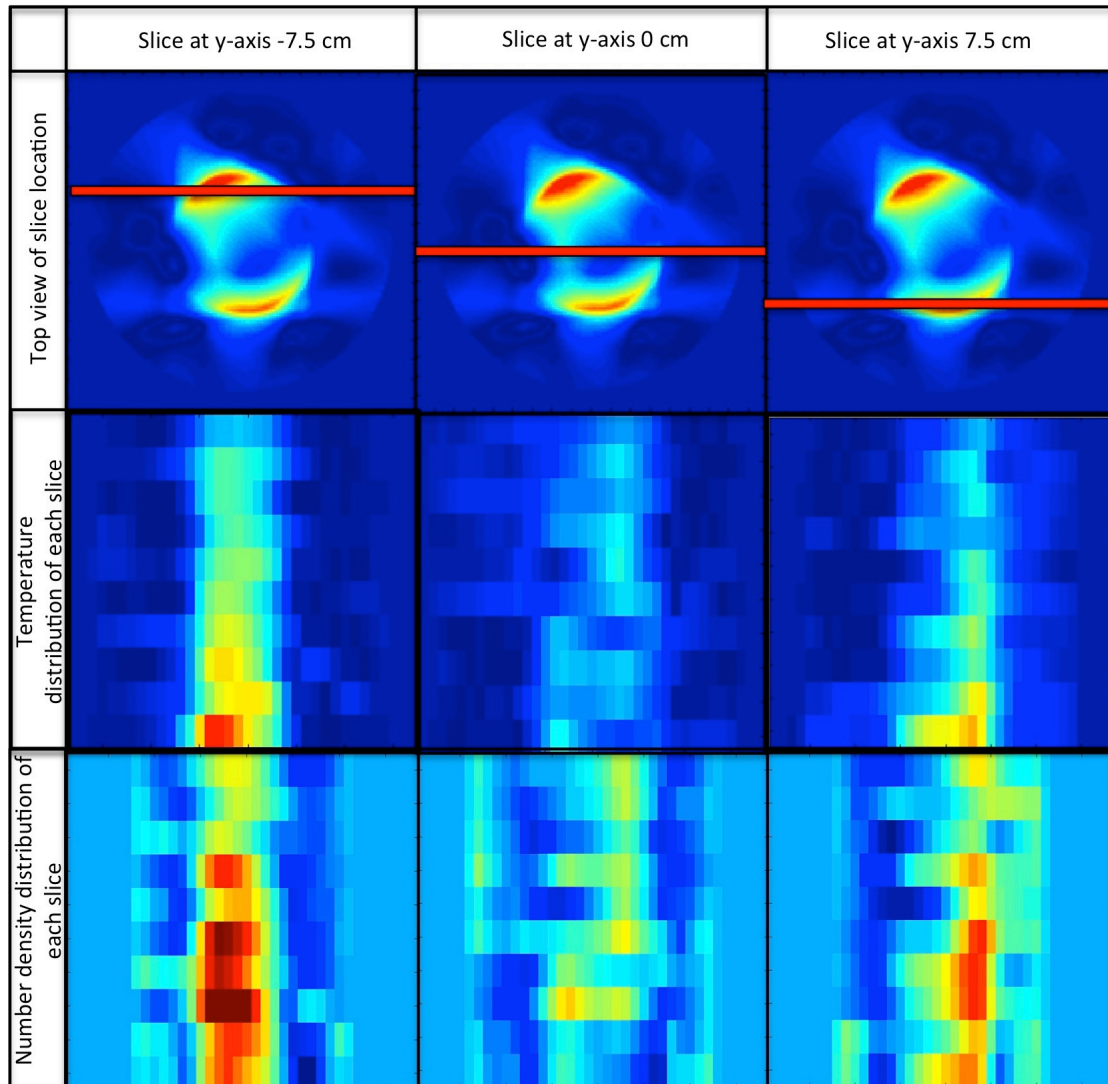


Figure 102 The location of the vertical slices is each shown on the top row as a red line superimposed on the bird eye view of the bottom most z-axis plane. The temperature and concentration vertical slices are individually shown below their slice location.

The first column in Figure 101 depicts the vertical slice image of x-axis at -7.5 cm, the second column at x-axis at 0 cm and the third column at an x-axis value of 7.5 cm. The first row depicts the location of the vertical slices via a red line with respect to the base flame image from the top (bird eye's view), the second row depicts the temperature distribution of each of the respective vertical slices within the column, whilst the final row depicts the concentration distribution of its respective column. The layout is similar in Figure 102, except that the vertical slices belong to the y-axis.

Note that between the two figures, the view from Figure 101 allows the user to view the cross-section and the presence of the two heaters as it moves along the x-axis, whilst in Figure 102, that information is not made available as it moves down the y-axis. However, a more detailed version of each flame can be seen instead. By changing the angle of perspective, different temperature and concentration patterns could be seen.

The total size of the volume constructed was 10 cm high and 37 by 37 cm. It is noted that the spatial resolution of the vertical slices was poorer (more "pixelated") compared to the horizontal slices as shown in Figure 101 and Figure

102. This is because the vertical slices are dependent on the spatial resolution of the horizontal slices but also on the number of original horizontal slices as well. However, the slices were interpolated with interp2 by power of 4 for smoothness. The vertical images from both the x-axis and y-axis were compiled over the base slice to form Figure 103. Each of these slices was set at 95% transparency and a total of 51 slices (vertical axis step size of 0.25 cm) were used from each axis to create a “translucent” volume of spatial temperature distribution.

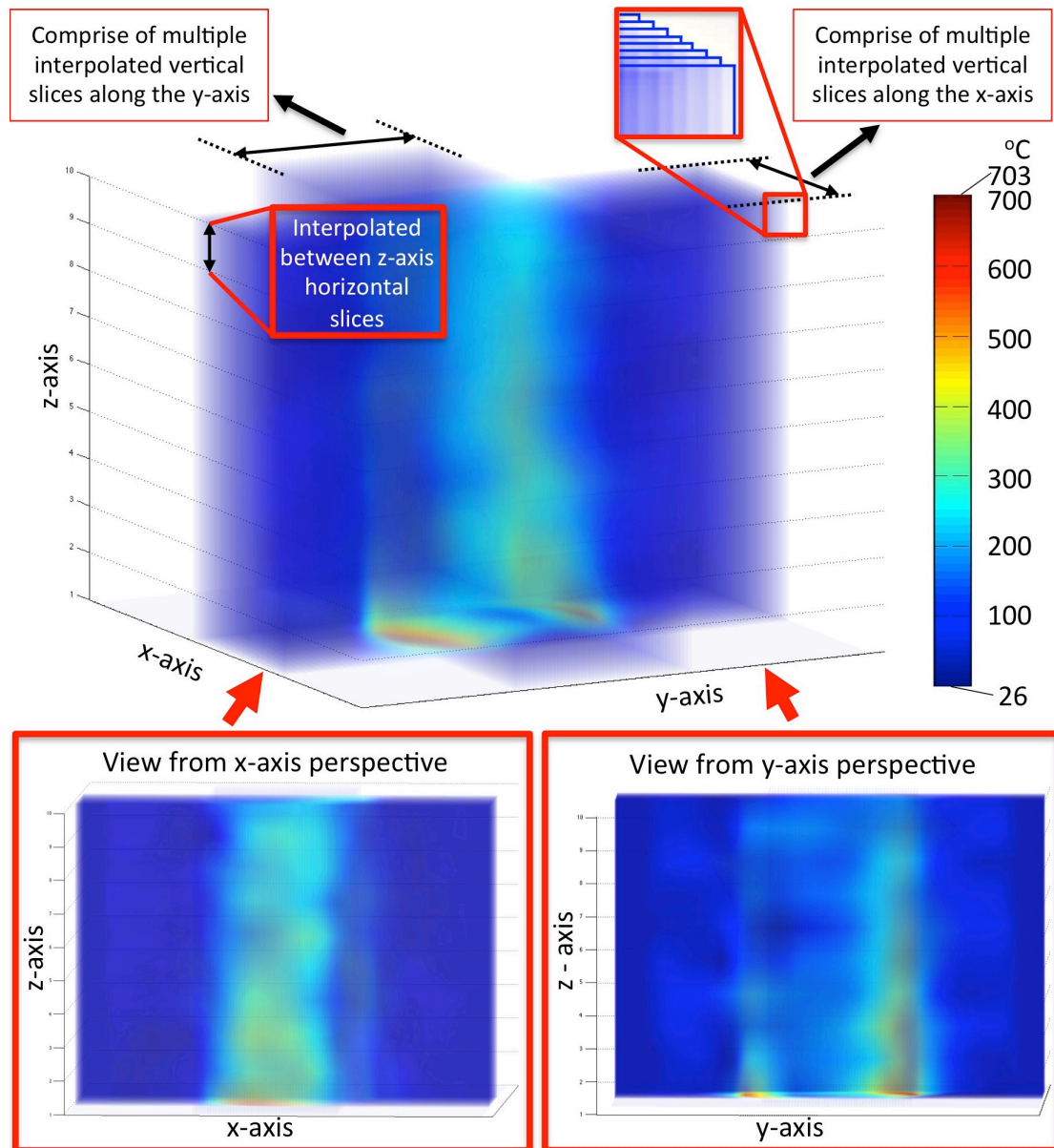


Figure 103 The combined volume is made of 51 slices from the x-axis (-25 cm to 25 cm) and 51 slices from the y-axis (-25 cm to 25 cm). Each slice is set at a transparency of 95% to create a final “translucent” looking volume.

The two views angled fully from both the x-axis and the y-axis is each presented in Figure 103. The view from the x-axis shows only 1 flame, whilst the y-axis shows two flames.

7.3 Temporal experiments

The objective of the temporal experiments was to use the system as a diagnostic tool to track temperature and concentration changes of the system during operation. This would be particularly useful in terms of monitoring changes in flow or heating patterns across a period of time at a particular section of a pipe, engine or reactor.

Ideally, the deployment of laser sources and detectors should be numerically sufficient to allow the capture of a full set of projections at different angles without the need for any other form of rotary movements which would allow ‘instant’ data acquisition. However, an alternative would be to project in a parallel fashion at different angles facilitated by the rotary motor.

The temporal experiments were conducted by performing a set of experiments as a function of time. Each experimental scenario consists of adjusting the flow of the fuel, thus affecting the temperature variation. The study was conducted in a series of 16 successive experiments, with a camera installed above the setup to provide a visual pictorial of the actual flame response to gas output manipulation. The time required for a single measurement (tomogram acquisition) to complete, was set at 3.6 seconds, each at 360 projections at 0.5 degrees step size. It took 57.6 seconds (or approximately 1 minute) to acquire 16 tomograms.

The gas flow was manipulated manually, and additional time was allocated for the user to adjust the fuel gas regulators in between experiments. A total time of 50 seconds (approximately 3 seconds per change for 16 settings) was added to the overall experiment run time, raising it to 107.6 seconds. However, because the time to adjust the fuel was allocated for fuel adjustment, and not the performance of the system itself, it was not added into the results presentation itself as shown. The stability of the flame after each adjustment to the gas flow, as well as the time required for the flame to enter steady state was discussed earlier in Section 5.3.4.

The temporal experiment was conducted at ambient temperatures of 20.4 °C, a pressure of 103.2 kPa and a relative humidity at 79%. The locations of the back burner (A) and the front burner (B) are shown in Figure 104.

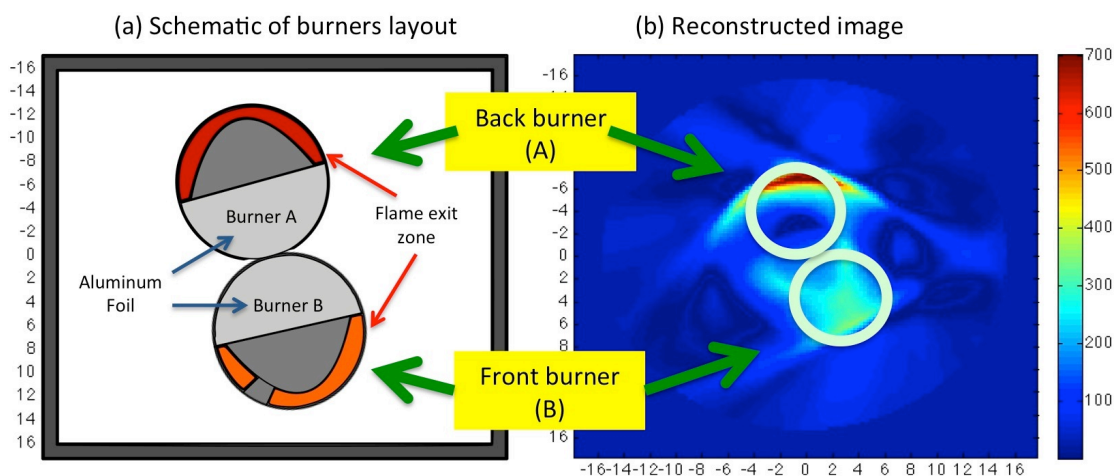


Figure 104 The location of the back burner (A) and the front burner (B) shown in both schematic and reconstructed image.

The gas regulators of each burner were adjusted based on notches, and the intensity of the each flame is colour coded in the burner schematics in the top rows of Figure 105. The temporal temperature results are presented underneath the schematic depictions of flame intensities and shown in the bottom rows of Figure 105. The start time of the experiment was 0 seconds, but the first tomogram could only be generated after the first rotation cycle at 3.6 seconds. When the regulator notch was tightened, the gas flow decreased and the flame intensity falls and vice versa. The experiment was deemed successful as the temperature reconstructions responded according to the change in fuel regulator gas changes.

It took a total of 57.6 seconds to reconstruct 16 images, which corresponds to 0.28-framerate per second (fps).

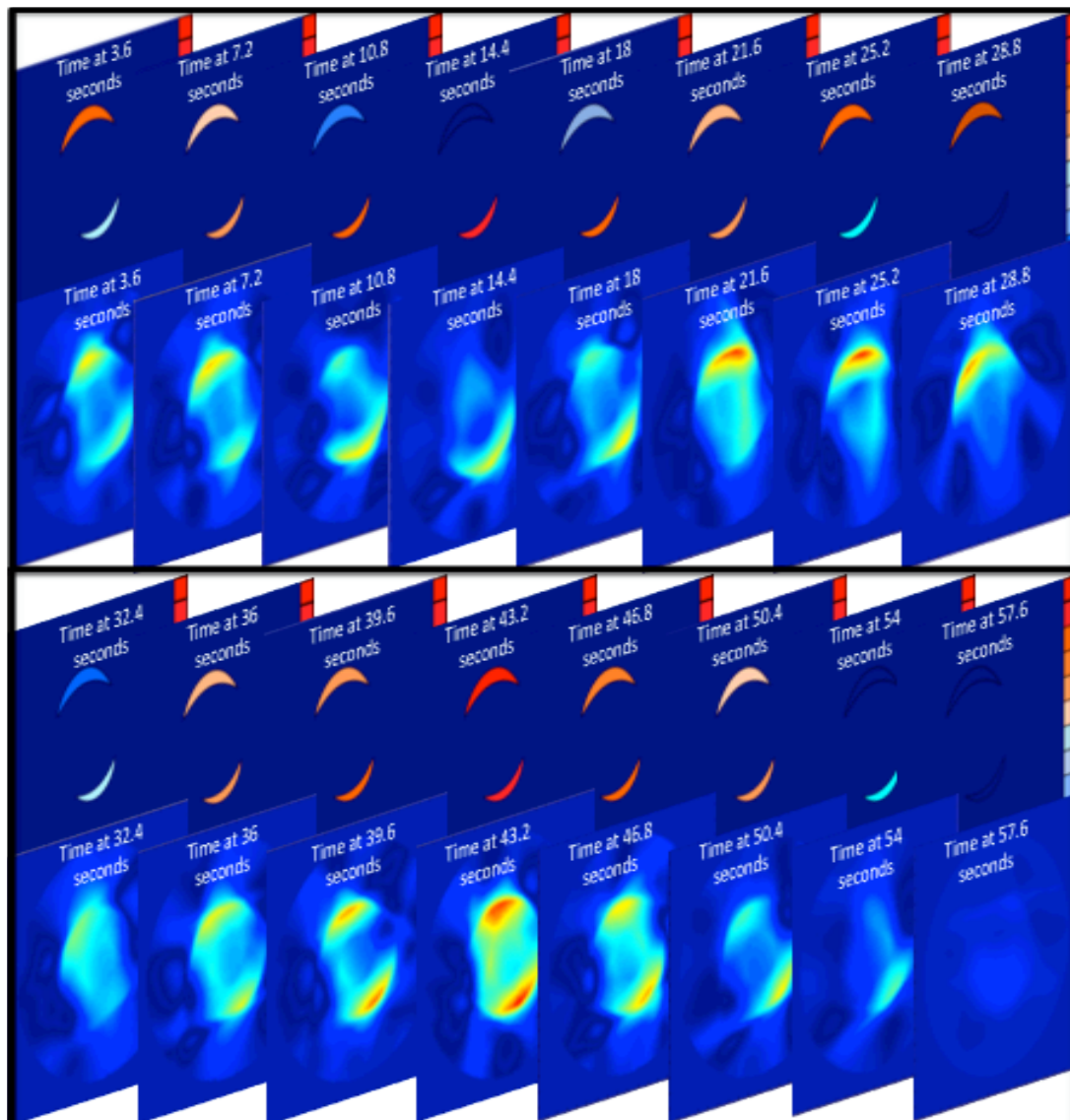


Figure 105 Temporal results of temperature distribution with time. The time taken for reconstruction since experimental start time (0 s) is shown in orange while the gas regulator notch settings of each burner is identified under Burner A and Burner B.

7.4 Image resolution

There are various definitions of image resolution, and they are often used synonymously, which may not be necessary true. In this thesis pixel, spatial and temporal resolutions are discussed. These 3 forms of resolution are factors that are interconnected in producing a well-resolved image.

Imagine watching a film on a television as an analogy for these three types of resolution. The spatial resolution is the quality of the film that is produced, if it is shot in high definition or low definition. The pixel resolution is the quality of the TV, if the TV is high definition or just a standard low definition screen. If the film is shot in high definition (high spatial resolution) but being played on a low definition TV (low pixel resolution), the viewer would still be watching it in low definition. Inversely, it doesn't matter if the TV is high definition (high pixel resolution) if the original film is shot in low definition (low spatial resolution) because the viewer could only receive the maximum quality of the film itself.

The temporal resolution relates to the frame rate per second at which the film was shot. If the temporal resolution is high, the film would run smoothly to the eye, whilst if the film was shot in low frame rate per second (low temporal resolution), the film would appear choppy to the viewer.

The pixel resolution depicts the number of pixels present in an image. This is not to be confused with image quality and will be further discussed in Section 7.4.1.

The spatial resolution depicts the amount of information an image holds, determined by both pixel resolution and the initial data acquisition phase. This will be further discussed in 7.4.2.

The temporal resolution refers to the amount of time it takes to acquire a measurement. For a tomography system, which can 'instantaneously' acquire all the projections, the temporal resolution would be very high and usually down to the settings of wavelength modulation discussed in Section 5.2.3. In this setting, where there is an additional motorised motion of the projections rotating around the peripherals of the burners, the temporal resolution would be bound to the maximum speed of the motor power and would be significantly lower.

The temporal resolution here is mixed with the spatial resolution because by increasing the time it takes to complete a rotation, it means that the angular step size of data acquisition is smaller (more projections could be acquired); and thus has a higher spatial resolution due to an increase in data.

Since one of the goals of this work was to perform imaging as quickly as possible, the only way to improve the temporal resolution would be to decrease the number of projections per angle. As discussed in Section 7.3, the temporal resolution is 0.28 fps.

7.4.1 Pixel resolution variation

Pixel resolution in general should be balanced between a well-produced image and computational speed/space. A well-produced image consists of image sharpness (where individual pixels could not be seen or that the image should not appear 'blocky') and numerical accuracy of its individual cells.

The pixel resolution can only improve as much as its original data allows it to, which means that it is bound by the spatial resolution of that image. If the spatial resolution of the original image is poor, increasing the level of pixel resolution is redundant (imagine a film shot in high definition being played on a non-high definition TV).

Balancing the pixel resolution with its spatial resolution is important as a high spatial resolution image presented at a low pixel resolution would yield a highly pixelated or 'blocky' image whilst inversely, a high spatial and pixel resolution would yield a smooth looking image.

Figure 106 compares the variation of pixel resolution on a well-sampled image during its original data acquisition phase of 4 beams per 360 projection angles. The resolutions were varied from 6 by 6 to 256 by 256.

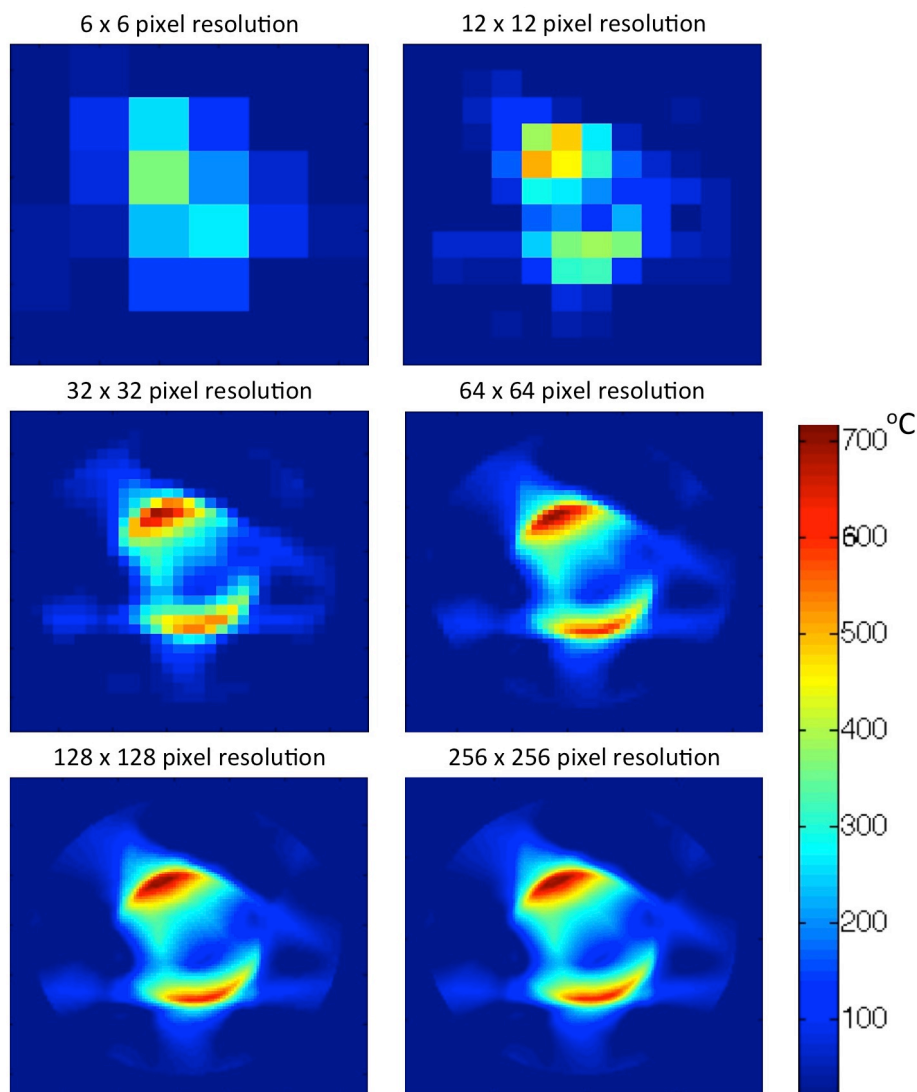


Figure 106 Variation of pixel resolution to the same image.

Careful observation of Figure 106 shows that low pixel resolutions from 6 by 6 to 32 by 32 appear heavily pixelated and also numerically incorrect (significantly lower by a few hundred degrees Celsius). This is because the information present within the high spatial resolution image was averaged into larger cells, thus reducing the sharpness and numerical accuracy of the image.

64 by 64 improves the numerical accuracy of the image but still exhibits pixelated edges. 128 by 128 exhibits similar smoothness (where pixels are no longer detectable by eye) to 256 by 256 and it can be seen that for the spatial resolution of the original image, a 128 by 128 pixel resolution representation is sufficient.

7.4.2 Spatial resolution

7.4.2.1 Varying number of projections (experimentally)

Spatial resolution is very much determined by the initial data acquisition, and in this tomography system, the data acquisition is tied to the temporal resolution (maximum/minimum motor speeds) and desire to shorten the overall experimental time. As such, the only method of increasing the spatial resolution was to increase the number of emitters/detectors per projection angle. However that was also not possible due to the equipment space constraints. Therefore a simulation was conducted using a larger amount of sampling versus experimental condition sampling earlier in Section 6.8.

A sample demonstration is shown Figure 107 with variation of the number of overall projections affecting image quality and numerical accuracy. The relationship between the number of projections or the theta step size is interconnected and Table 8 marks the relationship between the two. The experiment for varying spatial resolution was conducted at an ambient temperature of 19.3 °C; a pressure is 101 kPa and a relative humidity at 87%. The individual images were produced at pixel resolutions of 128 by 128. Here the experiment criterion is to produce a numerically accurate image with the smallest number of projection/time available.

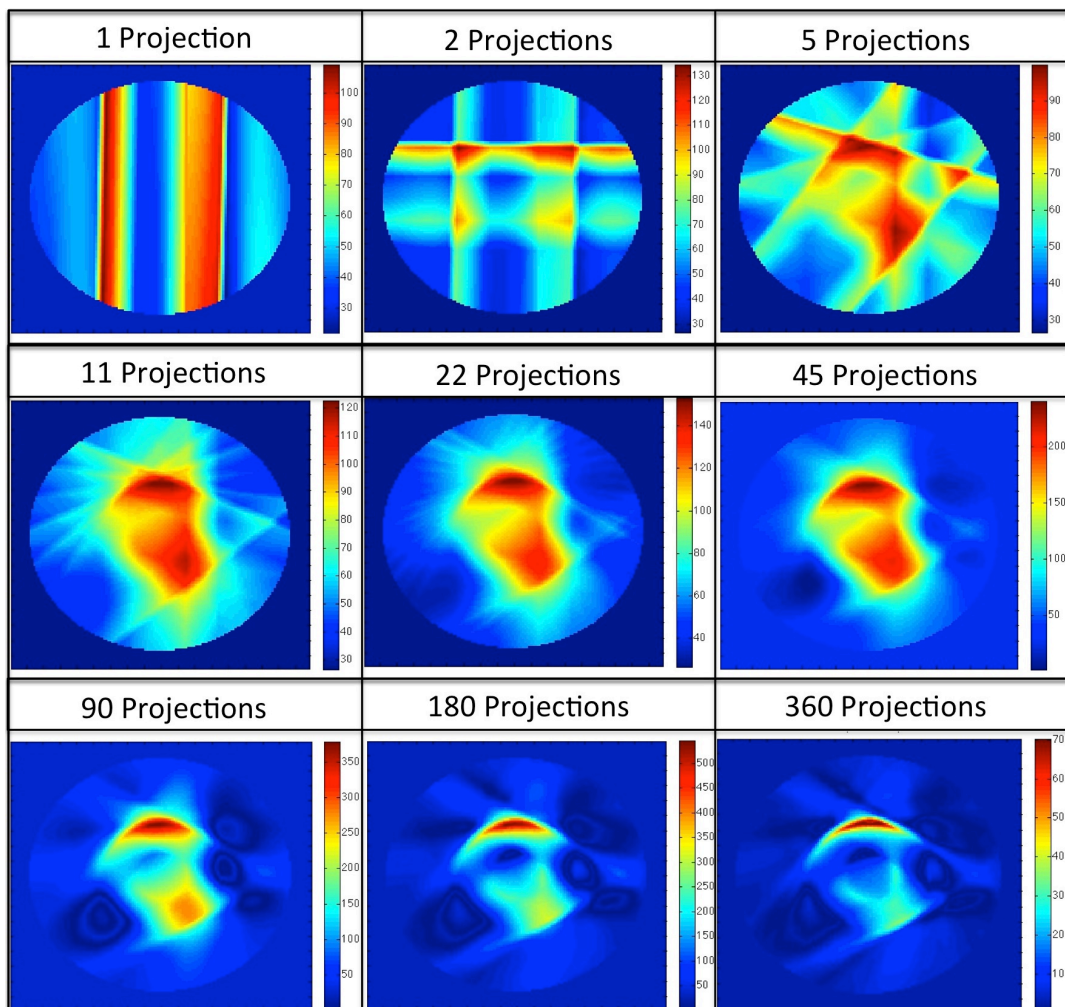


Figure 107 Resulting reconstructions from variation of theta step size with number of projections

Table 8 Relationship of theta step size with number of parallel projections

Theta step size	0.5	1	2	4	8	16	36	90	180
Projections	360	180	90	45	22	11	5	2	1

The comparison of spatial resolution is shown in Figure 107. Using just 1 or 2 projections resembles a single or dual back-smearing process of an FBP method. However with 5 projections, a rough representation of the correct image can already be discerned. From using 11 to 45 projections, an image similar to a FBP reconstruction can be observed. These images, due to the lack of projections, showed blurring on the reconstruction due to back smearing of data in the FBP process. The temperature values were also substantially suppressed by approximately 400°C to 600°C.

Most of the streak artefacts present in projections 5 to projections 45 in Figure 107 are no longer present at projection 90. The image has already sharpened significantly and seems to match the visual representation of the flame pattern. However the temperatures were still not very accurate. There was not much difference between the physical reconstructed images of 180 to 360 projections, yielding similar sharpness.

However, it was not possible to calculate the spatial resolution without the use of a phantom, and simulations were conducted to recover the spatial resolution of the system.

7.4.2.2 Varying beams per projection (simulation)

The method described here to conduct in-plane (or 2D) spatial resolution was to compare the contrast of phantom to background using a set of line-pair structures [206]. In this thesis, the base background was set at values of 0, whilst the line-pair structures were created with the values of 1. This creates a grid matrix comprising of primarily zeros, and the values of the line-pair structures at values of ones.

The line-pairs were observed by comparing alternating black lines (values of 1) with equally sized white lines (background value of 0). Figure 108 shows a zoomed version of 2 sets of line-pair structures, arranged perpendicularly to each other. The red structures are valued at 1 and the blue background is valued at 0. Each structure within the two sets contain different line-pair patterns, ranging from 0.5 to 5 lp/cm (line-pair per cm). By examining the ability to resolve the patterns at different levels, the system's capacity could be determined. The smaller the value of the line-pair structure, the less spatially resolved the reconstructed image is.

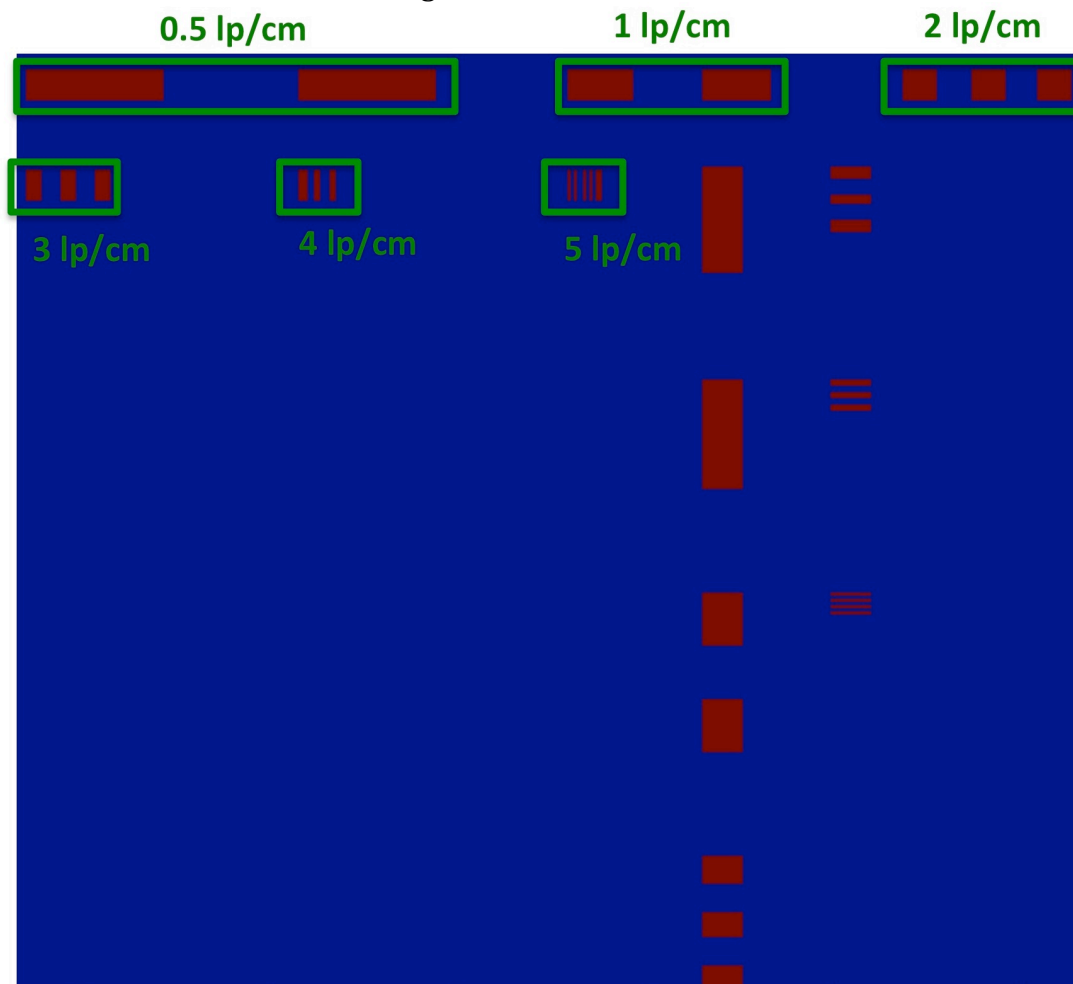


Figure 108 Zoomed in view of 2 sets of line-pairs structures to allow clearer view of smaller line-pairs structures, ranging from 0.5 to 5 lp/cm. The original dimension of the phantoms is 36 by 36 cm.

The phantom shown in Figure 108 was evaluated with the DFR method at 700 zero padding value, with a total of 360 projections at intervals of 0.5° angular step size. Variations of beams were conducted, ranging from 16 to 512 equally spaced beams per projection. These beams were interpolated between each other during the reconstruction phase.

Figure 109 was reconstructed using 512 beams per projection, and it allows a simple comparison with Figure 108 on how spatially resolved the reconstructed structures are. Even though 512 beams per projections are physically unrealistic for the application within this thesis, it can be seen that it could not resolve 5 lp/cm structures, and could just about reconstruct 4 lp/cm structures.

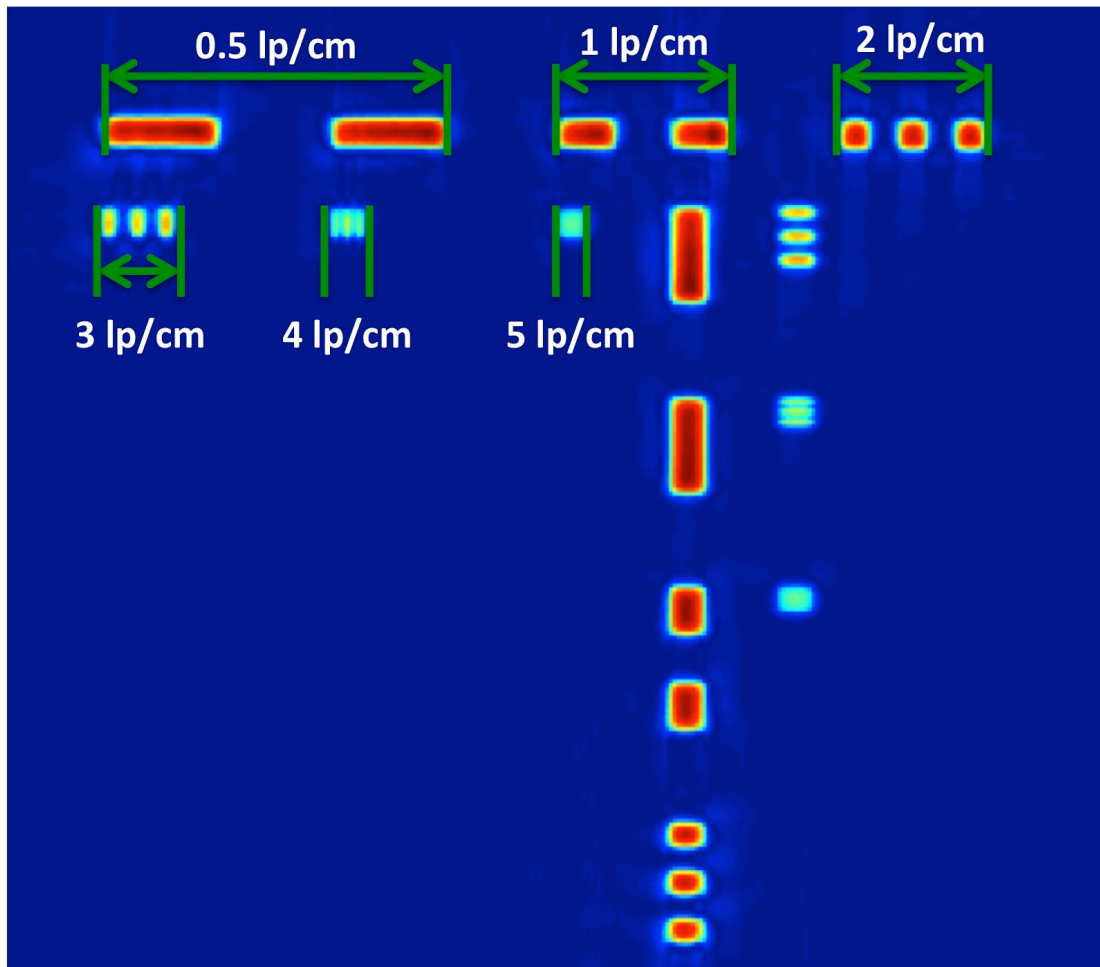


Figure 109 Zoomed in view of reconstruction using 512 equally spaced beams per projection.

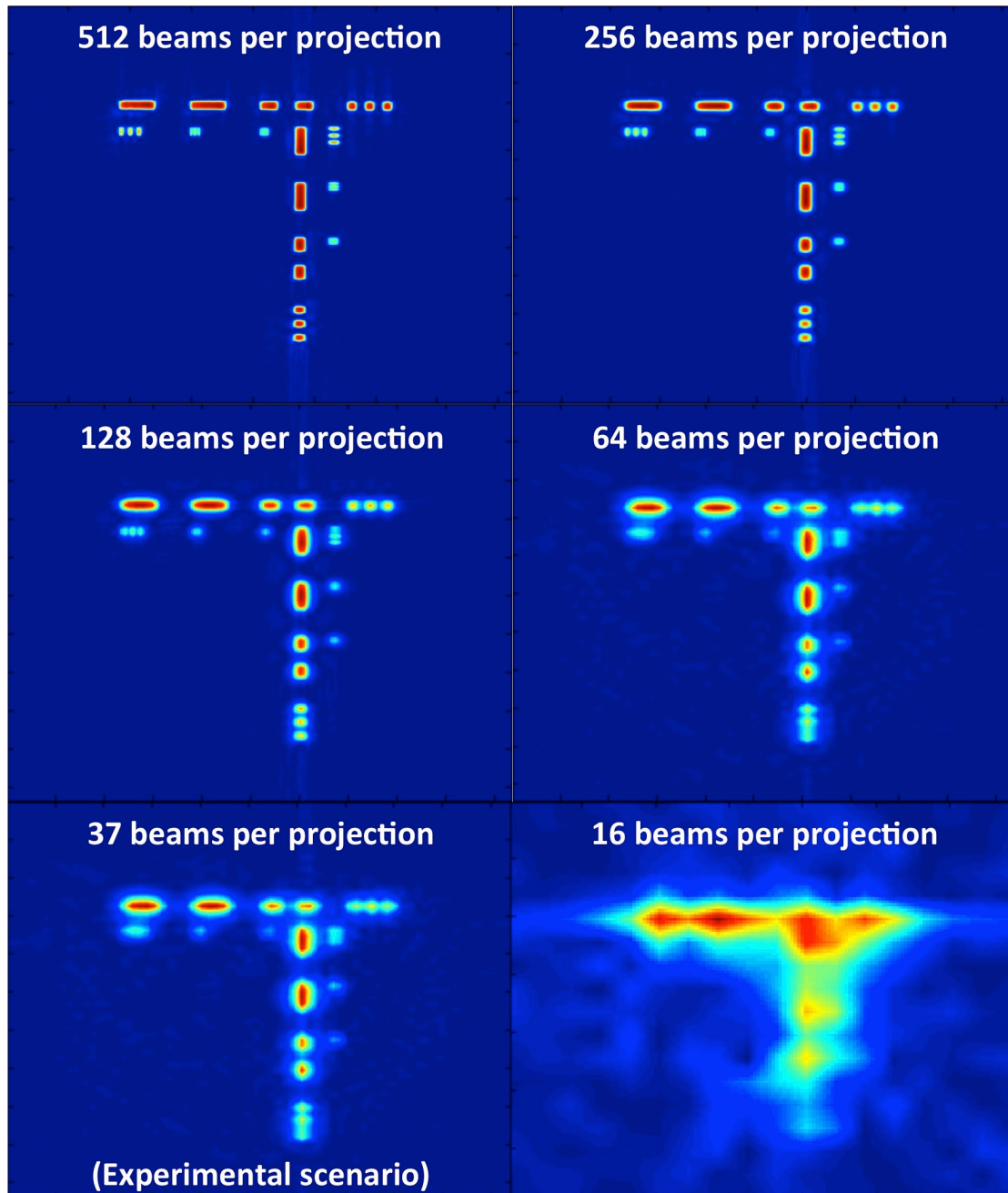


Figure 110 Comparison of simulations of different beams per projection simulation scenarios, where 37 beams per projection mimic the experimental scenarios.

Figure 110 compares the different equidistance beams per projection to provide a general idea of how much spatial resolution improvement there could be should the number of beams be increased from 37 (experimental conditions). Note that the beams were interpolated with 4 original beams with known external boundaries (0 in this case).

The simulation from Figure 110 (37 beams), shows that it could spatially resolve from 0.5 to 1 lp/cm. Substantial blurring occurs after 2 lp/cm. Conditions with high numbers of beams, from 128 to 512 were used, but even they could only resolve up to 3 to 4 lp/cm, leaving this system/beam geometry unsuitable for 5 lp/cm and higher without increasing the amount of projections.

7.5 Repeatability

The objective of the repeatability experiments was to test the precision of the system and the ability to reproduce results based on the same conditions. The repeatability experiment consists of a set of measurement readings taken within a minute. The goal was to produce consistent and repeatable results.

Experimental conditions involved igniting the two burners in the carriage holder and left burning for a minute before measurements were taken. The gas outputs of the heaters were set at two notches on the opening valve. Three consecutive measurements were then taken after the first minute.

As discussed earlier in Section 7.2, it was challenging to maintain a constant gas output of the burners, which will result in a slight variation of the flame produced. Therefore the repeatability experiment shown in Figure 111 was conducted within 40 seconds.

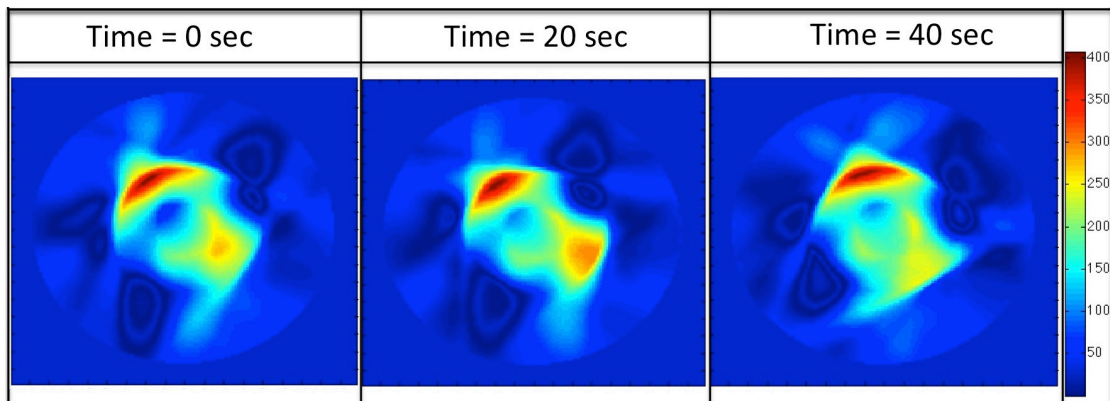


Figure 111 Consecutive reconstructions in the span of 1 minute.

The results produced were consistent in the temperature distributions. There was a slight decrease in temperature when comparing the first result ($t = 0$ seconds) with the third result ($t = 40$ seconds) and it was assumed that it was attributed to the gas output fluctuation over time. This appears to mirror the trend where the gas output decreases if a sample canister was left burning over a period of time. The temperature, as well as the visual observation of flame intensity could be seen declining with time.

Although the tomography experimental procedures prove to be repeatable, the gas canister flows may not be. To combat this variation and reduce its impact as much as possible, a new canister was used for each documented experiment listed in the thesis.

7.6 Chapter Summary

The 3D experiments were conducted in 2D slices of 10 and linearly interpolated to fill in the missing data in between the levels. It was assumed that because the slices were placed close enough (1 cm) that it would justify a linear interpolation between the slices. Several different perspectives were shown on the 3D reconstruction, revealing different set of information.

The temporal experiments that were conducted responded well with the fast change in flame manipulations. Although a 0.28 frame rate per second may compare poorly with respect to current video recording devices with an average 30 fps, it marks an important step towards a higher accuracy and precision in optical tomography.

The pixel resolution of the results were presented in 128 by 128 pixels and the spatial resolution recorded using projection intervals at every 0.5 degrees, from 0 degrees to 179.5 degrees, with a total of 360 projections is 0.5 to 1 lp/cm.

Finally, the repeatability experiments were conducted using the DFR reconstruction method generated the results faithfully with respect to time.

8 DISCUSSION, CONCLUSIONS AND FURTHER WORK

The primary aim of this thesis was to develop an optical tomography system, which could measure concentration and temperature variations in 3D and as a function of time. This was achieved in two stages.

8.1 On the designing of line-of-sight (LOS) laser system

8.1.1 Short note on designing the LOS system for MICC

The first stage consisted of designing a line-of-sight (LOS) near infrared (NIR) tunable diode laser absorption spectroscopy (TDLAS) system for use in the Manchester Ice Cloud Chamber (MICC). This LOS system was used as a foundation to develop a multiple projections tomography system.

Although most current interest in optical spatial imaging is focused on combustion monitoring as stated in the literature review in Section 2.2, optical imaging techniques have traditionally proven to be flexible with regards to their field of deployment (from medical to process industry for example). Therefore, the initial deployment of a LOS system in the MICC could be further developed into a tomography system in the future.

Moreover, the MICC bares a similar resemblance to the challenges typically faced by combustion systems. They both work in harsh environments such as extreme temperatures or pressures (high/low temperatures/pressures), possibility of scattering (from soot or ice crystals) as well as low optical access (requires retrofitting of optical access panels).

8.1.2 Review of aims and objectives of LOS system for MICC

The objectives of stage 1, the designing of a LOS TDLAS system, are summarised in Table 9.

Table 9 Review of MICC experiment objectives.

Design a TDL system to monitor the relative humidity in the MICC.	<ul style="list-style-type: none"> • A TDL system was designed and a program was written using LabVIEW to control the TDL setup.
Can the TDL results be validated?	<ul style="list-style-type: none"> • The TDL results were calibrated to remove the water molecules present in the chilled room. • The monitoring of relative humidity was done simultaneously with the chilled mirror hygrometer and performed well, with small discrepancies attributed to the differences in measurement locations. • The differences could also be attributed to the fact that the chilled mirror uses a point measurement whilst the TDLAS had to average its result along the laser path length inside the MICC.
Could the system	<ul style="list-style-type: none"> • The monitoring of the TDL performed well from

detect rapid changes in relative humidity at varying pressures and temperature?

- pressures 1000 hPa to 750 hPa.
- An increase in standard deviation could be seen as pressure drops from 750 hPa to 700 hPa, attributed to detector over saturation.
 - The system could sample measurements per second during an expansion process, something the original chilled mirror hygrometer could not.

8.1.3 Conclusions on the LOS system for the MICC

The experiments tracked the changes of relative humidity in the presence of ammonium sulphate as CCN and Snomax as IN exhibited similar trends to the APCIM cloud parcel simulation conducted. As the pressure and temperature in the MICC decreases, the relative humidity rises to saturation point and maintained, implying that no ice nucleation occurred. This proves the APCIM simulation theory that there is suppressed freezing in the presence of CCN.

The LOS results were separately validated against a chilled mirror hygrometer during equilibrium conditions and mild discrepancies of relative humidity were accounted due to a difference in sampling locations. It was also attributed to the chilled mirror sampling from a point measurement while the LOS results were attributed to an averaged value along the laser path.

The frequency of monitoring the relative humidity was set at 1 sample per second, but could be increased up to 100 samples per second if required.

The standard deviation increases as the pressure drops, which could have been due to icing of condensed water from repeated warming and cooling of the chamber on the optical panels. The standard deviation ranges from 0.0008 to 0.0016 for the overall peak fittings, corresponding to the relative humidity range from $\pm 3.2\%$ to $\pm 7.9\%$.

8.2 On the development of tomography system

8.2.1 Short note on developing the tomography system

The second stage consisted of using the LOS TDLAS system designed for the MICC and developing it into a tomography system for 3D and temporal applications. The development of the tomography system was based on the LOS system and a design framework created from a former fan beam system.

The developed tomography system was based on similar primary 'ingredients' used in the LOS system. For example, a similar laser diode was used, both setups were based on fibre optics, similar laser controllers and the software programs written for the LOS system were used as a foundation for later tomography programs.

Prior to developing the new tomography system, a new laser was introduced into the original fan beam design as detailed in Section 5.2, which allowed better wavelength range and line choices. The updated laser was centred around 7178 cm^{-1} (1392 nm) with a range from 7155 cm^{-1} to 7185 cm^{-1} while the fan beam experiment was centred at 7185.6 cm^{-1} and a weak absorption line at 7185.394 cm^{-1} . This allowed a better signal to noise ratio

during the peak fitting process. The wavenumber sweep range of the new laser was also larger by 2 cm^{-1} , allowing the user to measure more absorption peaks per sweep. The original analysis program was also rewritten to decrease the length of overall fan beam experimental time. The fan beam system inspired a design framework crucial to the final design of the 3D and temporal enabled tomography system.

A suitable geometry (parallel) was selected due to experimental ease and physical space constraints of the equipment layout. Two mixed fuel, flat round surface burners were used as the combustion sources. Each of the burners was partially covered in aluminium foil to create asymmetrical phantoms. Three reconstruction algorithms (Filtered Back Projection (FBP), Fourier Slice Reconstruction (FSR) and Direct Fourier Reconstruction (DFR)) were compared using physical phantoms and simulated phantoms. DFR was used for experiments because it exhibited the lowest relative mean error and signal to noise ratio.

8.2.2 Review of aims and objectives on developing the tomography system

The objectives of stage 2, the development of a tomography system for 3D and temporal purposes, are summarised in Table 10.

Table 10 Review of tomography experiments objectives

Design tomography equipment through a set of guidelines.	<ul style="list-style-type: none"> • A set of guidelines were produced based on challenges and desired capabilities from the fan beam system. • These guidelines shaped the design of the final constructed setup.
Qualitative and quantitative comparison of reconstruction methods	<ul style="list-style-type: none"> • 3 methods were compared: FBP, FSR and DFR. • Comparisons were conducted using numerical analysis of radon slices at projection angle 0. • Spatial resolution was tested on both simulations of well sampled and sparsely sampled projection slices • Artefacts and image blurring were discussed for qualitative comparison. • Physical phantoms were also generated and compared for temperature correctness using thermocouple. • Relative mean error and standard deviations were calculated against the simulated images. • DFR was selected as it outperformed the other 2 methods in all categories.
Repeatability of system and could the results be validated?	<ul style="list-style-type: none"> • Repeatability experiments were conducted and reproduced results with fair degree of mild discrepancy, possibly due to the change of room and fuel conditions. • Thermocouple validation was also used to check for accurate temperature reconstructions.
Could temporal experiments be conducted?	<ul style="list-style-type: none"> • Temporal experiments were conducted at a frame rate of 0.28 fps.

Could it resolve objects that are 4 cm apart?	<ul style="list-style-type: none"> • Results of spatial resolution simulations showed that it could resolve from 0.5 to 1 lp/cm, which allows it to resolve objects approximately 2 to 1 cm apart.
Could 3D experiments be conducted?	<ul style="list-style-type: none"> • The experiments involve firstly acquiring z-axis image slices, which were conducted in 1 cm step size. • Vertical slices along the x-axis and y-axis could be retrieved next by interpolating the z-axis slices.

8.2.3 Conclusions on developing the tomography system

Building on the design framework and the LOS system, a parallel beam geometry tomography system was designed for the reconstruction experiments. A high frequency pass filter was used (Ram Lak) but a low frequency pass filter was ignored (e.g. Shepp-Logan/ Hamming) because it would reduce its spatial resolution at the cost of image smoothness. Variations of zero padding were conducted instead to smooth out the final reconstructed images and the ideal number for this setup was 700.

The 3 methods FBP, FSR and DFR were compared numerically by taking the radon slices of the reconstructed images from each method at projection angle 0 as well as thermocouple temperature validations. The DFR method provided the most faithful reconstructed images with respect to these validation studies with a $\pm 5^{\circ}\text{C}$ difference to the thermocouple samplings.

Simulations were also conducted on the 3 reconstruction methods. The first involved using well-sampled projection slices, while the other mirrored the experimental conditions of having further spaced data per projection slice. They were linearly interpolated to populate the projection slice. Simulation results confirmed that interpolating between beams per projection slice weaken the overall reconstruction and provided a much lower standard deviation and relative mean error with respect to well-sampled projection slices. The simulations also showed that the DFR method yielded the lowest standard deviation and relative mean error for both sets of simulation.

Simulation results were important because it was impossible to calculate the actual deviation and relative mean error of the experiments as there was nothing to compare it to. Based on the DFR simulations under experimental conditions, the standard deviation was 0.0066 and relative mean error was 8.12%.

The ideal spatial resolution acquired from this current setup using 360 projections at 0.5-theta intervals is 0.5 to 1 lp/cm. The pixel resolution was set at 128 by 128.

The temporal experiments involved manipulation of combustion intensities using two mix-fuel burners. The set up recorded the changes of combustion accurately at 0.28 fps (3 seconds per frame), which is also the value of the temporal resolution.

Finally, the 3D tomography experiments were conducted by lowering the Carriage further away from the optical plane. By varying the z-axis in steps of 1 cm, multiple viewing angles of the volumetric space above the combustion source could be seen. Slices in the z- axis were used to interpolate between each other to formulate vertical slices that moves along the x-axis and y-axis.

Based on the Beer-Lambert law, the two unknowns (temperature and concentration) were solved by determining the temperature first via two-line thermometry. As the temperatures were already validated using thermocouple samplings, as well as the image validated using comparisons for Radon slices (integrated absorbance across a path length), the spatial concentration was considered to be well reconstructed. Although it would be preferable to validate the concentration distribution via other sampling tools such as a mass spectrometer, this equipment were not available at this point of thesis completion.

8.3 Future work and Potential applications

8.3.1 Future work

- Improving 3D results

Building on this current system, it could be possible to build a temporal 3D system with the aid of more optical fibres. By arranging rows of emitters each at different height, it would allow simultaneous measurements of different height in one measurement, which could then be interpolated.

One literature argument about interpolating between slices is that they are considered more of 2.5D than 3D as discussed in Chapter 2.4.1. There is consideration of using an optical lens to increase the size of the laser beam and use array detectors. This would decrease the use of physical sources to detectors combination, or positioned correctly, used for true 3D detection without the need to interpolate between slices.

- Improving temporal results

One issue raised was that future work should achieve temporal monitoring at a much higher frame rate, and one way to achieve this is to reduce the time spent on physical motions. One option could be the incorporation of slip rings that can be used to increase the amount of rotary possibilities. Currently, the rotary motion within this setup consists of a 180-degree movement which is a fairly common configuration in industry, however with the use of electrical and fibre optic rotary joints, it allows constant rotation and thus a system capable of constant scanning and monitoring. The second advantage of using rotary joints is that with a 360-degree movement, it allows the positioning of laser beams in an asymmetrical manner, which allows the scanning of larger objects with a heavier amount of projection and data density.

Stationary projections could be implemented next, where projections at all potential angles be taken instantaneous, removing the need of a rotational movement. However, this option typically requires both an increase in equipment, thus capital cost.

- Improving spatial resolution
-

The spatial resolution could be improved by creating a denser sampling slice. With increased laser sources that are more densely placed together, it could reconstruct images at higher spatial resolution.

- Improved algorithms that allow a lower number of projections

One of the biggest challenges with optical tomography is the retrofitting of imaging systems into pre-existing systems. Large amount of peripheral space and optical access may often be a luxury, which means that applications demand tomography systems to require low projection geometries with high spatial resolution.

The development of more refined algorithms such as hyperspectral tomography discussed in Chapter 2.3.2.2 could be an answer to this problem. However, hyperspectral tomography so far requires high computational time, and may be unsuitable and undesirable for most uses. Therefore, more research on more efficient algorithms could be developed for faster and better reconstructions in a shorter time. Another aspect of better algorithms could also mean better scalability of the tomography systems. Fewer projections tend to mean less space, providing more manoeuvrability for fitting into smaller equipment.

- Monitoring multiple species

Simultaneous monitoring of multiple species by multiplexing the laser source is an attractive option of diagnosing different reactants or products at once. For example, detecting CO, CO₂ and H₂O at once could give insight of the efficiency of a combustion system.

8.3.2 Potential applications

- MICC

Further experiments on CCN and IN configuration could be performed in the future, including the use of mineral salts as IN for example. A particular interesting study relevant to the thesis would be to further develop the monitoring of singular line of sight relative humidity to both 2D and 3D spatial monitoring. By monitoring the space in multiple dimensions, it provides more angles in seeing the microphysics of cloud formation. This could potentially include the imaging of the change of gaseous water to ice as cross sectional slices within the MICC and further developed to a 3D analysis of the chamber itself. This may require additional portholes to be added and potentially a fan beam fibre optic system combined with ART algorithm system.

- Large area monitoring and detection

Large areas could also be monitored passively for spatial gas leaks in plants for example. Optical access would not be a problem, accuracy of reconstruction in a wide system boundary and cost from minimum equipment capital would be of importance. This could be coupled with an alarm system that would go off and pin point the exact location of the leak.

9 REFERENCES

- [1] "United Nation Framework Convention on Climate Change, United Nations," 1992.
- [2] CoreWritingTeam, R. K. Pachauri, and L. A. Meyer, "IPCC, 2014: Climate Change 2014: Synthesis Report. Contribution of Working Groups I, II and III to the Fifth Assessment Report of the Intergovernmental Panel on Climate Change," *IPCC, Geneva, Switz.*, 2014.
- [3] N. Hansen, T. A. Cool, P. R. Westmoreland, and K. Kohse-H??inghaus, "Recent contributions of flame-sampling molecular-beam mass spectrometry to a fundamental understanding of combustion chemistry," *Prog. Energy Combust. Sci.*, vol. 35, no. 2, pp. 168–191, 2009.
- [4] B. T., I. A. Bashmakov, Y. Mulugetta, H. Chum, A. de la V. Navarro, J. Edmond, A. Faaij, B. Fungtammasan, A. Garg, E. Hertwich, D. Honner, D. Infield, M. Kainuma, S. Khennas, S. Kim, H. B. Nimir, K. Riahi, N. Strachan, R. Wisser, and X. Zhang, "2014: Energy Systems. In: Climate Change 2014: Mitigation of Climate Change. Contribution of Working Group III to the Fifth Assessment Report of the Intergovernmental Panel on Climate Change," *Cambridge Univ. Press*, pp. 511–598, 2014.
- [5] R. T. Watson, H. Rodhe, H. Oeschger, and U. Siegenthaler, "Greenhouse gases and aerosols," *Clim. Chang. IPCC Sci. Assess.*, pp. 1–40, 1990.
- [6] Y. Yan, T. Qiu, G. Lu, M. M. Hossain, G. Gilabert, and S. Liu, "Recent advances in flame tomography," *Chinese J. Chem. Eng.*, vol. 20, no. 2, pp. 389–399, 2012.
- [7] J. Ballester and T. Garc??a-Armingol, "Diagnostic techniques for the monitoring and control of practical flames," *Prog. Energy Combust. Sci.*, vol. 36, no. 4, pp. 375–411, 2010.
- [8] G. A. Richards, M. M. McMillian, R. S. Gemmen, W. A. Rogers, and S. R. Cully, "Issues for low-emission, fuel-flexible power systems," *Prog. Energy Combust. Sci.*, vol. 27, no. 2, pp. 141–169, 2001.
- [9] "U.S. Department of Energy- A Technology Roadmap by and for the Industrial Combustion Community," 1999.
- [10] Z. Gut and P. Wolanski, "Flame imaging using 3D electrical capacitance tomography," *Combust. Sci. Technol.*, vol. 182, no. 11–12, pp. 1580–1585, 2010.
- [11] Z. Gut, P. Wolanski, and P. Oleszczak, "Monitoring of Combustion Processes in Industrial Burners Using Electrical Capacitance Tomography," *J. KONES Powertrain Transp.*, vol. 18, no. 3, pp. 117–121, 2011.
- [12] J. W. Daily, "Laser induced fluorescence spectroscopy in flames," *Prog. Energy Combust. Sci.*, vol. 23, no. 2, pp. 133–199, 1997.
- [13] X. An, T. Kraetschmer, K. Takami, S. T. Sanders, L. Ma, W. Cai, X. Li, S. Roy, and J. R. Gord, "Validation of temperature imaging by H₂O absorption spectroscopy using hyperspectral tomography in controlled experiments," *Appl. Opt.*, vol. 50, no. 4, pp. A29–37, Feb. 2011.
- [14] S. Pal, K. B. Ozanyan, and H. McCann, "A computational study of tomographic measurement of carbon monoxide at minor concentrations," *Meas. Sci. Technol.*, vol. 19, no. 9, p. 094018, 2008.
- [15] K. Salem, E. Tsotsas, and D. Mewes, "Tomographic measurement of

- breakthrough in a packed bed adsorber," *Chem. Eng. Sci.*, vol. 60, no. 2, pp. 517–522, Jan. 2005.
- [16] T. York, H. McCann, and K. B. Ozanyan, "Agile sensing systems for tomography," *IEEE Sens. J.*, vol. 11, no. 12, pp. 3086–3105, 2011.
- [17] F. El-Mahallawy and S. E.-D. Habik, "Combustion Fundamentals," 2002.
- [18] H. Neij and M. Aldén, "Application of two-photon laser-induced fluorescence for visualization of water vapor in combustion environments.," *Appl. Opt.*, vol. 33, no. 27, pp. 6514–23, 1994.
- [19] V. I. Babushok, G. T. Linteris, and P. T. Baker, "Influence of water vapor on hydrocarbon combustion in the presence of hydrofluorocarbon agents," *Combust. Flame*, vol. 162, no. 5, pp. 2307–2310, 2015.
- [20] P. Chelin, C. Camy-Peyret, V. Pina, P. Alkhoury, and D. Davidenko, "Emission spectroscopy of hot water vapor from H₂-air deflagrative combustion in a closed cylinder," *Combust. Flame*, vol. 140, no. 4, pp. 319–331, 2005.
- [21] F. Liu, J. Consalvi, and A. Fuentes, "Effects of water vapor addition to the air stream on soot formation and flame properties in a laminar coflow ethylene/air diffusion flame," *Combust. Flame*, vol. 161, no. 7, pp. 1724–1734, 2014.
- [22] a. N. Mazas, B. Fiorina, D. a. Lacoste, and T. Schuller, "Effects of water vapor addition on the laminar burning velocity of oxygen-enriched methane flames," *Combust. Flame*, vol. 158, no. 12, pp. 2428–2440, 2011.
- [23] K. Kohse-Höinghaus, R. S. Barlow, M. Aldén, and J. Wolfrum, "Combustion at the focus: Laser diagnostics and control," *Proc. Combust. Inst.*, vol. 30 I, pp. 89–123, 2005.
- [24] M. G. Allen, "Diode laser absorption sensors for gas-dynamic and combustion flows.," *Meas. Sci. Technol.*, vol. 9, no. 4, pp. 545–562, 1998.
- [25] P. V Terek, D. L. Hall, T. a Miller, and M. S. Wooldridge, "H₂O absorption spectroscopy for determination of temperature and H₂O mole fraction in high-temperature particle synthesis systems.," *Appl. Opt.*, vol. 41, no. 12, pp. 2274–2284, 2002.
- [26] V. Nagali and R. K. Hanson, "Design of a diode-laser sensor to monitor water vapor in high-pressure combustion gases.," *Appl. Opt.*, vol. 36, no. 36, pp. 9518–9527, 1997.
- [27] F. Xing, Y. Huang, M. Zhao, and J. Zhao, "The Brief Introduction of Different Laser Diagnostics Methods Used in Aeroengine Combustion Research," *J. Sensors*, vol. 2016, 2016.
- [28] M. N. Wernick and J. N. Aarsvold, *Emission Tomography: The Fundamentals of PET and SPECT*. 2004.
- [29] D. Hoffman, K.-U. Münch, and A. Leipertz, "Two-dimensional temperature determination in sooting flames by filtered Rayleigh scattering.," *Opt. Lett.*, vol. 21, no. 7, pp. 525–527, 1996.
- [30] C. Schulz and V. Sick, "Tracer-LIF diagnostics: quantitative measurement of fuel concentration, temperature and fuel/air ratio in practical combustion systems," *Prog. Energy Combust. Sci.*, vol. 31, no. 1, pp. 75–121, 2005.
- [31] O. M. Feroughi, H. Kronemayer, T. Dreier, and C. Schulz, "Effect of fluctuations on time-averaged multi-line NO-LIF thermometry measurements of the gas-phase temperature," *Appl. Phys. B Lasers Opt.*, vol. 120, no. 3, pp. 429–440, 2015.

-
- [32] C. Gessenhardt, C. Schulz, and S. A. Kaiser, "Endoscopic temperature imaging in a four-cylinder IC engine via two-color toluene fluorescence," *Proc. Combust. Inst.*, vol. 35, no. 3, pp. 3697–3705, 2015.
- [33] C. Hecht, a. Abdali, T. Dreier, and C. Schulz, "Gas-Temperature Imaging in a Microwave-Plasma Nanoparticle-Synthesis Reactor Using Multi-Line NO-LIF Thermometry," *Zeitschrift für Phys. Chemie*, vol. 225, no. 11–12, pp. 1225–1235, 2011.
- [34] B. Coriton, J. H. Frank, and A. Gomez, "Effects of strain rate, turbulence, reactant stoichiometry and heat losses on the interaction of turbulent premixed flames with stoichiometric counterflowing combustion products," *Combust. Flame*, vol. 160, no. 11, pp. 2442–2456, 2013.
- [35] L. Ma, Q. Lei, Y. Wu, W. Xu, T. M. Ombrello, and C. D. Carter, "From ignition to stable combustion in a cavity flameholder studied via 3D tomographic chemiluminescence at 20 kHz," *Combust. Flame*, vol. 165, pp. 1–10, 2016.
- [36] B. Coriton, A. M. Steinberg, and J. H. Frank, "High-speed tomographic PIV and OH PLIF measurements in turbulent reactive flows," *Exp. Fluids*, vol. 55, no. 6, 2014.
- [37] P. P. Panda, M. Roa, C. D. Slabaugh, S. Peltier, C. D. Carter, W. R. Laster, and R. P. Lucht, "High-repetition-rate planar measurements in the wake of a reacting jet injected into a swirling vitiated crossflow," *Combust. Flame*, vol. 163, pp. 241–257, 2016.
- [38] I. Boxx, C. M. Arndt, C. D. Carter, and W. Meier, "High-speed laser diagnostics for the study of flame dynamics in a lean premixed gas turbine model combustor," *Exp. Fluids*, vol. 52, no. 3, pp. 555–567, 2012.
- [39] N. Soulopoulos, Y. Hardalupas, and A. M. K. P. Taylor, "Mixing and scalar dissipation rate statistics in a starting gas jet," *Phys. Fluids*, vol. 27, no. 12, pp. 0–24, 2015.
- [40] R. L. Gordon, C. Heeger, and A. Dreizler, "High-speed mixture fraction imaging," *Appl. Phys. B Lasers Opt.*, vol. 96, no. 4, pp. 745–748, 2009.
- [41] J. A. Sutton and J. F. Driscoll, "Measurements and statistics of mixture fraction and scalar dissipation rates in turbulent non-premixed jet flames," *Combust. Flame*, vol. 160, no. 9, pp. 1767–1778, 2013.
- [42] G. E. Elsinga, B. Wieneke, F. Scarano, and A. Schr, *Tomographic 3D-PIV and Applications*, vol. 125. 2008.
- [43] J. Nygren, J. Hult, M. Richter, M. Aldén, M. Christensen, A. Hultqvist, and B. Johansson, "Three-dimensional laser induced fluorescence of fuel distributions in an HCCI engine," *Proc. Combust. Inst.*, vol. 29, no. 1, pp. 679–685, 2002.
- [44] R. K. Hanson, "Combustion diagnostics: Planar imaging techniques," *Symp. Combust.*, vol. 21, no. 1, pp. 1677–1691, 1988.
- [45] R. D. Keane, R. J. Adrian, and Y. Zhang, "Super-resolution particle imaging velocimetry," *Meas. Sci. Technol.*, vol. 6, pp. 754–768, 1995.
- [46] K. Y. Cho, A. Satija, T. L. Pourpoint, S. F. Son, and R. P. Lucht, "Time-Resolved 3D OH Planar Laser-Induced Fluorescence System for Multiphase Combustion Kevin," *8th U.S. Natl. Combust. Meet.*, 2013.
- [47] K. Y. Cho, A. Satija, T. L. Pourpoint, S. F. Son, and R. P. Lucht, "High-repetition-rate three-dimensional OH imaging using scanned planar laser-induced fluorescence system for multiphase combustion.," *Appl. Opt.*, vol. 53, pp. 316–26, 2014.
-

-
- [48] M. Luong, R. Zhang, C. Schulz, and V. Sick, "Toluene laser-induced fluorescence for in-cylinder temperature imaging in internal combustion engines," *Appl. Phys. B Lasers Opt.*, vol. 91, no. 3–4, pp. 669–675, 2008.
- [49] L. M. Itani, G. Bruneaux, A. Di Lella, and C. Schulz, "Two-tracer LIF imaging of preferential evaporation of multi-component gasoline fuel sprays under engine conditions," *Proc. Combust. Inst.*, vol. 35, no. 3, pp. 2915–2922, 2015.
- [50] K. J. Rensberger, J. B. Jeffries, R. a Copeland, K. Kohse-Höinghaus, M. L. Wise, and D. R. Crosley, "Laser-induced fluorescence determination of temperatures in low pressure flames," *Appl. Opt.*, vol. 28, no. 17, pp. 3556–66, 1989.
- [51] T. Etzkorn, J. Fitzer, S. Muris, and J. Wolfrum, "Determination of absolute methyl-and hydroxyl-radical concentrations in a low pressure methane-oxygen flame," *Chem. Phys. Lett.*, vol. 208, no. 3–4, pp. 307–310, 1993.
- [52] C. Schulz, "Advanced Laser Imaging Diagnostics in Combustion," *Zeitschrift für Phys. Chemie*, vol. 219, pp. 509–554, 2005.
- [53] R. Suntz, H. Becker, P. Monkhouse, and J. Wolfrum, "Two-dimensional visualization of the flame front in an internal combustion engine by laser induced fluorescence of OH radicals," *Appl. Phys. B*, vol. 47, no. 4, pp. 287–293, 1988.
- [54] M. J. Dyer and D. R. Crosley, "Two-dimensional imaging of OH laser-induced fluorescence in a flame," *Opt. Lett.*, vol. 7, no. 8, pp. 382–384, 1982.
- [55] W. Koban, J. Schorr, and C. Schulz, "Oxygen-distribution imaging with a novel two-tracer laser-induced fluorescence technique," *Appl. Phys. B*, vol. 74, pp. 111–114, 2002.
- [56] S. Einecke, C. Schulz, and V. Sick, "Measurement of temperature, fuel concentration and equivalence ratio fields using tracer LIF in IC engine combustion," *Appl. Phys. B Lasers Opt.*, vol. 71, pp. 717–723, 2000.
- [57] S. Böckle, J. Kazenwadel, T. Kunzelmann, and C. Schulz, "Laser-diagnostic multi-species imaging in strongly swirling natural gas flames," *Appl. Phys. B Lasers Opt.*, vol. 71, no. 5, pp. 741–746, 2000.
- [58] S. Böckle, J. Kazenwadel, T. Kunzelmann, D.-I. Shin, C. Schulz, and J. Wolfrum, "Simultaneous single-shot laser-based imaging of formaldehyde, OH, and temperature in turbulent flames," *Proc. Combust. Inst.*, vol. 28, no. 1, pp. 279–286, 2000.
- [59] I. S. Burns and C. F. Kaminski, "Diode Laser Induced Fluorescence for Gas-Phase Diagnostics," *Zeitschrift für Phys. Chemie*, vol. 225, no. 11–12, pp. 1343–1366, 2011.
- [60] R. W. Pitz, T. S. Cheng, J. a. Wehrmeyer, and C. F. Hess, "Two-photon predissociative fluorescence of H₂O by a KrF laser for concentration and temperature measurement in flames," *Appl. Phys. B Photophysics Laser Chem.*, vol. 56, no. 2, pp. 94–100, 1993.
- [61] P. Andresen, a Bath, W. Gröger, H. W. Lulf, G. Meijer, and J. J. Meulen, "Laser-induced fluorescence with tunable excimer lasers as a possible method for instantaneous temperature field measurements at high pressures: checks with an atmospheric flame," *Appl. Opt.*, vol. 27, no. 2, pp. 365–78, 1988.
- [62] J. Hult, U. Meier, W. Meier, A. Harvey, and C. F. Kaminski, "Experimental
-

- analysis of local flame extinction in a turbulent jet diffusion flame by high repetition 2-D laser techniques and multi-scalar measurements," *Proc. Combust. Inst.*, vol. 30, no. 1, pp. 701–708, 2005.
- [63] C. F. Kaminski, J. Hult, and M. Alden, "Rapid communication High repetition rate planar laser induced fluorescence of OH in a turbulent non-premixed flame," *Combustion*, vol. 68, pp. 757–760, 1999.
- [64] R. Wellander, M. Richter, and M. Aldén, "Time resolved, 3D imaging (4D) of two phase flow at a repetition rate of 1 kHz," *Opt. Express*, vol. 19, no. 22, p. 21508, 2011.
- [65] N. Jiang, R. A. Patton, W. R. Lempert, and J. A. Sutton, "Development of high-repetition rate CH PLIF imaging in turbulent nonpremixed flames," *Proc. Combust. Inst.*, vol. 33, no. 1, pp. 767–774, 2011.
- [66] V. A. Miller, V. A. Troutman, M. G. Mungal, and R. K. Hanson, "20kHz toluene planar laser-induced fluorescence imaging of a jet in nearly sonic crossflow," *Appl. Phys. B Lasers Opt.*, vol. 117, no. 1, pp. 401–410, 2014.
- [67] V. Sick, "High speed imaging in fundamental and applied combustion research," *Proc. Combust. Inst.*, vol. 34, no. 2, pp. 3509–3530, 2013.
- [68] J. Köser, L. G. Becker, N. Vorobiev, M. Schiemann, V. Scherer, B. Böhm, and A. Dreizler, "Characterization of single coal particle combustion within oxygen-enriched environments using high-speed OH-PLIF," *Appl. Phys. B Lasers Opt.*, vol. 121, no. 4, pp. 459–464, 2015.
- [69] B. Zhou, Q. Li, Y. He, P. Petersson, Z. Li, M. Aldén, and X. S. Bai, "Visualization of multi-regime turbulent combustion in swirl-stabilized lean premixed flames," *Combust. Flame*, vol. 162, no. 7, pp. 2954–2958, 2015.
- [70] B. Zhou, C. Brackmann, Z. Li, and M. Aldén, "Development and application of CN PLIF for single-shot imaging in turbulent flames," *Combust. Flame*, vol. 162, no. 2, pp. 368–374, 2015.
- [71] J. Weinkauff, M. Greifenstein, A. Dreizler, and B. Böhm, "Time resolved three-dimensional flamebase imaging of a lifted jet flame by laser scanning," *Meas. Sci. Technol.*, vol. 26, no. 10, p. 105201, 2015.
- [72] F. Wang, Q. Wu, Q. Huang, H. Zhang, J. Yan, and K. Cen, "Simultaneous measurement of 2-dimensional H₂O concentration and temperature distribution in premixed methane/air flame using TDLAS-based tomography technology," *Opt. Commun.*, vol. 346, pp. 53–63, 2015.
- [73] M. Linne, "Imaging in the optically dense regions of a spray: A review of developing techniques," *Prog. Energy Combust. Sci.*, vol. 39, no. 5, pp. 403–440, 2013.
- [74] B. R. Halls, T. J. Heindel, A. L. Kastengren, and T. R. Meyer, "Evaluation of X-ray sources for quantitative two- and three-dimensional imaging of liquid mass distribution in atomizing sprays," *Int. J. Multiph. Flow*, vol. 59, pp. 113–120, 2014.
- [75] R. Hain, C. J. Kähler, and D. Michaelis, "Tomographic and time resolved PIV measurements on a finite cylinder mounted on a flat plate," *Exp. Fluids*, vol. 45, no. 4, pp. 715–724, 2008.
- [76] G. E. Elsinga, F. Scarano, B. Wieneke, and B. W. van Oudheusden, "Tomographic particle image velocimetry," *6th Int. Symp. Part. Image Velocim.*, pp. 1–12, 2005.
- [77] G. Stewart, W. Johnstone, J. R. . Bain, K. Ruxton, and K. Duffin, "Recovery of

- Absolute Gas Absorption Line Shapes Using Tunable Diode Laser Spectroscopy With Wavelength Modulation—Part I: Theoretical Analysis,” *J. Light. Technol.*, vol. 29, no. 6, pp. 811–821, 2011.
- [78] J. R. . Bain, W. Johnstone, K. Ruxton, G. Stewart, M. Lengden, and K. Duffin, “Recovery of Absolute Gas Absorption Line Shapes Using Tunable Diode Laser Spectroscopy With Wavelength Modulation—Part 2: Experimental Investigation,” *J. Light. Technol.*, vol. 29, no. 7, pp. 987–996, 2011.
- [79] M. P. Arroyo, T. P. Birbeck, D. S. Baer, and R. K. Hanson, “Dual diode-laser fiber-optic diagnostic for water-vapor measurements,” *Opt. Lett.*, vol. 19, no. 14, pp. 1091–3, Jul. 1994.
- [80] M. P. Arroyo, S. Langlois, and R. K. Hanson, “Diode-laser absorption technique for simultaneous measurements of multiple gasdynamic parameters in high-speed flows containing water vapor,” *Appl. Opt.*, vol. 33, no. 15, pp. 3296–3307, 1994.
- [81] M. P. Arroyo and R. K. Hanson, “Absorption measurements of water-vapor concentration, temperature, and line-shape parameters using a tunable InGaAsP diode laser,” *Appl. Opt.*, vol. 32, no. 30, pp. 6104–16, Oct. 1993.
- [82] X. Liu, J. B. Jeffries, R. K. Hanson, K. M. Hinckley, and M. a. Woodmansee, “Development of a tunable diode laser sensor for measurements of gas turbine exhaust temperature,” *Appl. Phys. B*, vol. 82, no. 3, pp. 469–478, Dec. 2005.
- [83] P. Werle, “Spectroscopic trace gas analysis using semiconductor diode lasers,” *Spectrochim. Acta Part A Mol. Biomol. Spectrosc.*, vol. 52, no. 8, pp. 805–822, 1996.
- [84] P. Werle, F. Slemr, K. Maurer, R. Kormann, R. Mücke, and B. Jänker, “Near- and mid-infrared laser-optical sensors for gas analysis,” *Opt. Lasers Eng.*, vol. 37, no. 2–3, pp. 101–114, 2002.
- [85] L. C. Philippe and R. K. Hanson, “Laser-absorption mass flux sensor for high-speed airflows,” *Opt. Lett.*, vol. 16, no. 24, pp. 2002–4, Dec. 1991.
- [86] L. C. Philippe and R. K. Hanson, “Laser diode wavelength-modulation spectroscopy for simultaneous measurement of temperature, pressure, and velocity in shock-heated oxygen flows,” *Appl. Opt.*, vol. 32, no. 30, pp. 6090–103, Oct. 1993.
- [87] D. B. Oh and a C. Stanton, “Measurement of nitric oxide with an antimonide diode laser,” *Appl. Opt.*, vol. 36, no. 15, pp. 3294–3297, 1997.
- [88] V. Ebert, T. Fernholz, C. Giesemann, H. Pitz, H. Teichert, J. Wolfrum, and H. Jaritz, “Simultaneous diode-laser-based in situ detection of multiple species and temperature in a gas-fired power plant,” *Proc. Combust. Inst.*, vol. 28, no. 1, pp. 423–429, 2000.
- [89] W. Cai and C. F. Kaminski, “A numerical investigation of high-resolution multispectral absorption tomography for flow thermometry,” *Appl. Phys. B Lasers Opt.*, vol. 119, no. 1, pp. 29–35, 2015.
- [90] P. A. Martin, “Near-infrared diode laser spectroscopy in chemical process and environmental air monitoring,” *Chem. Soc. Rev.*, vol. 31, no. 4, pp. 201–210, Jun. 2002.
- [91] J. a Silver, D. J. Kane, and P. S. Greenberg, “Quantitative species measurements in microgravity flames with near-IR diode lasers,” *Appl. Opt.*, vol. 34, no. 15, pp. 2787–801, 1995.
- [92] J. Song, Y. Hong, G. Wang, and H. Pan, “Algebraic tomographic

- reconstruction of two-dimensional gas temperature based on tunable diode laser absorption spectroscopy," *Appl. Phys. B*, pp. 1–9, 2013.
- [93] V. L. Kasyutich and P. A. Martin, "Towards a two-dimensional concentration and temperature laser absorption tomography sensor system," *Appl. Phys. B*, vol. 102, no. 1, pp. 149–162, Jul. 2010.
- [94] Y. Deguchi, D. Yasui, and A. Adachi, "Development of 2D Temperature and Concentration Measurement Method Using Tunable Diode Laser Absorption Spectroscopy," *J. Mech. Eng. Autom.*, vol. 2, pp. 543–549, 2012.
- [95] R. Villarreal and P. L. Varghese, "Frequency-resolved absorption tomography with tunable diode lasers," *Appl. Opt.*, vol. 44, no. 31, pp. 6786–95, Nov. 2005.
- [96] C. Belotti, F. Cuccoli, L. Facheris, and O. Vaselli, "An Application of Tomographic Reconstruction of Atmospheric CO₂ over a Volcanic Site Based on Open-Path IR Laser Measurements," *IEEE Trans. Geosci. Remote Sens.*, vol. 41, no. 11 PART I, pp. 2629–2637, 2003.
- [97] David M. Scott and Richard A. Williams, *Frontiers in industrial process tomography: proceedings of the Engineering Foundation Conference held at The Cliffs, Shell Beach*. Engineering Foundation, 1995.
- [98] D. T. Ginat and R. Gupta, "Advances in computed tomography imaging technology," *Annu. Rev. Biomed. Eng.*, vol. 16, no. November 2015, pp. 431–53, 2014.
- [99] R. A. Williams and M.S. Beck, *Process tomography: principles, techniques, and applications*. Butterworth-Heinemann, 1995.
- [100] L. A. Shepp and J. B. Kruskal, "Computerized Tomography: The New Medical X-Ray Technology," *Am. Math. Mon.*, vol. 85, no. 6, pp. 420–439, 1978.
- [101] G. T. Herman, "Image reconstruction from projections," *Real-Time Imaging*, vol. 1, pp. 3–18, 1995.
- [102] K. J. Daun, "Infrared species limited data tomography through Tikhonov reconstruction," *J. Quant. Spectrosc. Radiat. Transf.*, vol. 111, no. 1, pp. 105–115, Jan. 2010.
- [103] C. Liu, L. Xu, Z. Cao, and Y. Yang, "Fan-beam TDLAS tomography for gas concentration distribution with limited data," *IST 2012 - 2012 IEEE Int. Conf. Imaging Syst. Tech. Proc.*, pp. 117–120, 2012.
- [104] L. Wondraczek, A. Khorsandi, U. Willer, G. Heide, W. Schade, and G. H. Frischat, "Mid-infrared laser-tomographic imaging of carbon monoxide in laminar flames by difference frequency generation," *Combust. Flame*, vol. 138, no. 1–2, pp. 30–39, 2004.
- [105] K. E. Bennett, G. W. Faris, and R. L. Byer, "Experimental optical fan beam tomography," *Appl. Opt.*, vol. 23, no. 16, p. 2678, Aug. 1984.
- [106] N. Terzija, J. L. Davidson, C. a Garcia-Stewart, P. Wright, K. B. Ozanyan, S. Pegrum, T. J. Litt, and H. McCann, "Image optimization for chemical species tomography with an irregular and sparse beam array," *Meas. Sci. Technol.*, vol. 19, no. 9, p. 094007, Sep. 2008.
- [107] C. Lindstrom, C.-J. Tam, R. Givens, D. Davis, and S. Williams, "Diode laser absorption tomography using data compression techniques," *Comput. Imaging Vi*, vol. 6814, pp. 1–17, 2008.
- [108] P. Wright, C. A. Garcia-Stewart, S. J. Carey, F. P. Hindle, S. H. Pegrum, S. M. Colbourne, P. J. Turner, W. J. Hurr, T. J. Litt, S. C. Murray, and others,

- “Toward in-cylinder absorption tomography in a production engine,” *Appl. Opt.*, vol. 44, no. 31, pp. 6578–6592, 2005.
- [109] P. Wright, N. Terzija, J. L. Davidson, S. Garcia-Castillo, C. Garcia-Stewart, S. Pegrum, S. Colbourne, P. Turner, S. D. Crossley, and T. Litt, “High-speed chemical species tomography in a multi-cylinder automotive engine,” *Chem. Eng. J.*, vol. 158, no. 1, pp. 2–10, Mar. 2010.
- [110] A. C. Kak and M. Slaney, “Principles of Computerized Tomographic Imaging Chpt7,” pp. 275–296, Jan. 2001.
- [111] H. Li, G. B. Rieker, X. Liu, J. B. Jeffries, and R. K. Hanson, “Extension of wavelength-modulation spectroscopy to large modulation depth for diode laser absorption measurements in high-pressure gases,” *Appl. Opt.*, vol. 45, no. 5, pp. 1052–1061, 2006.
- [112] X. Ouyang and P. L. Varghese, “gases with thermal and concentration boundary layers,” vol. 28, no. 18, pp. 3979–3984, 1989.
- [113] E. D. Tornaiainen and F. C. Gouldin, “Tomographic Reconstruction of 2-D Absorption Coefficient Distributions from a Limited Set of Infrared Absorption Data,” *Combust. Sci. Technol.*, vol. 131, no. 1–6, pp. 85–105, Jan. 1998.
- [114] R. Santoro, H. Semerjian, and P. Emmerman, “Optical tomography for flow field diagnostics,” *Int. J. Heat Mass Transf.*, vol. 24, no. 7, 1981.
- [115] S. Shimizu and S. Sakai, “High-Speed Tomography for Simultaneous Measurement of the Histories of Two-Dimensional Distributions of Temperature and Density of Burnt Gases,” *JSME Int. J. Ser. B Fluids Therm. Eng.*, vol. 37, 1994.
- [116] S. Carey and H. McCann, “Near infra-red absorption tomography for measurement of chemical species distribution,” *1st World Congr. Ind. Process Tomogr.*, pp. 480–487, 1999.
- [117] S. J. Carey, H. McCann, F. Hindle, K. Ozanyan, D. Winterbone, and E. Clough, “Chemical species tomography by near infra-red absorption,” *Chem. Eng. J.*, vol. 77, no. 1–2, pp. 111–118, 2000.
- [118] B. Gillet, Y. Hardalupas, C. Kavounides, and a. M. K. P. Taylor, “Infrared absorption for measurement of hydrocarbon concentration in fuel/air mixtures (MAST-B-LIQUID),” *Appl. Therm. Eng.*, vol. 24, no. 11–12, pp. 1633–1653, Aug. 2004.
- [119] J. Hult, R. S. Watt, and C. F. Kaminski, “Dispersion measurement in optical fibers using supercontinuum pulses,” *J. Light. Technol.*, vol. 25, no. 3, pp. 820–824, 2007.
- [120] J. M. Langridge, T. Laurila, R. S. Watt, R. L. Jones, C. F. Kaminski, and J. Hult, “Cavity enhanced absorption spectroscopy of multiple trace gas species using a supercontinuum radiation source,” *Opt. Express*, vol. 16, no. 14, pp. 10178–10188, 2008.
- [121] R. S. Watt, C. F. Kaminski, and J. Hult, “Generation of supercontinuum radiation in conventional single-mode fibre and its application to broadband absorption spectroscopy,” *Appl. Phys. B Lasers Opt.*, vol. 90, no. 1, pp. 47–53, 2008.
- [122] C. F. Kaminski, R. S. Watt, A. D. Elder, J. H. Frank, and J. Hult, “Supercontinuum radiation for applications in chemical sensing and microscopy,” *Appl. Phys. B Lasers Opt.*, vol. 92, no. 3 SPECIAL ISSUE, pp. 367–378, 2008.

-
- [123] S. Welzel, F. Hempel, M. Hübner, N. Lang, P. B. Davies, and J. Röpcke, "Quantum cascade laser absorption spectroscopy as a plasma diagnostic tool: An overview," *Sensors*, vol. 10, no. 7, pp. 6861–6900, 2010.
- [124] R. F. Curl, F. Capasso, C. Gmachl, A. A. Kosterev, B. McManus, R. Lewicki, M. Pusharsky, G. Wysocki, and F. K. Tittel, "Quantum cascade lasers in chemical physics," *Chem. Phys. Lett.*, vol. 487, no. 1–3, pp. 1–18, 2010.
- [125] C. S. Kim, M. Kim, J. Abell, W. W. Bewley, C. D. Merritt, C. L. Canedy, I. Vurgaftman, and J. R. Meyer, "Mid-IR distributed-feedback interband cascade lasers," vol. 8631, p. 863110, 2013.
- [126] W. Zeller, L. Naehle, P. Fuchs, F. Gerschuetz, L. Hildebrandt, and J. Koeth, "DFB lasers between 760 nm and 16 μm for sensing applications," *Sensors*, vol. 10, no. 4, pp. 2492–2510, 2010.
- [127] O. Witzel, A. Klein, C. Meffert, S. Wagner, S. Kaiser, C. Schulz, and V. Ebert, "VCSEL-based, high-speed, in situ TDLAS for in-cylinder water vapor measurements in IC engines," *Opt. Express*, vol. 21, no. 17, p. 19951, 2013.
- [128] C. S. Goldenstein, C. L. Strand, I. a Schultz, K. Sun, J. B. Jeffries, and R. K. Hanson, "Fitting of calibration-free scanned-wavelength-modulation spectroscopy spectra for determination of gas properties and absorption lineshapes.," *Appl. Opt.*, vol. 53, no. 3, pp. 356–67, 2014.
- [129] C. S. Goldenstein, R. M. Spearrin, J. B. Jeffries, and R. K. Hanson, "Wavelength-modulation spectroscopy near 2.5 μm for H₂O and temperature in high-pressure and -temperature gases," *Appl. Phys. B Lasers Opt.*, vol. 116, no. 3, pp. 705–716, 2014.
- [130] R. Sur, K. Sun, J. B. Jeffries, R. K. Hanson, R. J. Pummill, T. Waind, D. R. Wagner, and K. J. Whitty, "TDLAS-based sensors for in situ measurement of syngas composition in a pressurized, oxygen-blown, entrained flow coal gasifier," *Appl. Phys. B Lasers Opt.*, vol. 116, no. 1, pp. 33–42, 2014.
- [131] W. Cai and C. F. Kaminski, "A tomographic technique for the simultaneous imaging of temperature, chemical species, and pressure in reactive flows using absorption spectroscopy with frequency-agile lasers," *Appl. Phys. Lett.*, vol. 104, no. 3, pp. 0–5, 2014.
- [132] L. Ma and W. Cai, "Numerical investigation of hyperspectral tomography for simultaneous temperature and concentration imaging.," *Appl. Opt.*, vol. 47, no. 21, pp. 3751–9, Jul. 2008.
- [133] W. Cai and C. F. Kaminski, "Multiplexed absorption tomography with calibration-free wavelength modulation spectroscopy," *Appl. Phys. Lett.*, vol. 104, no. 15, pp. 2012–2017, 2014.
- [134] W. Cai, D. J. Ewing, and L. Ma, "Application of simulated annealing for multispectral tomography," *Comput. Phys. Commun.*, vol. 179, no. 4, pp. 250–255, 2008.
- [135] Y. Ju, *Recent progress and challenges in fundamental combustion research*, vol. 44, no. 1. 2014.
- [136] J. W. Walewski and S. T. Sanders, "Rapid wavelength scans over one octave and application to laser-induced fluorescence.," *Opt. Lett.*, vol. 30, no. 18, pp. 2394–6, Oct. 2005.
- [137] L. a. Kranendonk, R. Huber, J. G. Fujimoto, and S. T. Sanders, "Wavelength-agile H₂O absorption spectrometer for thermometry of general combustion gases," *Proc. Combust. Inst.*, vol. 31, no. 1, pp. 783–790, Jan. 2007.
-

-
- [138] J. W. Walewski and S. T. Sanders, "High-resolution wavelength-agile laser source based on pulsed super-continua," *Appl. Phys. B*, vol. 79, no. 4, pp. 415–418, Jul. 2004.
- [139] a. J. Pertzborn, J. W. Walewski, and S. T. Sanders, "Wavelength-agile source based on a potassium atomic vapor cell and application for absorption spectroscopy of iodine," *Opt. Commun.*, vol. 254, no. 1–3, pp. 173–183, Oct. 2005.
- [140] L. Ma, X. Li, S. T. Sanders, A. W. Caswell, S. Roy, D. H. Plemmons, and J. R. Gord, "50-kHz-rate 2D imaging of temperature and H₂O concentration at the exhaust plane of a J85 engine using hyperspectral tomography.," *Opt. Express*, vol. 21, no. 1, pp. 1152–62, Jan. 2013.
- [141] C. Hagen and S. Sanders, "Toward hyperspectral sensing in practical devices: measurements of fuel, H₂O and gas temperature in a metal homogeneous charge compression ignition engine," *J. Near Infrared Spectrosc.*, vol. 15, no. 2, p. 217, 2007.
- [142] L. Ma, W. Cai, A. W. Caswell, T. Kraetschmer, S. T. Sanders, S. Roy, and J. R. Gord, "Tomographic imaging of temperature and chemical species based on hyperspectral absorption spectroscopy.," *Opt. Express*, vol. 17, no. 10, pp. 8602–13, May 2009.
- [143] W. Cai and L. Ma, "Hyperspectral tomography based on proper orthogonal decomposition as motivated by imaging diagnostics of unsteady reactive flows.," *Appl. Opt.*, vol. 49, no. 4, pp. 601–610, 2010.
- [144] R. Wajman, R. Banasiak, L. Mazurkiewicz, T. Dyakowski, and D. Sankowski, "Spatial imaging with 3D capacitance measurements," *Meas. Sci. Technol.*, vol. 18, no. 11, pp. 3671–3671, 2007.
- [145] I. Ihrke and M. Magnor, "Image-based tomographic reconstruction of flames," *ACM SIGGRAPH 2004 Sketches SIGGRAPH 04*, p. 16, 2004.
- [146] W. Cai, X. Li, F. Li, and L. Ma, "Numerical and experimental validation of a three-dimensional combustion diagnostic based on tomographic chemiluminescence.," *Opt. Express*, vol. 21, no. 6, pp. 7050–64, 2013.
- [147] Y. Ishino and N. Ohiwa, "Three-Dimensional Computerized Tomographic Reconstruction of Instantaneous Distribution of Chemiluminescence of a Turbulent Premixed Flame," *JSME Int. J. Ser. B*, vol. 48, no. 1, pp. 34–40, 2005.
- [148] N. Anikin, R. Suntz, and H. Bockhorn, "Tomographic reconstruction of the OH*-chemiluminescence distribution in premixed and diffusion flames," *Appl. Phys. B Lasers Opt.*, vol. 100, no. 3, pp. 675–694, 2010.
- [149] P. M. Brisley, G. Lu, Y. Yan, and S. Cornwell, "Three-dimensional temperature measurement of combustion flames using a single monochromatic CCD camera," *IEEE Trans. Instrum. Meas.*, vol. 54, no. 4, pp. 1417–1421, 2005.
- [150] N. Polydorides and W. R. B. Lionheart, "A Matlab toolkit for three-dimensional electrical impedance tomography: a contribution to the Electrical Impedance and Diffuse Optical Reconstruction Software project," *Meas. Sci. Technol.*, vol. 13, no. 12, pp. 1871–1883, 2002.
- [151] D. P. Correia, P. Ferrão, and a. Caldeira-Pires, "Flame three-dimensional tomography sensor for in-furnace diagnostics," *Proc. Combust. Inst.*, vol. 28, no. 1, pp. 431–438, 2000.
- [152] A. Chatterjee, "An introduction to the proper orthogonal decomposition,"
-

- Curr. Sci.*, vol. 78, no. 7, pp. 808–817, 2000.
- [153] S. Member and S. Member, “Optical Time-Division Multiplexing For Very High Bit-Rate Transmission,” 1988.
- [154] T. Kraetschmer, D. Dagel, and S. T. Sanders, “Simple multiwavelength time-division multiplexed light source for sensing applications,” *Opt. Lett.*, vol. 33, no. 7, pp. 738–40, May 2008.
- [155] D. Baer, R. Hanson, M. Newfield, and N. Gopaul, “Multiplexed diode-laser sensor system for simultaneous H₂O, O₂, and temperature measurements,” *Opt. Lett.*, vol. 19, no. 22, pp. 1900–1902, 1994.
- [156] Y. Mao, S. Chang, E. Murdock, and C. Flueraru, “Simultaneous dual-wavelength-band common-path swept-source optical coherence tomography with single polygon mirror scanner,” *Opt. Lett.*, vol. 36, no. 11, pp. 1990–2, Jun. 2011.
- [157] M. E. Webber, J. Wang, S. T. Sanders, D. S. Baer, and R. K. Hanson, “In-situ Combustion Measurements of CO, CO₂, H₂O and Temperature Using Diode Laser Absorption Sensors,” vol. 28, pp. 1–24, 2000.
- [158] S. T. Sanders, J. A. Baldwin, T. P. Jenkins, D. S. Baer, and R. K. Hanson, “Diode-Laser Sensor for Monitoring Multiple Combustion parameters in pulse detonation engines,” *Proc. Combust. Inst.*, vol. 28, pp. 587–594, 2000.
- [159] R. M. Mihalcea, D. S. Baer, and R. K. Hanson, “Advanced diode laser absorption sensor for in situ combustion measurements of CO₂, H₂O, and gas temperature,” *Symp. Combust.*, vol. 27, no. 1, pp. 95–101, 1998.
- [160] E. R. Furlong, D. S. Baer, and R. K. Hanson, “Combustion control using a multiplexed diode-laser sensor system,” *Symp. Combust.*, vol. 26, no. 2, pp. 2851–2858, 1996.
- [161] C. N. Banwell and Elaine M. McCash, *Fundamentals of molecular spectroscopy*, 4th ed. McGraw-Hill, 1994.
- [162] H. Li, R. K. Hanson, and J. B. Jeffries, “Diode laser-induced infrared fluorescence of water vapour,” *Meas. Sci. Technol.*, vol. 15, pp. 1285–1290, 2004.
- [163] W. Demtröder, *Laser Spectroscopy: Vol. 1: Basic Principles*, vol. 1. Springer, 2008.
- [164] Stefan Welzel, *New Enhanced Sensitivity Infrared Laser Spectroscopy Techniques Applied to Reactive Plasmas and Trace Gas Detection*. 2009.
- [165] “OriginLab.” [Online]. Available: <http://www.originlab.com/doc>. [Accessed: 26-Aug-2015].
- [166] S. Welzel, “New enhanced sensitivity infrared laser spectroscopy techniques applied to reactive plasmas and trace gas detection,” p. 197, 2009.
- [167] W. Demtroder, *Laser Spectroscopy Vol. 1*, vol. 1. 2008.
- [168] R. Gamache and S. Kennedy, “Total internal partition sums for molecules in the terrestrial atmosphere,” *J. Mol. ...*, vol. 518, pp. 407–425, 2000.
- [169] A. L. Laraia, R. R. Gamache, J. Lamouroux, I. E. Gordon, and L. S. Rothman, “Total internal partition sums to support planetary remote sensing,” *Icarus*, vol. 215, no. 1, pp. 391–400, 2011.
- [170] J. Fischer, R. R. Gamache, a. Goldman, L. S. Rothman, and a. Perrin, “Total internal partition sums for molecular species in the 2000 edition of the HITRAN database,” *J. Quant. Spectrosc. Radiat. Transf.*, vol. 82, no. 1–4, pp. 401–412, 2003.

-
- [171] X. Zhou, X. Liu, J. B. Jeffries, and R. K. Hanson, "Development of a sensor for temperature and water concentration in combustion gases using a single tunable diode laser," *Meas. Sci. Technol.*, vol. 14, no. 8, pp. 1459–1468, 2003.
- [172] X. Zhou, J. B. Jeffries, and R. K. Hanson, "Development of a fast temperature sensor for combustion gases using a single tunable diode laser," *Appl. Phys. B Lasers Opt.*, vol. 81, no. 5, pp. 711–722, 2005.
- [173] M. G. Allen, K. L. Carleton, S. J. Davis, W. J. Kessler, C. E. Otis, D. a Palombo, and D. M. Sonnenfroh, "Ultrasensitive dual-beam absorption and gain spectroscopy: applications for near-infrared and visible diode laser sensors," *Appl. Opt.*, vol. 34, no. 18, pp. 3240–3249, 1995.
- [174] X. Liu, X. Zhou, J. B. Jeffries, and R. K. Hanson, "Experimental study of H₂O spectroscopic parameters in the near-IR (6940-7440 cm⁻¹) for gas sensing applications at elevated temperature," *J. Quant. Spectrosc. Radiat. Transf.*, vol. 103, no. 3, pp. 565–577, 2007.
- [175] B. C. Smith, "Quantitative Spectroscopy: Theory and Practice: Theory and Practice," 2002.
- [176] M. Silberberg, *Chemistry: the molecular nature of matter and change*. McGraw-Hill Higher Education, 2008.
- [177] A. L. Buck, "New equations for computing vapor pressure and enhancement factor," *J. Appl. Meteorol.*, vol. 20, pp. 1527–1532, 1981.
- [178] A. D. Poularikas, *The Transforms and Applications Handbook, Second Edition*. CRC Press, 2000.
- [179] F. Träger, *Springer Handbook of Lasers and Optics*, vol. 72. 2007.
- [180] W. A. Gambling, "The Rise and Rise of Optical Fibers," vol. 6, no. 6, pp. 1084–1093, 2000.
- [181] "Multicom Products and Solutions." [Online]. Available: <http://www.multicominc.com>.
- [182] B. Buchholz, N. Böse, and V. Ebert, "Absolute validation of a diode laser hygrometer via intercomparison with the German national primary water vapor standard," *Appl. Phys. B*, vol. 116, no. 4, pp. 883–899, 2014.
- [183] T. Tajiri, M. Murakami, N. Orikasa, A. Saito, and K. Kusunoki, "Laboratory Experiments of Ice Formation in."
- [184] K. E. Trenberth, J. T. Fasullo, and J. Kiehl, "Earth's Global Energy Budget," *Bull. Am. Meteorol. Soc.*, vol. 90, no. 3, pp. 311–323, 2009.
- [185] D. L. Mitchell, P. Rasch, D. Ivanova, G. McFarquhar, and T. Nousiainen, "Impact of small ice crystal assumptions on ice sedimentation rates in cirrus clouds and GCM simulations," *Geophys. Res. Lett.*, vol. 35, no. 9, pp. 1–5, 2008.
- [186] B. M. Sanderson, C. Piani, W. J. Ingram, D. a. Stone, and M. R. Allen, "Towards constraining climate sensitivity by linear analysis of feedback patterns in thousands of perturbed-physics GCM simulations," *Clim. Dyn.*, vol. 30, pp. 175–190, 2008.
- [187] S. Iacobellis and G. McFarquhar, "The sensitivity of radiative fluxes to parameterized cloud microphysics," *J. Clim.*, vol. 16, pp. 2979–2996, 2003.
- [188] B. J. Murray, D. O'Sullivan, J. D. Atkinson, and M. E. Webb, "Ice nucleation by particles immersed in supercooled cloud droplets," *Chem. Soc. Rev.*, vol. 41, no. 19, pp. 6519–54, 2012.
- [189] M. O. Andreae and D. Rosenfeld, "Aerosol–cloud–precipitation interactions.
-

- Part 1. The nature and sources of cloud-active aerosols," *Earth-Science Rev.*, vol. 89, no. 1–2, pp. 13–41, 2008.
- [190] K. M. Lau, "Warm rain processes over tropical oceans and climate implications," *Geophys. Res. Lett.*, vol. 30, no. 24, pp. 2–6, 2003.
- [191] M. . Yau and R. . Rogers, *A short course in cloud physics*. 1989.
- [192] B. J. Murray, T. W. Wilson, S. Dobbie, Z. Cui, S. M. R. K. Al-Jumur, O. Möhler, M. Schnaiter, R. Wagner, S. Benz, M. Niemand, H. Saathoff, V. Ebert, S. Wagner, and B. Kärcher, "Heterogeneous nucleation of ice particles on glassy aerosols under cirrus conditions," *Nat. Geosci.*, vol. 3, no. 4, pp. 233–237, 2010.
- [193] M. Niemand, O. Möhler, B. Vogel, H. Vogel, C. Hoose, P. Connolly, H. Klein, H. Bingemer, P. DeMott, J. Skrotzki, and T. Leisner, "A Particle-Surface-Area-Based Parameterization of Immersion Freezing on Desert Dust Particles," *J. Atmos. Sci.*, vol. 69, no. 10, pp. 3077–3092, Oct. 2012.
- [194] B. Ervens and G. Feingold, "On the representation of immersion and condensation freezing in cloud models using different nucleation schemes," *Atmos. Chem. Phys.*, pp. 5807–5826, 2012.
- [195] J. Sun and P. Ariya, "Atmospheric organic and bio-aerosols as cloud condensation nuclei (CCN): A review," *Atmos. Environ.*, vol. 40, no. 5, pp. 795–820, 2006.
- [196] H. R. Smith, P. J. Connolly, A. J. Baran, E. Hesse, A. R. D. Smedley, and A. R. Webb, "Cloud chamber laboratory investigations into scattering properties of hollow ice particles," *J. Quant. Spectrosc. Radiat. Transf.*, vol. 157, pp. 106–118, 2015.
- [197] E. Simpson, "First Year Report," University of Manchester.
- [198] D. J. Bösenberg, Jens, Brassington and P. C. Simon, *Instrument Development for Atmospheric Research and Monitoring*. 1997.
- [199] A. C. Eckbreth, "Laser Diagnostics for combustion temperature and species measurements," *J. Chem. Inf. Model.*, vol. 53, p. 160, 1989.
- [200] P. C. D. Hobbs and K. L. Haller, "Double beam laser absorption spectroscopy: shot-noise limited performance at baseband with a novel electronic noise canceller," *Optical Methods for Ultrasensitive Detection and Analysis: Techniques and Applications*. pp. 298–309, 1991.
- [201] C. Grupen and I. Buvat, *Handbook of Particle Detection and Imaging*. 2012.
- [202] J. L. Semmlow and B. Griffel, *Biosignal and Medical Image Processing, Third Edition*. 2014.
- [203] J. Hsieh, *Computed Tomography: Principles, Design, Artifacts, and Recent Advances*. 2003.
- [204] C. Ozdemir, *Inverse Synthetic Aperture Radar Imaging With MATLAB Algorithms*. 2012.
- [205] A. C. Kak and M. Slaney, "Principles of Computerized Tomographic Imaging Chpt2."
- [206] A. Staude and J. Goebbels, "Determining the Spatial Resolution in Computed Tomography – Comparison of MTF and Line-Pair Structures," *Int. Symp. Digit. Ind. Radiol. Comput. Tomogr.*, pp. 1–9, 2006.
- [207] A. C. Kak and Malcolm Slaney, *Principles of Computerized Tomographic Imaging*. IEEE Press, 1988.

10 Publications and achievements

10.1 University of Manchester

- PGR first year conference (Poster)
- PGR second year conference (Poster)
- PGR third year conference (Presentation)
 - Best presentation for segment prize

10.2 Others

- CPACT 2013 (Presentation)
- Chemical Engineering Day UK 2014
- FLAIR 2016 conference (Poster)
(Field Laser Applications in Industry and Research)

10.3 Pending publication

- Tomographic Image of reaction flows in 3D Laser Absorption Spectroscopy (Applied Physics B)
-

11 APPENDICES

11.1 Original horizontal slices for 3D tomography

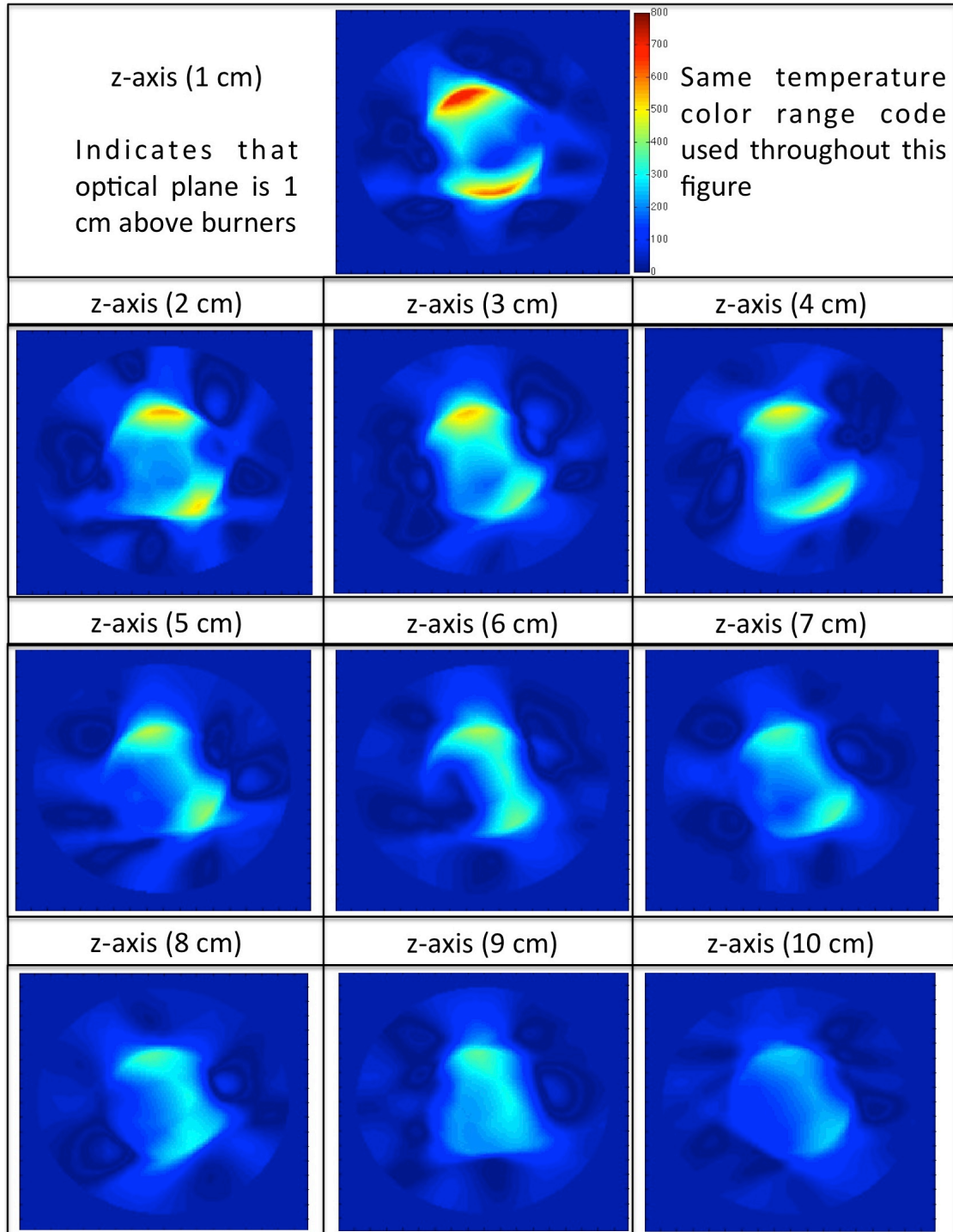


Figure 112 Individual 2D measurement slices in the z-axis.

11.2 TOMOGRAPHY MOTOR CONTROL AND DATA ACQUISITION

11.2.1 Overview

This portion of the appendix contains the LabVIEW program that controls the main experimental interface. It has 3 main purposes. The first is to control and command the speed and direction of rotation of the Rotator. The second is the pattern and frequency of the laser current generated. Finally it is the acquisition of data from the detectors as well as the saving of these data for further tomography processing. The front panel interface of the program is shown in Figure 113. The appendix will be organized into 4 smaller sections, following the flow of program's block diagram as depicted in Figure 114. The data acquisition of the work conducted in the MICC is similar in programming principle. Therefore only the tomography data acquisition is listed.

11.2.2 Motor operation loop

This section consists of a program to allow communication between the laptop and the motor control PCB board. This section requires downloading written VIs from Phidgets to facilitate the communication process.

This section begins by communicating with the PCB command board and checking which motors have been plugged to this board. It starts with an open VI, referenced with a unique number that corresponds to a motor. If there are several motors connected to the board, several VIs and their respective number will be needed.

The operational commands occur inside a while loop. Its control mechanism is fairly simple, and is represented by a single number. A middle arbitrary point of the motor needs to be found prior to experiment, and its exact number, although fairly close, are not the same. An example is that a comparison with the current experimental motor with a spare motor, their middle values is 87 and 91 respectively.

This middle value once keyed into the program represents 'zero' and the motor will not operate even though the power is on. Anything below this 'zero', for example operating at 70, will command the motor to turn anti-clockwise. Any value above 'zero' commands the motor to turn clockwise.

The speed of the rotation depends on the weight or load of the work, on the motor, as well as the distance the number keyed in away from 'zero'. The further away the value keyed from this 'zero' point, the faster it will rotate – until its maximum physical rotational speed after which the speed will be capped. Any further increment of value distance from 'zero' point will just allow the motor to rotate at its capped maximum speed.

This section of the command operates using an on/off toggle button, and is linked to the saving of data on/off toggle. The data will only save when the motor is operational. There is also a separate test motor on/off toggle button for testing the motor without saving data, as well as an overall motor loop shut down button.

11.2.3 Laser control

This section of codes controls the operation of the laser. VI1 controls maximum and minimum of the laser current. This is the first level of laser current maximum safety control, which prevents accidental programming current ramping past the laser's physical threshold.

VI2 as shown in Figure 115 controls the shape and frequency of the data ramping. The 'ampl' defines the gradient of the slope, while the offset defines the y intercept of the slope. The n0 represents the amount of data that rests at zero before the ramp is repeated. The total number of data points per spectrum is set at 200, so the laser will ramp for 180 data points from the y intercept at x=0 to maximum current before it drops to 0 and rest for 20 data points. The laser ramp shape follows the straight-line equation of $y = mx + c$. The total frequency (rate) is at 100000 data points per second.

11.2.4 Primary data acquisition loop

This section focuses on the data acquisition from the detectors. It starts off at the DAQ assistant where the synchronization of the laser output and detectors inputs is carried out. The DAQ assistant will also be triggered by an analog input of the laser current ramp as well.

The loop will show the triggering ramp as shown by the top left corner window. Beside this window, an initial example of the laser current ramp sampling can also be seen. The sampling is done in sets of 1000 data points, 5 times more than 200 data point ramps. This is because averaging of 5 would be done to over the detector inputs. The axes of these detector inputs are in data point units, and these axes will be converted by a polynomial relationship pre-calculated prior to the experiment. The final detector inputs are then presented as an averaged of 5 spectrums with relation to relative wavenumber axis.

11.2.5 Output save loop

The final loop contains the file saving loops. The file saving loop is triggered by the switching on/off of the motor operation. The file output will be in text form and will save the spectrums in columns. Each file represents a single parallel projection, consisting of a column of relative wavenumber x-axis, and 4 columns of rays (spectrums).

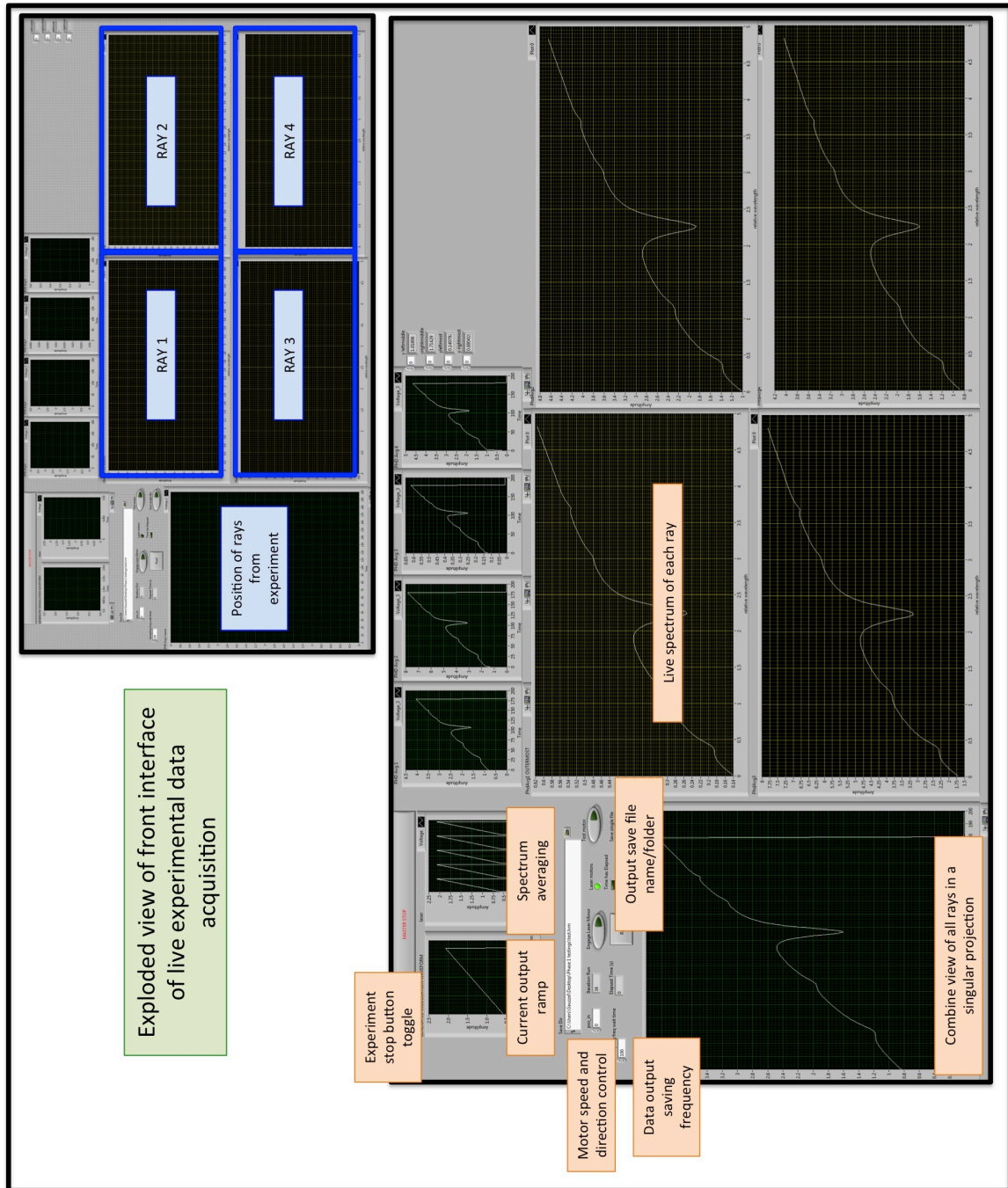


Figure 113 The front panel of the data acquisition program.

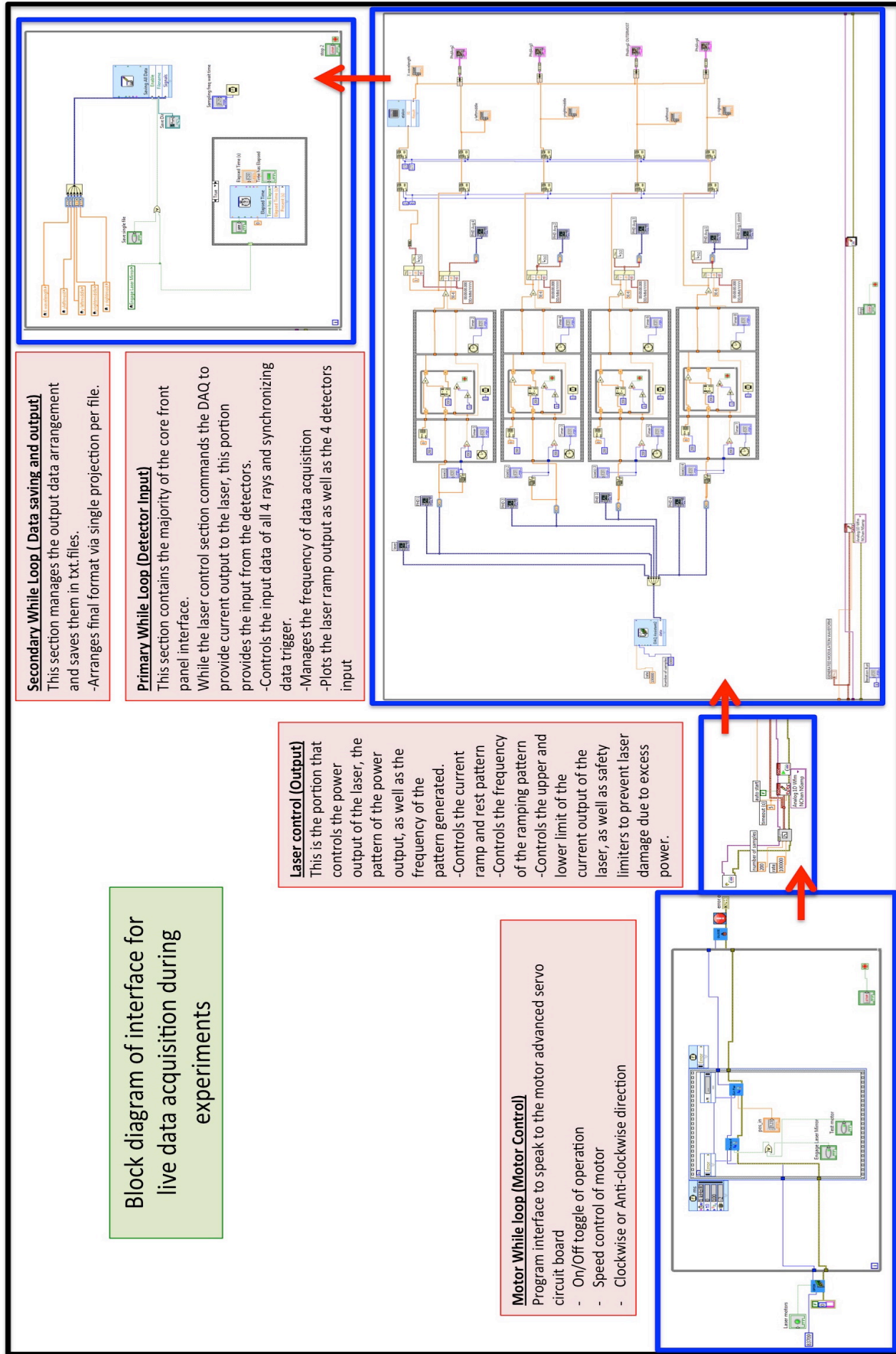
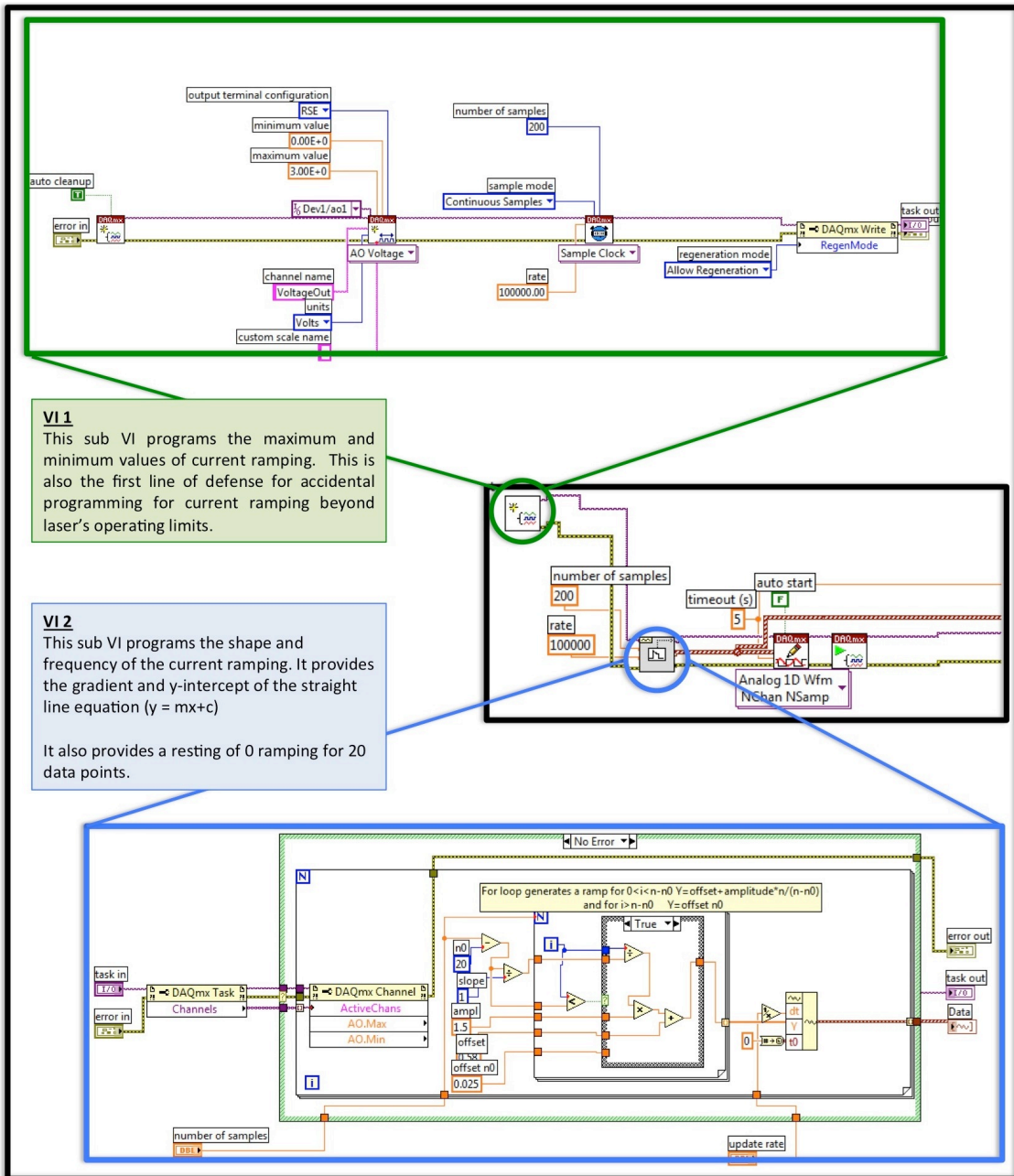


Figure 114 Block diagram of the program.



VI 1
 This sub VI programs the maximum and minimum values of current ramping. This is also the first line of defense for accidental programming for current ramping beyond laser's operating limits.

VI 2
 This sub VI programs the shape and frequency of the current ramping. It provides the gradient and y-intercept of the straight line equation ($y = mx+c$)
 It also provides a resting of 0 ramping for 20 data points.

Figure 115 Exploded version of the laser current output section from the block diagram.

11.3 SPECTRUM FITTING

11.3.1 Overview

This portion of the appendix focuses on the LabVIEW program used for fitting of the transmission spectrums from the tomography experiments as shown in Figure 116. It will be divided into 3 sub-sections, the first section consist of a While Loop, which comprises of opening the folder containing all the individual projection files. The next one is the For Loop, which processes each ray individually from each projection. The final section consists of a file saving section where the integrated absorbance of all the spectrum peaks are written into output files. The fitting of transmission spectrum conducted in the MICC is similar in programming principle. Therefore only the fitting program used for tomography experiments is listed.

11.3.2 While-loop used to open projection files

This section consists of a while-loop that encompasses the rest of the program. However, the sections of codes that are being focused in this section are contained in the upper left corner of Figure 117. It starts by opening the primary folder storing the projection files and counting the total amount of files inside the folder. The amount is fed into the for-loop as an iteration number. There is also a conversion of the point base x-axis to a relative wavenumber scale.

11.3.3 For-loop to separate and process ray data

The projection files are individually opened inside the for-loop based on the projection / iteration number. The file is then arranged to 4 separate arrays, with each array a spectrum from each ray. Each of the arrays is then fed into their own true/false cases. The true / false cases are decided by if the there are any data inside the particular array. During the experiment, if the ray is being blocked by the Carrier's structure, the detector will record the spectrum as an array of zeros.

The case will detect that if the array's maximum value is less than 0.1, the case will switch to a false and fitting of spectrum will not occur. The peak values will be set to zero and sent to the end of the next portion of the program. If there is a spectrum, then the array's maximum value will be more than 0.1. In this scenario, the transmission fitting of the spectrum will occur.

First, the spectrum's centre will be detected by using first order derivative method. The spectrum will be centred at the maximum of Peak 3. A small amount of cropping is done to remove the extreme ends of the spectrum before non-linear curve fitting is carried out. The cropping is decided prior to experiment to make sure that the wings of the extreme peaks are not removed accidentally.

The non-linear curve fit is carried out with a customised curve fit model as shown in Figure 118. This non-linear curve fit is capped by upper and lower bounds, which are also experimental pre-calibrated to make sure that the bounds are suitable for a variety of experimental situations. An error message will be generated should the fit be unsuccessful. After the transmission fitting of

the spectrum is carried out, the peaks will be sent out of the case and into the for-loop. Once out of the for-loop, the values will be sent to a waiting matrix before being written into the output file.

11.3.4 File saving

The projection files are individually opened inside the for-loop based on the projection / iteration number. The file is then arranged to 4 separate arrays, with each array a spectrum from each ray. Each of the arrays is then fed into their own true/false cases. The true / false cases are decided

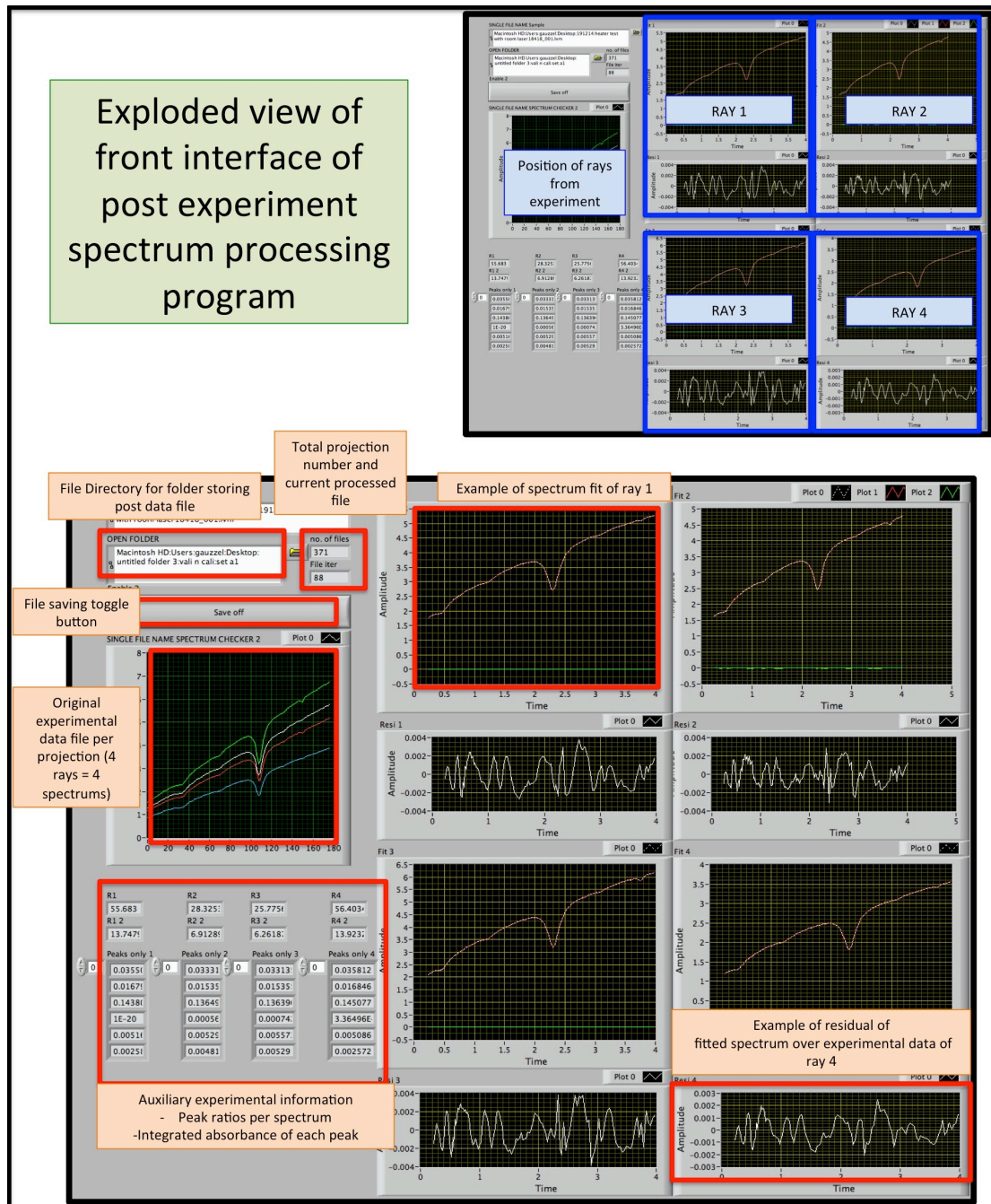


Figure 116 Front panel of the peak-fitting program.

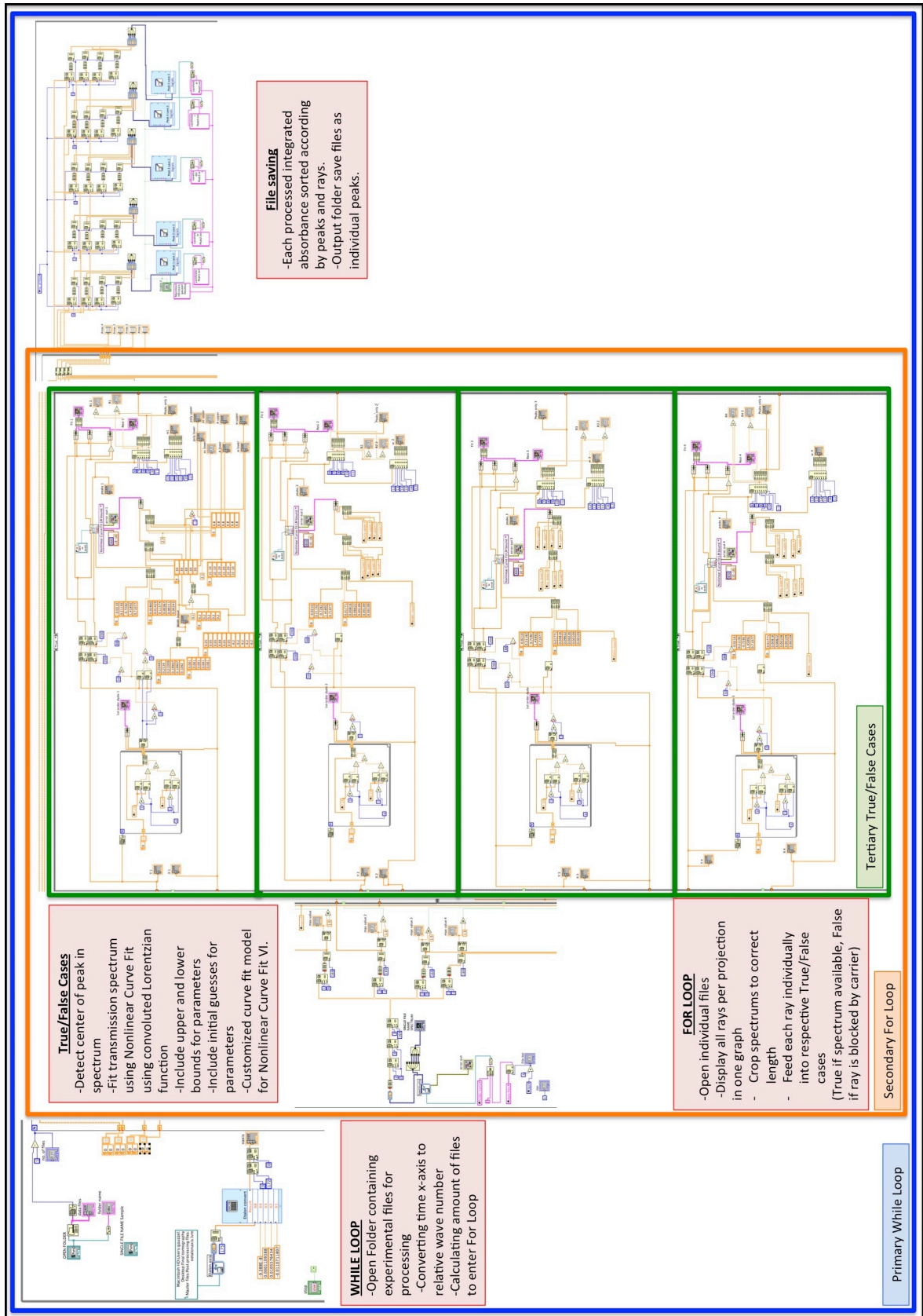


Figure 117 The block diagram of the peak-fitting program.

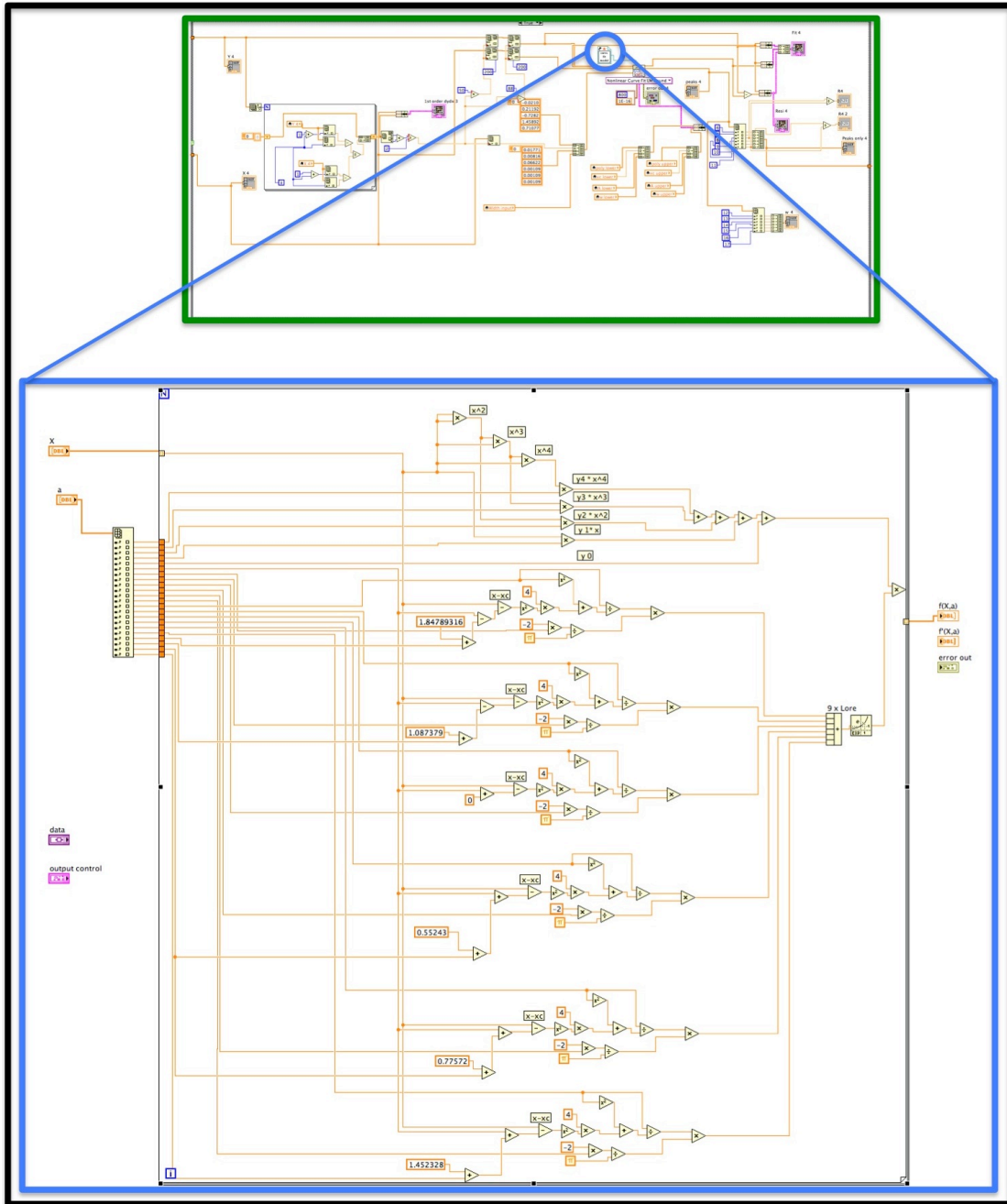


Figure 118 The expanded sub-VI block diagram of the curve fitting model.

11.4 FILTERED BACK PROJECTION (FBP) USING MATLAB

11.4.1 Overview

This MATLAB program begins from the opening of processed integrated absorbance processed prior by LabVIEW and reconstructing temperature and concentration spatial distribution images using the Filtered Back Projection (FBP) technique. This appendix chapter will be broken down to 7 sections to aid in program explanation.

11.4.2 Prepping data for reconstruction

The first section involves opening and priming the data for reconstruction. The data consists of 4 rows of integrated absorbance with arbitrary number of columns. Each single column represents a single projection at a certain degree (theta) while each row on each column represents individual laser ray / detector reading.

The program begins by clearing previous data and opening the correct data files. Peak 3 and 5 were discussed earlier as the prime candidates for two-line thermometry and therefore only these two peaks were opened. They will be labelled as rays3 and rays5 respectively. The two data sets, rays3 and rays5, will change as data priming modifies the information down the program.

Numstep specifies the amount of projections there are in total in the experiment.

thetas is a vector of each individual theta increment with respect to step size and their projection location.

avg3 is used as a reference for integrated absorbance of peak 3 to normal room conditions at time of experiment without heat interference. (External boundary value)

avg5 is used as a reference for integrated absorbance of peak 5 to normal room conditions at time of experiment without heat interference. (External boundary value)

rays3 changes over the course of the program. While initially just a matrix of 4 rows and an arbitrary amount of columns, it changes to matrix of 8 columns with same number of rows. The room temperature reference is added to the start and end of the matrix as an assumption that anything outside a boundary are room conditions.

rays5 changes over the course of the program. While initially just a matrix of 4 rows and an arbitrary amount of columns, it changes to matrix of 8 columns with same number of rows. The room temperature reference is added to the start and end of the matrix as an assumption that anything outside a boundary are room conditions.

11.4.3 Interpolation of data in between rays

This section is about filling the data in between the rays. One of the restrictions was that there were insufficient physical detectors and laser sources to form a higher projection-sampling rate. It was therefore assumed that it would be considered accurate enough to approximate the change between each known ray position by a linear relationship. This was based on 2 points, the first where the approximations are only for 3 data points provided that 1 cm is the step size.

E.g. For known x_1 at 3 cm and x_2 at 7 cm, the approximated integrated absorption linear guesses would be at 4 cm, 5 cm and 6 cm.

The second point would be that the accuracy of the final image would be balanced out by increasing the amount of projections instead.

interpo1 is the method choice of approximating data between known points. The method chosen was 'linear'.

taxis is the length of the measurement space. The total length of projection is 37 cm. However the centre point is cantered at 0 cm, and therefore the range will be from -18 cm to 18 cm.

zerologic3 identifies the rays in each loop that are partially blocked by the carrier and removes them during the interpolation process.

interay3 is the final product of approximating the integrated absorbance at every 1cm step size. The format of this matrix is 37 rows of integrated absorbance per every column. The column size depends on the amount of projections taken during experiment.

zerologic5 identifies the rays in each loop that are partially blocked by the carrier and removes them during the interpolation process.

interay5 is the final product of approximating the integrated absorbance at every 1cm step size. The format of this matrix is 37 rows of integrated absorbance per every column. The column size depends on the amount of projections taken during experiment.

for i = 1 to last projection

- A.1. zerologic3 / zerologic5 - Find the zeros (all blocked rays) in each column and remove them
- A.2. Allocate the positions of each remaining data in the column (which 'cm' do they belong to)
- A.3. interay3 / interay5 – Interpolate the data so that every 'cm' contains a value of integrated absorbance.

end

11.4.4 Decreasing the interval between each step size

This section of the program could be removed unless there is a desire to alter the tightness of data in each projection. By reducing the step size between each ray, it is essentially increasing the amount of data per projection. Because the interpolations between the 4 original points are linearly approximated, increasing the data point changes little on the actual shape of the final reconstruction. However, a tighter projection yields a sharper reconstructed image due to an increase in final grid resolution.

querysteps contains the range between the extreme values of the projection, namely -18 cm to 18 cm. Step (1-6) determines the size of the step size from 1 cm to 0.03125 cm.

interay3 the newly interpolated projections with smaller step size between each ray.

interay5 the newly interpolated projections with smaller step size between each ray.

for i = 1 to last projection

1. Interpolate the distance between each data point with a specified value (step (1-6)).

end

11.4.5 Creating the filter

This section is about building the impulse response of the ramp filter as shown by Kak [207].

numofinterrays is the new number of rays per projection.

rampFilter is the constructed ramp filter from -18 cm to 18 cm, with 0 the lowest value.

impRes is the impulse response of the ramp filter, with the highest point at 0 cm.

11.4.6 Reconstruction

This section is about taking the primed initial data to reconstruct the two images of peaks 3 and 5. Upon reconstruction, the two-line thermometry technique is initiated by dividing each grid over each other.

sinogram3 is averaged of interay3. Each of the individual integrated absorbance value of interay3 has been averaged according to the path length.

sinogram5 is averaged of interay5. Each of the individual integrated absorbance value of interay5 has been averaged according to the path length.

Eg.1 The path length is 37 cm, and the laser passes through a total of 37 cells to complete the path length, the averaged integrated absorbance of each cell is the original starting amount divided by 37.

Eg.2 If the path length is 37cm, and the laser passes through a total of 75 cells to complete this path length (because the cells are half the size), then the averaged integrated absorbance of each cell is the original starting amount divided by 75.

numofrays is the number of rays per projection in the sinogram3 and sinogram5.

degreestepsize is amount of back smearing loops.

thetas is now the value of degrees increment in radians.

middlecell is the centre number of the grid in both x and y axis.

filtered3 is the sinogram3 where its projections have been individually filtered.

filtered5 is the sinogram5 where its projections have been individually filtered.

newcords is the index of where each data should be placed during the back smearing process.

img3 is initially an empty grid, constructed to conserve memory, and later the reconstructed grid of peak 3 after the back smearing process.

img5 is initially an empty grid, constructed to conserve memory, and later the reconstructed grid of peak 3 after the back smearing process.

ratioimg is the grid constructed by dividing img5 with img3 and later used for constructing temperature using the ratio to temperature relationship.

for i = 1 to last projection

1. Calculate the indexes for which angle the projection needs to be smeared based on projection with respect to theta.
2. Convolute the projection with the filter
3. Back smear the filtered projection across the image based on projection angle.

end

11.4.7 Recovery of spatial temperature distribution

The relationship between ratios of peaks to temperature has already been pre-calculated as a polynomial order-6 equation.

p_6 to p_0 depicts the coefficients of the polynomial equation respectively. p_6 corresponds to the polynomial coefficient of x^6 while p_0 corresponds to the polynomial coefficient x^0 .

Temping is the reconstructed grid of temperature.

11.4.8 Recovery of spatial concentration distribution

Line strengths have their behavioural dependent on temperature, and peak 3 and 5 have their line strength to temperature behaviour categorized under their polynomial relationship coefficients of S_a and S_b . They will be used to calculate individual grids of integrated absorbance and finally a grid of concentration of mole per cm^3 .

S_{6a} to S_{0a} depicts the coefficients of the polynomial equation for line strengths of peak 3 to temperature respectively. S_{6a} corresponds to the polynomial coefficient of x^6 while S_{0a} corresponds to the polynomial coefficient x^0 .

S_{6b} to S_{0b} depicts the coefficients of the polynomial equation for line strengths of peak 5 to temperature respectively. S_{6b} corresponds to the polynomial coefficient of x^6 while S_{0b} corresponds to the polynomial coefficient x^0 .

S_a is the reconstructed grid of line strength of peak 3 with respect to temperature.

S_b is the reconstructed grid of line strength of peak 5 with respect to temperature.

c_1 is initially the reconstructed grid of integrated absorbance of peak 3 and later converted to concentration of mole per cm^3 .

C_2 is initially the reconstructed grid of integrated absorbance of peak 5 and later converted to concentration of mole per cm^3 .

IC2 is setting the values outside a certain boundary size as the average room conditions measured prior to experiment.

11.4.9 MATLAB codes

Below is the compilation of the program used to reconstruct temperature and concentration spatial distribution.


```

step2=step1/2;
step3=step2/2;
step4=step3/2;
step5=step4/2;
step6=step5/2;

querysteps= [-18 :step1:18];

for i=1:Numstep

    reso3=interay3(:,i);
    interay3(:,i)=interp1(taxis,reso3,querysteps(:),interpo1);

    reso5=interay5(:,i);
    interay5(:,i)=interp1(taxis,reso5,querysteps(:),interpo1);

end

%%%%%%%%%%%%%%%%%%%%%%%%%%%%%%%%%%%%%%%%%%%%%%%%%%%%%%%%%%%%%%%%%%%%%%%%
%%%%%%%%%%%%%%%%%%%%%%%%%%%%%%%%%%%%%%%%%%%%%%%%%%%%%%%%%%%%%%%%%%%%%%%%
% E.4 Creating the filter
%%%%%%%%%%%%%%%%%%%%%%%%%%%%%%%%%%%%%%%%%%%%%%%%%%%%%%%%%%%%%%%%%%%%%%%%
%%%%%%%%%%%%%%%%%%%%%%%%%%%%%%%%%%%%%%%%%%%%%%%%%%%%%%%%%%%%%%%%%%%%%%%%

numofinterrays=size((interay5(:,1)));

rampFilter = [floor(numofinterrays-1/2):-1:0 1: ...
    ceil(numofinterrays-1/2-1)];
impRes = abs(fftshift(fft(rampFilter)));

%%%%%%%%%%%%%%%%%%%%%%%%%%%%%%%%%%%%%%%%%%%%%%%%%%%%%%%%%%%%%%%%%%%%%%%%
%%%%%%%%%%%%%%%%%%%%%%%%%%%%%%%%%%%%%%%%%%%%%%%%%%%%%%%%%%%%%%%%%%%%%%%%
% E.5 Peak image reconstruction and ratio grid
%%%%%%%%%%%%%%%%%%%%%%%%%%%%%%%%%%%%%%%%%%%%%%%%%%%%%%%%%%%%%%%%%%%%%%%%
%%%%%%%%%%%%%%%%%%%%%%%%%%%%%%%%%%%%%%%%%%%%%%%%%%%%%%%%%%%%%%%%%%%%%%%%

sinogram3=interay3/37;
sinogram5=interay5/37;

numofrays = size(sinogram3,1);
degreestepsize = length(thetas);
thetas = (pi/180)*thetas;

img3 = zeros(numofrays,numofrays);
img5=img3;
middlecell = floor(numofrays/2) + 1;

[xcord,ycord] = meshgrid(ceil(-numofrays/2):ceil(numofrays/2-1));

```

```

figure
plot(conv(sinogram3(:,1),impRes,'same'));
set(gca,'FontSize',15)
title({' Filtered Integrated absorbances ', 'of Peak 1 at theta=0'})
xlabel('Spatial x-axis (cm)')
ylabel('Integrated Absorbances')

figure
plot(conv(sinogram5(:,1),impRes,'same'));
set(gca,'FontSize',15)
title({' Filtered Integrated absorbances ', 'of Peak 2 at theta=0'})
xlabel('Spatial x-axis (cm)')
ylabel('Integrated Absorbances')

for i = 1:degreestepsize

    Rotacords = round(middlecell + xcord*sin(thetas(i)) +
ycord*cos(thetas(i)));

    indexes = find((Rotacords > 0) & (Rotacords <= numofrays));
    newcords = Rotacords(indexes);

    filtered3 = conv(sinogram3(:,i),impRes,'same');
    filtered5 = conv(sinogram5(:,i),impRes,'same');

    img3(indexes) = img3(indexes) +
filtered3(newcords)./degreestepsize;
    img5(indexes) = img5(indexes) +
filtered5(newcords)./degreestepsize;

end

img3=interp2(imrotate(img3,90),3);
img5=interp2(imrotate(img5,90),3);
ratioimg=(img5./img3);

figure;
imagesc(img3)
set(gca,'FontSize',15)
title('Reconstructed space domain of Peak 1 Integrated absorbance')
xlabel('Spatial x-axis (cm)')
ylabel('Spatial y-axis (cm)')
atick = 0:16.5:289;
set(gca,'XTick',atick);
set(gca,'XTickLabel', -18:2:18);
set(gca,'YTick',atick);
set(gca,'YTickLabel', -18:2:18);
colorbar;

```

```

figure;
imagesc(img5)
set(gca,'FontSize',15)
title('Reconstructed space domain of Peak 2 Integrated absorbance')
xlabel('Spatial x-axis (cm)')
ylabel('Spatial y-axis (cm)')
atick = 0:16.5:289;
set(gca,'XTick',atick);
set(gca,'XTickLabel', -18:2:18);
set(gca,'YTick',atick);
set(gca,'YTickLabel', -18:2:18);
colorbar;

%%%%%%%%%%%%%%%%%%%%%%%%%%%%%%%%%%%%%%%%%%%%%%%%%%%%%%%%%%%%%%%%%%%%%%%%
%%%%%%%%%%%%%%%%%%%%%%%%%%%%%%%%%%%%%%%%%%%%%%%%%%%%%%%%%%%%%%%%%%%%%%%%
% E.6 Temperature Reconstruction
%%%%%%%%%%%%%%%%%%%%%%%%%%%%%%%%%%%%%%%%%%%%%%%%%%%%%%%%%%%%%%%%%%%%%%%%
%%%%%%%%%%%%%%%%%%%%%%%%%%%%%%%%%%%%%%%%%%%%%%%%%%%%%%%%%%%%%%%%%%%%%%%%

p6=-709855.907012939000000;
p5= 1085192.157869590000000;
p4=-658289.120775743000000;
p3= 203447.875269558000000;
p2=-34437.822782179300000;
p1= 4455.665047719480000;
p0=- 27.135186464977200;
Tempimg=p6.*ratioimg.^6+p5.*ratioimg.^5+p4.*ratioimg.^4 ...
+p3.*ratioimg.^3+p2.*ratioimg.^2+p1.*ratioimg+p0;
Tempimg=abs(Tempimg);

figure;
imagesc(Tempimg)
set(gca,'FontSize',14)
title({'Reconstructed temperature ','spatial distribution'})
xlabel('Spatial x-axis (cm)')
ylabel('Spatial y-axis (cm)')
atick = 0:16.5:289;
set(gca,'XTick',atick);
set(gca,'XTickLabel', -18:2:18);
set(gca,'YTick',atick);
set(gca,'YTickLabel', -18:2:18);
colorbar;

figure
surf(Tempimg,'EdgeColor','none','LineStyle','none','FaceLighting','phong')
% view ([20 ,20 ,20])z
set(gca,'FontSize',15)
title({'Reconstructed temperature ','spatial distribution'})

```

```

xlabel('Spatial x-axis (cm)')
ylabel('Spatial y-axis (cm)')
atick = 0:16.5:289;
set(gca,'XTick',atick);
set(gca,'XTickLabel', -18:2:18);
set(gca,'YTick',atick);
set(gca,'YTickLabel', -18:2:18);
colorbar;

%%%%%%%%%%%%%%%%%%%%%%%%%%%%%%%%%%%%%%%%%%%%%%%%%%%%%%%%%%%%%%%%%%%%%%%%
% E.7 Concentration Reconstruction
%%%%%%%%%%%%%%%%%%%%%%%%%%%%%%%%%%%%%%%%%%%%%%%%%%%%%%%%%%%%%%%%%%%%%%%%

S6a=1.001480677006320E-38;
S5a= - 4.808084724561820E-35;
S4a=9.779820441422530E-32;
S3a= - 1.134086269659360E-28;
S2a=8.579527934951380E-26;
S1a= - 4.583700302199190E-23;
S0a= 1.593361318180310E-20;
Sa=S6a.*Tempimg.^6+S5a.*Tempimg.^5+S4a.*Tempimg.^4+...
  S3a.*Tempimg.^3+S2a.*Tempimg.^2+S1a.*Tempimg+S0a;

S6b=1.239167826939600E-38;
S5b= - 4.512478267044460E-35;
S4b=6.703722821440790E-32;
S3b= - 4.913179836378700E-29;
S2b= 1.412754760610980E-26;
S1b= 2.114604138705740E-24;
S0b= 1.327648970193470E-22;
Sb=S6b.*Tempimg.^6+S5b.*Tempimg.^5+S4b.*Tempimg.^4+S3b.*Tempi
mg.^3 ...
  +S2b.*Tempimg.^2+S1b.*Tempimg+S0b;

%no need divide by L cause this is per unit length via grid already
c1=(img3./Sa);
c2=(img5./Sb);

c1=c1/6.022E23;
c2=c2/6.022E23;

%Constructing X and Y axis/matrix
N=size(c1,1);
%number of points for corresponding to zero on axis
center = floor ((N+1)/2);
%value of minimum x axis value

```

```

xleft=-center+1;
%true x axis scale, min to zero to max
x=(1:N)-1+xleft;
%Repeat till full x dimension is plotted
x= repmat(x,N,1);
%repeat same steps for Y except top to bottom
ytop=center-1;
y=(N:-1:1).'-N+ytop;
y= repmat(y,1,N);
sca=(N-1)/2 -4;
boundary=sca-0.01;

IC= sqrt((x).^2+(y).^2)>=boundary;
c1(IC)=c1(150,5);
c2(IC)=c2(150,5);

figure;imagesc(c1)
set(gca,'FontSize',15)
title({'Reconstructed concentration peak 1', ...
      '(mole/cm ^3) spatial distribution'})
xlabel('Spatial x-axis (cm)')
ylabel('Spatial y-axis (cm)')
atick = 0:16.5:289;
set(gca,'XTick',atick);
set(gca,'XTickLabel', -18:2:18);
set(gca,'YTick',atick);
set(gca,'YTickLabel', -18:2:18);
colorbar;

figure;imagesc(c2)

set(gca,'FontSize',15)
title({'Reconstructed concentration peak 2', ...
      '(mole/cm ^3) spatial distribution'})
xlabel('Spatial x-axis (cm)')
ylabel('Spatial y-axis (cm)')
atick = 0:16.5:289;
set(gca,'XTick',atick);
set(gca,'XTickLabel', -18:2:18);
set(gca,'YTick',atick);
set(gca,'YTickLabel', -18:2:18);
colorbar;

%%%%%%%%%%
% end
%%%%%%%%%%

```

11.5 FOURIER SLICE RECONSTRUCTION (FSR) USING MATLAB

11.5.1 Overview

This MATLAB program begins from the opening of processed integrated absorbance processed prior by LabVIEW and reconstructing temperature and concentration spatial distribution images using the Fourier Slice Reconstruction (FSR) technique. This appendix chapter will be broken down to 7 sections to aid in program explanation.

11.5.2 Pre-processing data for reconstruction

This portion of the program is the same as the FBP process and could be found in section 11.4.2

11.5.3 Interpolation of data in between rays

This portion of the program is the same as the FBP process and could be found in section 11.4.3

11.5.4 Decreasing the interval between each step size

This portion of the program is the same as the FBP process and could be found in section 11.4.4.

11.5.5 Zero padding the data

Zero padding aids in removing artifacts from the final reconstructed image. This portion discusses the zero padding process.

vm3 is to remember the original non-padded interay3 for cropping of image later on in the program.

vm5 is to remember the original non-padded interay5 for cropping of image later on in the program.

padamt is the amount of zeros to pad at the ends of each projection.

sinogram3 started of exactly as interay3 but by the end of this section is now zero padded and ready for reconstruction.

sinogram5 started of exactly as interay5 but by the end of this section is now zero padded and ready for reconstruction.

11.5.6 Filtering and reconstruction

This section is about creating the filter and executing the Fourier slice theorem. Once images reconstructed from peaks 3 and 5 are achieved, the ratio of the grids are calculated to perform two-line thermometry in the next section.

amountofrays is the amount of rays per projection in sinogram3 and sinogram5.

amountofprojections is the amount projections in sinogram3 and sinogram5.

thetas is now the value of degrees increment in radians.

imageprime is the pre-calculated image in zeros to conserve computational power.

middlecell is the center number of the grid in both x and y axis.

rampFilter is the constructed ramp filter from -18 cm to 18 cm, with 0 the lowest value.

newcords is the index of where each data should be placed during the back smearing process.

filteredProfilea is the multiplication of the rampFilter to each projections in sinogram3.

filteredProfileb is the multiplication of the rampFilter to each projections in sinogram5.

for i = 1 to last projection

1. Calculate the indexes for which angle the projection needs to be allocated based on projection with respect to theta.
2. FFT (fast Fourier transform) the projections and multiply them with the rampFilter.
3. Inverse FFT the filtered projection
4. Back smear the filtered projection to the image based on projection angle.

end

snew is the new size of zero padded reconstructed images.

syup the new middle cell of zero padded reconstructed images.

img3 is initially an empty grid, constructed to conserve memory, and later the reconstructed zero padded grid of peak 3 after the Fourier slice reconstruction. The end of this section shows the zero padded borders cropped

off, revealing the final image in its correct size.

img5 is initially an empty grid, constructed to conserve memory, and later the reconstructed zero padded grid of peak 5 after the Fourier slice reconstruction. The end of this section shows the zero padded borders cropped off, revealing the final image in its correct size.

11.5.7 Recovery of spatial temperature distribution

This portion of the program is the same as the FBP process and could be found in section 11.4.7.

11.5.8 Recovery of spatial concentration distribution

This portion of the program is the same as the FBP process and could be found in section 11.4.8.

11.5.9 Fourier slice reconstruction (FSR) MATLAB codes

Below is the compilation of the program used to reconstruct the temperature and concentration spatial distributions.

```

%%%%%%%%%%%%%%%%%%%%%%%%%%%%%%%%%%%%%%%%%%%%%%%%%%%%%%%%%%%%%%%%%%%%%%%%
%%%%%%%%%%%%%%%%%%%%%%%%%%%%%%%%%%%%%%%%%%%%%%%%%%%%%%%%%%%%%%%%%%%%%%%%
% Start Fourier Slice Reconstruction
%%%%%%%%%%%%%%%%%%%%%%%%%%%%%%%%%%%%%%%%%%%%%%%%%%%%%%%%%%%%%%%%%%%%%%%%
%%%%%%%%%%%%%%%%%%%%%%%%%%%%%%%%%%%%%%%%%%%%%%%%%%%%%%%%%%%%%%%%%%%%%%%%

clear
clc

%%%%%%%%%%%%%%%%%%%%%%%%%%%%%%%%%%%%%%%%%%%%%%%%%%%%%%%%%%%%%%%%%%%%%%%%
%%%%%%%%%%%%%%%%%%%%%%%%%%%%%%%%%%%%%%%%%%%%%%%%%%%%%%%%%%%%%%%%%%%%%%%%
% F.1 Opening file and data priming
%%%%%%%%%%%%%%%%%%%%%%%%%%%%%%%%%%%%%%%%%%%%%%%%%%%%%%%%%%%%%%%%%%%%%%%%
%%%%%%%%%%%%%%%%%%%%%%%%%%%%%%%%%%%%%%%%%%%%%%%%%%%%%%%%%%%%%%%%%%%%%%%%

fileID = fopen('Peak3.txt','r');
formatSpec = '%f %f %f %f';
sizeA = [4 Inf];
rays3 = fscanf(fileID,formatSpec,sizeA);
fclose(fileID);

fileID = fopen('Peak5.txt','r');
formatSpec = '%f %f %f %f';
sizeA = [4 Inf];
rays5 = fscanf(fileID,formatSpec,sizeA);
fclose(fileID);

```

```

rays3=rays3';
Numfile=size(rays3);
Numstep=Numfile(1);
rays3=rays3';

Stepsize=179/(Numstep-1);
StartTheta = 0;
EndTheta = 179;
thetas= StartTheta:Stepsize:EndTheta;

avg3=0.1464;
raysavg1a=zeros(1,Numstep);
raysavg1a(:,:)=avg3;
rays3= [raysavg1a;raysavg1a;rays3;raysavg1a;raysavg1a];

avg5=0.0025;
raysavg5a=zeros(1,Numstep);
raysavg5a(:,:)=avg5;
rays5= [raysavg5a;raysavg5a;rays5;raysavg5a;raysavg5a];

%%%%%%%%%%%%%%%%%%%%%%%%%%%%%%%%%%%%%%%%%%%%%%%%%%%%%%%%%%%%%%%%%%%%%%%%
%      F.2      Interpolation      of      data      in      between      rays
%%%%%%%%%%%%%%%%%%%%%%%%%%%%%%%%%%%%%%%%%%%%%%%%%%%%%%%%%%%%%%%%%%%%%%%%

interpo1='linear';
taxis = [-18 :1:18];
scale=[-18 -8 -7 -3 3 7 8 18];
s=scale';
s = scale(3:6);
sA = scale(1:2);
sB = scale(7:8);

for i=1:Numstep

    ray3 = rays3(:,i);
    r3 = ray3 (3:6);
    ray3A = ray3 (1:2);
    ray3B = ray3 (7:8);
    zerologic3 =r3~=0 ;
    r3 =r3(zerologic3);
    s3 =s(zerologic3) ;
    r3 = [ray3A;r3;ray3B] ;
    s3 = [sA s3 sB ] ;

    interay3(:,i)=interp1(s3,r3,taxis(:),interpo1);
    interay3(isnan(interay3)) = 0;

```

```

%%%%%%%%%%%%%%%%%%%%%%%%%%%%%%%%%%%%%%%%%%%%%%%%%%%%%%%%%%%%%%%%%%%%%%%%
sinogram3=interay3;
sinogram5=interay5;
sinogramori=size(sinogram3,1);

vm3=(sinogram3(:,1));
vm5=(sinogram5(:,1));

padamt=300;

sinogram3=padarray(sinogram3,padamt);
sinogram5=padarray(sinogram5,padamt);

%%%%%%%%%%%%%%%%%%%%%%%%%%%%%%%%%%%%%%%%%%%%%%%%%%%%%%%%%%%%%%%%%%%%%%%%
%%%%%%%%%%%%%%%%%%%%%%%%%%%%%%%%%%%%%%%%%%%%%%%%%%%%%%%%%%%%%%%%%%%%%%%%
% F.5 Creating filter, executing Fourier Slice Theorem and ratio grid
%%%%%%%%%%%%%%%%%%%%%%%%%%%%%%%%%%%%%%%%%%%%%%%%%%%%%%%%%%%%%%%%%%%%%%%%
%%%%%%%%%%%%%%%%%%%%%%%%%%%%%%%%%%%%%%%%%%%%%%%%%%%%%%%%%%%%%%%%%%%%%%%%

amountofrays=size(sinogram3,1);
amountofprojections = length(thetas);

thetas = (pi/180)*thetas;
imageprime = zeros(amountofrays,amountofrays);

middlecell = floor(amountofrays/2) + 1;
[xcoords,ycoords] = meshgrid(ceil(-amountofrays/2) ...
    :ceil(amountofrays/2-1));

img3=imageprime;
img5=imageprime;

% set up filter
rampFilter = [floor(amountofrays/2):-1:0 1:ceil(amountofrays/2-1)];
rampFilter = rampFilter/(max(rampFilter));

figure
plot(abs(fftshift( ifft( ifftshift(rampFilter.*(fftshift(fft ...
    (ifftshift(sinogram3(:,1))))))))))
set(gca,'FontSize',15)
title({' Filtered Integrated absorbances ', 'of Peak 1 at ', 'theta=0'})
xlabel('Zeropadded x-axis')
ylabel('Integrated Absorbances')
% atick = 0:19.2:355;
% set(gca,'XTick',atick);
% set(gca,'XTickLabel', -36:4:36);

```

```

figure
plot(abs(fftshift( ifft(fftshift(rampFilter.*(fftshift(fft ...
    (fftshift(sinogram5(:,2))))))))))
set(gca,'FontSize',15)
title({' Filtered Integrated absorbances ', 'of Peak 2 at ', 'theta=0'})
xlabel('Zeropadded x-axis')
ylabel('Integrated Absorbances')
% atick = 0:19.2:355;
% set(gca,'XTick',atick);
% set(gca,'XTickLabel', -36:4:36);

for i = 1:amountofprojections
    rotatecords = round(middlecell + xcords*sin(thetas(i)) ...
        + ycords*cos(thetas(i)));
    indexes = find((rotatecords > 0) & (rotatecords <= ...
        amountofrays));
    newcords = rotatecords(indexes);

    filteredProfilea=(abs(fftshift( ifft(fftshift(rampFilter.* ...
        (fftshift(fft(fftshift ...
        (sinogram3(:,i))))))))));
    img3(indexes) = img3(indexes) + filteredProfilea(newcords)./ ...
        amountofprojections;

    filteredProfileb=(abs(fftshift( ifft(fftshift(rampFilter.* ...
        (fftshift(fft(fftshift ...
        (sinogram5(:,i))))))))));
    img5(indexes) = img5(indexes) + filteredProfileb(newcords)./ ...
        amountofprojections;
end

figure; plot (rampFilter)
set(gca,'FontSize',14)
title(' Ramp filter')
xlabel('Frequency domain x-axis')
ylabel('Filter Intensity')

img3=imrotate(img3,90);
img5=imrotate(img5,90);

figure; imagesc(img3)
set(gca,'FontSize',15)
title({'Integrated absorbance of peak 1', ' spatial distribution', ...
    ' (zeropadded)'})
xlabel('Spatial x-axis (cm)')
ylabel('Spatial y-axis (cm)')
% atick = 0:19.2:1545;
% set(gca,'XTick',atick);

```

```
% set(gca,'XTickLabel', -36:4:36);
% set(gca,'YTick',atick);
% set(gca,'YTickLabel', -36:4:36);
colorbar;

figure;imagesc(img5)
set(gca,'FontSize',15)
title({'Integrated absorbance of peak 2',' spatial distribution ', ...
      '(zeropadded)'})
xlabel('Spatial x-axis (cm)')
ylabel('Spatial y-axis (cm)')
% atick = 0:19.2:355;
% set(gca,'XTick',atick);
% set(gca,'XTickLabel', -36:4:36);
% set(gca,'YTick',atick);
% set(gca,'YTickLabel', -36:4:36);
colorbar;

snew=size(img3,1);
syup=floor((snew-sinogramori)/2);
img3= imcrop(img3,[syup syup sinogramori sinogramori ] );
img5= imcrop(img5,[syup syup sinogramori sinogramori ] );

figure;imagesc(img3)
set(gca,'FontSize',14)
title({'Integrated absorbance of peak 1',' spatial distribution'})
xlabel('Spatial x-axis')
ylabel('Spatial y-axis')
atick = 0:8.2:146;
set(gca,'XTick',atick);
set(gca,'XTickLabel', -18:2:18);
set(gca,'YTick',atick);
set(gca,'YTickLabel', -18:2:18);
colorbar;

figure;imagesc(img5)
set(gca,'FontSize',14)
title({'Integrated absorbance of peak 2',' spatial distribution'})
xlabel('Spatial x-axis')
ylabel('Spatial y-axis')
atick = 0:8.2:146;
set(gca,'XTick',atick);
set(gca,'XTickLabel', -18:2:18);
set(gca,'YTick',atick);
set(gca,'YTickLabel', -18:2:18);
colorbar;

% % % %
sinosum3=sum(img3);
```

```

sinosum5=sum(img5);
lim1=size(vm5,1);
lim2=size(sinosum5,2);
vmx1=(1:1:lim1);
vmx2=(1:1:lim2);

figure;plot(vmx2,sinosum5,vmx1,vm5)
% axis([8 145 0.1 0.16])
set(gca,'FontSize',15)
title({'Numerical comparison of reconstructed and ', ...
'original intergrated absorbances for radon theta=0'})
xlabel('Spatial x-axis (cm)')
ylabel('Integrated absorbance')
atick = 3:8.2:146;
set(gca,'XTick',atick);
set(gca,'XTickLabel', -18:2:18);

ratioimg = abs(img5./img3);

%%%%%%%%%%%%%%%%%%%%%%%%%%%%%%%%%%%%%%%%%%%%%%%%%%%%%%%%%%%%%%%%%%%%%%%%
%                               F.6                               Reconstruction
%%%%%%%%%%%%%%%%%%%%%%%%%%%%%%%%%%%%%%%%%%%%%%%%%%%%%%%%%%%%%%%%%%%%%%%%

p6=-709855.907012939000000;
p5= 1085192.157869590000000;
p4=-658289.120775743000000;
p3= 203447.875269558000000;
p2=-34437.822782179300000;
p1= 4455.665047719480000;
p0=- 27.135186464977200;
Tempimg=p6.*ratioimg.^6+p5.*ratioimg.^5+p4.*ratioimg.^4+p3.*ratioim
g.^3 ...
+p2.*ratioimg.^2+p1.*ratioimg+p0;
Tempimg = medfilt2(Tempimg, [2 2]);

figure
surf(Tempimg, 'edgecolor', 'none')
set(gca,'FontSize',14)
title({'Temperature',' spatial distribution'})
xlabel('Spatial x-axis (cm)')
ylabel('Spatial y-axis (cm)')
atick = 0:8.2:146;
set(gca,'XTick',atick);
set(gca,'XTickLabel', -18:2:18);
set(gca,'YTick',atick);
set(gca,'YTickLabel', -18:2:18);
view([40, 20 , 20])

```

```

colorbar;

figure
imagesc(Tempimg)
set(gca,'FontSize',14)
title({'Temperature spatial distribution'})
xlabel('Spatial x-axis (cm)')
ylabel('Spatial y-axis (cm)')
atick = 0:8.2:146;
set(gca,'XTick',atick);
set(gca,'XTickLabel', -18:2:18);
set(gca,'YTick',atick);
set(gca,'YTickLabel', -18:2:18);
colorbar;

%%%%%%%%%%%%%%%%%%%%%%%%%%%%%%%%%%%%%%%%%%%%%%%%%%%%%%%%%%%%%%%%%%%%%%%%
%%%%%%%%%%%%%%%%%%%%%%%%%%%%%%%%%%%%%%%%%%%%%%%%%%%%%%%%%%%%%%%%%%%%%%%%
% F.7 Concentration Reconstruction
%%%%%%%%%%%%%%%%%%%%%%%%%%%%%%%%%%%%%%%%%%%%%%%%%%%%%%%%%%%%%%%%%%%%%%%%
%%%%%%%%%%%%%%%%%%%%%%%%%%%%%%%%%%%%%%%%%%%%%%%%%%%%%%%%%%%%%%%%%%%%%%%%

S6a=1.001480677006320E-38;
S5a= - 4.808084724561820E-35;
S4a=9.779820441422530E-32;
S3a= - 1.134086269659360E-28;
S2a=8.579527934951380E-26;
S1a= - 4.583700302199190E-23;
S0a= 1.593361318180310E-20;
Sa=S6a.*Tempimg.^6+S5a.*Tempimg.^5+S4a.*Tempimg.^4+S3a.*Tempi
mg.^3 ...
+S2a.*Tempimg.^2+S1a.*Tempimg+S0a;

S6b=1.239167826939600E-38;
S5b= - 4.512478267044460E-35;
S4b=6.703722821440790E-32;
S3b= - 4.913179836378700E-29;
S2b= 1.412754760610980E-26;
S1b= 2.114604138705740E-24;
S0b= 1.327648970193470E-22;
Sb=S6b.*Tempimg.^6+S5b.*Tempimg.^5+S4b.*Tempimg.^4+S3b.*Tempi
mg.^3 ...
+S2b.*Tempimg.^2+S1b.*Tempimg+S0b;

%no need divide by L cause this is per unit length via grid already
c1=(img3./Sa);
c2=(img5./Sb);

c1=c1/6.022E23;
c2=c2/6.022E23;

```

```
%Constructing X and Y axis/matrix
N=size(c1,1);
%number of points for corresponding to zero on axis
center = floor ((N+1)/2);
%value of minimum x axis value
xleft=-center+1;
%true x axis scale, min to zero to max
x=(1:N)-1+xleft;
%Repeat till full x dimension is plotted
x=repmat(x,N,1);
%repeat same steps for Y except top to bottom
ytop=center-1;
y=(N:-1:1).'-N+ytop;
y=repmat(y,1,N);
sca=(N-1)/2 -4;

boundary=sca-13;

IC= sqrt((x).^2+(y).^2)>=boundary;
c1(IC)=0.7E-7;
c2(IC)=0.7E-7;

minval=0.7E-7;
maxval=1.8E-7;

figure;imagesc(c1,[minval,maxval])
set(gca,'FontSize',14)
title({'Reconstructed concentration of peak 1', ...
' (mole/cm^3)spatial distribution'})
xlabel('Spatial x-axis (cm)')
ylabel('Spatial y-axis (cm)')
atick = 0:8.2:146;
set(gca,'XTick',atick);
set(gca,'XTickLabel', -18:2:18);
set(gca,'YTick',atick);
set(gca,'YTickLabel', -18:2:18);
colorbar;

figure;imagesc(c1,[minval,maxval])
set(gca,'FontSize',14)
title({'Reconstructed concentration of peak 2', ...
' (mole/cm^3)spatial distribution'})
xlabel('Spatial x-axis (cm)')
ylabel('Spatial y-axis (cm)')
atick = 0:8.2:146;
set(gca,'XTick',atick);
set(gca,'XTickLabel', -18:2:18);
set(gca,'YTick',atick);
```


11.6 DIRECT FOURIER RECONSTRUCTION (DFR) USING MATLAB

11.6.1 Overview

This MATLAB program begins from the opening of processed integrated absorbance processed prior by LabVIEW and reconstructing temperature and concentration spatial distribution images using the Direct Fourier Reconstruction (DFR) technique.

11.6.2 Pre-processing data for reconstruction

This portion of the program is the same as the FBP process and could be found in section 11.4.2

11.6.3 Interpolation of data in between rays

This portion of the program is the same as the FBP process and could be found in section 11.4.3

11.6.4 Decreasing the interval between each step size

This portion of the program is the same as the FBP process and could be found in section 11.4.4.

11.6.5 Zero padding the data

Zero padding aids in removing artifacts from the final reconstructed image. This portion discusses the zero padding process.

padamt is the amount of zeros to pad at the ends of each projection.

sinogram3 is the renamed version of interay3.

sinogram5 is the renamed version of interay5.

padder is to remember the original non-padded size of sinogram3 and sinogram5 for cropping of image later on in the program.

R3 is the zero padded version of sinogram3 and ready for reconstruction.

R5 is the zero padded version of sinogram5 and ready for reconstruction.

11.6.6 Filtering and reconstruction

This section is about taking the primed initial data to reconstruct the two

images of peaks 3 and 5. Upon reconstruction, the two-line thermometry technique is initiated by dividing each grid over each other.

numOfParallelProjections is the number of projections in sinogram3 and sinogram5.

F3 is a matrix of Fourier slices for each projection.

F5 is a matrix of Fourier slices for each projection.

imageprime is a grid of zeros to conserve memory for future data allocation.

middlecell is the center number of the grid in both x and y axis.

rampFilter2D is the two dimensional filter created to for frequency domain filtering.

img3 is initially an empty grid, constructed to conserve memory, and later the reconstructed grid of peak 3 after the back smearing process.

img5 is initially an empty grid, constructed to conserve memory, and later the reconstructed grid of peak 5 after the back smearing process.

img3cropped is the cropped version of the final reconstructed image of peak 3.

img5cropped is the cropped version of the final reconstructed image of peak 5.

ratioimg is the grid constructed by dividing img5cropped with img3cropped and later used for constructing temperature using the ratio to temperature relationship.

for i = 1 to last projection

1. Calculate the indexes for which angle the projection needs to be allocated based on projection with respect to theta.

for k= 1 to last ray in projection

2. Allocate the Fourier slice at the specified indexes with respect to projection angle.

end

end

11.6.7 Recovery of spatial temperature distribution

This portion of the program is the same as the FBP process and could be found in section 11.4.7.

11.6.8 Recovery of spatial concentration distribution

This portion of the program is the same as the FBP process and could be found in section 11.4.8.

11.6.9 Fourier slice reconstruction (FSR) MATLAB codes

Below is the compilation of the program used to reconstruct temperature and concentration spatial distributions.

```

%%%%%%%%%%%%%%%%%%%%%%%%%%%%%%%%%%%%%%%%%%%%%%%%%%%%%%%%%%%%%%%%%%%%%%%%
%%%%%%%%%%%%%%%%%%%%%%%%%%%%%%%%%%%%%%%%%%%%%%%%%%%%%%%%%%%%%%%%%%%%%%%%
% Start Direct Fourier Reconstruction
%%%%%%%%%%%%%%%%%%%%%%%%%%%%%%%%%%%%%%%%%%%%%%%%%%%%%%%%%%%%%%%%%%%%%%%%
%%%%%%%%%%%%%%%%%%%%%%%%%%%%%%%%%%%%%%%%%%%%%%%%%%%%%%%%%%%%%%%%%%%%%%%%

clear
clc

%%%%%%%%%%%%%%%%%%%%%%%%%%%%%%%%%%%%%%%%%%%%%%%%%%%%%%%%%%%%%%%%%%%%%%%%
%%%%%%%%%%%%%%%%%%%%%%%%%%%%%%%%%%%%%%%%%%%%%%%%%%%%%%%%%%%%%%%%%%%%%%%%
% G.1 Opening file and data priming
%%%%%%%%%%%%%%%%%%%%%%%%%%%%%%%%%%%%%%%%%%%%%%%%%%%%%%%%%%%%%%%%%%%%%%%%
%%%%%%%%%%%%%%%%%%%%%%%%%%%%%%%%%%%%%%%%%%%%%%%%%%%%%%%%%%%%%%%%%%%%%%%%

fileID = fopen('Peak3.txt','r');
formatSpec = '%f %f %f %f';
sizeA = [4 Inf];
rays3 = fscanf(fileID,formatSpec,sizeA);
fclose(fileID);

fileID = fopen('Peak5.txt','r');
formatSpec = '%f %f %f %f';
sizeA = [4 Inf];
rays5 = fscanf(fileID,formatSpec,sizeA);
fclose(fileID);

rays3=rays3';
Numfile=size(rays3);
Numstep=Numfile(1);
rays3=rays3';

Stepsize=179/(Numstep-1);
StartTheta = 0;

```

```

EndTheta = 179;
thetas= StartTheta:Stepsize:EndTheta;

avg3=0.1464;
raysavg3a=zeros(1,Numstep);
raysavg3a(:,:)=avg3;
rays3= [raysavg3a;raysavg3a;rays3;raysavg3a;raysavg3a];

avg5=0.0025;
raysavg5a=zeros(1,Numstep);
raysavg5a(:,:)=avg5;
rays5= [raysavg5a;raysavg5a;rays5;raysavg5a;raysavg5a];

%%%%%%%%%%%%%%%%%%%%%%%%%%%%%%%%%%%%%%%%%%%%%%%%%%%%%%%%%%%%%%%%%%%%%%%%
%%%%%%%%%%%%%%%%%%%%%%%%%%%%%%%%%%%%%%%%%%%%%%%%%%%%%%%%%%%%%%%%%%%%%%%%
% G.2 Interpolation of data in between rays
%%%%%%%%%%%%%%%%%%%%%%%%%%%%%%%%%%%%%%%%%%%%%%%%%%%%%%%%%%%%%%%%%%%%%%%%
%%%%%%%%%%%%%%%%%%%%%%%%%%%%%%%%%%%%%%%%%%%%%%%%%%%%%%%%%%%%%%%%%%%%%%%%

interpo1='linear';
taxis = [-18 :1:18];
scale=[-18 -8 -7 -3 3 7 8 18];
s=scale';
s = scale(3:6 );
sA = scale(1:2);
sB = scale(7:8);

for i=1:Numstep

    ray3 = rays3(:,i);
    r3   = ray3 (3:6 );
    ray3A = ray3 (1:2);
    ray3B = ray3 (7:8);
    zerologic1 =r3~=0 ;
    r3   =r3(zerologic1);
    s1   =s(zerologic1) ;
    r3 = [ray3A;r3;ray3B] ;
    s1 = [sA s1 sB  ];

    interray1(:,i)=interp1(s1,r3,taxis(:),interpo1);
    interray1(isnan(interray1)) = 0;

    ray5 = rays5(:,i);
    r5   = ray5 (3:6 );
    ray5A = ray5 (1:2);
    ray5B = ray5 (7:8);
    zerologic5 =r5~=0 ;
    r5   =r5(zerologic5);
    s5   =s(zerologic5) ;

```

```

r5 = [ray5A;r5;ray5B] ;
s5 = [sA s5 sB  ];

interay5(:,i)=interp1(s5,r5,taxis(:),interpo1);
interay5(isnan(interay5)) = 0;

end

%%%%%%%%%%%%%%%%%%%%%%%%%%%%%%%%%%%%%%%%%%%%%%%%%%%%%%%%%%%%%%%%%%%%%%%%
%%%%%%%%%%%%%%%%%%%%%%%%%%%%%%%%%%%%%%%%%%%%%%%%%%%%%%%%%%%%%%%%%%%%%%%%
% G.3 Decreasing the interval step size
%%%%%%%%%%%%%%%%%%%%%%%%%%%%%%%%%%%%%%%%%%%%%%%%%%%%%%%%%%%%%%%%%%%%%%%%
%%%%%%%%%%%%%%%%%%%%%%%%%%%%%%%%%%%%%%%%%%%%%%%%%%%%%%%%%%%%%%%%%%%%%%%%

step1=1;
step2=step1/2;
step3=step2/2;
step4=step3/2;
step5=step4/2;
step6=step5/2;
intestep=step3;

querysteps= [-18 :intestep:18];

for i=1:Numstep

    reso1=interay1(:,i);
    interay1a(:,i)=interp1(taxis,reso1,querysteps(:),interpo1);

    reso5=interay5(:,i);
    interay5a(:,i)=interp1(taxis,reso5,querysteps(:),interpo1);

end

interay1=interay1a;
interay5=interay5a;

%%%%%%%%%%%%%%%%%%%%%%%%%%%%%%%%%%%%%%%%%%%%%%%%%%%%%%%%%%%%%%%%%%%%%%%%
%%%%%%%%%%%%%%%%%%%%%%%%%%%%%%%%%%%%%%%%%%%%%%%%%%%%%%%%%%%%%%%%%%%%%%%%
% G.4 Zero padding the matrix
%%%%%%%%%%%%%%%%%%%%%%%%%%%%%%%%%%%%%%%%%%%%%%%%%%%%%%%%%%%%%%%%%%%%%%%%
%%%%%%%%%%%%%%%%%%%%%%%%%%%%%%%%%%%%%%%%%%%%%%%%%%%%%%%%%%%%%%%%%%%%%%%%

padamt=700;
sinogram3=interay1;
sinogram5=interay5;

figure;
imagesc(sinogram3)

```

```

set(gca,'FontSize',14)
title('Sinogram of Peak 1')
xlabel('\theta / Projection angle')
ylabel({'Integrated absorbance of ','parallel beams in cm'})
atick = 0:20.7:360;
btick = 0:8.1:240;
set(gca,'XTick',atick);
set(gca,'XTickLabel', 0:10:180);
set(gca,'YTick',btick);
set(gca,'YTickLabel', -18:2:18);
colorbar;

```

```

figure;
imagesc(sinogram5)
set(gca,'FontSize',14)
title('Sinogram of Peak 2')
xlabel('\theta / Projection angle')
ylabel({'Integrated absorbance of ','parallel beams in cm'})
atick = 0:20.7:360;
btick = 0:8.1:240;
set(gca,'XTick',atick);
set(gca,'XTickLabel', 0:10:180);
set(gca,'YTick',btick);
set(gca,'YTickLabel', -18:2:18);
colorbar;

```

```

padder=size(sinogram3,1);
R3=padarray(sinogram3,padamt);
R5=padarray(sinogram5,padamt);

```

```

%%%%%%%%%%%%%%%%%%%%%%%%%%%%%%%%%%%%%%%%%%%%%%%%%%%%%%%%%%%%%%%%%%%%%%%%
%%%%%%%%%%%%%%%%%%%%%%%%%%%%%%%%%%%%%%%%%%%%%%%%%%%%%%%%%%%%%%%%%%%%%%%%
% G.5 Creating filter, executing Fourier Slice Theorem and ratio grid
%%%%%%%%%%%%%%%%%%%%%%%%%%%%%%%%%%%%%%%%%%%%%%%%%%%%%%%%%%%%%%%%%%%%%%%%
%%%%%%%%%%%%%%%%%%%%%%%%%%%%%%%%%%%%%%%%%%%%%%%%%%%%%%%%%%%%%%%%%%%%%%%%

```

```

numOfParallelProjections = size(R3,1);
rampFilter = [floor(numOfParallelProjections/2):-1:0 ...
1:ceil(numOfParallelProjections/2-1)];
rampFilter = rampFilter/(max(rampFilter));

```

```

F3=fftshift(fft(ifftshift(R3)));
F5=fftshift(fft(ifftshift(R5)));

```

```

figure;plot(abs(F3 (:,1)))
set(gca,'FontSize',14)
title('Fourier slice at theta 0 of Sinogram 1')
xlabel('Zeropadded, FFTShifted bin locations')
ylabel('Absolute value')

```

```
figure;imagesc(abs(F3))
set(gca,'FontSize',14)
title({'(Absolute value) Fourier transform of Sinogram 1',' FFTShifted'})
xlabel('\theta / Projection angle')
ylabel('Zeropadded, FFTShifted bin locations')
atick = 0:20.7:360;
% btick = 0:86:1545;
set(gca,'XTick',atick);
set(gca,'XTickLabel', 0:10:180);
% set(gca,'YTick',btick);
% set(gca,'YTickLabel', -18:2:18);
colorbar;
```

```
figure;plot(abs(F5(:,1)))
set(gca,'FontSize',14)
title('Fourier slice at theta 0 of Sinogram 2')
xlabel('Zeropadded, FFTShifted bin locations')
ylabel('Absolute value')
```

```
figure;imagesc(abs(F5))
set(gca,'FontSize',14)
title({'(Absolute value) Fourier transform of Sinogram 2',' FFTShifted'})
xlabel('\theta / Projection angle')
ylabel('Zeropadded, FFTShifted bin locations')
atick = 0:20.7:360;
% btick = 0:86:1545;
set(gca,'XTick',atick);
set(gca,'XTickLabel', 0:10:180);
% set(gca,'YTick',btick);
% set(gca,'YTickLabel', -18:2:18);
colorbar;
```

```
N=size(F3,1);
kend=size(F3,1);
e=(kend-1)/2;
radius= [-e:1:e];
```

```
imageprime=zeros(N,N);
img3=imageprime;
```

```
for i=1:Numstep
thetarad=degtorad(thetas(i));
[x,y]=pol2cart(thetarad,radius);
z1=F3(:,i);
```

```
x=round(x)+e+1;
y=round(y)+e+1;
```

```
for k=1:kend
    imageprime(x(k),y(k))=z1(k);
end

img3=imageprime;

end

imageprime=zeros(N,N);
img5=imageprime;

for i=1:Numstep
thetarad=degtorad(thetas(i));
[x,y]=pol2cart(thetarad,radius);
z2=F5(:,i);

x=round(x)+e+1;
y=round(y)+e+1;

for k=1:kend
    imageprime(x(k),y(k))=z2(k);
end

img5=imageprime;

end

figure; mesh(abs(img3))
set(gca,'FontSize',14)
title({'(Peak 1) Interpolated frequenxy domain of', ...
    ' compiled fourier slices'})
xlabel('Frequency domain x-axis')
ylabel('Frequency domain y-axis')
axis([0 N 0 N 0 25]);
colorbar;

figure; imagesc(abs(img3))
set(gca,'FontSize',14)
title({'(Peak 1) Interpolated frequenxy domain of', ...
    ' compiled fourier slices'})
xlabel('Frequency domain x-axis')
ylabel('Frequency domain y-axis')
axis([0 N 0 N ]);
colorbar;

figure; mesh(abs(img5))
set(gca,'FontSize',14)
title({'(Peak 2) Interpolated frequenxy domain of', ...
    ' compiled fourier slices'})
```

```
xlabel('Frequency domain x-axis')
ylabel('Frequency domain y-axis')
axis([0 N 0 N 0 1]);
colorbar;

figure; imagesc(abs(img5))
set(gca,'FontSize',14)
title({'(Peak 2) Interpolated frequency domain of', ...
' compiled fourier slices'})
xlabel('Frequency domain x-axis')
ylabel('Frequency domain y-axis')
axis([0 N 0 N]);
colorbar;

middlecell = floor(size(img3,1)/2) + 1;
[xcords3,ycords3] = meshgrid(1 - middlecell:size(img3,1) - middlecell);
[xCoords2,yCoords2] = meshgrid(1 - middlecell:size(img5,1) -
middlecell);

rampFilter2D = sqrt(xcords3.^2 + ycords3.^2);
rampFilter2D=rampFilter2D./(max(max(rampFilter2D))));

figure; mesh(rampFilter2D)
set(gca,'FontSize',15)
title(' 2D Ramp filter')
xlabel('Frequency domain x-axis')
ylabel('Frequency domain y-axis')

img3=abs(iffshift(iff2(fftshift(img3))));
img3=imrotate(img3,90);

img5=abs(fftshift(iff2(fftshift(img5))));
img5=imrotate(img5,90);

figure; imagesc(img3)
set(gca,'FontSize',14)
title({'(Zeropadded)Reconstructed space domain of', ...
' Peak 1 intergrated absorbances'})
xlabel('Spatial x-axis in cm')
ylabel('Spatial y-axis in cm')
colorbar;

figure; imagesc(abs(img5))
set(gca,'FontSize',14)
title({'(Zeropadded)Reconstructed space domain of', ...
' Peak 2 intergrated absorbances'})
xlabel('Spatial x-axis in cm')
ylabel('Spatial y-axis in cm')
colorbar;
```

```
snew=size(img3,1);
soriginal=padder;
syup=floor((snew-soriginal)/2);
img3= imcrop(img3,[syup syup soriginal soriginal ] );
img5= imcrop(img5,[syup syup soriginal soriginal ] );
```

```
figure; imagesc(abs(img3))
set(gca,'FontSize',14)
title({'(Cropped) Reconstructed space domain ', ...
      'of Peak 1 intergrated absorbances'})
xlabel('Frequency domain x-axis')
ylabel('Frequency domain y-axis')
atick = 0:8.2:145;
btick = 0:8.2:145;
set(gca,'XTick',atick);
set(gca,'XTickLabel', -18:2:18);
set(gca,'YTick',btick);
set(gca,'YTickLabel', -18:2:18);
colorbar;
```

```
figure; imagesc(abs(img5))
set(gca,'FontSize',14)
title({'(Cropped) Reconstructed space domain of ', ...
      'Peak 2 intergrated absorbances'})
xlabel('Frequency domain x-axis')
ylabel('Frequency domain y-axis')
atick = 0:8.2:145;
btick = 0:8.2:145;
set(gca,'XTick',atick);
set(gca,'XTickLabel', -18:2:18);
set(gca,'YTick',btick);
set(gca,'YTickLabel', -18:2:18);
colorbar;
```

```
ratioimg=img5./img3;
```

```
%Constructing X and Y axis/matrix
N=size(ratioimg,1);
%number of points for corresponding to zero on axis
center = floor ((N+1)/2);
%value of minimum x axis value
xleft=-center+1;
%true x axis scale, min to zero to max
x=(1:N)-1+xleft;
%Repeat till full x dimension is plotted
x= repmat(x,N,1);
%repeat same steps for Y except top to bottom
ytop=center-1;
```

```

y=(N:-1:1).'-N+ytop;
y= repmat(y,1,N);
sca=(N-1)/2 -4;

boundary1=sca-5;
mid=sca+1;

IC= sqrt((x).^2+(y).^2)>=boundary1;

calib=(sinogram5(1:1))/(sinogram3(1:1));
cali=calib/N;

ratioimg=abs(ratioimg);
ratioimg(IC)=cali;
ratioimg(ratioimg < cali) = cali;

%%%%%%%%%%%%%%%%%%%%%%%%%%%%%%%%%%%%%%%%%%%%%%%%%%%%%%%%%%%%%%%%%%%%%%%%
% G.6 Temperature Reconstruction
%%%%%%%%%%%%%%%%%%%%%%%%%%%%%%%%%%%%%%%%%%%%%%%%%%%%%%%%%%%%%%%%%%%%%%%%

p6=-709855.907012939000000;
p5= 1085192.157869590000000;
p4=-658289.120775743000000;
p3= 203447.875269558000000;
p2=-34437.822782179300000;
p1= 4455.665047719480000;
p0=- 27.135186464977200;
Tempimg=p6.*ratioimg.^6+p5.*ratioimg.^5+p4.*ratioimg.^4+p3.*ratioimg.^3 ...
+p2.*ratioimg.^2+p1.*ratioimg+p0;
Tempimg=abs(Tempimg);
Tempimg = medfilt2(Tempimg, [1 1]);

figure;imagesc(Tempimg)
% axis([0 1161 0 1161]);colorbar;
set(gca,'FontSize',15)
title('Reconstructed temperature spatial distribution')
xlabel('Spatial x-axis (cm)')
ylabel('Spatial y-axis (cm)')
atick = 0:8.2:146;
set(gca,'XTick',atick);
set(gca,'XTickLabel', -18:2:18);
set(gca,'YTick',atick);
set(gca,'YTickLabel', -18:2:18);
colorbar;

surf(Tempimg, 'edgecolor' , 'none')

```

```

view ([20,20,20])
set(gca,'FontSize',14)
title('Reconstructed temperature spatial distribution')
xlabel('Spatial x-axis (cm)')
ylabel('Spatial y-axis (cm)')
atick = 0:8.2:146;
set(gca,'XTick',atick);
set(gca,'XTickLabel', -18:2:18);
set(gca,'YTick',atick);
set(gca,'YTickLabel', -18:2:18);
colorbar;

%%%%%%%%%%%%%%%%%%%%%%%%%%%%%%%%%%%%%%%%%%%%%%%%%%%%%%%%%%%%%%%%%%%%%%%%
%%%%%%%%%%%%%%%%%%%%%%%%%%%%%%%%%%%%%%%%%%%%%%%%%%%%%%%%%%%%%%%%%%%%%%%%
% G.7 Concentration Reconstruction
%%%%%%%%%%%%%%%%%%%%%%%%%%%%%%%%%%%%%%%%%%%%%%%%%%%%%%%%%%%%%%%%%%%%%%%%
%%%%%%%%%%%%%%%%%%%%%%%%%%%%%%%%%%%%%%%%%%%%%%%%%%%%%%%%%%%%%%%%%%%%%%%%

S6a=1.001480677006320E-38;
S5a= - 4.808084724561820E-35;
S4a=9.779820441422530E-32;
S3a= - 1.134086269659360E-28;
S2a=8.579527934951380E-26;
S1a= - 4.583700302199190E-23;
S0a= 1.593361318180310E-20;
Sa=S6a.*Tempimg.^6+S5a.*Tempimg.^5+S4a.*Tempimg.^4 ...
+S3a.*Tempimg.^3+S2a.*Tempimg.^2+S1a.*Tempimg+S0a;

S6b=1.239167826939600E-38;
S5b= - 4.512478267044460E-35;
S4b=6.703722821440790E-32;
S3b= - 4.913179836378700E-29;
S2b= 1.412754760610980E-26;
S1b= 2.114604138705740E-24;
S0b= 1.327648970193470E-22;
Sb=S6b.*Tempimg.^6+S5b.*Tempimg.^5+S4b.*Tempimg.^4 ...
+S3b.*Tempimg.^3+S2b.*Tempimg.^2+S1b.*Tempimg+S0b;

%no need divide by L cause this is per unit length via grids
c1=(img3./Sa);
c2=(img5./Sb);

c1=c1/6.022E23;
c2=c2/6.022E23;

%Constructing X and Y axis/matrix
N=size(c1,1);
%number of points for corresponding to zero on axis
center = floor ((N+1)/2);

```

%%%

% end

%%%

%%%